FUNCTIONAL COLLOIDS FROM AMPHIPHILIC POLYMER ASSEMBLIES AND PEPTIDES/POLYPEPTIDES

A Dissertation
Submitted to the Graduate Faculty
of the
North Dakota State University
of Agriculture and Applied Science

By

Oksana Zholobko

In Partial Fulfillment of the Requirements
for the Degree of
DOCTOR OF PHILOSOPHY

Major Department:
Coatings and Polymeric Materials

July 2019

Fargo, North Dakota

North Dakota State University

Graduate School

Title

FUNCTIONAL COLLOIDS FROM AMPHIPHILIC POLYMER ASSEMBLIES AND PEPTIDES/POLYPEPTIDES

By

Oksana Zholobko

The Supervisory Committee certifies that this ***disquisition*** complies with North Dakota State University's regulations and meets the accepted standards for the degree of

DOCTOR OF PHILOSOPHY

SUPERVISORY COMMITTEE:

Dr. Andriy Voronov

Chair

Dr. Dante Battocchi

Dr. Mohiuddin Quadir

Dr. Scott W. Pryor

Approved:

July 31, 2019

Date

Dr. Dean Webster

Department Chair

ABSTRACT

The use of responsive polymers, where even minor changes in one of the macromolecular characteristics triggered by the external stimuli can cause drastic changes in the material function or performance, is widely studying area of research. Formation of the thermodynamically stable polymer-peptide colloids, such as mixed micellar assemblies or polymer-enzyme conjugates, loading capacity of the colloids, and cargo activity all depend on the macromolecular interactions within the peptide/polypeptide-polymer system.

The goal of this work is to investigate interactions between range of new polymers and various cargo molecules and determine whether those interactions affect the physicochemical properties of the resulted colloids. For this purpose, two types of colloid systems were explored: i) peptide-loaded invertible micellar assemblies (IMAs), formed using hydrophobic interactions between amphiphilic invertible polymers (AIP) and peptides (HA, V5, or peptide-based vaccine), and ii) polymeric cellulosomes made from polymer ligand (PL), copolymer of glycidyl methacrylate (GMA) and poly(ethylene glycol) methyl ether methacrylate (PEGMA) and mixture of cellulases, using covalent bonding. The purpose of the research was to evaluate if colloids properties are affected by changes in responsive polymer characteristics as well as if the developed macromolecular structure and composition need further synthetic modification/optimization.

AIP-related part of this dissertation is focused on i) understanding of interaction between peptides and AIPs, and formation of mixed micellar assemblies; ii) further behavior of cargo peptide molecules in the micellar interior under the AIP conformational changes, triggered by IMAs localization at polar and nonpolar interface; iii) evaluation of the impact of IMAs on model lipid membrane diffusivity and permeability. Besides, AIP-peptide assemblies were tested in vitro

and in vivo in order to evaluate the cargo delivery, antibody response, and immunity protection in vaccinated pigs against Swine influenza viruses (SIV).

To explore the feasibility of covalent bonding in formation of responsive polymer-based colloids, enzyme-polymer conjugates (EPCs) were designed and their enzymatic catalytic activity for the biomass hydrolysis was further tested. The effect of conjugation on catalytic activity, conjugation efficiency, glucose inhibition effect, type of substrate, and type of biomass pretreatment were evaluated and compared to free enzymes.

ACKNOWLEDGEMENTS

First and foremost, I would like to express my sincere gratitude to my advisor, Dr. Andriy Voronov, for his guidance and support during my research. He is a phenomenal mentor. Without his help this work would not be possible.

I would also like to thank the members of my Examination Committee, Dr. Dante Battocchi, Dr. Mohiuddin Quadir, and Dr. Scott W. Pryor for their time, support, and assistance throughout my graduate research.

My deepest appreciation goes to the members of Dr. Voronov's group: Zoriana Demchuk, Yehor Polunin, Dr. Ananiy Kohut, Dr. Ivan Hevus, Dr. Olena Kudina, Dr. Ihor Tarnavchyk, Dr. Andriy Popadyuk, Dr. Kyle Kingsley, Dr. Vasylyna Kirianchuk, Dr. Oleh Shevchuk, and Dr. Vitalii Serdiuk for their support and assistance with some experiments. Especial thanks to the students I had an honor to supervise: Vaida Crofutt and Angeline Utomo during Governor's School program; Joseph Domine and Jae Hyun Park during their undergraduate studies.

My sincere gratitude to our collaborators: Dr. Sergiy Minko and his group members Dr. Andrey Zakharchenko and Dr. Nataraja Sekhar Yadavalli (University of Georgia, Athens, GA, USA); Dr. S. Pryor's group members Ademola Hammed and Dr. Nurun Nahar; Dr. Igor Luzinov and Dr. Nikolay Borodinov (Clemson University, Clemson, SC, USA); Dr. Zhongyu Yang and Dr. Yanxiong Pan; Dr. Sheela Ramamoorthy and Dr. Gagandeep Singh; Shane Stafslien and Lyndsi Vanderwal; Dr. Tia Keyes and Sivaramakrishnan Ramadurai (Dublin City University, Dublin 9, Ireland) for working with our group on different projects, for their guidance, support, and helpful suggestions.

I would like to thank Dr. Chunju Gu, James Bahr, Greg Strommen, and Dr. Angel Ugrinov for their support in the instrumental analysis of my work.

I am very thankful to all present and past faculty, staff, and students in the Coating and Polymeric Materials Department for very supportive and friendly atmosphere.

My sincere gratitude to my parents Yuriy and Kateryna Zholobko and my sister Mariana Zholobko for all their support throughout this journey.

Finally, I would like to thank the National Science Foundation and ND Department of Commerce for providing financial support for my research.

DEDICATION

To my lovely family and friends. I am gratefully thankful for all your support.

TABLE OF CONTENTS

LIST OF TABLES

LIST OF FIGURES

LIST OF SCHEMES

LIST OF ABBREVIATIONS

4-Amino-TEMPO……... 4-Amino-(2,2,6,6-Tetramethylpiperidin-1-yl)oxyl

ACF……. Autocorrelation Function

AIPs……..Amphiphilic Invertible Polymers

ATTO……...DOPE-Atto655

BCA……. Bicinchoninic Acid Assay

BODIPY…….. ethyl-BODIPY

CMC…….……Carboxy Methyl Cellulose

cmc……...Critical Micelle Concentration

C_{pp}…….……... Critical Packing Parameter

CPS…….. Counts Per Second

D…….. Diffusion Coefficient

DLS……..Dynamic Light Scattering

DMF…….Dimethylformamide

DMSO……..Dimethyl Sulfoxide

DOPC……...1, 2-dioleoyl-*sn*-glycero-3-Phosphocholine

DPV…….....Day Post Vaccination

ECM……Equivalent Circuit Model

EIS……Electrochemical Impedance Spectroscopy

ELISA…….. Enzyme-Linked Immunosorbent Assay

EPCs…….... Enzyme-Polymer Conjugates

EPR…….. Electron Paramagnetic Resonance

FLCS……Fluorescence Lifetime Correlation Spectroscopy

GPC …….Gel Permeation Chromatography

HBSS……Hank's Balanced Salt Solution

HLB……..Hydrophilic Lipophilic Balance

IAV…….. Influenza A Viruses

IFA…….. Immunofluorescence Assay

IHC…….. Immunohistochemistry

IMAs…..…….. Invertible Micellar Assemblies

IP…….…Interstitial Pneumonia

M_n……..…….. Number Average Molecular Weight

MS……Mass Spectrometry

MSLB…….. Microcavity Supported Lipid Bilayer

M_w…….……... Weight Average Molecular Weight

NMR…… Nuclear Magnetic Resonance

PBS…….. Phosphate Buffered Saline

PDI…….. Polydispersity Index

PDMS…….. Polydimethylsiloxane

PEG……..Polyethylene Glycol

PICM……Polyion Complex Micelles

PL…….Polymer Ligand

PTHF…….…….. Polytetrahydrofuran

SDSL……Site-Directed Spin Labeling

SIV……..…….. Swine Influenza Viruses

THF…….. Tetrahydrofuran

CHAPTER 1. INTRODUCTION: RESPONSIVE POLYMERIC SYSTEMS. TYPES, FORMATION AND THEIR INTERACTION WITH BIOMOLECULES

1.1. Introduction to responsive polymers

Responsive polymers are polymeric macromolecules that are able to respond to certain external and/or internal physical/chemical stimuli, including pH, light, temperature, chemicals, environmental polarity, and magnetic fields. [1–10] The triggered polymers produce visible or detectable micro- or nanoscale changes, such as molecular bond rearrangement/cleavage, morphology, and molecular motion that can encourage macroscopic properties changes, such as shape, color, and functionality. Due to the variety of functional groups and backbone selection, responsive polymers can be made to provide a diversity of specific chemical, biological, mechanical, optical, electrical, or other properties and variety of forms, such as micro/nanoparticles, thin film, bulk, and composites. The development of responsive polymers is frequently motivated by the desire to mimic nature. [11,12] Such smart polymers have found their applications in variety of the fields of medicine and biology. They can be used for controlled drug delivery, tissue engineering scaffolds, as biosensors and sensors, chemo-mechanical actuators, environmental remediation, and for a lot of other applications. [13–19] Furthermore, multi-responsive polymers can be generated by integrating other functional groups into the responsive polymers. [20,21] Additionally, biologically responsive systems, such as glucose responsive polymers [22,23] and enzyme responsive polymers [24,25] can also be synthesized. This allows responsive polymers the ability to respond to stimuli presented in biological samples. [26]

Over the years, a lot of efforts have been directed to optimizing the functionality of responsive polymers and discovering new and advanced applications.

1.2. Types of commonly used responsive polymeric system

Living systems triggered by the external stimuli adapting themselves to varying conditions. A lot of efforts have been made to mimic the nature resulting in development of smart polymers. [27,28] They have found to be very promising in biomedical applications, such as drug delivery systems or enzymatic hydrolysis. The development of thermosensitive liposomes that release the drugs via hyperthermia was firstly reported in 1970s and provide a great ability to design of responsive polymers for drug delivery. [6,29–32] The application of newly synthesized systems is related to the administration in the body. Therefore, they should be simple to use, manage the delivery to the specific locations triggered by a stimulus, and be non-toxic. [33]

A variety of responsive polymer based materials has been developed, including non-crosslinked block copolymer assemblies and crosslinked gel networks. The most widely used responsive polymers architectures in biomedical applications are micelles, dendrimers, polymersomes, hydrogels, and nanoparticles (**Figure 1.1**.).

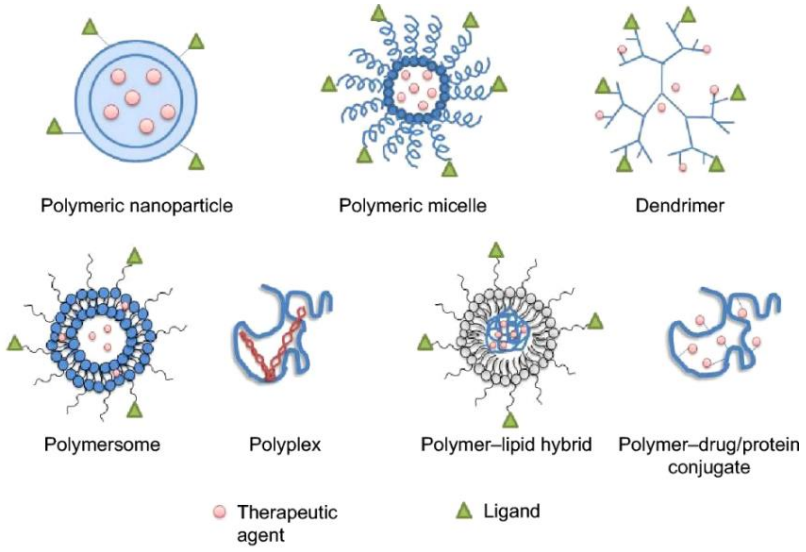

Figure 1.1. Types of polymeric systems used in biomedical applications. [34]

Hydrogels have been widely used for a variety of biomedical applications because of their porous structure and ability to swell in water. Additionally, some hydrogels can change their swelling degree in response to environmental changes. [35–38] The most important feature for hydrogel responsive polymers is the swelling triggered release mechanism. [39] Incorporation of stimuli-responsive unit into hydrogels allow the on demand drug release triggered by external stimuli, e.g. electricity. [40] Recently, the combination of the hydrogel-forming microneedles and light responsive drug conjugates resulted in the development of a devices for an on-demand transdermal delivery of drugs. [41]

Other class of widely used polymeric architectures – dendrimers that are three-dimensional, highly branched, well-organized nanoscopic macromolecules. Mostly, they are built layer-by-layer starting from a central core, by the repetition of two consecutive reaction steps. Each new branching layer produces a new "generation" (noted G). Due to their structure, dendrimers are widely used in a variety of areas, such as catalysis, biomedical applications including nanomedicine. [42,43] Several mechanisms of encapsulation of cargo molecules with different properties (hydrophobic, hydrophilic, or amphiphilic character) into dendritic structures are possible, such as hydrophobic, electrostatic, acid–base effects, hydrogen bonding, and in the inner part of the dendrimer. Cargo molecules can also be covalently conjugated to the dendrimer molecule. [44–46]

Natural cell membranes made up of a phospholipid bilayer. Later, the natural lipids (mostly phospholipids) or their synthetic alternatives can self-assemble into vesicles, termed liposomes. Liposomes are low toxic, biocompatible structures that are able to provide target delivery and controlled release of cargo molecules. [47] Liposomes are phospholipid bilayers membranes that can form spherical structures with internal hydrophilic compartment and external phospholipids.

A few types of liposomes are existing, depending on the lamellar number, their form, size, and formulation of constitutes. Liposomes are effective in clinical diagnostic, therapeutic, such as drug and gene delivery, and vaccine improvement. Importantly, that the use of a variety of liposomal formulations in clinical trials is usually more problematic than the use of conventional liposomal types, such as these formulations is not providing a complete system, moreover, each one has its own deficiency. [48–50]

Polymersomes are vesicles made from a bilayer membrane of synthetic amphiphilic block copolymers. Compared to liposomes, polymersomes are more stable, robust, and less permeable. They are typically hollow spheres containing an aqueous media in the core surrounded by a bi-layer membrane (**Fig. 1.2**). The bilayer membrane consists of hydrophilic coronas that separating the hydrophobic middle part of the membrane and protecting the core from the outside medium. The core can be used for the encapsulation of therapeutic cargo molecules such as enzymes, drugs, other peptides and proteins, and RNA and DNA fragments. [51,52]

Generally, block copolymers can achieve a variety of microstructures due to incompatibility between two blocks and connectivity constraint, such as polymersomes, micelles, and nanoparticles. Micelles formation is based on the self-assembly and is driven by solution thermodynamics. The nanoparticles formation is ‘kinetically’ controllable with various factors, such as solvent contents, pH level, temperature, etc.

Polymeric nanoparticles are widely used materials for nanomedicine. The particle size, shape, dimensions, and aspect ratio influence on the cellular uptake, pharmacodynamics, and pharmacokinetics in nanomedicine applications. Particle size affects the toxicity, targeting, uptake mechanisms, degradation, and functions of circulation. Particle size can be controlled by either the factors related to the material selection (e.g., surfactant, polymer, and concentrations) or

fabrication methods (e.g., type of method, monomer, control agent, polymerization type, initiator, flow rate, and nozzle diameter). The interactions between cell membrane and particle can be affected by the route of nanoparticle uptake that can be defined in two following stages: an adhesion process of the particle to the cell membrane and an internalization process. The particle size significantly affects on the adhesion process and the interaction with biological cells. [54]

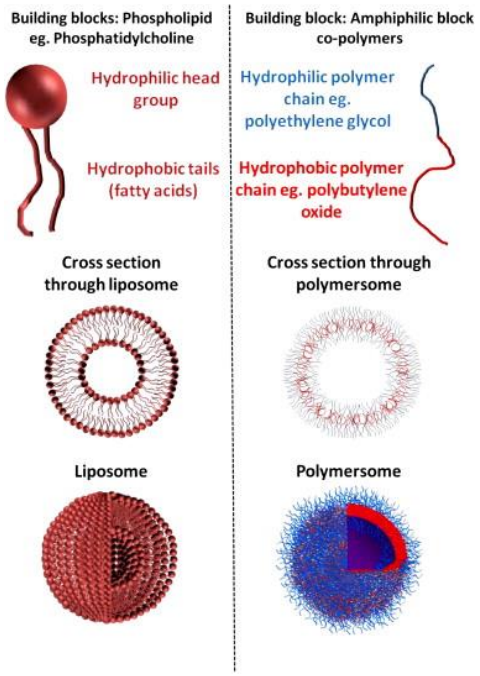

Figure 1.2. Liposome and polymersome structures. [53]

Particle shape also dictates the adhesion process and transport of particles. Spherical nanoparticles are the most commonly used shape of polymeric nanoparticles due to their advantages, such as shape and size, high surface-to-volume ratio, unique optical properties, and modifiable and versatile platform to build upon. Asymmetrical and nonspherical particles are commonly used to perform complicated tasks and imitate complex biological systems. By tailoring the geometric features of polymeric particles, the specific chemical and physical properties of the particles can be achieved. The anisotropic shapes of particles allow exceptional interactions with

complicated biological systems in drug delivery/release, transport, movement, circulation time, and adhesion. Asymmetrically shaped particles can be used in numerous nanomedicine applications, such as self-assembly, sensing, immunoengineering, tissue engineering, and therapeutic and diagnostic delivery. [55]

1.3. Polymeric micelles

Polymeric micellar structures that are formed by self-assembling from amphiphilic block or graft copolymers are very widely studied subjects in nanomedicine and nanotechnology. Amphiphilic polymers in the selective solvents self-organize in supramolecular assemblies with cylindrical, spherical, and vesicular morphologies. [23,56,57] Their morphology and size critically rely on the compositions and chemical structures of the block copolymers. The type of micelles depends on the architecture of amphiphilic molecule and on solution parameters (polymer concentration, type of solvent, pH, solvent/cosolvent ratio, temperature, ionic strength, and others) (**Figure 1.3**). [58,59]

Generally, the hydrophobic blocks of polymer macromolecules assemble forming a core that provides a microenvironment appropriate for the lipophilic drugs incorporation, while the hydrophilic blocks form a corona or outer shell, serving as stabilizing interface between the external medium and the hydrophobic core. [61]

Usually, the inner core of micelle is formed by hydrophobic interactions between copolymer blocks. At the same time, different types of interactions can be used for micelles formation. The electrostatic interactions between charged block copolymers result in the creation of polyion complex micelles. Also, formation of complex through hydrogen bonding and metal-ligand coordination can take a place in the micelles formation. [62–64]

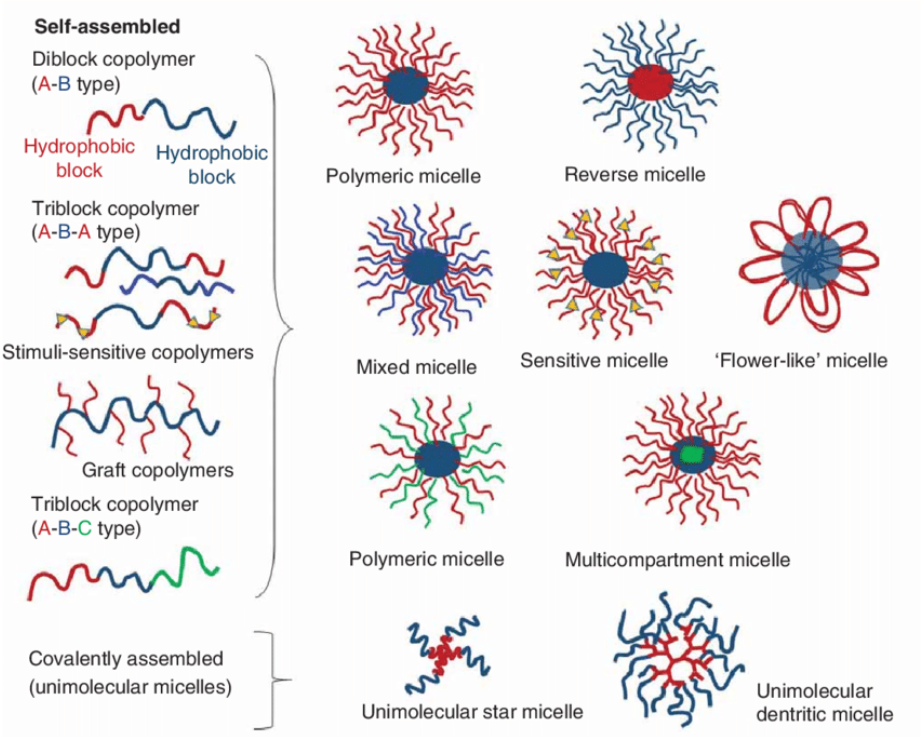

Figure 1.3. Types of polymeric micelles that can be formed depending on the copolymer architecture and the intermolecular forces. [60]

By using a triblock copolymers, multi-compartment micelles with few well-differentiated compartments can be formed. [65,66] At the same time, using of triblock copolymers with short hydrophobic ends and long hydrophilic midsection will result in formation of a 'flower-like' polymeric micelles in aqueous media. These micelles can be used for the incorporation of poorly soluble drugs in the hydrophobic core and for sustainable drug release for long periods of time. Recent studies showed that the hydrophobic interactions between 'flower-like' polymeric micelles formed from poly(L-lactic acid)-b-poly(oxide ethylene)-b-poly(L-lactic acid) block copolymer and incorporated biomolecule lead to the prolonged release. The rate of the release can be modified by block copolymer composition and crystallinity. Increasing the crystallinity of the copolymer blocks results in increasing of drug release rate, possibly due to the fact that crystalline units stack

together, leaving the drug largely at the periphery. At the same time, using of more amorphous blocks results in better integration/dispersion of the drug within the polymer matrix. [60]

Unimolecular chains that exhibit three-dimensional domains with discriminate polarity may form micelle-like structures as well. Unimolecular polymeric micelles are a type of single-molecule micelles that have a shell and a core with two different polarities and covalently linked together. Unimolecular micelles are formed when the amphiphilic polymeric macromolecules are dispersed in a suitable solvent that is a good solvent for the fragment with one polarity and precipitant for the fragment with the opposite polarity. The hydrophobic polymeric core is stabilized by the hydrophilic shell and, therefore, is able to avoid the core-core intermolecular interactions. Contrarily to conventional micelles that are thermodynamic aggregates of amphiphilic macromolecules above a certain concentration, known as critical micelle concentration (cmc), unimolecular micelles are stable at high dilutions and can be formed below expected cmc values, predicted based on hydrophilic/lipophilic balance of the amphiphilic polymer. In order to prepare the unimolecular micelles, highly branched macromolecules, such as hyperbranched, multi-arm, star, bottlebrush, Y shaped, and cyclic polymers can be used. [67] The size and the area of application of these polymeric micelles can be affected by the molecular weight and composition of polymers. Increasing the amount of soluble branches, hindrance and complexity of polymeric structures more favored will result in the smaller size of the micelles. [68]

Mixed micelles can be formed from two or more copolymers that have similar blocks of different length or dissimilar blocks. However, the hydrophobic blocks should have similar molecular weight and different hydrophilic/hydrophobic balance of copolymers. [69,70] Mixed polymeric micelles showed improved kinetic and thermodynamic stability in comparison to single

copolymer micelles and, therefore, favor drug encapsulation and prevent early release. Under ideal conditions, the cmc of a mixed micelle formed from two copolymers can be estimated using the following equation:

$$\frac{1}{cmc} = \frac{X_1}{cmc_1} + \frac{X_2}{cmc_2} \quad (1.1)$$

where X_1 and X_2 represent the molar fractions of each copolymer, and cmc_1 and cmc_2 the cmc values of the copolymers in separate.

However, the chemical and physical interactions between polymeric fragments can cause the deviations of the additivity rule. [71] Some recent studies reported that the mixed micelles showed more efficient incorporation of the poorly soluble drug, in comparison to conventional micelles. At the same time, the stability of mixed micelles was not affected by the dilutions and, therefore, decreasing of polymer concentration in the solution, which is important for the drug delivery systems due to the dilution effect under *in vivo* administration. Additionally, the mixed micelles with the incorporated drug were physically stable at room temperature for at least 6 months. [72]

All the above-mentioned micellar types have been designed for the largely hydrophobic drugs delivery and not for the delivery of hydrophilic drugs. Reverse polymeric micelles can be used for the delivery of hydrophilic drugs. In nonaqueous media, the reverse polymeric micelles can be formed with the hydrophilic core and hydrophobic shell. Some recent studies reported the formation of reverse micelles from hyperbranched polymers and dendrimers. The hydrophobic modification of poly(amidoamine) and poly(glycerol) leads to the creation of the amphiphilic polymers. The hydrophobic shell-forming fragments provide the micelles solubility in organic solvents. [73]

Reverse micelles are specifically useful for application in oily systems. The injections of steroids or nutrients that mandatory for comatose patients are made as oily injections. At the same time, the reverse micelles can be used for the hydrophilic drug incorporation in such injections. Additionally, the reverse micellar assemblies can be used for oral delivery of drugs. Drugs incorporated in reverse micelles demonstrate good biological activity, however, the stability of the micelles is often contrariwise related to the water content of the formulation. [60]

Commonly, micelles are spherical if the hydrophobic block is shorter than the hydrophilic one. The micelles of lamellae and rod morphologies are forming from the copolymers with shorter hydrophilic blocks. [74]

J.N. Israelachvili and co-authors proposed to use the critical packing parameter (C_{pp}) for the surfactant molecule: $C_{pp} = v/a_0l_c$ (**Fig. 1.4**). It allows to understand the relationship between the resulting morphology of the particle and the structure of the polymeric molecule, such as hydrophobic tail length (l_c), head group area (a_0), and volume of the hydrophobic segment (v). [75] Changes in these parameters will result in different morphology of the micellar structures. The packing parameter can be used for amphiphilic block copolymers as well, such as the hydrophobic fragment is a mimic of the tail of surfactant, while the hydrophilic block mimicking the polar head group. [76] According to the concept, at the equilibrium, if $C_{pp} \leq ⅓$ - spherical micelles are formed. Cylinders will form when p is between $⅓ < C_{pp} \leq ½$, while vesicles will form when $½ < C_{pp} \leq 1$. (**Fig. 1.4**). [77] However, in case of block copolymers some kinetically trapped structures that are out-of-equilibrium are possible. In this case, the morphology cannot be predicted using critical packing parameter and relate to the process of self-assembly. In practice, critical packing parameter calculation is extremely difficult and hence only occasionally used. While the mass and volume fractions of hydrophobic and hydrophilic blocks are more commonly measured

parameters. [78] However, it should be noticed, that the relative changes in volume are different for different monomers, such as monomers with branched side chains occupy more volume in comparison to the linear monomer with the same mass. [79]

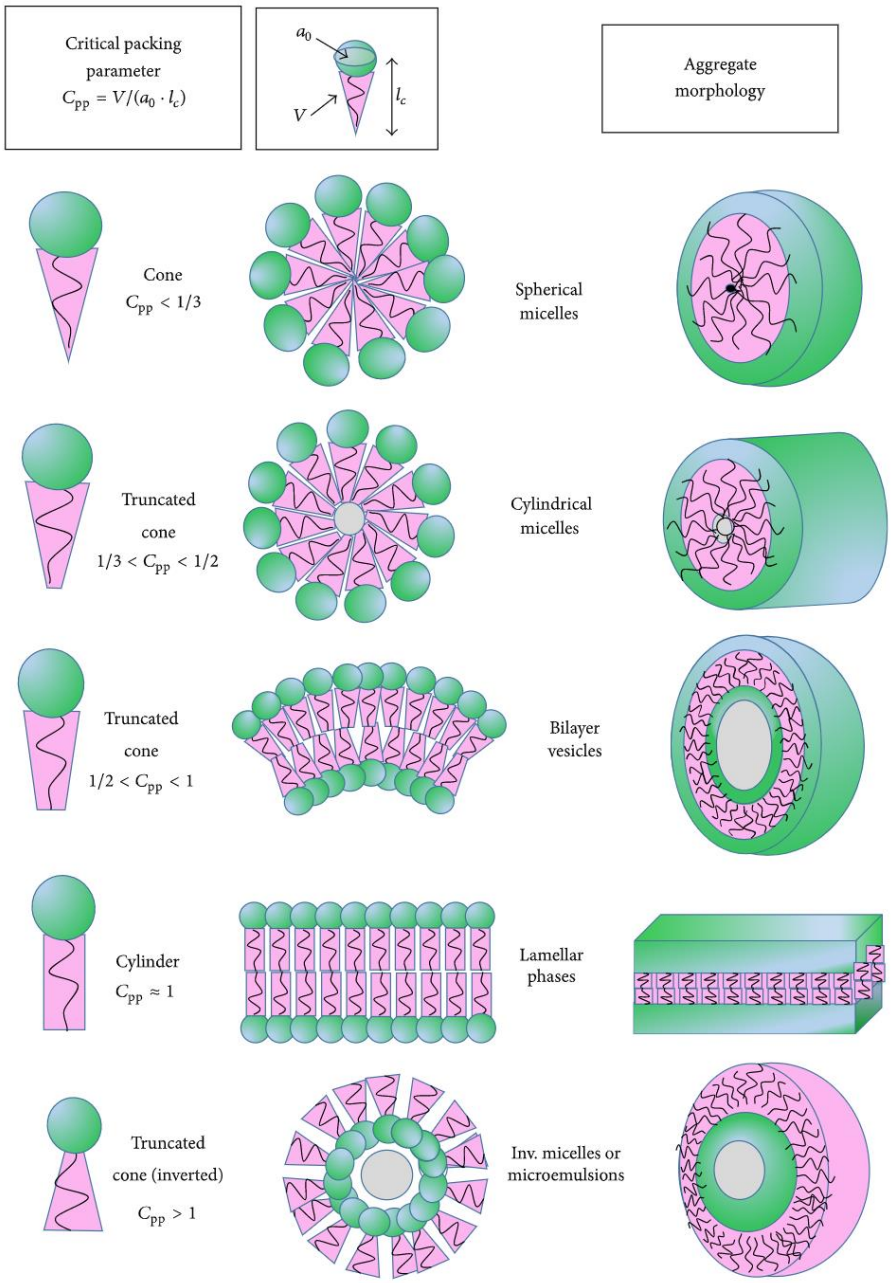

Figure 1.4. Different morphologies that can be predicted from the critical packing parameter C_{pp}. [77]

Specific morphology can be obtained by regulating the volume fraction of hydrophobic and hydrophilic blocks through polymerization. At the same time, the morphology predicted using the critical packing parameter calculations is corresponded to the thermodynamic equilibrium. If the system cannot reach the equilibrium then intermediate morphologies can be formed, but the morphology that was predicted by critical packing parameter will not be reached. [79]

Classification of micellar assemblies formed from block copolymers due to the type of intermolecular forces that resulted in core segment segregation from aqueous media can be divided in three main categories: amphiphilic micelles, polyion complex micelles (PICM), and micelles originated from metal complexation.

Amphiphilic block copolymers self-assembly in aqueous media due to hydrophobic and non-polar interactions between the hydrophobic polymer chains that formed core. At the same time, micellar formation is also triggered by the increase in solvent molecules entropy caused by the removal of hydrophobic components from the water. [58] Amphiphilic copolymers that are used in biomedical applications commonly composed from either poly(amino acid) derivative or polyester as the hydrophobic fragment. Poly(lactic acid) (PLA), poly(glycolic acid), and poly(q-caprolactone) biocompatible polyesters were approved by the Food and Drug Administration (FDA) and widely used for biomedical applications in humans. Also, poly(l-amino acid) (PAA), poly(aspartic acid) (PAsp), poly(l-lysine) (PLys), poly(glutamic acid) (PGlu), and poly(histidine) (Phis) are commonly used. By changing the chemical structure of PAA, the degree of immunogenicity and enzymatic degradability can be tailored. [80] Polyethers, the other promising class of compounds that can be used to form the amphiphilic micelles. Poloxamers, such as copolymers of poly(ethylene glycol)-b-poly(propylene oxide)-bpoly(ethylene glycol)) (PEG-b-PPO-b-PEG) are the mostly known polyethers. [81] By using the temperature responsive polymer

blocks, the micelles formation can occur above the lower critical solution temperature (LCST) of polymer owing to the hydrophobic interaction between the dehydrated polymer chains. [82–84] Copolymer, synthesized using poly (N-isopropylacrylamide) as a comonomer, e.g. poly (ethylene oxide)-block-poly(N-isopropylacrylamide) (PEO-b-pNIPAm), becomes amphiphilic in aqueous media above 37 °C and self-assembles into micellar assemblies that can encapsulate both hydrophobic and hydrophilic molecules. Decreasing the temperature leads to the disassembling of micelles and release the cargo occurs. [85]

Due to the electrostatic interactions between oppositely charged polyelectrolytes under an electrically neutral conditions, polyions form visible aggregates, such as precipitates or coacervates. In contrast, the mixture of oppositely charged block copolymers that compose from hydrophilic and hydrophobic fragments exhibits no precipitation and remains transparent. The formation of PICM combines features of interpolyelectrolyte complexes and amphiphilic micelles. PICM is formed from the polymers that consist of a polyionic fragment and hydrophilic segment that ensures the solubility in aqueous media (**Fig. 1.5**). [86] Obviously, a wide variety of polyelectrolytes can be used for the formation of PICM core. PICM formed from polymers that contain protonated amines at physiological pH, e.g. PLys, poly(ethyleneimine) (PEI), and polyamidoamide, can be used for incorporation of polyanionic molecules, including plasmid DNA, polysaccharides, oligodeoxyribonucleotides (ODN), and enzymes. [87–91] For the incorporation of polycationic drugs, polymers with negatively charged units must be used, such as PAsp or poly(methacrylic acid) (PMAA). [92]

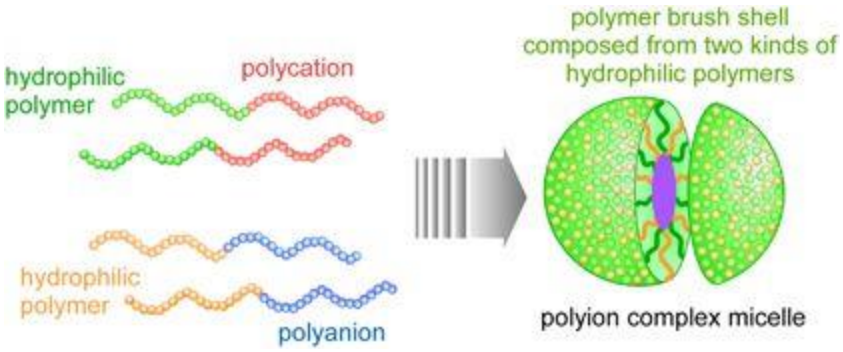

Figure 1.5. PICM formation from a pair of oppositely charged block copolymers. [93]

The properties of polymeric micellar structures, such as physical and biological, rely on the properties of initial blocks used for the formation of micelle. Therefore, the choice of appropriate polymers is important for the formation of micellar structures for specific applications. [94]

1.4. Types of interactions between polymer and biological compound

To design the polymer-based system for biomedical application, several parameters should be considered, including the loading capacity of biological compound, size of the assemblies, stability, *etc.* [95] The procedure that is used to incorporate the drug is important as well. Based on the physical and chemical properties of the block copolymer, the cargo loading procedures can be divided into two main categories. [61] The first category is direct dissolution. In this case, the block copolymer is directly dissolving with the cargo in an aqueous media. This technique is mostly used for moderately hydrophobic copolymers, such as poloxamers or to prepare PICM. In some cases, the heating of the aqueous media may be necessary for micellization due to the dehydration of the core forming fragments.

The second class of cargo-loading procedures applies to amphiphilic copolymers that are not willingly soluble in aqueous media and for which an organic solvent common to both the copolymer and the drug is needed. The mechanism by which micelle formation is persuaded

depends on the solvent-removal procedure. The dialysis of the copolymer mixture against water can be used for water-miscible organic solvents. Here, the micellization is triggered by the slow removal of the organic phase. Alternatively, the thin-film technique entails organic phase evaporation to yield a polymeric film where polymer–cargo interactions are favored. Following rehydration of the thin film with an aqueous solution produces cargo-loaded micelles. Physical entrapment of a hydrophobic drug can be further attained through an oil-in-water emulsion procedure which involves the use of a non-water-miscible organic solvent. In addition, the lyophilization process of the dissolved both the polymer and the biomolecule in a water/organic solvent mixture can be used. Cargo-loaded micelles are formed spontaneously upon re-dissolving of the freeze-dried polymer–cargo sample in target media.

However, interactions between polymer carrier and cargo molecules highly influencing on the loading capacity and system stability and can either enhance or diminish the efficiency of cargo. Therefore, some common interactions between polymer macromolecules (**Fig. 1.6**) and biological molecules will be discussed further.

1.4.1. Hydrogen bonding interactions between polymer macromolecules and cargo

Hydrogen bonding between the polymer macromolecules and cargo in the micellar core improves the kinetic stability and increases the loading capacity and efficiency of the drug. Addition of small molecule linkers to the polymeric system will promote the formation of hydrogen bonds within the micellar core and improve the stability. [96]

It was shown that the incorporation of urea functionalities, which promote the hydrogen bond interactions, to the hydrophobic block of amphiphilic copolymers results in decreasing of cmc of copolymers, enhancing the micellar stability, and improving the loading capacity, while not significantly influence on cytotoxicity. [97,98] It was reported that the micelles formed from

carboxylic acid-functionalized poly(carbonate) and polyethylene glycol (PEG) copolymers after the drug incorporation formed aggregates with the 595 nm particle size. Which can be explain by the strong ionic interactions between the amine group in the drug and the acid group in the polymer. However, the incorporation of urea functionalities results in formation of mixed micelles and drug loading, while remaining the stable system with high loading capacity. [99]

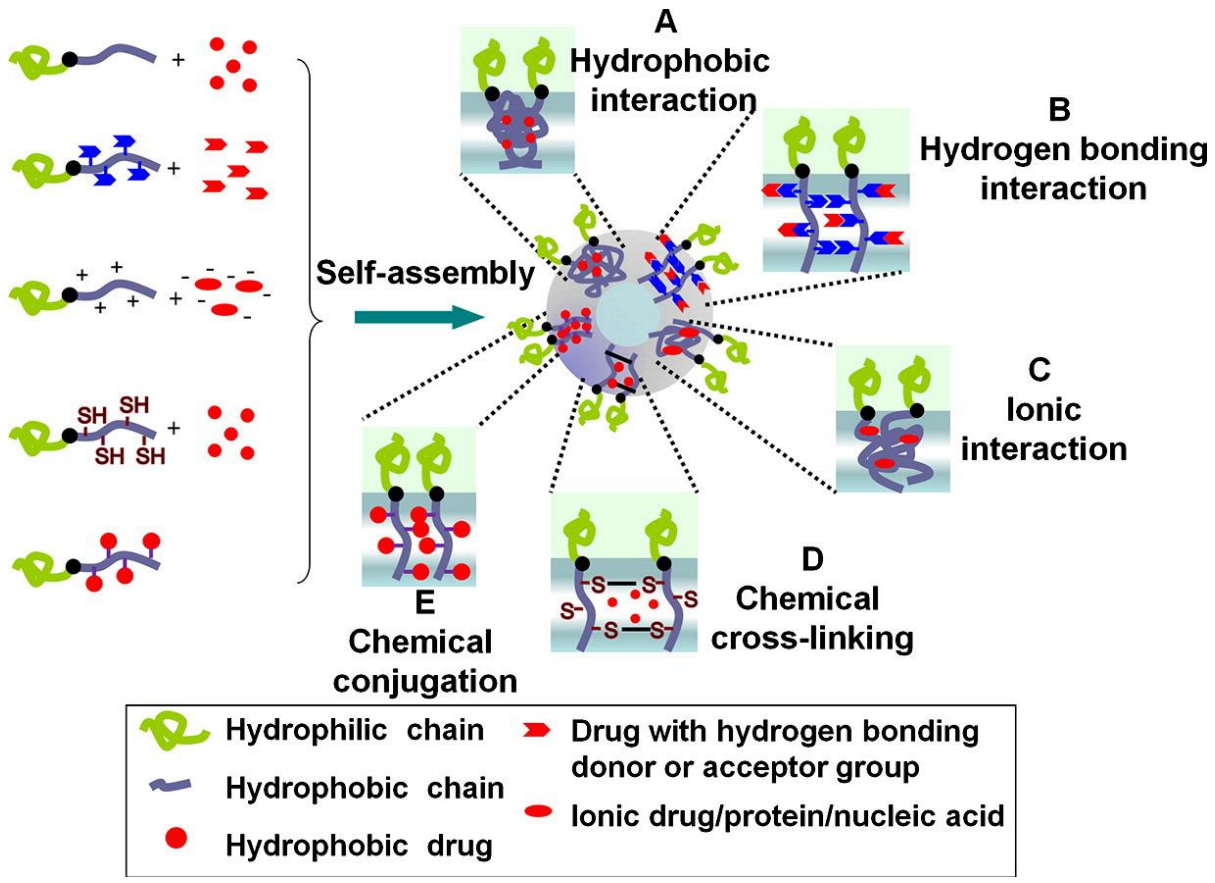

Figure 1.6. Schematic presentation of micellar drug delivery systems self-assembled through (A) hydrophobic interaction; (B) hydrogen bonding interaction; (C) ionic interaction; (D) chemical cross-linking and (E) chemical conjugation. [95]

Furthermore, some recent research showed the influence of hydrogen bonds formation on micelles self-assembly. [100] Dextran-graft-poly (N-isopropylacrylamide) polymer was dialyzed with three model drugs, such as norethisterone, ibuprofen, and nitrendipine to form micelles. As a

result, drug-loaded micelles were formed only with the ibuprofen, probably due to the strong hydrogen bond interactions between the carboxylic acid moiety of ibuprofen and the amide groups of poly (N-isopropylacrylamide).

The structure of the active compound and the copolymer composition can affect the hydrogen bond interactions. Increasing the amount of urea groups in the hydrophobic fragments of copolymer resulting in reducing the cmc, decreasing the size of the micelles while increasing the drug loading capacity. Obviously, due to the promoting the hydrogen bond interactions by incorporation of the larger amount of urea groups. [98]

1.4.2. Hydrophobic interactions between polymer macromolecule and cargo

Among all non-covalent types of interactions, hydrophobic ones are the most widely studied. [95] They are the driving force for the self-assembly of amphiphilic copolymers into micellar assemblies in aqueous media and widely used in the formation of most micellar systems for biomedical applications. Actually, hydrophobic interactions are the result of the barring from water molecules of other molecules. Amphiphilic copolymer molecules with various architectures such as block, hyperbranched, graft, and star copolymers (**Fig. 1.6**) have been examined for micellar formation and the relationships between functions and copolymer architecture have been established. The first polymeric micelle formulation that was commercialized under the trade name Genexol®-PM compose of monomethoxy poly(ethylene glycol)-block-poly(d,l-lactide) copolymer and is widely used for the treatment of ovarian cancer, non-small-cell lung carcinoma, gastric cancer, and breast cancer. [101] Here, the hydrophobic anticancer drug Paclitaxel (PTX) was encapsulated into polymeric micelles through hydrophobic interactions. Recently, the development of different micellar system for Paclitaxel delivery was reported. In order to improve the drug loading, by increasing the hydrophobicity of hydrophobic fragment, poly(ethylene

glycol)–poly(aspartic acid) block copolymer was conjugated with 4-phenyl-1-butanol through acid groups in poly(aspartic acid). [102]

The hydrophobic interactions within the polymeric micelles can be affected by the temperature, hydrophobicity of the polymeric moieties and the drugs, and the polymer-cargo compatibility. To study the influence, three amphiphilic copolymers with different lengths of hydrophobic fragments were synthesized via coupling methoxy polyethylene glycol with behenic acid, stearic acid and myristic acid by an ester linkage. [103] As fatty acid chain length increases, the cmc decreases enhancing the interactions between the hydrophobic micellar core and the hydrophobic cargo, which leads to increasing the solubility and loading capacity of cargo. The hydrophobicity of the loaded cargo also influences on hydrophobic interactions with the hydrophobic micellar core. The incorporation of more hydrophobic cargo results in cmc value reduction and micellization promotion. [104] It should be also noted, that increasing of temperature leads to the enhancing of the strength of the hydrophobic bond. [105]

1.4.3. Ionic interactions between polymer macromolecule and cargo

Ionic interactions are long-range interactions involving the electrostatic attraction between oppositely-charged ions, i.e. anions (negative) and cations (positive). Ionic interactions are widely studied interactions for micelles formation for drug delivery. Compared with micellar assemblies that are formed through other non-covalent interactions, micelles formed by ionic interactions can encapsulate ionic compounds, including small molecule drugs, therapeutic nucleic acids, peptides, and proteins. Ionic interactions can happen between two polymer chains or between polymer functional groups and functional groups of the loaded molecule that are oppositely-charged. Some common systems including PICM self-assembled from copolymers composed from a hydrophilic segment and polyionic segment. Moreover, PICM are forming primarily through ionic

interactions. [106] At the same time, peptides and proteins contain charged amino acids moieties and can show an overall positive or negative charge, which depends on values of isoelectric point, in different pH. Therefore, they are suitable for the incorporation into micelles using ionic interactions. For example, the encapsulation of the anticancer protein lectin A-chain into cationic micellar structures formed from biodegradable amphiphilic copolymers results in smaller size of the micelles and stronger positive charges in comparison to the commercially available product BioPorter. [107]

The strength of ionic interactions can be controlled by pH. Increasing the pH will lead to the decreasing of ionization and finally neutralizing of cationic cargo molecule.

The presence of other ions in an aqueous media also affecting the strength of ionic interactions within the polymer micelles. Increasing of ion concentration leads to their interaction with the charged loaded cargo or copolymer molecules, resulting in the weakening or destruction of ionic interactions within the polymer micelles. Kataoka and co-workers reported that the binding between the copolymer molecules and DNA was stabilized after the decreasing of salt concentration. [108]

1.4.4. Covalent bonding formation between polymer macromolecule and cargo

The conjugation of polymer with bioactive molecule can be done by either the convergent approach or the divergent methodology. In convergent approach or “grafting-to” method, the polymers are synthesized prior to conjugation with the bioactive compound. The divergent approach can be divided into “grafting-from” and “grafting through” methods. In the first one, the polymer chain of bioactive molecule is growing during the conjugation. While in “grafting through” approach the cargo is linked to one of the structural units of the polymer macromolecule

that can be polymerized with other comonomers to yield a polymer-biomolecule conjugate (**Fig. 1.7**). [109]

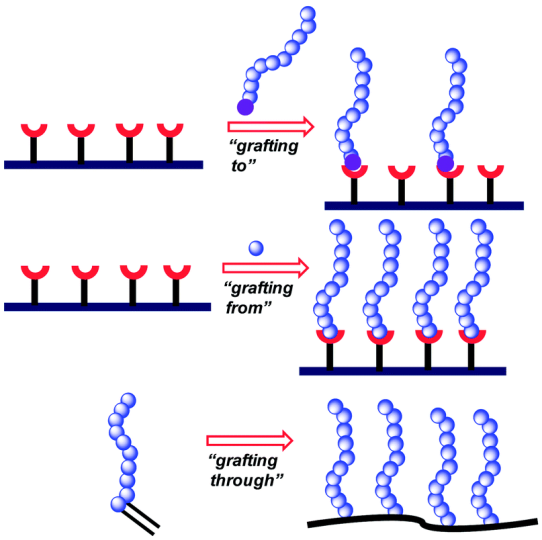

Figure 1.7. Possible strategies for the synthesis of peptide-polymer conjugates. [110]

The formation of covalent bonding between polymer and active compound provides several features to the linked molecules, such as increasing the half-life of the molecule, protecting against degrading enzymes, increasing the solubility in water due to the polymeric hindrance, and targeted delivery. [111] However, although the immobilization of enzyme enhances the thermostability, it is commonly resulted in the decreasing of catalytic activity of an enzyme. At the same time, some recent studies effectively reduced the loss in activity of conjugated enzyme and enhanced it stability at high pH and temperature. [112,113]

Among the polymers used for conjugation, poly ethylene glycol (PEG) has been studied most widely. Actually, nine PEG-protein conjugates are currently using in clinical practice. [114] The approval to use PEG in humans by FDA marked the beginning of its safe use in clinical practice. Among the advantages that PEGylation provides to nanoparticles, proteins, micelles,

liposomes and other systems, limited toxicity in humans and animals was approved by a number of studies. [115]

At the same time, there are a lot of other promising polymer–biomolecule conjugate systems reported in the literature. Some of them used a non-biodegradable polymeric backbone while few contain degradable polymer backbone, such as PLA, polycarbonate (PCB), and polyphosphoester (PPE). [116–118] The chemical conjugation of the PEG-b-PCB copolymer with doxorubicin (DOX) using the reaction between a benzaldehyde moiety from copolymer and the $–NH_2$ group on cargo, results in the formation of imino-bonds that are pH-sensitive, which might enhance intracellular release. [119] More importantly, obtained drug-conjugated micelles were more powerful against DOX-resistant human breast cancer cells in comparison to the free drug. A lot of studies reported the formation of conjugates with bioactive components using polyethylene oxide-*block*- polyphosphoester or PLA based copolymers. Where the authors demonstrated the increasing in cargo activity and anticancer properties. [120–123]

At the same time, a lot of studies were done on evaluation of curcumin as an anticancer agent. Chemical conjugation of curcumin with hydrophilic polymers improves the curcumin solubility in aqueous media. [124–126] Promising results were obtained for the conjugates made using PEG–PLA copolymers linked via ester bonds with cargo molecule. Chemical conjugation leads to the increasing of the curcumin loading capacity and reducing of the CMC values of polymer, while improved the thermodynamic stability of micelles due to stronger hydrophobic interaction within the polymeric core. [127] At the same time, it was showed, that the ester bonds can easily be cleaved enzymatically or by acid/base-catalyzed hydrolysis.

The polymer–biomolecule conjugation chemistry area is actively growing both in the academic laboratories and in the pharmaceutical industry. In spite of all the advantages of

polymer–cargo conjugates, including enhancement of targeting specificity, chemically-conjugated polymeric systems often suffer from slow release of the drug owing to the strong covalent interactions. To facilitate the controlled drug release at targeted locations, stimuli-responsive cleavage of polymer-cargo linkages is critical. A variety of strategies can be used, including pH-sensitive linkers, biologically reductive-sensitive linkages, and enzymatically cleavable short peptide linkers. [128–130]

1.5. Problem statement

Among a variety of studies on smart polymers (e.g., sensitive to changes in pH, temperature, light, moisture, electric and magnetic field), only few of them report on the polymers that respond to changes in a polarity of medium [131]. And they can be considered to be promising candidates for micellar delivery of poorly water-soluble drugs. Therefore, the synthesized in Dr. Voronov group new amphiphilic invertible polymers (AIPs) that comprise of short hydrophilic and lipophilic fragments in the backbone can be of great interest. The major difference between the new macromolecules and other block copolymers is that the incompatibility of the copolymer fragments is achieved at a much smaller fragment length. Varying the chemical structure of fragments enables greater control over the micellar self-assembly in the solution and the formation of micellar assemblies with well-defined structure and a fast response to the changing medium polarity. The difference in the hydrophilic−lipophilic balance (HLB) affects the AIP surface activity and the ability of macromolecules to self-assemble. Using ^{1}H NMR spectroscopy, the environment-dependent self-assembly for various micellar assemblies with various HLBs was revealed. It was shown that micellar assemblies undergo inversion when the medium polarity is changed. [132–134]

The advantage of the AIPs over the alternative copolymers is the chemical flexibility of micellar structure, which allows the design of custom-made carriers that can be developed with respect to drug properties, administration pathway, and site of action. The conventional mechanism of delivery of incorporated cargo molecules from the polymeric micellar carriers usually occurs by diffusion (**Fig. 1.8A**). Loaded with a poorly water-soluble drug, invertible micellar assemblies (IMAs) can successfully transfer cargo molecules to a polar/nonpolar interface and release the drug upon inversion by contacting/entering the less polar medium (**Fig. 1.8 B,C**). In this way, the enhanced solubility of the cargo molecule and promoted release are achieved. [135]

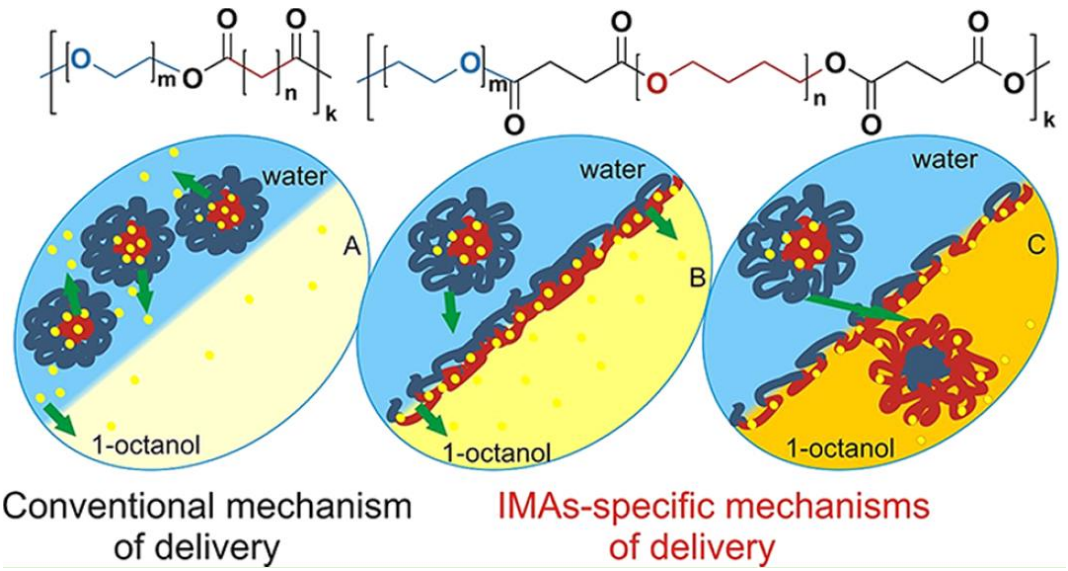

Figure 1.8. Diffusion mechanism (A) and stimuli-responsive (inversion) mechanisms (B, C) for delivery of poorly water-soluble drugs using polymeric micellar platforms. Chemical structures of AIPs are shown on top. [135]

The ability of IMAs to solubilize insoluble substances, both in nonpolar and polar solvents, was demonstrated using a variety of compounds, including poorly water-soluble dyes and drugs.[135–139] Hydrophobic cargo molecules can be incorporated into the hydrophobic exterior of IMAs in an aqueous media and released upon solvent change. Moreover, curcumin-loaded IMAs essentially reduced cell survival in three human osteosarcoma cell lines. [140] In addition,

the incorporation into IMAs significantly improved curcumin bioavailability in aqueous medium. Thus, it was shown that IMAs are nontoxic to human cells and able to solubilize, deliver and release small poorly water-soluble curcumin molecules.

Another promising application of IMAs can be to carry peptides/polypeptides as potential drugs, drug targets, or even micellar antigens (when antigenic peptide is incorporated in IMAs) which often need to be delivered between media with different polarities. Therefore, in this dissertation IMAs were tested as potential carriers for big cargo molecules, such as peptides/polypeptides.

1.6. Conclusions

Despite widespread research efforts dedicated to the development and characterization of different responsive polymeric systems, some questions are still to be answered, such as the influence of polymer-cargo interactions on targeting properties, the impact of type and structure of polymer on biomolecule activity and behavior. Hence, the change in polymer-biomolecule interactions as well as polymeric structure can be considered as a tool in regulating the targeted properties. The results of this work can be used to develop and/or optimize the responsive polymeric systems, such as micellar assemblies and polymer-biomolecule conjugates, with an appropriate morphology, polymer composition and polymer-biomolecule interactions for the specific applications in nanomedicine and bioconversion.

1.7. References

(1) Theato, P. Synthesis of Well-Defined Polymeric Activated Esters. *J. Polym. Sci. Part Polym. Chem.* **2008**, *46* (20), 6677–6687. https://doi.org/10.1002/pola.22994.

(2) Hoffman, A. S. “Intelligent” Polymers in Medicine and Biotechnology. *Macromol. Symp.* **1995**, *98* (1), 645–664. https://doi.org/10.1002/masy.19950980156.

(3) *Smart Polymers: Applications in Biotechnology and Biomedicine*, 2nd ed.; Galaev, I., Mattiasson, B., Eds.; CRC Press: Boca Raton, FL, 2008.

(4) Dai, S.; Ravi, P.; Tam, K. C. PH-Responsive Polymers: Synthesis, Properties and Applications. *Soft Matter* **2008**, *4* (3), 435. https://doi.org/10.1039/b714741d.

(5) Davis, D. A.; Hamilton, A.; Yang, J.; Cremar, L. D.; Van Gough, D.; Potisek, S. L.; Ong, M. T.; Braun, P. V.; Martínez, T. J.; White, S. R.; et al. Force-Induced Activation of Covalent Bonds in Mechanoresponsive Polymeric Materials. *Nature* **2009**, *459* (7243), 68–72. https://doi.org/10.1038/nature07970.

(6) Colson, Y. L.; Grinstaff, M. W. Biologically Responsive Polymeric Nanoparticles for Drug Delivery. *Adv. Mater.* **2012**, *24* (28), 3878–3886. https://doi.org/10.1002/adma.201200420.

(7) Tanaka, T.; Nishio, I.; Sun, S.-T.; Ueno-Nishio, S. Collapse of Gels in an Electric Field. *Science* **1982**, *218* (4571), 467–469. https://doi.org/10.1126/science.218.4571.467.

(8) Thévenot, J.; Oliveira, H.; Sandre, O.; Lecommandoux, S. Magnetic Responsive Polymer Composite Materials. *Chem. Soc. Rev.* **2013**, *42* (17), 7099. https://doi.org/10.1039/c3cs60058k.

(9) Irie, M. Properties and Applications of Photoresponsive Polymers. *Pure Appl. Chem.* **1990**, *62* (8), 1495–1502. https://doi.org/10.1351/pac199062081495.

(10) Heskins, M.; Guillet, J. E. Solution Properties of Poly(N-Isopropylacrylamide). *J. Macromol. Sci. Part - Chem.* **1968**, *2* (8), 1441–1455. https://doi.org/10.1080/10601326808051910.

(11) Zhang, Q. M.; Serpe, M. J. Responsive Polymers as Sensors, Muscles, and Self-Healing Materials. In *Polymer Mechanochemistry*; Boulatov, R., Ed.; Springer International Publishing: Cham, 2015; Vol. 369, pp 377–424. https://doi.org/10.1007/128_2015_626.

(12) Zhai, L. Stimuli-Responsive Polymer Films. *Chem. Soc. Rev.* **2013**, *42* (17), 7148. https://doi.org/10.1039/c3cs60023h.

(13) Parasuraman, D.; Serpe, M. J. Poly (*N* -Isopropylacrylamide) Microgels for Organic Dye Removal from Water. *ACS Appl. Mater. Interfaces* **2011**, *3* (7), 2732–2737. https://doi.org/10.1021/am2005288.

(14) Zhao, Q.; Dunlop, J. W. C.; Qiu, X.; Huang, F.; Zhang, Z.; Heyda, J.; Dzubiella, J.; Antonietti, M.; Yuan, J. An Instant Multi-Responsive Porous Polymer Actuator Driven by Solvent Molecule Sorption. *Nat. Commun.* **2014**, *5* (1). https://doi.org/10.1038/ncomms5293.

(15) Ma, M.; Guo, L.; Anderson, D. G.; Langer, R. Bio-Inspired Polymer Composite Actuator and Generator Driven by Water Gradients. *Science* **2013**, *339* (6116), 186–189. https://doi.org/10.1126/science.1230262.

(16) Hu, J.; Liu, S. Responsive Polymers for Detection and Sensing Applications: Current Status and Future Developments. *Macromolecules* **2010**, *43* (20), 8315–8330. https://doi.org/10.1021/ma1005815.

(17) Bajpai, A. K.; Shukla, S. K.; Bhanu, S.; Kankane, S. Responsive Polymers in Controlled Drug Delivery. *Prog. Polym. Sci.* **2008**, *33* (11), 1088–1118. https://doi.org/10.1016/j.progpolymsci.2008.07.005.

(18) Koerner, H.; Price, G.; Pearce, N. A.; Alexander, M.; Vaia, R. A. Remotely Actuated Polymer Nanocomposites—Stress-Recovery of Carbon-Nanotube-Filled Thermoplastic Elastomers. *Nat. Mater.* **2004**, *3* (2), 115–120. https://doi.org/10.1038/nmat1059.

(19) Wang, F.; Lai, Y.-H.; Han, M.-Y. Stimuli-Responsive Conjugated Copolymers Having Electro-Active Azulene and Bithiophene Units in the Polymer Skeleton: Effect of Protonation and p-Doping on Conducting Properties. *Macromolecules* **2004**, *37* (9), 3222–3230. https://doi.org/10.1021/ma035335q.

(20) Sorrell, C. D.; Carter, M. C. D.; Serpe, M. J. Color Tunable Poly (N-Isopropylacrylamide)-Co-Acrylic Acid Microgel-Au Hybrid Assemblies. *Adv. Funct. Mater.* **2011**, *21* (3), 425–433. https://doi.org/10.1002/adfm.201001714.

(21) Connal, L. A.; Li, Q.; Quinn, J. F.; Tjipto, E.; Caruso, F.; Qiao, G. G. PH-Responsive Poly(Acrylic Acid) Core Cross-Linked Star Polymers: Morphology Transitions in Solution and Multilayer Thin Films. *Macromolecules* **2008**, *41* (7), 2620–2626. https://doi.org/10.1021/ma7019557.

(22) Kataoka, K.; Miyazaki, H.; Bunya, M.; Okano, T.; Sakurai, Y. Totally Synthetic Polymer Gels Responding to External Glucose Concentration: Their Preparation and Application to On−Off Regulation of Insulin Release. *J. Am. Chem. Soc.* **1998**, *120* (48), 12694–12695. https://doi.org/10.1021/ja982975d.

(23) Gu, Z.; Dang, T. T.; Ma, M.; Tang, B. C.; Cheng, H.; Jiang, S.; Dong, Y.; Zhang, Y.; Anderson, D. G. Glucose-Responsive Microgels Integrated with Enzyme Nanocapsules for Closed-Loop Insulin Delivery. *ACS Nano* **2013**, *7* (8), 6758–6766. https://doi.org/10.1021/nn401617u.

(24) Thornton, P. D.; Mart, R. J.; Ulijn, R. V. Enzyme-Responsive Polymer Hydrogel Particles for Controlled Release. *Adv. Mater.* **2007**, *19* (9), 1252–1256. https://doi.org/10.1002/adma.200601784.

(25) Hu, J.; Zhang, G.; Liu, S. Enzyme-Responsive Polymeric Assemblies, Nanoparticles and Hydrogels. *Chem. Soc. Rev.* **2012**, *41* (18), 5933. https://doi.org/10.1039/c2cs35103j.

(26) Miyata, T.; Asami, N.; Uragami, T. A Reversibly Antigen-Responsive Hydrogel. *Nature* **1999**, *399* (6738), 766–769. https://doi.org/10.1038/21619.

(27) Wegst, U. G. K.; Bai, H.; Saiz, E.; Tomsia, A. P.; Ritchie, R. O. Bioinspired Structural Materials. *Nat. Mater.* **2015**, *14* (1), 23–36. https://doi.org/10.1038/nmat4089.

(28) Sanchez, C.; Arribart, H.; Guille, M. M. G. Biomimetism and Bioinspiration as Tools for the Design of Innovative Materials and Systems. *Nat. Mater.* **2005**, *4* (4), 277–288.

(29) Yatvin, M. B.; Weinstein, J. N.; Dennis, W. H.; Blumenthal, R. Design of Liposomes for Enhanced Local Release of Drugs by Hyperthermia. *Science* **1978**, *202* (4374), 1290–1293.

(30) Stuart, M. A. C.; Huck, W. T. S.; Genzer, J.; Müller, M.; Ober, C.; Stamm, M.; Sukhorukov, G. B.; Szleifer, I.; Tsukruk, V. V.; Urban, M.; et al. Emerging Applications of Stimuli-Responsive Polymer Materials. *Nat. Mater.* **2010**, *9* (2), 101–113. https://doi.org/10.1038/nmat2614.

(31) Mura, S.; Nicolas, J.; Couvreur, P. Stimuli-Responsive Nanocarriers for Drug Delivery. *Nat. Mater.* **2013**, *12* (11), 991–1003. https://doi.org/10.1038/nmat3776.

(32) Blum, A. P.; Kammeyer, J. K.; Rush, A. M.; Callmann, C. E.; Hahn, M. E.; Gianneschi, N. C. Stimuli-Responsive Nanomaterials for Biomedical Applications. *J. Am. Chem. Soc.* **2015**, *137* (6), 2140–2154. https://doi.org/10.1021/ja510147n.

(33) Gao, Y.; Wei, M.; Li, X.; Xu, W.; Ahiabu, A.; Perdiz, J.; Liu, Z.; Serpe, M. J. Stimuli-Responsive Polymers: Fundamental Considerations and Applications. *Macromol. Res.* **2017**, *25* (6), 513–527. https://doi.org/10.1007/s13233-017-5088-7.

(34) Ayre, A.; Kadam, V.; Dand, N.; Patel, P. Polymeric Micelles as a Drug Carrier for Tumor Targeting. *Chron. Young Sci.* **2013**, *4* (2), 94. https://doi.org/10.4103/2229-5186.115544.

(35) Hong, X.; Wu, Z.; Chen, L.; Wu, F.; Wei, L.; Yuan, W. Hydrogel Microneedle Arrays for Transdermal Drug Delivery. *Nano-Micro Lett.* **2014**, *6* (3). https://doi.org/10.5101/nml140021r.

(36) Donnelly, R. F.; Singh, T. R. R.; Garland, M. J.; Migalska, K.; Majithiya, R.; McCrudden, C. M.; Kole, P. L.; Mahmood, T. M. T.; McCarthy, H. O.; Woolfson, A. D. Hydrogel-Forming Microneedle Arrays for Enhanced Transdermal Drug Delivery. *Adv. Funct. Mater.* **2012**, *22* (23), 4879–4890. https://doi.org/10.1002/adfm.201200864.

(37) Gao, Y.; Zago, G. P.; Jia, Z.; Serpe, M. J. Controlled and Triggered Small Molecule Release from a Confined Polymer Film. *ACS Appl. Mater. Interfaces* **2013**, *5* (19), 9803–9808. https://doi.org/10.1021/am4029894.

(38) Gao, Y.; Wong, K. Y.; Ahiabu, A.; Serpe, M. J. Sequential and Controlled Release of Small Molecules from Poly(N-Isopropylacrylamide) Microgel-Based Reservoir Devices. *J. Mater. Chem. B* **2016**, *4* (30), 5144–5150. https://doi.org/10.1039/C6TB00864J.

(39) Donnelly, R. F.; McCrudden, M. T. C.; Zaid Alkilani, A.; Larrañeta, E.; McAlister, E.; Courtenay, A. J.; Kearney, M.-C.; Singh, T. R. R.; McCarthy, H. O.; Kett, V. L.; et al. Hydrogel-Forming Microneedles Prepared from "Super Swelling" Polymers Combined with Lyophilised Wafers for Transdermal Drug Delivery. *PLoS ONE* **2014**, *9* (10), e111547. https://doi.org/10.1371/journal.pone.0111547.

(40) Cahill, E. M.; O'Cearbhaill, E. D. Toward Biofunctional Microneedles for Stimulus Responsive Drug Delivery. *Bioconjug. Chem.* **2015**, *26* (7), 1289–1296. https://doi.org/10.1021/acs.bioconjchem.5b00211.

(41) Hardy, J. G.; Larrañeta, E.; Donnelly, R. F.; McGoldrick, N.; Migalska, K.; McCrudden, M. T. C.; Irwin, N. J.; Donnelly, L.; McCoy, C. P. Hydrogel-Forming Microneedle Arrays Made from Light-Responsive Materials for On-Demand Transdermal Drug Delivery. *Mol. Pharm.* **2016**, *13* (3), 907–914. https://doi.org/10.1021/acs.molpharmaceut.5b00807.

(42) Rolland, O.; Turrin, C.-O.; Caminade, A.-M.; Majoral, J.-P. Dendrimers and Nanomedicine: Multivalency in Action. *New J. Chem.* **2009**, *33* (9), 1809. https://doi.org/10.1039/b901054h.

(43) Khandare, J.; Calderón, M.; Dagia, N. M.; Haag, R. Multifunctional Dendritic Polymers in Nanomedicine: Opportunities and Challenges. *Chem Soc Rev* **2012**, *41* (7), 2824–2848. https://doi.org/10.1039/C1CS15242D.

(44) Caminade, A.-M.; Turrin, C.-O. Dendrimers for Drug Delivery. *J Mater Chem B* **2014**, *2* (26), 4055–4066. https://doi.org/10.1039/C4TB00171K.

(45) Pandita, D.; Poonia, N.; Kumar, S.; Lather, V.; Madaan, K. Dendrimers in Drug Delivery and Targeting: Drug-Dendrimer Interactions and Toxicity Issues. *J. Pharm. Bioallied Sci.* **2014**, *6* (3), 139. https://doi.org/10.4103/0975-7406.130965.

(46) Sánchez-Purrà, M. Development of Novel Vesicle-like Nanocarriers for Targeted Drug Delivery. *Unpublished* **2015**. https://doi.org/10.13140/rg.2.2.15538.30407.

(47) Alavi, M.; Karimi, N.; Safaei, M. Application of Various Types of Liposomes in Drug Delivery Systems. *Adv. Pharm. Bull.* **2017**, *7* (1), 3–9. https://doi.org/10.15171/apb.2017.002.

(48) Hua, S.; Wu, S. Y. The Use of Lipid-Based Nanocarriers for Targeted Pain Therapies. *Front. Pharmacol.* **2013**, *4*. https://doi.org/10.3389/fphar.2013.00143.

(49) Allen, T. M.; Cullis, P. R. Liposomal Drug Delivery Systems: From Concept to Clinical Applications. *Adv. Drug Deliv. Rev.* **2013**, *65* (1), 36–48. https://doi.org/10.1016/j.addr.2012.09.037.

(50) Li, J.; Wang, X.; Zhang, T.; Wang, C.; Huang, Z.; Luo, X.; Deng, Y. A Review on Phospholipids and Their Main Applications in Drug Delivery Systems. *Asian J. Pharm. Sci.* **2015**, *10* (2), 81–98. https://doi.org/10.1016/j.ajps.2014.09.004.

(51) Massignani, M.; Lomas, H.; Battaglia, G. Polymersomes: A Synthetic Biological Approach to Encapsulation and Delivery. In *Modern Techniques for Nano- and Microreactors/-reactions*; Caruso, F., Ed.; Springer Berlin Heidelberg: Berlin, Heidelberg, 2010; Vol. 229, pp 115–154. https://doi.org/10.1007/12_2009_40.

(52) Meng, F.; Zhong, Z. Polymersomes Spanning from Nano- to Microscales: Advanced Vehicles for Controlled Drug Delivery and Robust Vesicles for Virus and Cell Mimicking. *J. Phys. Chem. Lett.* **2011**, *2* (13), 1533–1539. https://doi.org/10.1021/jz200007h.

(53) Hearnden, V.; Sankar, V.; Hull, K.; Juras, D. V.; Greenberg, M.; Kerr, A. R.; Lockhart, P. B.; Patton, L. L.; Porter, S.; Thornhill, M. H. New Developments and Opportunities in Oral Mucosal Drug Delivery for Local and Systemic Disease. *Adv. Drug Deliv. Rev.* **2012**, *64* (1), 16–28. https://doi.org/10.1016/j.addr.2011.02.008.

(54) Tao, L.; Hu, W.; Liu, Y.; Huang, G.; Sumer, B. D.; Gao, J. Shape-Specific Polymeric Nanomedicine: Emerging Opportunities and Challenges. *Exp. Biol. Med.* **2011**, *236* (1), 20–29. https://doi.org/10.1258/ebm.2010.010243.

(55) Banik, B. L.; Fattahi, P.; Brown, J. L. Polymeric Nanoparticles: The Future of Nanomedicine: Polymeric Nanoparticles. *Wiley Interdiscip. Rev. Nanomed. Nanobiotechnol.* **2016**, *8* (2), 271–299. https://doi.org/10.1002/wnan.1364.

(56) Discher, D. E. Polymer Vesicles. *Science* **2002**, *297* (5583), 967–973. https://doi.org/10.1126/science.1074972.

(57) Zhang, L.; Wang, S.; Zhang, M.; Sun, J. Nanocarriers for Oral Drug Delivery. *J. Drug Target.* **2013**, *21* (6), 515–527. https://doi.org/10.3109/1061186X.2013.789033.

(58) Gaucher, G.; Dufresne, M.-H.; Sant, V. P.; Kang, N.; Maysinger, D.; Leroux, J.-C. Block Copolymer Micelles: Preparation, Characterization and Application in Drug Delivery. *J. Controlled Release* **2005**, *109* (1–3), 169–188. https://doi.org/10.1016/j.jconrel.2005.09.034.

(59) Owen, S. C.; Chan, D. P. Y.; Shoichet, M. S. Polymeric Micelle Stability. *Nano Today* **2012**, *7* (1), 53–65. https://doi.org/10.1016/j.nantod.2012.01.002.

(60) Simões, S. M.; Figueiras, A. R.; Veiga, F.; Concheiro, A.; Alvarez-Lorenzo, C. Polymeric Micelles for Oral Drug Administration Enabling Locoregional and Systemic Treatments. *Expert Opin. Drug Deliv.* **2015**, *12* (2), 297–318. https://doi.org/10.1517/17425247.2015.960841.

(61) Allen, C.; Maysinger, D.; Eisenberg, A. Nano-Engineering Block Copolymer Aggregates for Drug Delivery. *Colloids Surf. B Biointerfaces* **1999**, *16* (1–4), 3–27. https://doi.org/10.1016/S0927-7765(99)00058-2.

(62) Luo, Y.; Yao, X.; Yuan, J.; Ding, T.; Gao, Q. Preparation and Drug Controlled-Release of Polyion Complex Micelles as Drug Delivery Systems. *Colloids Surf. B Biointerfaces* **2009**, *68* (2), 218–224. https://doi.org/10.1016/j.colsurfb.2008.10.014.

(63) Kuo, S.-W.; Tung, P.-H.; Lai, C.-L.; Jeong, K.-U.; Chang, F.-C. Supramolecular Micellization of Diblock Copolymer Mixtures Mediated by Hydrogen Bonding for the Observation of Separated Coil and Chain Aggregation in Common Solvents. *Macromol. Rapid Commun.* **2008**, *29* (3), 229–233. https://doi.org/10.1002/marc.200700697.

(64) Tian, H.; Wang, D.; Xu, W.; Song, A.; Hao, J. Balance of Coordination and Hydrophobic Interaction in the Formation of Bilayers in Metal-Coordinated Surfactant Mixtures. *Langmuir* **2013**, *29* (11), 3538–3545. https://doi.org/10.1021/la4003669.

(65) Moughton, A. O.; Hillmyer, M. A.; Lodge, T. P. Multicompartment Block Polymer Micelles. *Macromolecules* **2012**, *45* (1), 2–19. https://doi.org/10.1021/ma201865s.

(66) Wang, L.; Xu, R.; Wang, Z.; He, X. Kinetics of Multicompartment Micelle Formation by Self-Assembly of ABC Miktoarm Star Terpolymer in Dilute Solution. *Soft Matter* **2012**, *8* (45), 11462. https://doi.org/10.1039/c2sm26886h.

(67) Inoue, K. Functional Dendrimers, Hyperbranched and Star Polymers. *Prog. Polym. Sci.* **2000**, *25* (4), 453–571. https://doi.org/10.1016/S0079-6700(00)00011-3.

(68) Ordanini, S.; Cellesi, F. Complex Polymeric Architectures Self-Assembling in Unimolecular Micelles: Preparation, Characterization and Drug Nanoencapsulation. *Pharmaceutics* **2018**, *10* (4), 209. https://doi.org/10.3390/pharmaceutics10040209.

(69) Lo, C.-L.; Lin, S.-J.; Tsai, H.-C.; Chan, W.-H.; Tsai, C.-H.; Cheng, C.-H. D.; Hsiue, G.-H. Mixed Micelle Systems Formed from Critical Micelle Concentration and

Temperature-Sensitive Diblock Copolymers for Doxorubicin Delivery. *Biomaterials* **2009**, *30* (23–24), 3961–3970. https://doi.org/10.1016/j.biomaterials.2009.04.002.

(70) Ribeiro, A.; Sosnik, A.; Chiappetta, D. A.; Veiga, F.; Concheiro, A.; Alvarez-Lorenzo, C. Single and Mixed Poloxamine Micelles as Nanocarriers for Solubilization and Sustained Release of Ethoxzolamide for Topical Glaucoma Therapy. *J. R. Soc. Interface* **2012**, *9* (74), 2059–2069. https://doi.org/10.1098/rsif.2012.0102.

(71) Torchilin, V. P. Structure and Design of Polymeric Surfactant-Based Drug Delivery Systems. *J. Control. Release Off. J. Control. Release Soc.* **2001**, *73* (2–3), 137–172.

(72) Li, X.; Zhang, Y.; Fan, Y.; Zhou, Y.; Wang, X.; Fan, C.; Liu, Y.; Zhang, Q. Preparation and Evaluation of Novel Mixed Micelles as Nanocarriers for Intravenous Delivery of Propofol. *Nanoscale Res. Lett.* **2011**, *6* (1), 275. https://doi.org/10.1186/1556-276X-6-275.

(73) Jones, M.-C.; Leroux, J.-C. Reverse Micelles from Amphiphilic Branched Polymers. *Soft Matter* **2010**, *6* (23), 5850. https://doi.org/10.1039/c0sm00272k.

(74) Zhang, L.; Eisenberg, A. Multiple Morphologies of "Crew-Cut" Aggregates of Polystyrene-b-Poly(Acrylic Acid) Block Copolymers. *Science* **1995**, *268* (5218), 1728–1731. https://doi.org/10.1126/science.268.5218.1728.

(75) Israelachvili, J. N.; Mitchell, D. J.; Ninham, B. W. Theory of Self-Assembly of Lipid Bilayers and Vesicles. *Biochim. Biophys. Acta* **1977**, *470* (2), 185–201.

(76) Jain, S. On the Origins of Morphological Complexity in Block Copolymer Surfactants. *Science* **2003**, *300* (5618), 460–464. https://doi.org/10.1126/science.1082193.

(77) Lombardo, D.; Kiselev, M. A.; Magazù, S.; Calandra, P. Amphiphiles Self-Assembly: Basic Concepts and Future Perspectives of Supramolecular Approaches. *Adv. Condens. Matter Phys.* **2015**, *2015*, 1–22. https://doi.org/10.1155/2015/151683.

(78) Dionzou, M.; Morère, A.; Roux, C.; Lonetti, B.; Marty, J.-D.; Mingotaud, C.; Joseph, P.; Goudounèche, D.; Payré, B.; Léonetti, M.; et al. Comparison of Methods for the Fabrication and the Characterization of Polymer Self-Assemblies: What Are the Important Parameters? *Soft Matter* **2016**, *12* (7), 2166–2176. https://doi.org/10.1039/C5SM01863C.

(79) Doncom, K. E. B.; Blackman, L. D.; Wright, D. B.; Gibson, M. I.; O'Reilly, R. K. Dispersity Effects in Polymer Self-Assemblies: A Matter of Hierarchical Control. *Chem. Soc. Rev.* **2017**, *46* (14), 4119–4134. https://doi.org/10.1039/C6CS00818F.

(80) Lavasanifar, A.; Samuel, J.; Kwon, G. S. Poly(Ethylene Oxide)-Block-Poly(L-Amino Acid) Micelles for Drug Delivery. *Adv. Drug Deliv. Rev.* **2002**, *54* (2), 169–190.

(81) Kabanov, A. V.; Batrakova, E. V.; Alakhov, V. Y. Pluronic Block Copolymers as Novel Polymer Therapeutics for Drug and Gene Delivery. *J. Control. Release Off. J. Control. Release Soc.* **2002**, *82* (2–3), 189–212.

(82) Topp, M. D. C.; Dijkstra, P. J.; Talsma, H.; Feijen, J. Thermosensitive Micelle-Forming Block Copolymers of Poly(Ethylene Glycol) and Poly(*N* -Isopropylacrylamide). *Macromolecules* **1997**, *30* (26), 8518–8520. https://doi.org/10.1021/ma9710803.

(83) Virtanen, J.; Holappa, S.; Lemmetyinen, H.; Tenhu, H. Aggregation in Aqueous Poly(*N* -Isopropylacrylamide)- *Block* -Poly(Ethylene Oxide) Solutions Studied by Fluorescence Spectroscopy and Light Scattering. *Macromolecules* **2002**, *35* (12), 4763–4769. https://doi.org/10.1021/ma012239l.

(84) Zhang, W.; Shi, L.; Ma, R.; An, Y.; Xu, Y.; Wu, K. Micellization of Thermo- and PH-Responsive Triblock Copolymer of Poly(Ethylene Glycol)- *b* -Poly(4-Vinylpyridine)- *b* -Poly(*N* -Isopropylacrylamide). *Macromolecules* **2005**, *38* (21), 8850–8852. https://doi.org/10.1021/ma050998o.

(85) Qin, S.; Geng, Y.; Discher, D. E.; Yang, S. Temperature-Controlled Assembly and Release from Polymer Vesicles of Poly(Ethylene Oxide)-Block- Poly(N-Isopropylacrylamide). *Adv. Mater.* **2006**, *18* (21), 2905–2909. https://doi.org/10.1002/adma.200601019.

(86) Kabanov, A. V.; Bronich, T. K.; Kabanov, V. A.; Yu, K.; Eisenberg, A. Soluble Stoichiometric Complexes from Poly(*N* -Ethyl-4-Vinylpyridinium) Cations and Poly(Ethylene Oxide)- *Block* -Polymethacrylate Anions. *Macromolecules* **1996**, *29* (21), 6797–6802. https://doi.org/10.1021/ma960120k.

(87) Harada, A.; Kataoka, K. Pronounced Activity of Enzymes through the Incorporation into the Core of Polyion Complex Micelles Made from Charged Block Copolymers. *J. Control. Release Off. J. Control. Release Soc.* **2001**, *72* (1–3), 85–91.

(88) Dufresne, M.-H.; Leroux, J.-C. Study of the Micellization Behavior of Different Order Amino Block Copolymers with Heparin. *Pharm. Res.* **2004**, *21* (1), 160–169. https://doi.org/10.1023/B:PHAM.0000012164.60867.c6.

(89) Wakebayashi, D.; Nishiyama, N.; Yamasaki, Y.; Itaka, K.; Kanayama, N.; Harada, A.; Nagasaki, Y.; Kataoka, K. Lactose-Conjugated Polyion Complex Micelles Incorporating Plasmid DNA as a Targetable Gene Vector System: Their Preparation and Gene Transfecting Efficiency against Cultured HepG2 Cells. *J. Controlled Release* **2004**, *95* (3), 653–664. https://doi.org/10.1016/j.jconrel.2004.01.003.

(90) Oishi, M.; Sasaki, S.; Nagasaki, Y.; Kataoka, K. PH-Responsive Oligodeoxynucleotide (ODN)−Poly(Ethylene Glycol) Conjugate through Acid-Labile β-Thiopropionate Linkage: Preparation and Polyion Complex Micelle Formation. *Biomacromolecules* **2003**, *4* (5), 1426–1432. https://doi.org/10.1021/bm034164u.

(91) Novoa-Carballal, R.; Pergushov, D. V.; Müller, A. H. E. Interpolyelectrolyte Complexes Based on Hyaluronic Acid-Block-Poly(Ethylene Glycol) and Poly-l-Lysine. *Soft Matter* **2013**, *9* (16), 4297. https://doi.org/10.1039/c3sm27549c.

(92) Govender, T.; Stolnik, S.; Xiong, C.; Zhang, S.; Illum, L.; Davis, S. S. Drug–Polyionic Block Copolymer Interactions for Micelle Formation: Physicochemical Characterisation. *J. Controlled Release* **2001**, *75* (3), 249–258. https://doi.org/10.1016/S0168-3659(01)00353-4.

(93) Harada, A.; Kataoka, K. Polyion Complex Micelle Formation from Double-Hydrophilic Block Copolymers Composed of Charged and Non-Charged Segments in Aqueous Media. *Polym. J.* **2018**, *50* (1), 95–100. https://doi.org/10.1038/pj.2017.67.

(94) Deshmukh, A. S.; Chauhan, P. N.; Noolvi, M. N.; Chaturvedi, K.; Ganguly, K.; Shukla, S. S.; Nadagouda, M. N.; Aminabhavi, T. M. Polymeric Micelles: Basic Research to Clinical Practice. *Int. J. Pharm.* **2017**, *532* (1), 249–268. https://doi.org/10.1016/j.ijpharm.2017.09.005.

(95) Ke, X.; Ng, V. W. L.; Ono, R. J.; Chan, J. M. W.; Krishnamurthy, S.; Wang, Y.; Hedrick, J. L.; Yang, Y. Y. Role of Non-Covalent and Covalent Interactions in Cargo Loading Capacity and Stability of Polymeric Micelles. *J. Controlled Release* **2014**, *193*, 9–26. https://doi.org/10.1016/j.jconrel.2014.06.061.

(96) Kuang, H.; Wu, S.; Xie, Z.; Meng, F.; Jing, X.; Huang, Y. Biodegradable Amphiphilic Copolymer Containing Nucleobase: Synthesis, Self-Assembly in Aqueous Solutions, and Potential Use in Controlled Drug Delivery. *Biomacromolecules* **2012**, *13* (9), 3004–3012. https://doi.org/10.1021/bm301169x.

(97) Tan, J. P. K.; Kim, S. H.; Nederberg, F.; Fukushima, K.; Coady, D. J.; Nelson, A.; Yang, Y. Y.; Hedrick, J. L. Delivery of Anticancer Drugs Using Polymeric Micelles Stabilized by Hydrogen-Bonding Urea Groups. *Macromol. Rapid Commun.* **2010**, *31* (13), 1187–1192. https://doi.org/10.1002/marc.201000105.

(98) Kim, S. H.; Tan, J. P. K.; Nederberg, F.; Fukushima, K.; Colson, J.; Yang, C.; Nelson, A.; Yang, Y.-Y.; Hedrick, J. L. Hydrogen Bonding-Enhanced Micelle Assemblies for Drug Delivery. *Biomaterials* **2010**, *31* (31), 8063–8071. https://doi.org/10.1016/j.biomaterials.2010.07.018.

(99) Yang, C.; Ebrahim Attia, A. B.; Tan, J. P. K.; Ke, X.; Gao, S.; Hedrick, J. L.; Yang, Y.-Y. The Role of Non-Covalent Interactions in Anticancer Drug Loading and Kinetic Stability of Polymeric Micelles. *Biomaterials* **2012**, *33* (10), 2971–2979. https://doi.org/10.1016/j.biomaterials.2011.11.035.

(100) Tan, S. W.; Wang, H. J.; Tu, K. H.; Jiang, H. L.; Wang, L. Q. Ibuprofen Induced Drug Loaded Polymeric Micelles. *Chin. Chem. Lett.* **2011**, *22* (9), 1123–1126. https://doi.org/10.1016/j.cclet.2011.04.005.

(101) Gong, J.; Chen, M.; Zheng, Y.; Wang, S.; Wang, Y. Polymeric Micelles Drug Delivery System in Oncology. *J. Controlled Release* **2012**, *159* (3), 312–323. https://doi.org/10.1016/j.jconrel.2011.12.012.

(102) Kato, K.; Chin, K.; Yoshikawa, T.; Yamaguchi, K.; Tsuji, Y.; Esaki, T.; Sakai, K.; Kimura, M.; Hamaguchi, T.; Shimada, Y.; et al. Phase II Study of NK105, a Paclitaxel-Incorporating Micellar Nanoparticle, for Previously Treated Advanced or Recurrent Gastric Cancer. *Invest. New Drugs* **2012**, *30* (4), 1621–1627. https://doi.org/10.1007/s10637-011-9709-2.

(103) Varshosaz, J.; Hasanzadeh, F.; Eslamdoost, M. Optimization of Self-Assembling Properties of Fatty Acids Grafted to Methoxy Poly(Ethylene Glycol) as Nanocarriers for Etoposide. *Acta Pharm.* **2012**, *62* (1), 31–44. https://doi.org/10.2478/v10007-012-0006-1.

(104) Alexander, S.; Cosgrove, T.; Prescott, S. W.; Castle, T. C. Flurbiprofen Encapsulation Using Pluronic Triblock Copolymers. *Langmuir* **2011**, *27* (13), 8054–8060. https://doi.org/10.1021/la201124c.

(105) Reverberi, R.; Reverberi, L. Factors Affecting the Antigen-Antibody Reaction. *Blood Transfus.* **2007**. https://doi.org/10.2450/2007.0047-07.

(106) Ebrahim Attia, A. B.; Ong, Z. Y.; Hedrick, J. L.; Lee, P. P.; Ee, P. L. R.; Hammond, P. T.; Yang, Y.-Y. Mixed Micelles Self-Assembled from Block Copolymers for Drug Delivery. *Curr. Opin. Colloid Interface Sci.* **2011**, *16* (3), 182–194. https://doi.org/10.1016/j.cocis.2010.10.003.

(107) Lee, A. L. Z.; Wang, Y.; Ye, W.-H.; Yoon, H. S.; Chan, S. Y.; Yang, Y.-Y. Efficient Intracellular Delivery of Functional Proteins Using Cationic Polymer Core/Shell Nanoparticles. *Biomaterials* **2008**, *29* (9), 1224–1232. https://doi.org/10.1016/j.biomaterials.2007.11.021.

(108) Kim, W.; Yamasaki, Y.; Jang, W.-D.; Kataoka, K. Thermodynamics of DNA Condensation Induced by Poly(Ethylene Glycol)- *Block* -Polylysine through Polyion

Complex Micelle Formation. *Biomacromolecules* **2010**, *11* (5), 1180–1186. https://doi.org/10.1021/bm901305p.

(109) Dehn, S.; Chapman, R.; Jolliffe, K. A.; Perrier, S. Synthetic Strategies for the Design of Peptide/Polymer Conjugates. *Polym. Rev.* **2011**, *51* (2), 214–234. https://doi.org/10.1080/15583724.2011.566404.

(110) Banerjee, S.; Paira, T. K.; Mandal, T. K. Surface Confined Atom Transfer Radical Polymerization: Access to Custom Library of Polymer-Based Hybrid Materials for Speciality Applications. *Polym. Chem.* **2014**, *5* (14), 4153. https://doi.org/10.1039/c4py00007b.

(111) Pasut, G.; Veronese, F. M. PEG Conjugates in Clinical Development or Use as Anticancer Agents: An Overview. *Adv. Drug Deliv. Rev.* **2009**, *61* (13), 1177–1188. https://doi.org/10.1016/j.addr.2009.02.010.

(112) Cheng, H.; Zhao, Y.-L.; Luo, X.-J.; Xu, D.-S.; Cao, X.; Xu, J.-H.; Dai, Q.; Zhang, X.-Y.; Ge, J.; Bai, Y.-P. Cross-Linked Enzyme-Polymer Conjugates with Excellent Stability and Detergent-Enhanced Activity for Efficient Organophosphate Degradation. *Bioresour. Bioprocess.* **2018**, *5* (1). https://doi.org/10.1186/s40643-018-0236-2.

(113) Romero, O.; Rivero, C. W.; Guisan, J. M.; Palomo, J. M. Novel Enzyme-Polymer Conjugates for Biotechnological Applications. *PeerJ* **2013**, *1*, e27. https://doi.org/10.7717/peerj.27.

(114) Pasut, G.; Veronese, F. M. State of the Art in PEGylation: The Great Versatility Achieved after Forty Years of Research. *J. Controlled Release* **2012**, *161* (2), 461–472. https://doi.org/10.1016/j.jconrel.2011.10.037.

(115) Webster, R.; Didier, E.; Harris, P.; Siegel, N.; Stadler, J.; Tilbury, L.; Smith, D. PEGylated Proteins: Evaluation of Their Safety in the Absence of Definitive Metabolism Studies. *Drug Metab. Dispos.* **2006**, *35* (1), 9–16. https://doi.org/10.1124/dmd.106.012419.

(116) Pasut, G. Polymers for Protein Conjugation. *Polymers* **2014**, *6* (1), 160–178. https://doi.org/10.3390/polym6010160.

(117) Twaites, B.; de las Heras Alarcón, C.; Alexander, C. Synthetic Polymers as Drugs and Therapeutics. *J Mater Chem* **2005**, *15* (4), 441–455. https://doi.org/10.1039/B410799N.

(118) Delplace, V.; Couvreur, P.; Nicolas, J. Recent Trends in the Design of Anticancer Polymer Prodrug Nanocarriers. *Polym Chem* **2014**, *5* (5), 1529–1544. https://doi.org/10.1039/C3PY01384G.

(119) Ke, X.; Coady, D. J.; Yang, C.; Engler, A. C.; Hedrick, J. L.; Yang, Y. Y. PH-Sensitive Polycarbonate Micelles for Enhanced Intracellular Release of Anticancer Drugs: A Strategy to Circumvent Multidrug Resistance. *Polym. Chem.* **2014**, *5* (7), 2621. https://doi.org/10.1039/c3py01784b.

(120) Zhang, S.; Zou, J.; Elsabahy, M.; Karwa, A.; Li, A.; Moore, D. A.; Dorshow, R. B.; Wooley, K. L. Poly(Ethylene Oxide)-Block-Polyphosphester-Based Paclitaxel Conjugates as a Platform for Ultra-High Paclitaxel-Loaded Multifunctional Nanoparticles. *Chem. Sci.* **2013**, *4* (5), 2122. https://doi.org/10.1039/c3sc50252j.

(121) Yin, Q.; Tong, R.; Xu, Y.; Baek, K.; Dobrucki, L. W.; Fan, T. M.; Cheng, J. Drug-Initiated Ring-Opening Polymerization of *O* -Carboxyanhydrides for the Preparation of Anticancer Drug–Poly(*O* -Carboxyanhydride) Nanoconjugates. *Biomacromolecules* **2013**, *14* (3), 920–929. https://doi.org/10.1021/bm301999c.

(122) Tong, R.; Cheng, J. Ring-Opening Polymerization-Mediated Controlled Formulation of Polylactide−Drug Nanoparticles. *J. Am. Chem. Soc.* **2009**, *131* (13), 4744–4754. https://doi.org/10.1021/ja8084675.

(123) Tong, R.; Cheng, J. Drug-Initiated, Controlled Ring-Opening Polymerization for the Synthesis of Polymer–Drug Conjugates. *Macromolecules* **2012**, *45* (5), 2225–2232. https://doi.org/10.1021/ma202581d.

(124) Manju, S.; Sreenivasan, K. Synthesis and Characterization of a Cytotoxic Cationic Polyvinylpyrrolidone–Curcumin Conjugate. *J. Pharm. Sci.* **2011**, *100* (2), 504–511. https://doi.org/10.1002/jps.22278.

(125) Manju, S.; Sreenivasan, K. Conjugation of Curcumin onto Hyaluronic Acid Enhances Its Aqueous Solubility and Stability. *J. Colloid Interface Sci.* **2011**, *359* (1), 318–325. https://doi.org/10.1016/j.jcis.2011.03.071.

(126) Dey, S.; Sreenivasan, K. Conjugation of Curcumin onto Alginate Enhances Aqueous Solubility and Stability of Curcumin. *Carbohydr. Polym.* **2014**, *99*, 499–507. https://doi.org/10.1016/j.carbpol.2013.08.067.

(127) Yang, R.; Zhang, S.; Kong, D.; Gao, X.; Zhao, Y.; Wang, Z. Biodegradable Polymer-Curcumin Conjugate Micelles Enhance the Loading and Delivery of Low-Potency Curcumin. *Pharm. Res.* **2012**, *29* (12), 3512–3525. https://doi.org/10.1007/s11095-012-0848-8.

(128) Gao, W.; Chan, J. M.; Farokhzad, O. C. PH-Responsive Nanoparticles for Drug Delivery. *Mol. Pharm.* **2010**, *7* (6), 1913–1920. https://doi.org/10.1021/mp100253e.

(129) Meng, F.; Hennink, W. E.; Zhong, Z. Reduction-Sensitive Polymers and Bioconjugates for Biomedical Applications. *Biomaterials* **2009**, *30* (12), 2180–2198. https://doi.org/10.1016/j.biomaterials.2009.01.026.

(130) Veronese, F. M.; Schiavon, O.; Pasut, G.; Mendichi, R.; Andersson, L.; Tsirk, A.; Ford, J.; Wu, G.; Kneller, S.; Davies, J.; et al. PEG−Doxorubicin Conjugates: Influence of Polymer Structure on Drug Release, in Vitro Cytotoxicity, Biodistribution, and Antitumor Activity. *Bioconjug. Chem.* **2005**, *16* (4), 775–784. https://doi.org/10.1021/bc040241m.

(131) Basu, S.; Vutukuri, D. R.; Shyamroy, S.; Sandanaraj, B. S.; Thayumanavan, S. Invertible Amphiphilic Homopolymers. *J. Am. Chem. Soc.* **2004**, *126* (32), 9890–9891. https://doi.org/10.1021/ja047816a.

(132) Tomalino, L. M.; Voronov, A.; Kohut, A.; Peukert, W. Study of Amphiphilic Polyester Micelles by Hyper-Rayleigh Scattering: Invertibility and Phase Transfer. *J. Phys. Chem. B* **2008**, *112* (20), 6338–6343. https://doi.org/10.1021/jp710499z.

(133) Voronov, A.; Kohut, A.; Peukert, W.; Voronov, S.; Gevus, O.; Tokarev, V. Invertible Architectures from Amphiphilic Polyesters. *Langmuir* **2006**, *22* (5), 1946–1948. https://doi.org/10.1021/la052225z.

(134) Kohut, A.; Voronov, A. Hierarchical Micellar Structures from Amphiphilic Invertible Polyesters: ^{1}H NMR Spectroscopic Study. *Langmuir* **2009**, *25* (8), 4356–4360. https://doi.org/10.1021/la900700u.

(135) Hevus, I.; Modgil, A.; Daniels, J.; Kohut, A.; Sun, C.; Stafslien, S.; Voronov, A. Invertible Micellar Polymer Assemblies for Delivery of Poorly Water-Soluble Drugs. *Biomacromolecules* **2012**, *13* (8), 2537–2545. https://doi.org/10.1021/bm3007924.

(136) Hevus, I.; Voronov, A.; Yaszemski, M. J.; Maran, A.; Kohut, A.; Voronov, S. Anticancer Efficiency of Curcumin-Loaded Invertible Polymer Micellar Nanoassemblies. In *Nanostructures for Cancer Therapy*; Elsevier, 2017; pp 351–382. https://doi.org/10.1016/B978-0-323-46144-3.00014-3.

(137) Hevus, I.; Kohut, A.; Voronov, A. Interfacial Micellar Phase Transfer Using Amphiphilic Invertible Polymers. *Polym. Chem.* **2011**, *2* (12), 2767. https://doi.org/10.1039/c1py00399b.

(138) Hevus, I.; Kohut, A.; Voronov, A. Micellar Assemblies from Amphiphilic Polyurethanes for Size-Controlled Synthesis of Silver Nanoparticles Dispersible Both in Polar and Nonpolar Media. *J. Nanoparticle Res.* **2012**, *14* (4). https://doi.org/10.1007/s11051-012-0820-x.

(139) Voronov, A.; Vasylyev, S.; Kohut, A.; Peukert, W. Surface Activity of New Invertible Amphiphilic Polyesters Based on Poly(Ethylene Glycol) and Aliphatic Dicarboxylic Acids. *J. Colloid Interface Sci.* **2008**, *323* (2), 379–385. https://doi.org/10.1016/j.jcis.2008.04.053.

(140) Kudina, O.; Shogren, K. L.; Gustafson, C. T.; Yaszemski, M. J.; Maran, A.; Voronov, A. Invertible Micellar Polymer Nanoassemblies Target Bone Tumor Cells but Not Normal Osteoblast Cells. *Future Sci. OA* **2015**, *1* (3). https://doi.org/10.4155/fso.15.14.

CHAPTER 2. RESEARCH SCOPE

Peptides and proteins are considered to be promising candidates in a variety of biomedical and nonbiological applications. However, due to several limitations, such as sensitivity to pH, temperature, degradation, organic solvents, etc., their practical usage is limited. To overcome those issues, peptide/protein-polymer assemblies can be used, where the advantages of each component may be balanced, resulting in the enhanced material properties. Furthermore, the use of responsive polymers, where even minor changes in one of the polymer characteristics triggered by the external stimuli can cause drastic changes in the functions and performance, is currently widely studying area of research.

Widespread efforts have been made on development of different types of responsive polymers and polymeric materials. The fundamental understanding of interactions between the responsive polymer and various cargo and how these interactions affect the resulting material properties can be used for formation of the thermodynamically stable polymer-peptide colloids, such as mixed micellar assemblies or polymer-enzyme conjugates. Moreover, the type of interaction can be the main driving force in the colloid formation, its stability, impact the loading capacity of the system, and enhancing of cargo activity. It has been reported that the covalent bonding between polymeric macromolecules and biological molecule can lead to the significant change in cargo activity. To elaborate on these factors, the understanding of fundamental aspects in formation of polymer-cargo assemblies as well as the impact of polymeric structure on their physicochemical properties should be studied.

Synthesized in our group amphiphilic invertible polymers (AIPs) can self-assemble into micellar architectures with the increasing of AIP concentration and rapidly switch macromolecular conformation in response to changes in solvent polarity. Resulted invertible micellar assemblies

(IMAs) can be potentially used as nanocontainers and nanocarriers in both polar and nonpolar media given their ability to localize substances inside the micellar domains. In addition, the macromolecular inversion can be a decisive factor in accomplishing the sustained release profile of IMAs-based adjuvants. Loaded with a hydrophobic drug, AIP micelles can successfully deliver cargo molecules from an aqueous medium to a polar/nonpolar interface and release the drug upon inverting the macromolecular conformation by entering/contacting the less polar biomembrane medium.

While the interactions between AIPs and hydrophobic cargo have been demonstrated, few fundamental questions still need to be answered. For example, upon incorporation what are the microenvironment (crowding, polarity), position, and partition of the cargo molecules in IMA lipophilic and hydrophilic domains? This information is important for understanding the potential impact of the IMAs on the peptide structure and stability, two important factors related to peptide delivery. In addition, upon IMA packing/conformation change triggered by changes in environment polarity, how does peptide position or partition change accordingly?

Given their potential value in the field of peptide delivery, understanding how the IMAs interact with lipid membranes, and the factors facilitating AIPs-mediated interaction with lipid bilayers, is equally important. Through such understanding the basic principles underlying the effective design of AIP-based polymeric carriers as membrane-active compounds can be established.

The goal of this work is to investigate interactions between range of new polymers and various cargo molecules and determine whether those interactions affect the physicochemical properties of the resulted colloids. For this purpose, two types of colloid systems were explored: i) peptide-loaded invertible micellar assemblies (IMAs), formed using hydrophobic interactions

between amphiphilic invertible polymers (AIP) and peptides (HA, V5, or peptide-based vaccine), and ii) polymeric cellulosomes made from polymer ligand (PL), copolymer of glycidyl methacrylate (GMA) and poly(ethylene glycol) methyl ether methacrylate (PEGMA) and mixture of cellulases, using covalent bonding. The purpose of the research was to evaluate if colloids properties are affected by changes in responsive polymer characteristics as well as if the developed macromolecular structure and composition need further synthetic modification/optimization.

Chapter 1 of this dissertation overviews the responsive polymers, their morphology, types, and properties. The main interactions used to form the polymer-cargo assemblies is also discussed.

Chapter 3 is focused on understanding "can IMAs serve as peptide carriers?". As a first step in demonstrating AIPs potential as micellar adjuvants, the "host–guest" interactions between IMAs and two different peptides (HA and V5) were confirmed using ^{1}H Nuclear Magnetic Resonance (NMR) spectroscopy. Microphase separation and further micellization of the AIP macromolecules in an aqueous solution lead to interactions between AIP and the peptide resulting in the formation of mixed micelles. The inner part of these micelles consists of the hydrophobic moieties of both AIP and the peptide whereas the hydrophilic fragments of AIP and the peptide build up a micellar exterior.

Chapter 4 is dedicated to the detailed study of the peptide localization within the IMAs. While IMAs have been demonstrated to interact with peptides, fundamental pictures of micellar inversion remain elusive and became the focus of this chapter, including the behavior of the incorporated peptide in IMAs at molecular level at different polarities of the environment and how polymer composition impacts such behavior. Electron spin labeling and Electron Paramagnetic Resonance (EPR) spectroscopy were used to monitor the mobility of the incorporated labeled

peptide in micellar interior in aqueous media. In addition, the mobility of peptide in IMAs under the changes in the polarity of the environment triggered by the addition of acetone was evaluated.

Chapter 5 estimates the feasibility of IMAs in cargo delivery and release. The interactions of AIPs with different hydrophilic-lipophilic balance (HLB) with a highly fluidic microcavity supported model lipid bilayer were investigated. The impact of IMAs on membrane diffusivity and permeability as well as capacity of the micelles to release an encapsulated fluorescent probe into the hydrophobic core of a lipid bilayer was evaluated. It was shown that the extent of this impact essentially depends on the HLB of the AIP.

Chapter 6 demonstrates that the IMAs can be used as adjuvants in development of polymer-peptide based vaccines against Swine influenza viruses (SIV). To enhance the delivery and immunogenicity of peptide-based vaccines, micellar assemblies from AIP and peptide were formed. Obtained peptide-loaded IMAs were tested in vitro and in vivo in order to evaluate the targeted delivery, antibody response, and immunity protection in vaccinated pigs. The data demonstrate that the IMAs are effective in delivering the peptide cargo to cells, and act as an adjuvant in stimulating strong antibody responses against the delivered antigen in vaccinated pigs.

In Chapter 7, polymer cellulosomes from PL and cellulases were designed in order to improve the enzymatic catalytic activity for the biomass hydrolysis. Copolymers from glycidyl methacrylate (GMA) and poly(ethylene glycol) methyl ether methacrylate (PEGMA) of different molar ratios were synthesized using free radical copolymerization and conjugated with cellulases. Combination of the reactive epoxy functional groups and oligomeric PEGMA side groups in the polymer structure provides the ability to improve the enzymatic catalytic activity. While PEGMA fragments ensure solubility of the PL in aqueous solutions and steric stabilization of cellulosomes, PL's epoxy groups react with multiple amino groups of the enzyme lysine creating a covalently

bonded enzyme-polymer conjugate (EPC). The catalytic activity of the obtained EPCs, conjugation efficiency, glucose inhibition effect, type of substrate, and type of biomass pretreatment were evaluated and compared to free enzymes.

Chapter 8 summarize the overall conclusions of this dissertation and suggests the future research directions of this work.

CHAPTER 3. ^{1}H NMR STUDY OF "HOST-GUEST" INTERACTIONS OF MICELLAR ASSEMBLIES FROM AMPHIPHILIC INVERTIBLE POLYMERS AND PEPTIDES*

3.1. Abstract

"Host-guest" interactions between self-assembled micellar nanostructures from amphiphilic invertible polymers (AIPs) and two peptides, swine-origin Influenza A surface protein Hemagglutinin (HA) and research antibody peptide V5, were investigated by changing the polymer concentration and polymer/peptide ratio in the aqueous solution. Formation of mixed micellar assemblies from AIP and each peptide is revealed using detailed ^{1}H NMR spectroscopic study. Peptide molecule localization in the micellar assemblies depends on the peptide chemical structure (specific interactions between amino acid functional groups and polymer fragments). The resulting mixed micellar structures can be considered as a promising material toward delivery and stimuli-responsive sustained release of peptides.

3.2. Introduction

Due to ability of self-assembling in aqueous solution, amphiphilic block copolymers form polymeric micelles consisting of hydrophilic and hydrophobic domains [1,2]. Driving force for the self-assembly is a hydrophobic interaction that leads to the formation of micellar architectures with a hydrophobic interior and a hydrophilic stabilizing exterior [3-5]. Self-assembled polymeric

* The material in this chapter was co-authored by Oksana Zholobko, Ananiy Kohut, Ivan Hevus, and Andriy Voronov. Oksana Zholobko had the primary responsibilities of synthesizing and characterizing polymers and formation of polymer-peptide micellar assemblies. Oksana Zholobko was also charged with characterizing the polymer-peptide micellar assemblies using ^{1}H NMR Spectroscopy and DLS analysis. Oksana Zholobko was involved in drafting and revising all versions of this chapter. Ananiy Kohut and Andriy Voronov helped explain the results collected by Oksana Zholobko. Published article can be found at https://doi.org/10.1002/macp.201700344.

architectures can effectively accommodate (solubilize) hydrophobic substances by physically entrapping them in the hydrophobic micellar interior [6-12]. Size of assemblies is typically 10-100 nm and can be precisely controlled by varying the structure of the amphiphilic macromolecules by the choice of the length of the hydrophobic fragments. A number of recent studies have discussed feasibility of polymeric micellar assemblies as carriers for various biomedical applications [13-21], including vaccine adjuvants (substances that are incorporated with a vaccine and enhance an immune response) [22-27]. Amphiphilic macromolecules provide an ability to tailor adjuvant properties by varying the macromolecular structure and facilitating the delivery of specific antigens [28]. Polymeric micelles also may offer advantages of sustained antigen release and demonstrated the potential for formation of single dose vaccines [29,30]. For loading of antigens into the micelles from block copolymers, several methods can be used including chemical conjugation, entrapment, and physical adsorption, as the potentially most effective process to boost an immune response [31].

Amphiphilic poloxamers (Pluronics) and poloxamines (Tetronics) of different molecular weight, synthesized from various ratios of poly(propylene oxide) and poly(ethylene oxide), have been reported as polymeric micellar adjuvants [22]. Being dissolved in water at physiological pH, these macromolecules self-assemble into micelles showing vaccine adjuvant potential [23]. The efficiency of micellar adjuvants depends on the hydrophilic–lipophilic balance of the copolymer (ratio and distribution of hydrophilic and hydrophobic fragments in macromolecules). Even minor differences in the polymer molecular weight, polydispersity index and hydrophilic-lipophilic balance could greatly affect the immune response. A larger presence of hydrophobic fragments can result in identifying the polymer adjuvants as “foreign” by the body, enhancing cell adhesion

and phagocytosis of macrophages [32,33]. Additionally, changing the molecular weight and hydrophilic–lipophilic balance can tailor the release profile of a polymer micellar adjuvant.

Synthesized in our group amphiphilic invertible polymers (AIPs) can: i. Self-assemble into micellar architectures as AIP concentration increases and ii. Rapidly switch macromolecular conformation in response to changes in solvent polarity [34-40]. The incompatibility of alternating fragments along the AIP macromolecules results in microphase separation with a great degree of tunability [34-36]. The invertible micellar assemblies (IMAs) from AIPs have a well-controlled size and morphology in both polar and nonpolar environments [38]. The morphology can be tuned by adjusting the molecular weight and ratio of the components of the macromolecules, allowing a variety of "guests" to interact within the "host" micellar assemblies [38-40]. The IMAs can be potentially used as nanocontainers and nanocarriers in both polar and nonpolar media given their ability to localize substances inside the micellar domains [37,38]. In addition, the macromolecular inversion can be a decisive factor in accomplishing the sustained release profile of IMAs-based adjuvants [35].

Peptide HA: FITC-Ahx-Tyr-Pro-Tyr-Asp-Val-Pro-Asp-Tyr-Ala

Peptide V5: FITC-Ahx-Gly-Lys-Pro-Ile-Pro-Asn-Pro-Leu-Leu-Gly-Leu-Asp-Ser-Thr

where FITC - fluorescein isothiocyanate, Ahx - amino hexanoic acid

Figure 3.1. Chemical structure of HA and V5.

As a step in demonstrating AIPs potential as micellar adjuvants, in this study the "host–guest" interactions between IMAs and two different peptides were reported. Antigenic glycoprotein, HA (Hemagglutinin) is a recently identified swine-origin Influenza A (H1N1) surface protein. It facilitates viral attachment to the cell that is being infected by swine flu. The HA can also draw immune responses that prevent infection and is a good candidate drug for influenza virus entry inhibition. The HA, in combination with other research antibody peptide V5,

were chosen as a model cargo in demonstrating IMAs-peptide interactions. The resulting stable mixed micellar structures can be considered as a promising material toward delivery and stimuli-responsive sustained release of peptides.

To address a specific question "can IMAs serve as peptide carriers?", V5 and HA (**Fig. 3.1**) were added to aqueous solutions of the AIPs synthesized from: (i) PEG (molecular weight 1000 g/mol) and sebacic acid (polyester S10); (ii) PEG (molecular weight 1000 g/mol) and dodecanedioic acid (polyester D10); and (iii) PEG (molecular weight 600 g/mol), PTHF (molecular weight 650 g/mol), and succinic anhydride (polyester $PEG_{600}PTHF_{650}$) to conduct a detailed ^{1}H NMR spectroscopy study on mixtures containing various ratios of the potential carrier (AIP macromolecules) and cargo (both peptides).

3.3. Experimental

3.3.1. Materials

Poly(ethylene glycol) (PEG, molecular weights 600 and 1000 g/mol), polytetrahydrofuran (PTHF, molecular weight 650 g/mol), sebacic acid, succinic anhydride, and deuterium oxide were purchased from Sigma-Aldrich. Dodecanedioic acid was obtained from TCI.

Peptides V5 (molecular weight 1923 g/mol, sequence of 14 amino acids including 7 nonpolar and 7 polar (1 acidic, 1 basic, and 5 neutral) amino acids) and HA (molecular weight 1603 g/mol, sequence of 9 amino acids including 4 nonpolar and 5 polar (2 acidic and 3 neutral) amino acids) (**Fig. 3.1**) were purchased from United BioSystems Inc.

3.3.2. Syntheses

Amphiphilic invertible polymers (**Fig. 3.2**) were synthesized using previously reported methods from PEG-1000 and sebacic acid (S10), PEG-1000 and dodecanedioic acid (D10), or

PEG-600, PTHF-650, and succinic anhydride ($PEG_{600}PTHF_{650}$) using the polycondensation of polyols with aliphatic dicarboxylic acids or anhydrides [34,35].

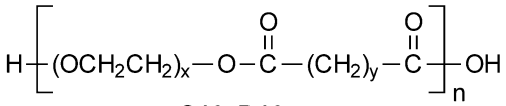

S10, D10

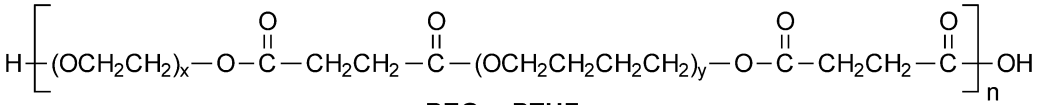

$PEG_{600}PTHF_{650}$

Figure 3.2. Chemical structure of the amphiphilic polymers.

3.3.3. ^1H NMR spectroscopy

Polymer samples for ^{1}H NMR spectroscopy were prepared by dissolving an appropriate amount of AIP in deuterated water under gentle agitation. AIP–peptide micellar structures were prepared using the thin film method [41]. According to this method, appropriate amounts of polymer and peptide were dissolved in 2 mL of acetone. The solvent was removed by rotary evaporation at 40°C for 1 h to obtain a solid peptide/AIP matrix. Residual acetone remaining in the peptide/AIP matrix was evaporated overnight under vacuum. The resultant thin film was hydrated with 1 mL of deuterated water. The solutions were left for at least 16 h to equilibrate at room temperature prior to the measurements. ^{1}H NMR spectra were recorded on an AVANCE III HDTM 400 high-performance digital NMR spectrometer at 400 MHz and 22.5°C. The spectra were referenced to a TMS signal as an internal standard.

3.3.4. Dynamic Light Scattering (DLS)

Size distribution of AIP micelles in aqueous solution were measured using Malvern Zetasizer Nano-ZS90 at 25 °C. The final numbers represent an average of a minimum of 10 individual measurements.

3.4. Results and discussion

3.4.1. ^{1}H NMR study of polymer self-assembly

In the past three decades, ^{1}H NMR spectroscopy was proven to be a very powerful technique for studying macromolecular conformation when macromolecules comprise the micelles in a wide range of temperatures and concentrations. For both low-molecular-weight and polymeric surfactants, micelle formation and morphology was extensively studied by ^{1}H NMR spectroscopy [42,43]. The main reason for this is that the chemical shifts of protons are sensitive to the electronic environment. Since neighboring molecules contribute to the electronic structure, NMR is sensitive to the solvent environment of a molecule and this "solvent effect" provides valuable molecular information. Below the cmc, the average environment for the atoms in the hydrophobic tails of a surfactant is aqueous. As the cmc is passed upon increasing the surfactant concentration, the hydrophobic tails mostly reside in the aliphatic environment of micellar interiors. It results in upfield shifts of the peaks attributed to the "hydrophobic" protons because they become localized in a nonpolar microenvironment upon micelle formation [44]. On the other hand, examining temperature- and/or concentration-dependent line-shape changes in ^{1}H NMR spectra is widely used for studying aggregation processes of amphiphilic macromolecules in D_2O solutions. Namely, the broadening of the proton signals indicates that upon micellization, the corresponding moieties are located in a more compact viscous microenvironment and cannot move freely [43]. NMR spectroscopy can also be applied for studying intermolecular interactions. One example is the molecular association of surfactants and cyclodextrin molecules that leaves an imprint in the chemical shifts along the surfactant hydrophobic tail which informs about the average structure of the molecular complex [45].

In our work, the ^{1}H NMR technique was used for the systematic study of polymer composition and concentration effect on both the micellization properties of the AIPs in aqueous solutions and the ability of the micellar assemblies formed from the AIP macromolecules to localize peptides inside the micellar domains and serve as peptide nanocarrier.

The chemical structure of the amphiphilic polymers that were used in this study for the formation of micellar assemblies is shown in **Figure 3.2**. The characteristics of the polymers such as their molecular weight, polydispersity index, lengths of the hydrophilic PEG chains and hydrophobic $(CH_2)_y$ or PTHF moieties, polymerization degree, hydrophilic lipophilic balance (HLB), and critical micelle concentrations (cmc) [40] are given in **Table 3.1**. The chemical structures of the S10, D10, and $PEG_{600}PTHF_{650}$ synthesized *via* step-growth polymerization were confirmed by ^{1}H NMR and FT-IR spectroscopies [34,35]. The HLB of the amphiphilic macromolecules was varied by changing length and length ratio of hydrophilic and hydrophobic fragments in macromolecules between 13.8 and 15.4.

Table 3.1. Characteristics of the amphiphilic polymers

AIP	M_w, g/mol	PDI	x[a]	y[b]	n[c]	degree of polymerization	HLB[d]	cmc, %
S10	9,600	1.18	22.3	8	8.2	16.5	15.4	$4.9 \cdot 10^{-2}$
D10	6,360	1.23	22.3	10	5.3	10.7	14.4	$3.3 \cdot 10^{-3}$
$PEG_{600}PTHF_{650}$	9,420	2.2	13.2	8.8	6.7	26.6	13.8	$3.5 \cdot 10^{-4}$

[a] *x* represents the average number of ethylene oxide units in hydrophilic fragments in the main AIP backbone (**Fig. 3.2**);
[b] *y* represents the number of methylene groups in hydrophobic fragments in the main S10 and D10 backbone or the average number of tetramethylene oxide units in hydrophobic fragments in the main $PEG_{600}PTHF_{650}$ backbone (**Fig. 3.2**);
[c] *n* represents the average number of repeat units in the main AIP backbone (**Fig. 3.2**);
[d] HLB is the hydrophilic-lipophilic balance of the polymers calculated according to Ref. [46].

As the first step in this study, ^{1}H NMR spectra were collected for three different concentrations of each polymer in deuterated water to demonstrate their self-assembly and formation of micellar assemblies. **Figures 3.3**, **3.4** show the local expanded spectra of each peak region for S10 and D10.

In the ^{1}H NMR spectra of the S10 and D10 solutions in D_2O at a polymer concentration of 0.1% (*i.e.*, above the cmc [40] for both polymers), the signal width corresponding to methylene groups localized in the internal part of the hydrophobic fragment (peak **c** in **Fig. 3.3** and **3.4**) is rather broad. It indicates that the methylene groups avoiding contact with an aqueous medium self-assemble and form a micellar interior environment, thus reducing their mobility due to the close packing of the hydrophobic moieties.

The recorded spectra indicate that each -CH_2- group in the α and β positions in relation to the carbonyl groups in the dicarboxylic acid moieties (**Fig. 3.3** and **3.4**, protons **a** and **b**, respectively) shows two different signals in D_2O. The significant upfield shifts of a part of protons **a** (signals at ~2.17 ppm for both S10 and D10) and **b** (signals at ~1.55 ppm for both S10 and D10) at a 0.1% concentration imply that these protons are apparently located in a nonpolar micellar interior. The chemical shift is known to be sensitive to the chemical nature of the related protons, and transferring part of protons **a** and **b** to the nonpolar microenvironment induces the shift toward lower ppm values as a result of the change in magnetic susceptibility of the protons [42].

The sudden ^{1}H downfield shifts experienced by the remaining protons **a** and **b** indicate that they are transferred to a polar aqueous medium. Because the interaction with water enhances the deshielding effect of the C–H protons, it results in the appearance of the peaks at ~2.43 and ~1.63 ppm for S10 and D10 (**a** and **b**, respectively). Thus, protons **a** and **b** are located partially in a

nonpolar micellar interior and partially in a polar aqueous medium. This is attributable to a strong electron-withdrawing inductive effect of the carbonyl groups resulting in enhanced polarizability of the C-H bonds in the α and β positions.

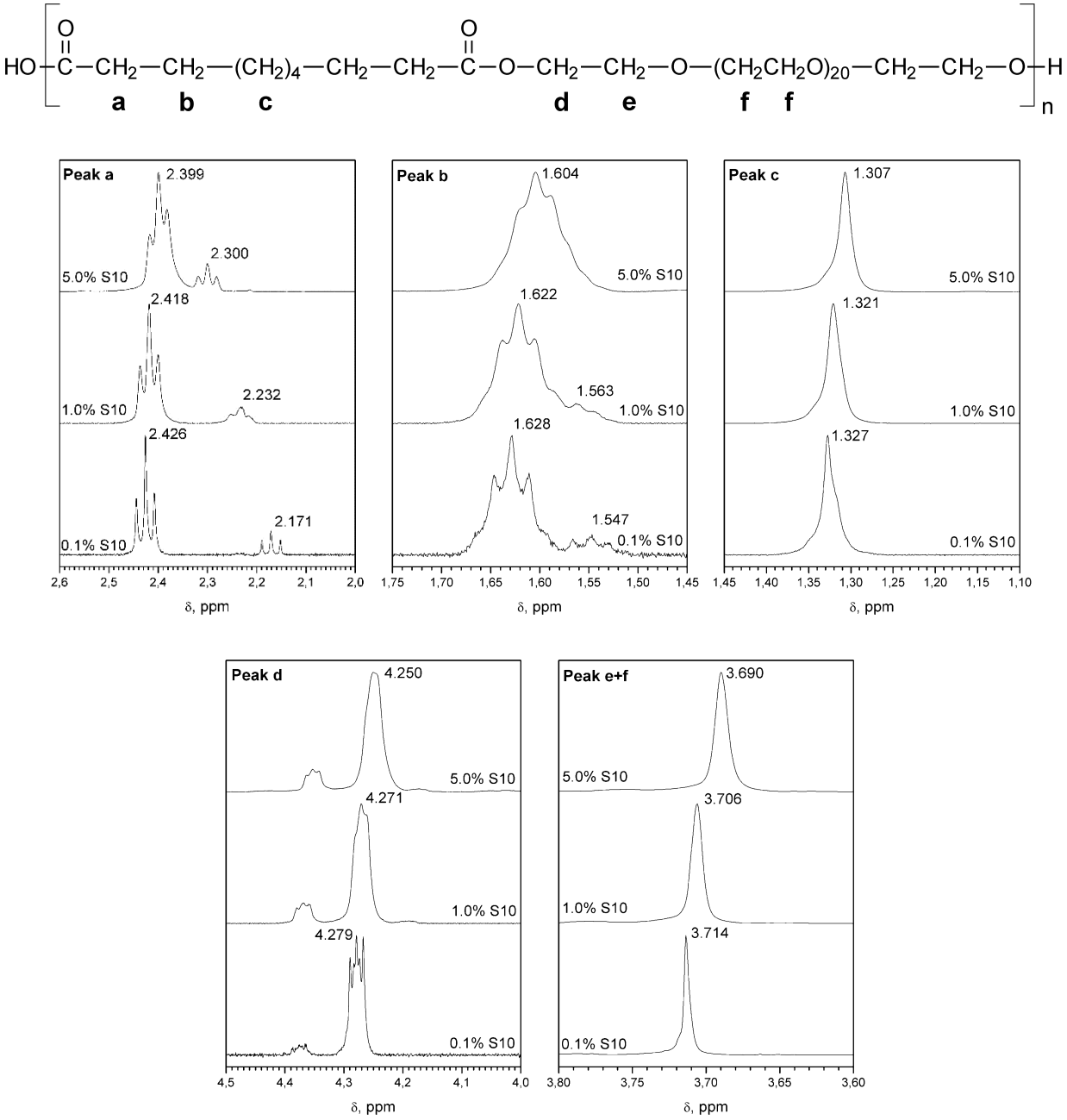

Figure 3.3. ^{1}H NMR spectra of the S10 solutions in D_2O at different concentrations.

At the same time, the peaks that are attributed to the poly(ethylene glycol) fragments of polyesters S10 and D10 (**Fig. 3.3**, **3.4**, protons **d-f**) move considerably downfield as compared with the chemical shifts of the same protons in the PEG fragments in $CDCl_3$ (~4.22 and ~3.65 ppm for protons **d** and **e-f** [37], respectively). It indicates that the PEG units reside in a polar aqueous medium at the micellar outer surface (in micellar exterior). The peaks remain sharp, showing that PEG fragments are long enough to move freely. As a result, at low concentrations in an aqueous solution, S10 and D10 build up micelles with a hydrophobic inner part formed by dicarboxylic acid moieties and an outer part made up of the hydrated PEG fragments.

It can be concluded from the data presented in **Figures 3.3**, **3.4** that the polyester micelles aggregate with increasing concentration to form micellar assemblies containing hydrophilic and lipophilic domains. Increasing the polyester concentration in water leads to a broadening of the signals attributed to the PEG protons **d-f**, indicating that the motions of the PEG fragments are limited owing to their closer packing in the hydrophilic domain. Disappearance of the hyperfine structures of the methylene groups **a** and **b** located in the area of the PEG fragments supports the idea that the mobility of the polar units decreases with increasing polyester concentration. A slight shift of the signal in **d-f** toward lower ppm values implies that the polarity within the hydrophilic domain is lower than those in the outer part of polyester micelles.

The signals of hydrophobic protons **c** experience a slight narrowing that shows inessential enhancement in the mobility of the $-(CH_2)_n-$ groups when they form a hydrophobic domain in water. In contrast to more hydrophobic polyesters synthesized from shorter PEGs (PEG-300 and PEG-600) [37], the signals **c** of S10 and D10 shift upfield with increasing polyester concentration in D_2O, indicating that the polarity of the hydrophobic domain of the self-assembled micellar assemblies is lower than that of the micelle inner part. These data are consistent with the results of

SANS analysis [38], which showed that the S10 and D10 macromolecules form micellar assemblies with well-defined hydrophobic domains at a polymer concentration of 1.0% and more.

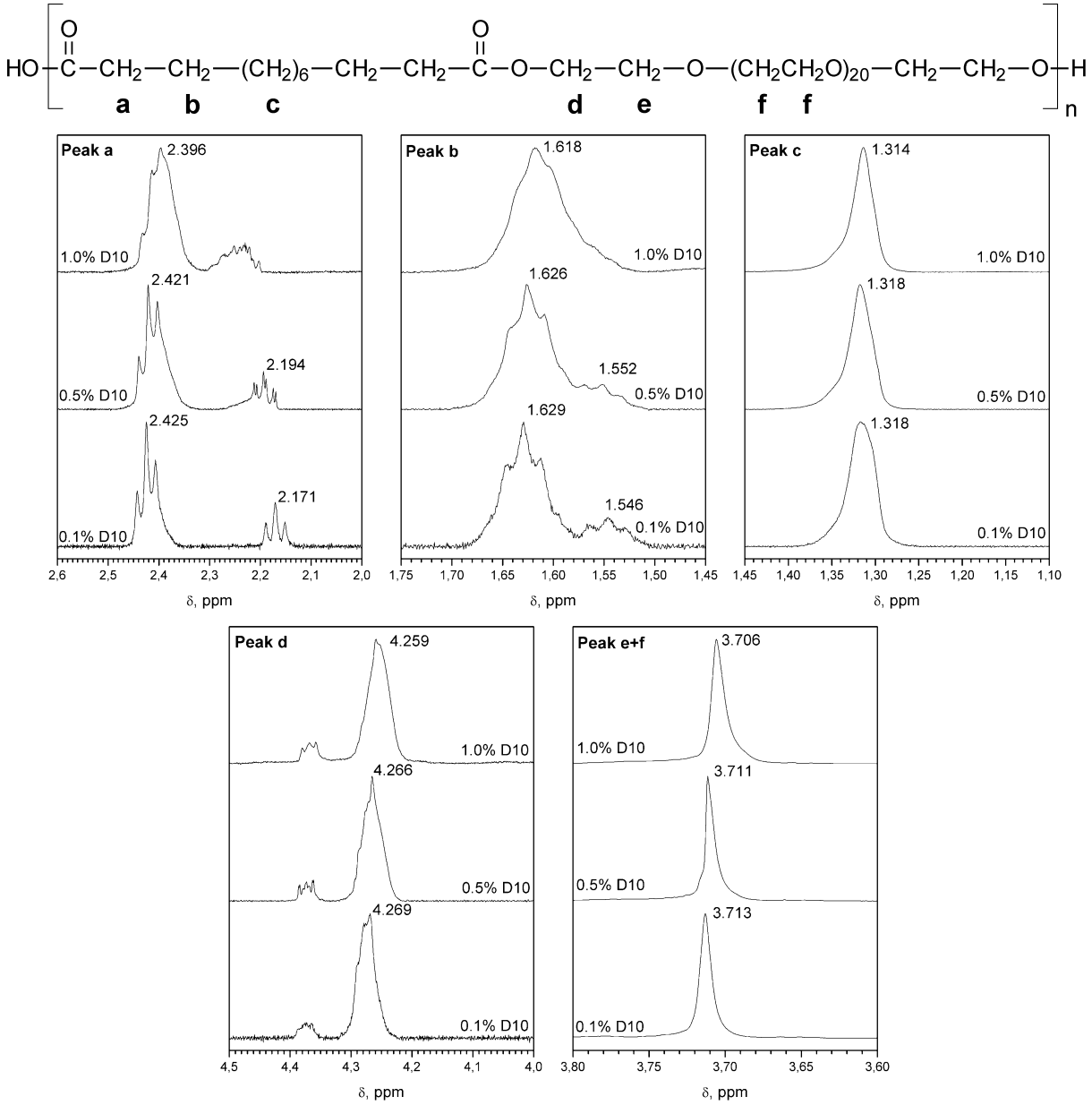

Figure 3.4. ^{1}H NMR spectra of the D10 solutions in D_2O at different concentrations.

Figure 3.5 shows the local expanded ^{1}H NMR spectra of each peak region for polyester $PEG_{600}PTHF_{650}$ at three different concentrations of polymer in deuterium oxide. The changes in the chemical shift and the appearance of hydrophilic PEG proton signals are similar to those

described for S10 and D10, and they suggest that $PEG_{600}PTHF_{650}$ also forms micelles with a polar exterior and a nonpolar interior in the aqueous medium at 0.1% (above the cmc).

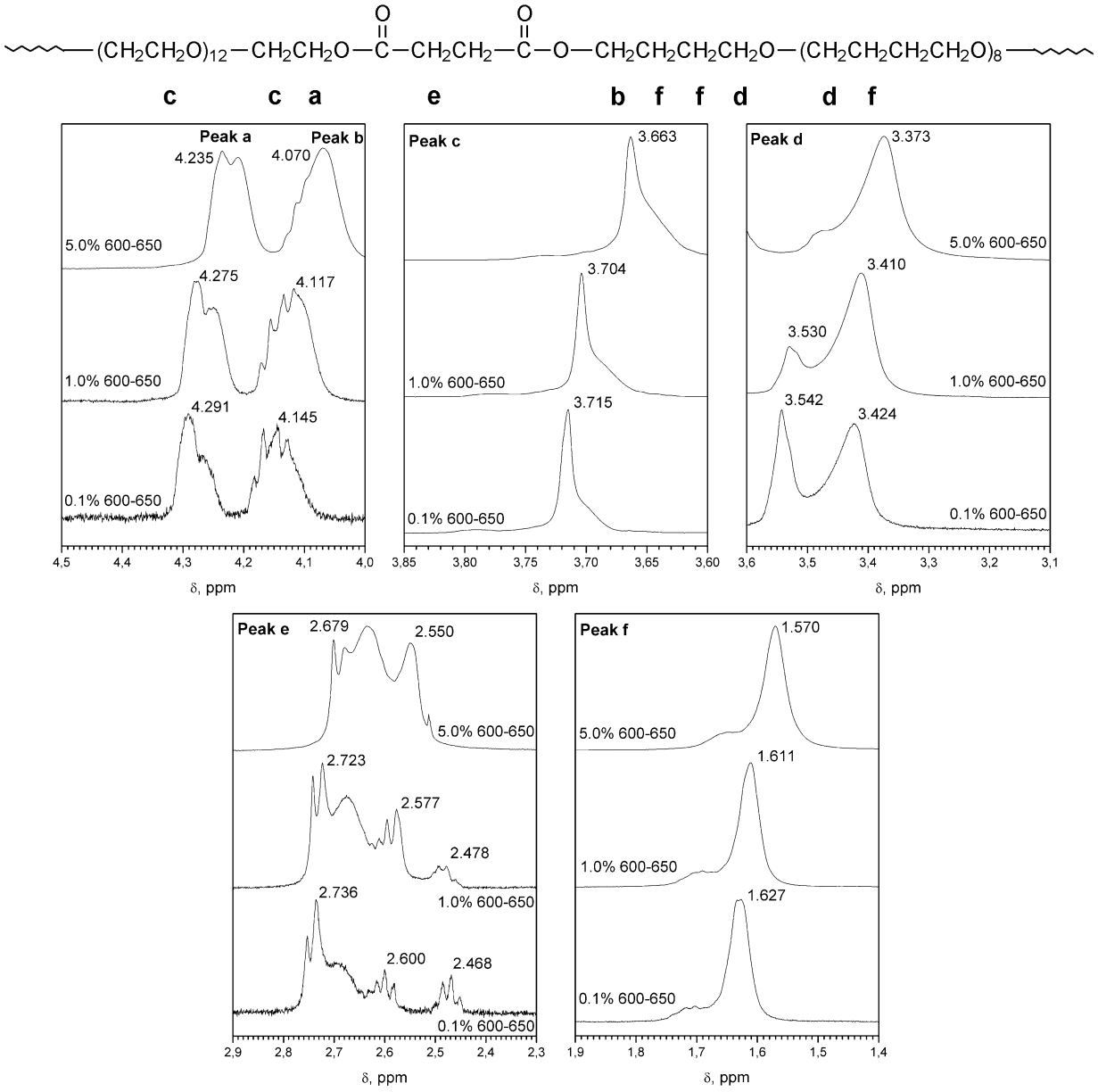

Figure 3.5. ^1H NMR spectra of the $PEG_{600}PTHF_{650}$ solutions in D_2O at different concentrations.

Splitting signals of protons **d** located in the α position to the PTHF ether oxygen atoms into two peaks (signals at 3.542 and 3.424 ppm) implies that these atoms are divided between the hydrophobic inner part and the hydrophilic corona of the micelle, similarly to protons **a** and **b** of

polyesters S10 and D10. Hence, the $PEG_{600}PTHF_{650}$ macromolecules arrange themselves in an aqueous medium, giving rise to micelles with a hydrophobic interior and a hydrophilic exterior.

As the $PEG_{600}PTHF_{650}$ concentration in water increases, the polymer micelles undergo self-assembly into micellar assemblies, similar to D10 and S10. The microenvironment in the formed assemblies is less polar than that in the individual micelles, causing upfield shifts of the NMR proton peaks. Increasing the $PEG_{600}PTHF_{650}$ concentration from 0.1% to 5% leads to a decrease in the width of the peak of the hydrogen atoms located in the hydrophobic PTHF fragments (peak **f** in **Fig. 3.5**). Narrowing the nonpolar proton peaks suggests that the mobility of the nonpolar fragments is enhanced in the larger hydrophobic domains of the micellar assemblies, as compared to the tight interior of the smaller micelles. In the case of $PEG_{600}PTHF_{650}$, the extent of the peak narrowing greatly decreases in the concentration range of 1%–5%, indicating that minor changes in the packing density of the hydrophobic fragments in the nonpolar domains are observed in this concentration range.

In contrast, broadening of the hydrophilic PEG proton peaks (signal **c**) is observed as the $PEG_{600}PTHF_{650}$ concentration increases. The increased width of the PEG signals (peaks **a** and **c** in **Fig. 3.5**) implies that the mobility of the poly(ethylene glycol) fragments is somewhat hindered because of their close packing in the polar domains.

Additionally, increasing the $PEG_{600}PTHF_{650}$ concentration from 0.1% to 5% results in the total majority of the PTHF protons **d** being transferred to the hydrophobic domains of the micellar assemblies, as indicated by a drastic reduction in the intensity of the peak at ~3.5 ppm with the simultaneous increase in the integral intensity of the peak at ~3.4 ppm (**Fig. 3.5**).

In summary, at a 0.1% concentration, each studied polymer forms micelles with a hydrophilic exterior composed of polar PEG chains and a hydrophobic interior made of nonpolar

PTHF ($PEG_{600}PTHF_{650}$) or $–(CH_2)_{8\text{-}10}–$ (S10 and D10) fragments in the aqueous solution. Increasing the polymer concentration leads to the formation of micellar assemblies composed of hydrophilic and hydrophobic domains due to the micellar self-assembly (**Fig. 3.6**).

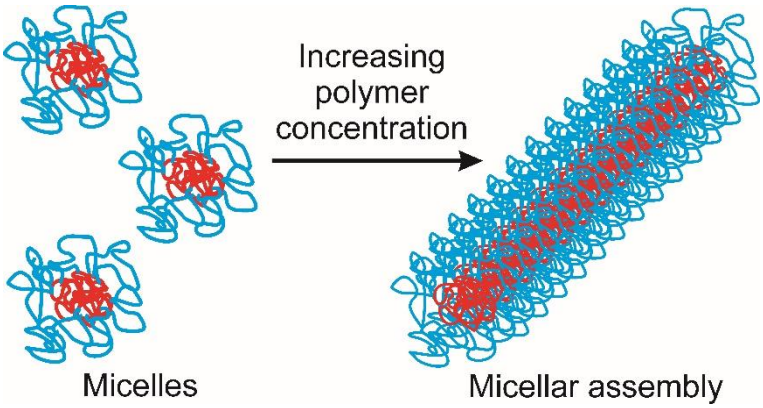

Figure 3.6. Formation of micellar assemblies due to self-assembly of AIP micelles in an aqueous medium.

3.4.2. ^{1}H NMR study of polymer-peptide interactions

After confirmation of AIPs micellization and further formation of micellar assemblies in water, the next step in this work was to probe the interactions between micellar assemblies and V5 and HA peptides. For this purpose, proton spectra were collected for polymer-peptide mixtures containing each peptide added to micellar assemblies from S10, D10, and PEG_{600}-$PTHF_{650}$ formed at different AIP concentrations in water (**Fig. 3.7–3.9**). The AIP concentration was fixed at 0.1% and 0.5% with various amounts of a peptide added to bring its concentration in water to 0.025%, 0.050%, or 0.125%. The shifts in ^{1}H signals of polymer protons (**Table 3.2**) are larger than would be anticipated for solvation effects (for instance, 0.5 Hz for crown ethers in CCl_4) [47].

Table 3.2. Shifts of AIP signals in ^{1}H NMR spectra caused by "host–guest" interaction at different polymer and peptide concentrations

AIP		**Peptide**		**Signal shifts[a], ± 0.24 Hz**					
abbreviation	conc., %	abbr.	conc., %	a	b	c	d	e	f
D10	0.1	V5	0.025	-1.6[b] +12.8[c]	-1.6[b] _[d]	-6.8	-1.2	-0.8	
D10	0.1	V5	0.05	-2.4[b] +11.2[c]	-2.0[b] _[d]	-6.8	-1.2	-1.2	
D10	0.1	HA	0.025	-2.0[b] _[d]	-27.6[b] _[d]	-6.8	-1.6[e] -17.6[f]	-1.6	
D10	0.1	HA	0.05	-2.8[b] _[d]	-31.6[b] _[d]	-7.2	-1.6[e] -21.6[f]	-2.4	
D10	0.5	V5	0.025	-8.8[b] +18.4[c]	-9.2[b] _[d]	-8.0	-2.0	-1.6	
D10	0.5	V5	0.05	-23.6[b] +23.2[c]	-17.2[b] _[d]	-9.2	-10.0	-2.0	
D10	0.5	V5	0.125	-32.0[b] +28.0[c]	-24.8[b] _[d]	-13.6	-15.6	-2.0	
S10	0.1	V5	0.05	-1.6[b] +10.0[c]	-1.6[b] +2.8[c]	-2.4	-1.6	-1.2	
$PEG_{600}PTHF_{650}$	0.1	V5	0.025	-0.8	+7.6	-1.6	-1.6[b] -4.4	-2.8	-4.8
$PEG_{600}PTHF_{650}$	0.1	V5	0.05	-1.2	+6.8	-2.0	-2.4[b] -4.4[c]	-2.8	-5.2

[a]Negative values stand for upfield shifts of signals in ^{1}H NMR spectra of the mixed micellar assemblies from AIP and peptides as compared to the position of the corresponding signals in the spectra of polymer at the same concentration. Positive values are downfield shifts.
[b]For a part of the signal with a higher ppm value.
[c]For a part of the signal with a lower ppm value.
[d]A part of the signal with a lower ppm value merged with a part of the signal with a higher ppm value;
[e]For a part of the signal with a higher ppm value (after adding the peptide, the signal split);
[f]For a part of the signal with a lower ppm value (after adding the peptide, the signal split).

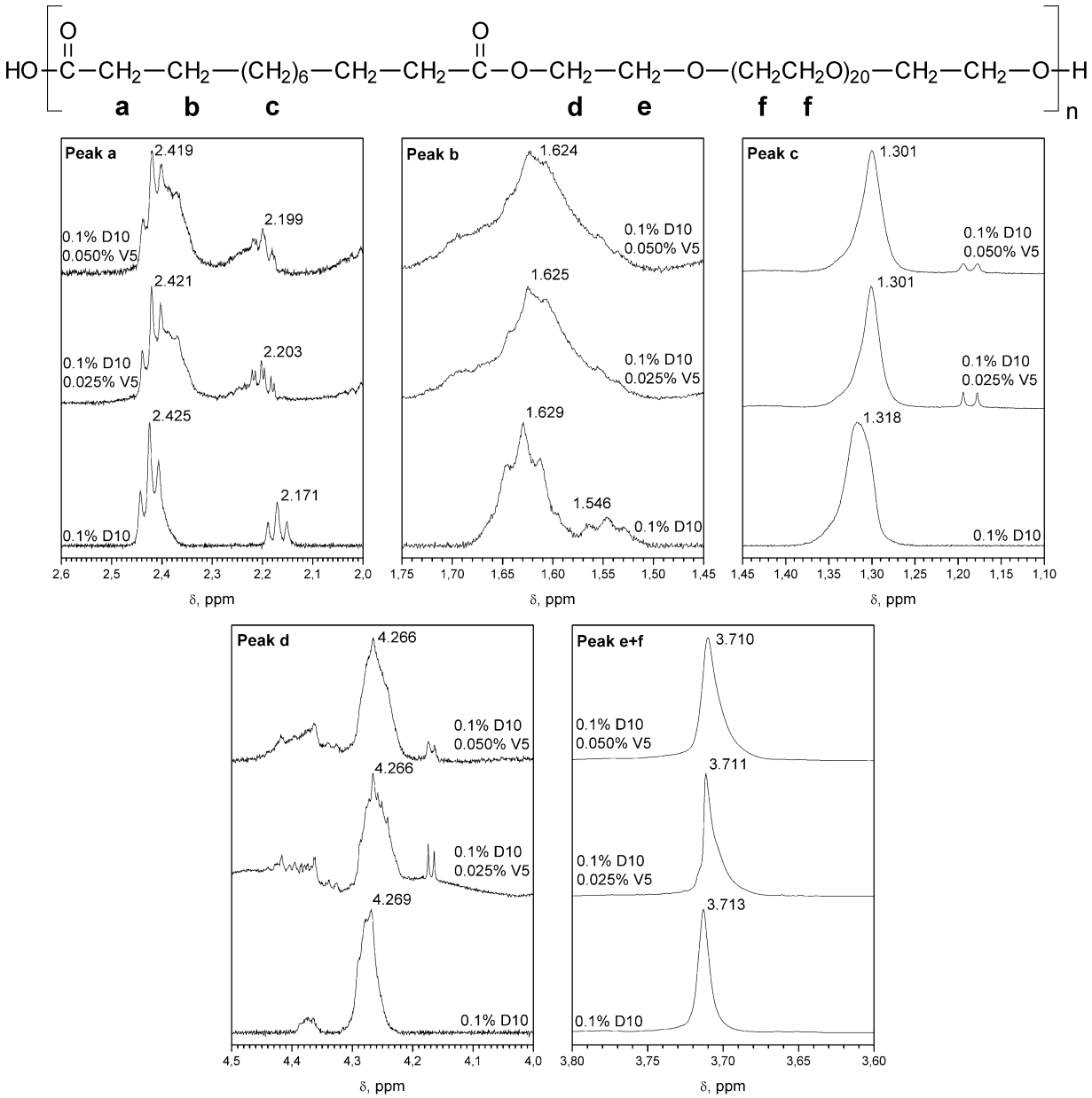

Figure 3.7. ^{1}H NMR spectra of the D10 solution (0.1%) in D_2O, and after adding of 0.025% and 0.05% of V5.

When 0.025% and 0.050% of V5 was added to the 0.1% solution of D10, the ^{1}H NMR spectrum of D10 changed considerably (**Fig. 3.7**). Adding the peptide leads to a broadening of the signals attributed to the PEG protons **d**–**f** indicating that the mobility of the PEG fragments becomes limited, obviously, owing to their interaction with peptide molecules. A plausible

explanation is hydrogen bonding which occurs between oxygen atoms in the PEG fragments and polar peptide's groups (*e.g.*, NH_2, OH, COOH). The outer part of the resulting mixed assemblies is more densely packed, causing signal broadening. Hence, it can be concluded that hydrophilic fragments of V5 are localized within the PEG exterior of the micellar assemblies. A slight shift of the signals **d**–**f** toward lower ppm values implies that the polarity within the micellar exterior is lower after interaction with V5, as compared with those of the initial micelles, evidently, due to the substitution of extremely polar water molecules with the less polar hydrophilic fragments of V5.

After adding V5 to the 0.1% solution of polyester D10 in D_2O, a peak of protons **c** of dodecanedioic acid moieties narrows slightly (half-height width decreases from 14.0 Hz to 9.0 Hz at 0.025% of V5 and 10.5 Hz at 0.05% of V5) and moves upfield. This can be explained by the fact that nonpolar fragments of the V5 are included into the hydrophobic interior of the micellar assemblies. The hydrophobic interior formed is of lower polarity and the mobility of the dodecanedioic acid moieties within this larger interior is slightly enhanced, which leads to certain narrowing of the dodecanedioic acid proton signal and its upfield shift in the spectrum. Such a behavior of protons **c** is similar to those observed for AIP solutions in D_2O (**Fig. 3.3**, **3.4**, protons **c**), when increasing polymer concentration led to the formation of a larger hydrophobic domain and inessential enhancement in the mobility of the hydrophobic $–(CH_2)_n–$ groups.

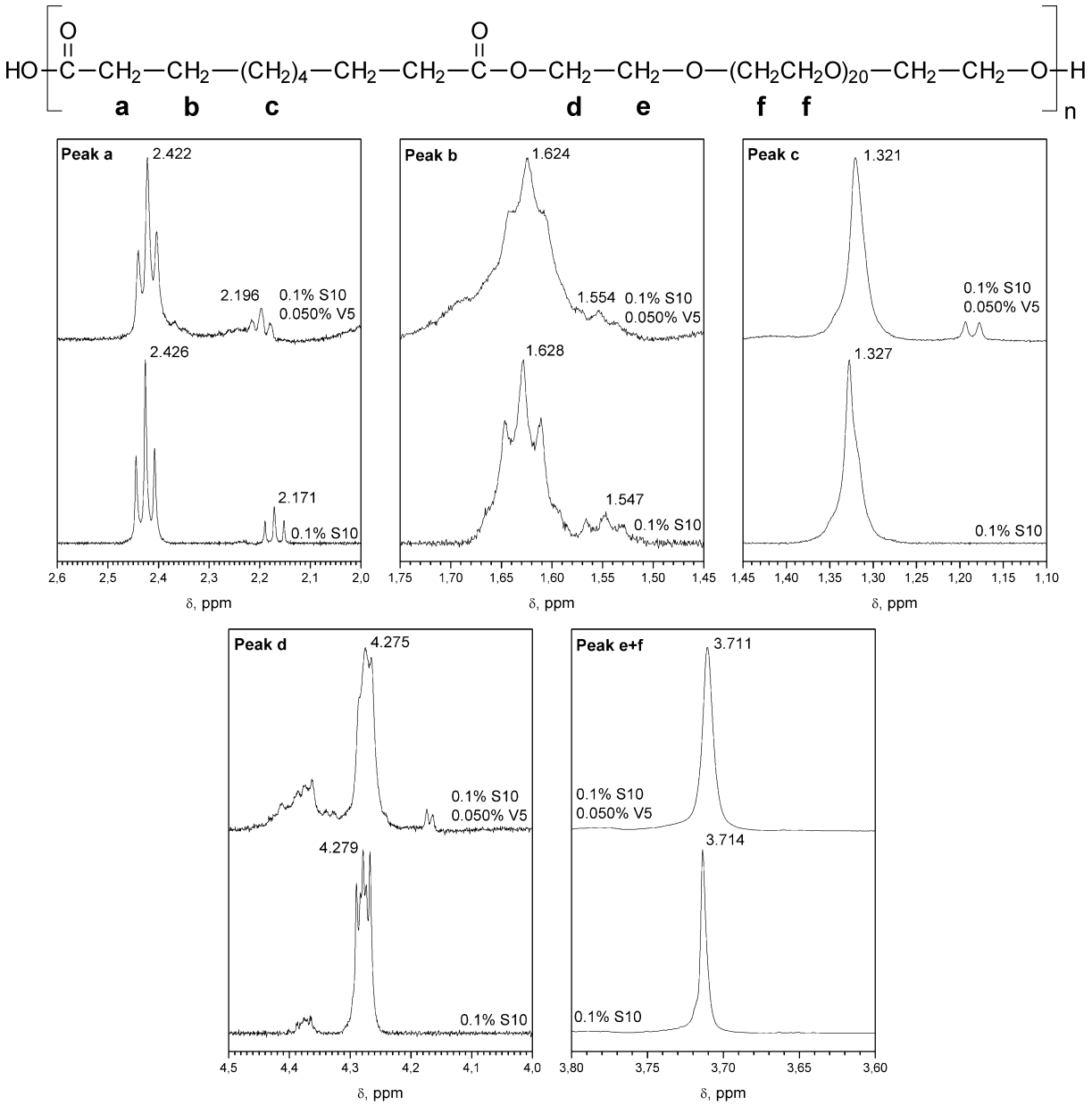

Figure 3.8. ^{1}H NMR spectra of the S10 solution (0.1%) in D_2O, and with 0.05% of V5.

As discussed above, each methylene group in the α and β positions to the carbonyl groups in the dicarboxylic acid moieties (**Fig. 3.4**, protons **a** and **b**, respectively) shows two different signals in D_2O. After adding V5, these signals tend to approach each other to form a single peak (particularly, protons **b**) indicating changes in the microenvironmental polarity of the area where the protons **a** and **b** are localized. The spectra show disappearance of the hyperfine structure of the

peaks of protons **a** and **b**, accompanied by a broadening of the signals. This indicates that the mobility of hydrophobic methylene group in the α and β positions to the carbonyl groups becomes limited owing to the formation of mixed AIP–peptide micellar assemblies.

Similar changes in the ^{1}H NMR spectra were recorded for the mixed micellar assemblies built up after adding V5 in a 0.1% aqueous solution of S10 (**Fig. 3.8**). When 0.05% of V5 was added to the 0.1% solution of the polyester S10, the signals of the PEG protons **d**–**f** broadened (*e.g.*, the half-height width of the peak **e+f** increased from 1.6 Hz to 3.1 Hz), implying that mobility of the PEG fragments became limited owing to their interaction with V5 molecules (**Fig. 3.8**). Owing to the localization of the V5 polar fragments within the PEG exterior, the outer part of the formed mixed assemblies is more densely packed, causing the PEG signal broadening. A slight upfield shift of the signals **d**–**f** indicates that after the interaction with the peptide V5, the polarity within the micellar exterior is lower in comparison with those of the initial micelles.

After adding V5 to the S10 solution, a peak of protons **c** of the sebacic acid groups moves toward lower ppm values (**Fig. 3.8**) implying that in the resulting mixed assemblies the hydrophobic interior is of lower polarity, owing to the inclusion of the nonpolar fragments of the peptide V5. The formation of mixed AIP–peptide micellar assemblies leads to the limited mobility of hydrophobic methylene groups in the α and β positions to the carbonyl groups, as evidenced by the disappearance of the hyperfine structure of peaks **a** and **b**, respectively, in the spectra (**Fig. 3.8**).

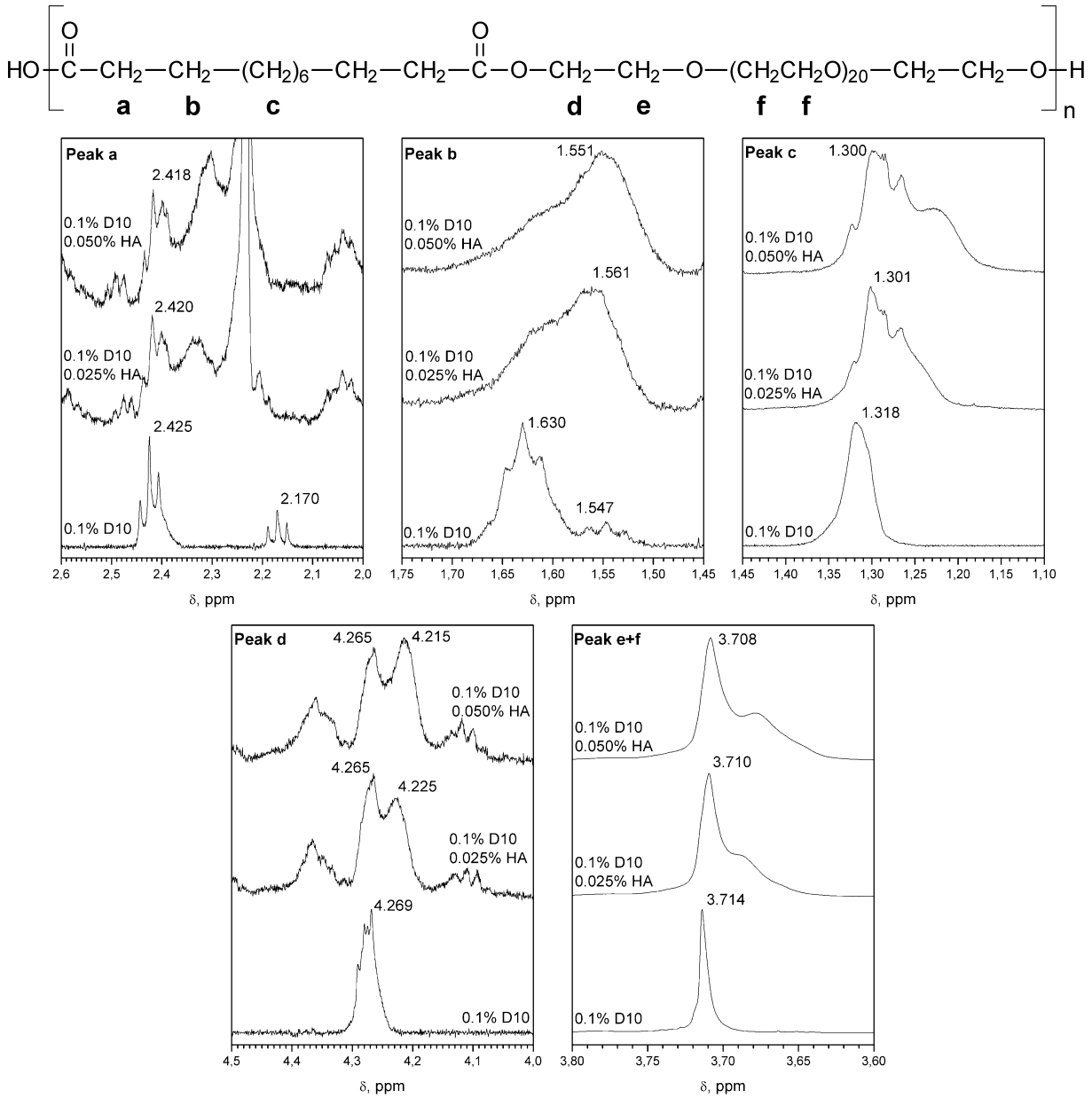

Figure 3.9. ^{1}H NMR spectra of the D10 solution (0.1%) in D_2O, with 0.025% and 0.05% of HA.

To further assess the feasibility of the AIP micellar as peptide nanocontainers, the interactions between D10 and the peptide HA were studied. As compared to V5, the HA chain is shorter, whereas the ratio between non-polar and polar amino acids is similar to V5 (50% of hydrophobic amino acids) (**Fig. 3.1**). When 0.025% and 0.05% of HA was added to the 0.1%

solution of D10, more drastic changes in the ^{1}H NMR spectrum of D10 (**Fig. 3.9**) were observed, than after adding V5 at the same concentration (**Fig. 3.7**).

The spectrum shows disappearance of the hyperfine structure of peak **b** (*i.e.*, the protons of CH_2 groups in the β position to the carbonyl groups in the sebacic acid moieties) accompanied by a broadening and an upfield shift of the signal. As described above, protons **b** show two different signals in D_2O. Similarly to V5, after adding HA, these signals tend to approach each other to form a single peak but, unlike the case of V5, this single peak appears at lower ppm values (1.55 ppm *vs.* 1.62 ppm). This indicates that most of protons **b** is transferred to the hydrophobic interior of the mixed micellar assemblies formed from D10 and HA (not observed in the experiment with V5). This could be attributed to the pushing out of the methylene groups into the interior of mixed assemblies caused by the localization of the HA polar fragments in the micellar exterior. Moreover, an upfield shift and very pronounced broadening of signal **c** (**Fig. 3.9**) indicate that the microenvironmental polarity of the micellar interior becomes lower and hydrophobic fragments are more densely packed after interaction with HA.

Changes observed by interactions between mixed micellar assemblies and two different peptides can be explained by the peptide chemical structure. Unlike in V5, each HA chain contains three polar tyrosine units with phenolic groups (**Fig. 3.10**). It is well known that PEG chains of nonionic surfactants serve as loci of solubilization for sparingly soluble phenolic compounds [48,49]. Our suggestion is that owing to the interaction with the tyrosine moieties (HA polar groups), the PEG fragments of D10 cannot move freely, causing an upfield shift and significant broadening of the signal **e+f** (**Fig. 3.9**) in the spectra, and supporting the fact that the HA polar fragments are localized in the micellar exterior.

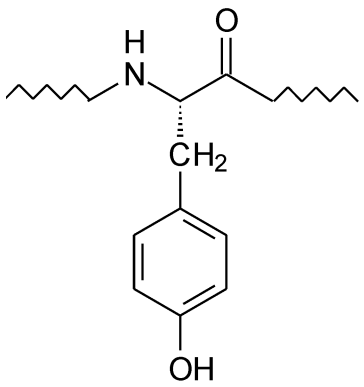

Figure 3.10. Chemical structure of a tyrosine unit in the peptide HA (each HA chain contains three tyrosine units).

The observed effects are even more pronounced in the case of micellar assemblies formed in more concentrated AIP solutions. **Figure 3.11** shows the local expanded spectra of each peak region for D10 in deuterated water at 0.5% before and after adding V5.

Strong upfield shifts of the hydrophobic protons **a**–**c**, disappearance of the hyperfine structure of protons **a** and **b** along with the broadening of the signals **a**–**c** (particularly, at 0.125% of V5) imply the formation of mixed micellar assemblies with a large hydrophobic interior composed of both the polymer and peptide hydrophobic moieties.

Increasing the peptide concentration from 0.025% to 0.125% leads to a significant part of protons **a** and a majority of protons **b** being transferred to the hydrophobic interior, as indicated by a decrease in intensity of the peaks at ~2.42 ppm and 1.63 ppm with the simultaneous increase in the integral intensity of the peak at ~2.26 ppm and 1.56 ppm (**Fig. 3.11**). Adding V5 to the 0.5% solution of D10 results in a broadening of the PEG proton signals **d**–**f** (**Fig. 3.11**), which is much more evident than in the case of the 0.1% solution of D10. This indicates that the mobility of the PEG fragments became more limited owing to their interaction with the V5 hydrophilic fragments and the formation of mixed polymer–peptide micellar assemblies.

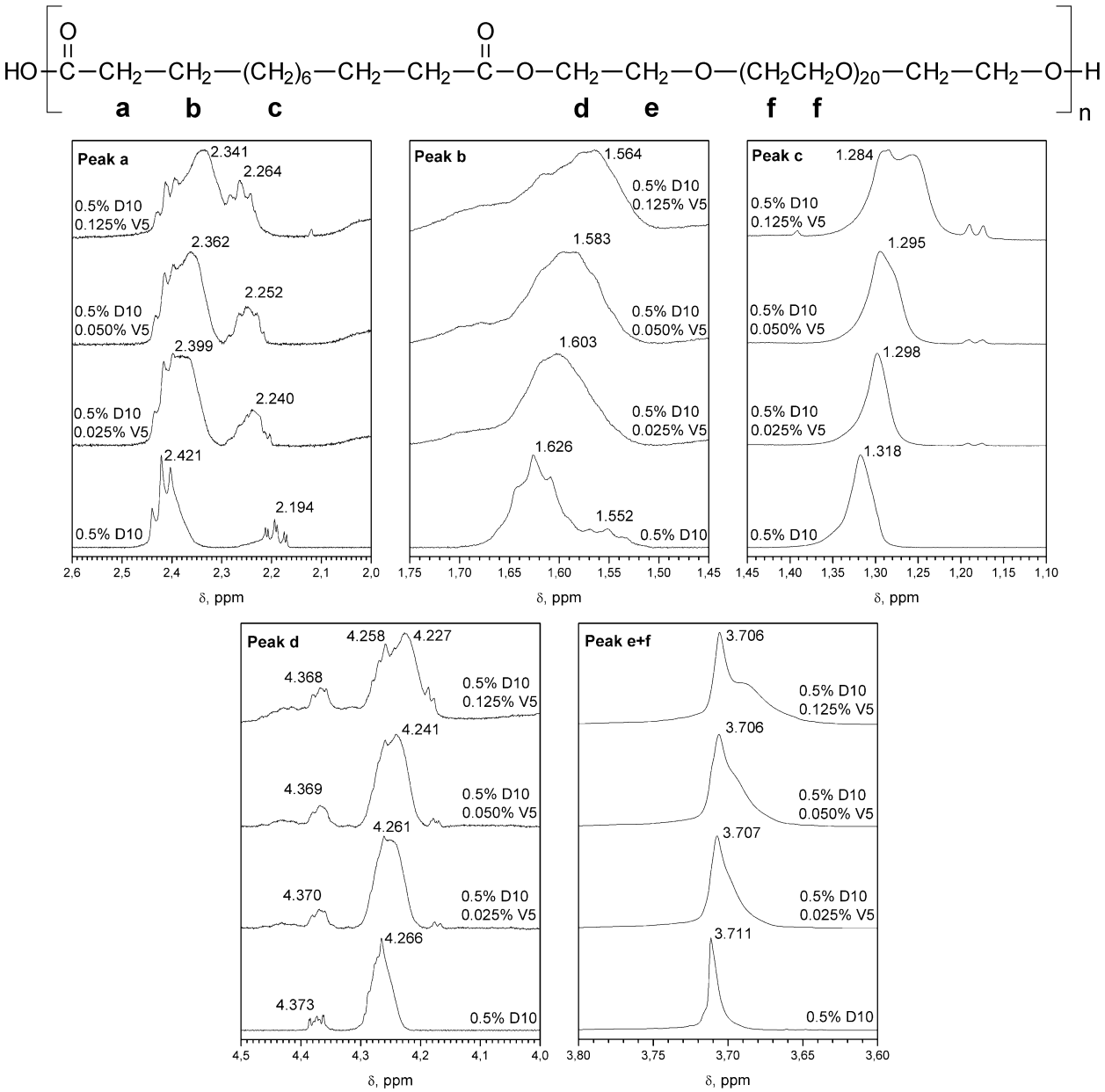

Figure 3.11. ^{1}H NMR spectra of the D10 solution (0.5%) in D_2O, and after adding 0.025% and 0.05%, and 0.125% of V5.

Figure 3.12 shows the local expanded ^{1}H NMR spectra of each peak region for $PEG_{600}PTHF_{650}$ at 0.1% without a peptide and with 0.025% and 0.05% of the added V5. The changes in appearance and chemical shift of the signals of hydrophilic PEG protons **a** and **c** suggest

that the hydrophilic moieties of V5 are localized within the PEG exterior of the $PEG_{600}PTHF_{650}$ micellar structures, similarly to those described for D10 and S10.

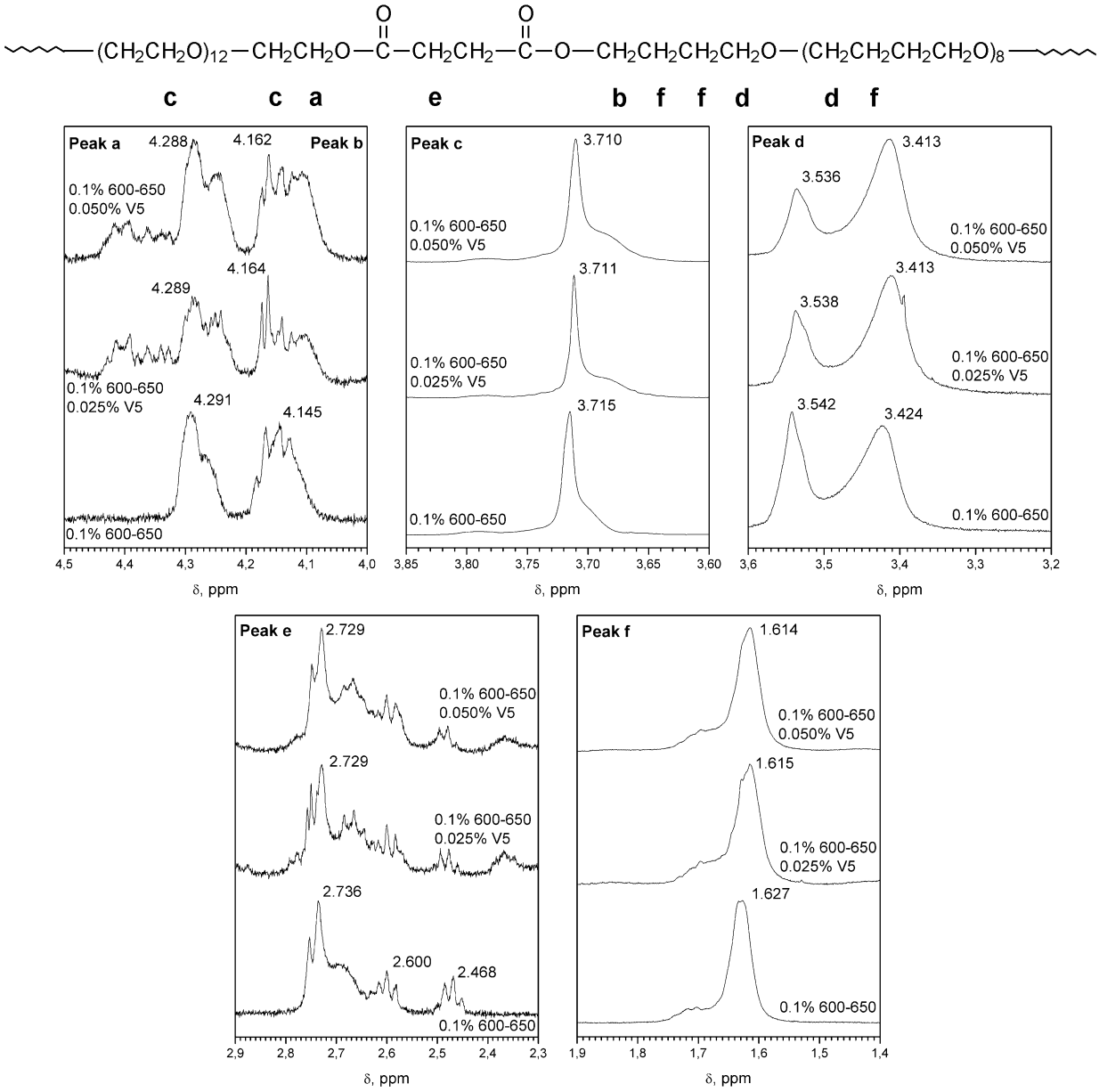

Figure 3.12. ^1H NMR spectra of the $PEG_{600}PTHF_{650}$ solution (0.1%) in D_2O, and after adding 0.025% and 0.050% of V5.

Upfield shifts of the hydrophobic protons **b**, **d**, and **f** accompanied by a broadening of the signals indicate the formation of mixed $PEG_{600}PTHF_{650}$–V5 micellar assemblies with a large hydrophobic interior composed of both the PTHF moieties of the polymer and the peptide nonpolar

fragments. Adding the peptide V5 results in the transfer of the PTHF protons **d** to the hydrophobic domains of the mixed assemblies, as can be concluded from the reduction of integral intensity of the peak at ~3.5 ppm with the simultaneous increase in intensity of the peak at ~3.4 ppm (**Fig. 3.12**).

Hydrodynamic diameters measured by dynamic light scattering were compared for the self-assembled micellar nanostructures from AIPs and mixed micellar assemblies from AIP and the peptide V5. The micellar assemblies were prepared using 0.5% and 1.0% polymer solutions. **Table 3.3** shows that the diameters of micellar assemblies vary between 4.1 ± 0.9 and 11.1 ± 3.8 nm for the studied polymers.

After adding V5, the mean diameter increases in comparison to micellar nanostructures from the polymers, which confirms the incorporation of peptide molecules into the self-assembled micellar nanostructures from AIPs and formation of the mixed polymer–peptide micellar assemblies. Small size and narrow unimodal size distribution (**Fig. 3.13**) indicate that the self-assembled micellar nanostructures from AIPs possess good physical properties for being considered as nanocarriers for peptides.

Table 3.3. Mean diameter of the AIPs micellar assemblies and mixed micellar assemblies from AIP and the peptide V5

AIP	Concentration of AIP, %	Concentration of peptide V5, %	Mean diameter, nm
PEG_{600}-$PTHF_{650}$	1.0	--	11.1 ± 3.8
	1.0	0.1	16.9 ± 4.9
S10	1.0	--	4.1 ± 0.9
	1.0	0.1	4.8 ± 1.5
D10	1.0	--	5.8 ± 1.9
	1.0	0.1	7.0 ±1.8
	0.5	--	5.8 ± 1.2
	0.5	0.025	6.4 ± 1.5
	0.5	0.05	6.4 ± 1.4
	0.5	0.125	6.8 ± 1.8

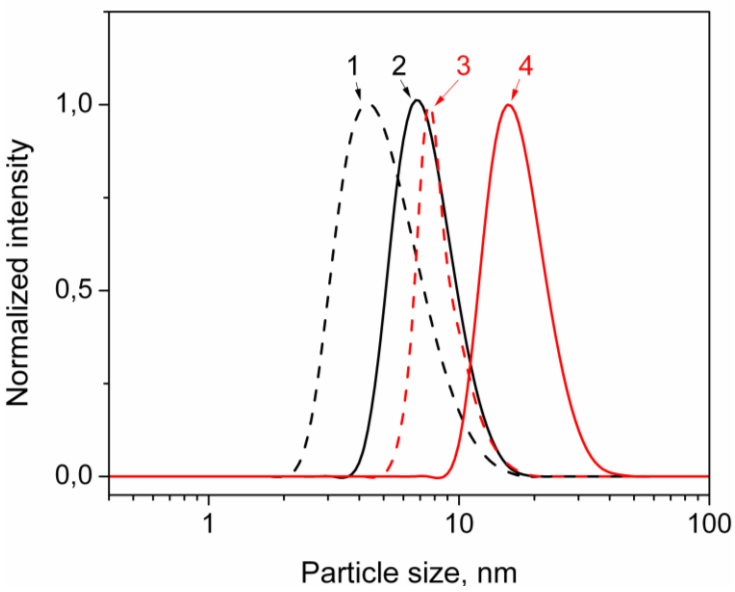

Figure 3.13. Size of self-assembled micellar nanostructures from AIPs (polymer concentration 1%) and mixed micellar assemblies from AIP and V5 peptide (polymer concentration 1% and peptide concentration 0.1%) as determined by dynamic light scattering: (1) D10, (2) D10−V5, (3) $PEG_{600}PTHF_{650}$, and (4) $PEG_{600}PTHF_{650}$−V5.

Thus, "host-guest" interactions between self-assembled micellar nanostructures from AIPs and two peptides (HA and V5) result in formation of mixed micellar assemblies. The interior of the assemblies consists predominantly of the hydrophobic moieties of both the polymer and the peptide, whereas the exterior is comprised of the hydrophilic fragments of the polymer and the peptide (**Fig. 3.14**).

3.5. Conclusions

A detailed ^{1}H NMR spectroscopic study along with DLS measurements revealed "host–guest" interactions between self-assembled micellar nanostructures from amphiphilic invertible polymers (AIPs) and two different peptides, swine-origin Influenza A surface protein Hemagglutinin (HA) and research antibody peptide V5. Mixed micellar assemblies with incorporated peptide molecules were formed in an aqueous solution at different polymer concentrations and the polymer/peptide ratio.

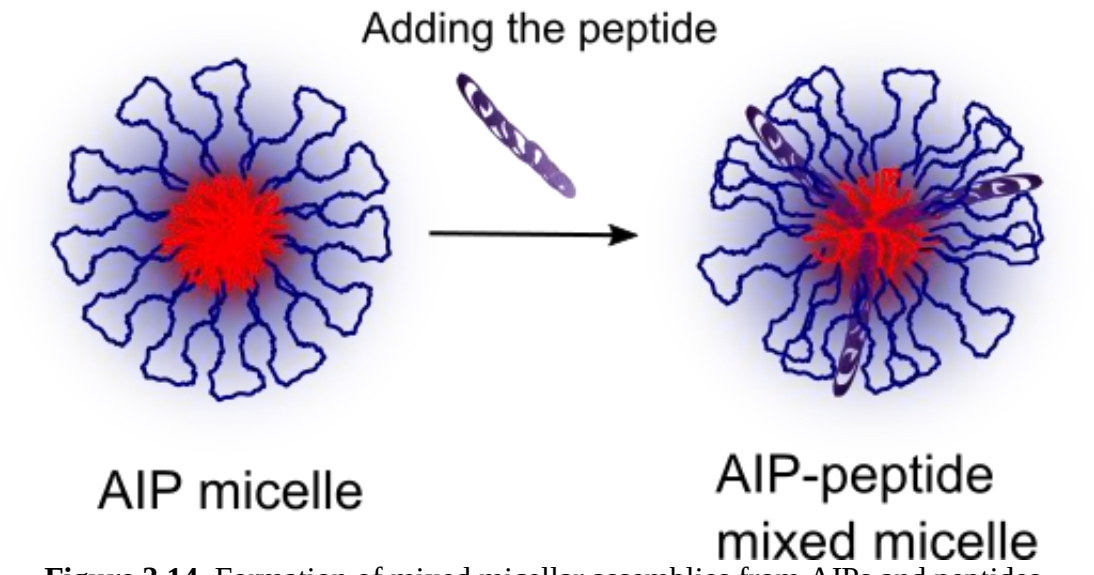

Figure 3.14. Formation of mixed micellar assemblies from AIPs and peptides.

The inner part of the assemblies consists predominantly of the hydrophobic moieties of both the polymer and the peptide, whereas the hydrophilic fragments of the polymer and peptide comprise the exterior of the mixed micellar nanostructures. The peptide loci in the assemblies appear to depend on the peptide chemical structure (particularly, specific interactions between amino acids and polymer fragments). Assuming the previously demonstrated AIPs ability to transform macromolecular conformation in response to changing polarity of environment [34-40], the mixed micellar assemblies from AIPs and peptides can be considered as promising candidates for developing new polymer-based micellar adjuvants.

3.6. References

(1) V.S. Trubetskoy, V.P. Torchilin, Use of polyoxyethylene-lipid conjugates as long-circulating carriers for delivery of therapeutic and diagnostic agents, *Adv. Drug Deliv. Rev.* **1995.** *16,* 311–320.

(2) G.S. Kwon, K. Kataoka, Block-copolymer micelles as long-circulating drug vehicles, *Adv. Drug Deliv. Rev*. **1995.** *16,* 295–309.

(3) G.S. Kwon, T. Okano, Soluble self-assembled block copolymers for drug delivery, *Pharm. Res*. **1999.** *16,* 597–600.

(4) A. Martin, Physical Pharmacy, fourth ed., Williams and Wilkins, Baltimore, 1993.

(5) Z. Gao, A. Eisenberg, A model of micellization for block copolymers in solutions. *Macromolecules.* **1993.** *26*, 7353–7360.

(6) E.V. Batrakova, A.V. Kabanov, Pluronic block copolymers: Evolution of drug delivery concept from inert nanocarriers to biological response modifiers. *J. Control. Release.* **2008.** *130*, 98–106.

(7) S.Y. Lin, Y. Kawashima, The influence of three poly(oxyethylene) poly(oxypropylene) surface-active block copolymers on the solubility behavior of indomethacin, *Pharm. Acta Helv*. **1985**. *60*, 339–344.

(8) M. Yokoyama, T. Okano, K. Kataoka, Improved synthesis of adriamycin-conjugated poly(ethylene oxide)-poly(aspartic acid) block copolymer and formation of unimodal micellar structure with controlled amount of physically entrapped adriamycin, *J. Control. Release.* **1994.** *32*, 269–277.

(9) M. Yokoyama, A. Satoh, Y. Sakurai, T. Okano, Y. Matsumura, T. Kakizoe, Incorporation of water-insoluble anticancer drug into polymeric micelles and control of their particle size, *J. Control. Release*. **1998.** *55*, 219–229.

(10) E.V. Batrakova, T.Y. Dorodnych, E.Y. Klinski, E.N. Kliushnenkova, O.V. Shemchukova, O.N. Goncharova, Anthracycline antibiotics non-covalently incorporated into the block copolymer micelles: in vivo evaluation of anticancer activity, *Brit. J. Cancer*. **1996**. *74*, 1545–1552.

(11) A.V. Kabanov, S.V. Vinogradov, U.G. Suzdaltseva, V.Yu. Alakhov, Water-soluble block polycations as carriers for oligonucleotide delivery, *Bioconj. Chem.* **1995**. *6,* 639–643.

(12) V.Yu. Alakhov, A.V. Kabanov, Block copolymeric biotransport carriers as versatile vehicles for drug delivery, *Expert Opin. Invest. Drugs.* **1998**. *7*, 1453–1473.

(13) T. Inoue, G. Chen, K. Nakamae, A.S. Hoffman, An AB block copolymers of oligo(methyl methacrylate) and poly(acrylic acid) for micellar delivery of hydrophobic drugs, *J. Control. Release.* **1998.** *51,* 221–229.

(14) J.G. Zeng, K.Y. Shi, Y.Y. Zhang, X.H. Sun, B.L. Zhang, Construction and micellization of a noncovalent double hydrophilic block copolymer, *Chem. Commun.* **2008**. 3753–3755.

(15) C.W. Zhao, X.L. Zhuang, C.L. He, X.S. Chen, X.B. Jing, Synthesis of novel thermo- and pH-responsive poly(L-lysine)-based copolymer and its micellization in water, *Macromol. Rapid Commun.* **2008**. *29,* 1810–1816.

(16) J.A. Mackay, A. Chilkoti, Temperature sensitive peptides: Engineering hyperthermia-directed therapeutics, *Int. J. Hyperth.* **2008.** *24,* 483–495.

(17) A. Napoli, M.J. Boerakker, N. Tirelli, R.J.M. Nolte, N.A.J.M. Sommerdijk, J.A. Hubbell, Glucose-oxidase based self-destructing polymeric vesicles, *Langmuir.* **2004.** *20,* 3487–3491.

(18) Y.H. Liu, X.H. Cao, M.B. Luo, Z.G. Le, W.Y. Xu, Self-assembled micellar nanoparticles of a novel star copolymer for thermo and pH dual-responsive drug release, *J. Colloid Interface Sci.* **2009.** *329,* 244–252.

(19) P. De, S.R. Gondi, B.S. Sumerlin, Folate-conjugated thermoresponsive block copolymers: Highly efficient conjugation and solution self-assembly, *Biomacromolecules* **2008.** *9,* 1064–1070.

(20) G.J. Chen, S. Amajjahe, M.H. Stenzel, Synthesis of thiol-linked neoglycopolymers and thermo-responsive glycomicelles as potential drug carrier, *Chem. Commun*. **2009,** 1198–1200.

(21) L. Deng, K. Shi, Y.Y. Zhang, H.M. Wang, J.G. Zeng, X.Z. Guo, Z.J. Du, B.L. Zhang, Synthesis of well-defined poly(N-isopropylacrylamide)-b-poly(L-glutamic acid) by a versatile approach and micellization, *J. Colloid Interface Sci.* **2008.** *323,* 169–175.

(22) S.M. Moghimi, A.C. Hunter, Poloxamers and poloxamines in nanoparticle engineering and experimental medicine, *Trends Biotechnol.* **2000.** *18,* 412–420.

(23) M.J. Newman, C.W. Todd, M. Balusubramanian, Design and development of adjuvant-active nonionic block copolymers, *J. Pharm. Sci.* **1998.** *87,* 1357–1362.

(24) K. Takayama, M. Olsen, P. Datta, R.L. Hunter, Adjuvant activity of non-ionic block copolymers. V. Modulation of antibody isotype by lipopolysaccharides, lipid A and precursors, *Vaccine.* **1991.** *9,* 257–265.

(25) J.R. Greenland, N.L. Letvin, Chemical adjuvants for plasmid DNA vaccines, *Vaccine.* **2007.** *25,* 3731–3741.

(26) N. Spitzer, A. Jardim, D. Lippert, R.W. Olafson, Long-term protection of mice against Leishmania major with a synthetic peptide vaccine, *Vaccine.* **1999.***17,* 1298–1300.

(27) A. Agarwal, R. Unter, S.K. Mallapragada, Novel cationic pentablock copolymers as non-viral vectors for gene therapy, *J. Control. Release.* **2005.** *103,* 245–258.

(28) J.R. Adams, S.K. Mallapragada, Effective polymer adjuvants for sustained delivery of protein subunit vaccines, *Technology.* **2014.** *2*, 1–12.

(29) A.K. Shakya, K.S. Nandakumar, Applications of polymeric adjuvants in studying autoimmune responses and vaccination against infectious diseases, *J. R. Soc. Interface.* **2013.** *10*, 20120536.

(30) J.C. Cox, A.R. Colter, Adjuvants–a classification and review of their modes of action, *Vaccine.* **1997.** *15*, 248–256.

(31) N. Rydell, I. Sjöholm, Oral vaccination against diphtheria using polyacryl starch microparticles as adjuvant, *Vaccine.* **2004.** *22*, 1265–1274.

(32) F. Danhier, E. Ansorena, J.M. Silva, R. Coco, A. Le Bretona, V. Préat, PLGA-based nanoparticles: an overview of biomedical applications, *J. Control. Release.* **2012.** *161*, 505–522.

(33) J. Kreuter, E. Liehl, U. Berg, M. Soliva, P.P. Speiser, Influence of hydrophobicity on the adjuvant effect of particulate polymeric adjuvants, *Vaccine.* **1988.** *6*, 253–256.

(34) A. Voronov, A. Kohut, S. Vasylyev, W. Peukert, Mechanism of silver ion reduction in concentrated solutions amphiphilic invertible polyesters in nonpolar solvent at room temperature, *Langmuir.* **2008.** *24*, 12587–12594.

(35) I. Hevus, A. Kohut, A. Voronov, Interfacial micellar phase transfer using amphiphilic invertible polymers, *Polym. Chem.* **2011.** *2*, 2767–2770.

(36) L. Martinez Tomalino, A. Voronov, A. Kohut, W. Peukert, Study of amphiphilic polyester micelles by hyper-Rayleigh scattering: invertibility and phase transfer, *J. Phys. Chem. B.* **2008.** *112*, 6338–6343.

(37) A. Kohut, A. Voronov, Hierarchical micellar structures from amphiphilic invertible polyesters: ^{1}H NMR spectroscopic study, *Langmuir.* **2009.** *25,* 4356–4360.

(38) O. Kudina, A. Kohut, I. Tarnavchyk, I. Hevus, A. Voronov, Solvent-responsive self-assembly of amphiphilic invertible polymers determined with SANS, *Langmuir.* **2014.** *30,* 3310–3318.

(39) A. Kohut, X. Dai, D. Pinnick, D. Schulz, A. Voronov, "Host–guest" interaction between cyclohexasilane and amphiphilic invertible macromolecules, *Soft Matter.* **2011.** *7,* 3717–3720.

(40) I. Hevus, A. Modgil, J. Daniels, A. Kohut, C. Sun, S. Stafslien, A. Voronov, Invertible micellar polymer assemblies for delivery of poorly water-soluble drugs, *Biomacromolecules.* **2012.** *13,* 2537–2545.

(41) X. Zhang, J.K. Jackson, H.M. Burt, Development of amphiphilic diblock copolymers as micellar carriers of taxol, *Int. J. Pharm.* **1996.** *132,* 195–206.

(42) B.J. Kim, S.S. Im, S.G. Oh, Investigation on the solubilization locus of aniline-HCl salt in SDS micelles with ^{1}H NMR spectroscopy, *Langmuir.* **2001.** *17,* 565–566.

(43) J.H. Ma, C. Guo, Y.L. Tang, H.Z. Liu, ^{1}H NMR spectroscopic investigations on the micellization and gelation of PEO-PPO-PEO block copolymers in aqueous solutions, *Langmuir.* **2007.** *23,* 9596–9605.

(44) I. Furó, NMR spectroscopy of micelles and related systems, *J. Mol. Liq.* **2005.** *117,* 117–137.

(45) W. Guo, B.M. Fung, S.D. Christian, NMR study of cyclodextrin inclusion of fluorocarbon surfactants in solution, *Langmuir.* **1992.** *8,* 446–451.

(46) J.T. Davies, E.K. Rideal, Interfacial Phenomena, Academic Press, New York, **1961**.

(47) S. Bhattacharya, A. Sharma, S.K. Nayak, S. Chattopadhyay, A.K. Mukherjee, NMR study of complexation of crown ethers with [60]- and [70] fullerenes, *J. Phys. Chem. B,* **2003.** *107,* 4213–4217.

(48) V.P. Torchilin, Structure and design of polymeric surfactant-based drug delivery systems, *J. Control. Release,* **2001.** *73,* 137–172.

(49) A. Parmar, K. Singh, A. Bahadur, G. Marangoni, P. Bahadur, Interaction and solubilization of some phenolic antioxidants in Pluronic® micelles, *Colloids Surfaces B: Biointerfaces,* **2011.** *86,* 319–326.

CHAPTER 4. INVERSION OF POLYMERIC MICELLES PROBED BY SPIN LABELED PEPTIDE INCORPORATION AND ELECTRON PARAMAGNETIC RESONANCE[*]

4.1. Abstract

As concentration of amphiphilic invertible polymers (AIPs) in both polar and nonpolar solvents increases, the AIP macromolecules self-assemble into polymeric micelles. The resulting invertible micellar assemblies (IMAs) have a controlled size and morphology determined by macromolecular composition and hydrophilic lipophilic balance (HLB) of the AIPs. It has been demonstrated that AIPs can rapidly switch the conformation in response to changes in the environmental polarity, thus facilitating, micellar inversion. In combination with IMAs ability to solubilize otherwise insoluble substances, inversion can be promising for rapid and controlled cargo delivery and release in applications that require simultaneous utility in polar and nonpolar media. While IMAs have been demonstrated to interact with peptides, fundamental pictures *of micellar inversion* remain elusive and became the focus of this work, including the behavior of the incorporated peptide in IMAs at molecular level at different polarities of the environment and how polymer composition impacts such behavior. To trigger conformational changes of micellar assemblies, “poor” solvent acetone (no self-assembly occurs in acetone) was added into the

[*] The material in this chapter was co-authored by Oksana Zholobko, Yanxiong Pan, Zhongyu Yang, and Andriy Voronov. Oksana Zholobko had the primary responsibilities of synthesizing and characterizing polymers and preparing micellar assemblies for Electron Paramagnetic Resonance analysis. Yanxiong Pan helped Oksana Zholobko perform and analyze results of EPR spectroscopy. Oksana Zholobko was involved in drafting and revising all versions of this chapter. Zhongyu Yang and Andriy Voronov helped explain and describe the results obtained by Oksana Zholobko and Yanxiong Pan. Published article can be found at https://doi.org/10.1021/acs.jpcc.8b09206.

peptide-loaded IMAs aqueous solutions. Electron Paramagnetic Resonance (EPR) in combination with peptide spin labeling was used to probe the local environment of an antigenic peptide at various acetone concentrations. The obtained results are consistent with the previously revealed micellar structure. Increasing acetone percentage clearly impacts the extent of IMA conformational changes (micellar inversion) as reported by the labeled peptide and quantified by semi-quantitative spectral analysis. The conformational changes are different for the two AIPs differing in the macromolecular composition. Conformational changes clearly relate to HLB of the AIPs macromolecules and can certainly be meaningful in controlling the IMAs-mediated peptide release.

4.2. Introduction

The preparation of micellar assemblies from amphiphilic invertible polymers (AIPs) (synthesized from hydrophobic and hydrophilic fragments alternately distributed along the polymer backbone) is an approach that exploits manipulation of polymer micelles and smart assembly formation by a simple tuning of the polymer concentration and solvent polarity. [1-3]

Synthesized from poly(ethylene glycol) (PEG) (as the hydrophilic constituent) and either aliphatic dicarboxylic acids or polytetrahydrofurane (PTHF) (as the hydrophobic constituent), the AIPs macromolecules self-assemble into polymeric micelles as polymer concentration increases both in polar and nonpolar solvents. [1-4] The resulting invertible micellar assemblies (IMAs) have a controlled size and morphology determined by the macromolecular composition (number and length of hydrophilic and hydrophobic fragments of the AIP macromolecules) and their hydrophilic lipophilic balance (HLB). [4-6] A combined ^{1}H NMR spectroscopy/SANS study demonstrated that AIPs macromolecules can rapidly switch their conformation in response to changes in the environmental polarity thus facilitating the micellar inversion. [1-4] The inversion

of the assemblies can be promising for rapid and controlled self-assembly in applications that require simultaneous utility in polar and nonpolar media, e.g., in drug delivery systems. [7,8]

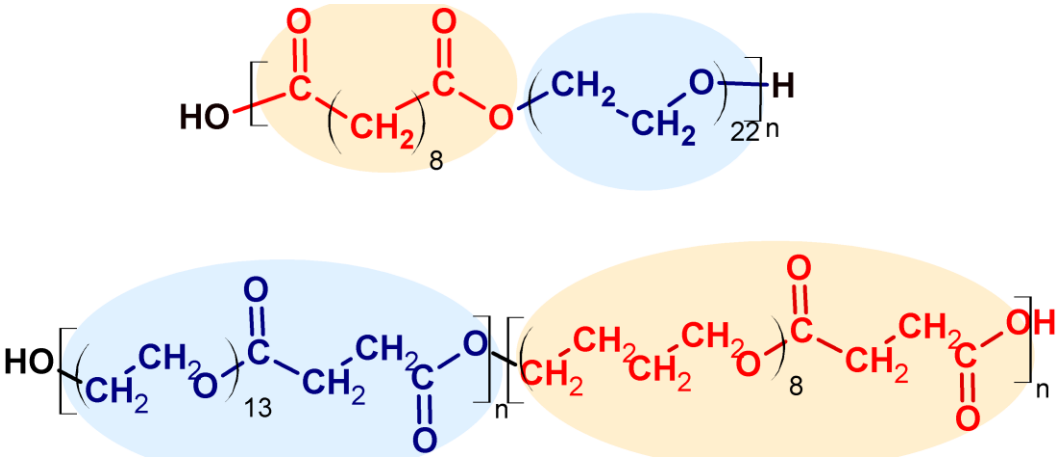

Figure 4.1. Chemical structure of AIPs used in this study (top – S10, bottom – $PEG_{600}PTHF_{650}$). The subscripted numbers in the PEG-PTHF copolymers indicate the average molecular weight of the copolymerized monomers.

The IMAs have been demonstrated to solubilize otherwise insoluble substances, including poorly water-soluble dyes [9-11] and drugs, [12] both in polar and nonpolar solvents. These properties make IMAs effective vehicles for encapsulating and delivering poorly water-soluble cargos in aqueous medium, such as curcumin or peptide molecules, wherein these molecules can be physically incorporated through hydrophobic interactions within the IMAs interior. Our recent study demonstrated effective IMAs-mediated curcumin delivery on osteosarcoma cells at different concentrations of loaded micelles. The presence of micellar curcumin essentially reduced cell survival in three human osteosarcoma cell lines, while the IMAs (with no cargo) at the same concentrations showed no effect on the survival of normal cells. This finding indicates that AIPs-based delivery can be a powerful approach for the targeted delivery of poorly-soluble drugs in bone cancer cells. Furthermore, confocal microscopy studies confirmed that curcumin was readily

taken up into osteosarcoma cells when delivered by the polymer micelles, but not into the normal cells. [7,8,12,13]

Another promising application of IMAs can be to carry peptides as potential drugs, drug targets, or even micellar antigens (when antigenic peptide is incorporated in IMAs) which often need to be delivered between media with different polarities. The "host–guest" interactions between peptides and IMAs resulted in formation of stable polymer–peptide mixed micellar structures in aqueous solution. While peptide loading has been demonstrated successful, a few fundamental questions of micellar inversion remain elusive but attract interest regarding the performance and behavior of the peptide in micelles at the molecular level. For example, upon incorporation what are the microenvironment (crowding, polarity), position, and partition of the peptide in IMA lipophilic and hydrophilic domains? This information is important for understanding the potential impact of the delivery vehicles on the peptide structure and stability, two important factors related to peptide delivery. In addition, upon polarity and IMA packing/conformation change triggered by adding a "poor" solvent (which does not support the formation of micelles) or one with an opposite polarity, how does peptide position or partition change accordingly? This information is critical for understanding the release mechanism of peptides. Lastly, what is the influence of polymer composition and HLB on peptide loading and release? Answering these questions requires detailed structural and dynamic insights into the loaded peptide. However, obtaining the needed information is a challenging task because it requires probing the local environment of the peptide "buried" in micelles.

A potential solution is to use the "penetrating" power of magnetic resonance to probe the peptide of interest buried in micelles. While Nuclear Magnetic Resonance (NMR) spectroscopy has been used to probe the "host-guest" interaction in IMAs, the background signals of micelles

limit the selective determination of peptide dynamics. Electron Paramagnetic Resonance (EPR) in combination with Site-Directed Spin Labeling (SDSL) has been proved to be powerful in determining otherwise inaccessible structural information in complex biological systems. [14-20] SDSL relies on attaching an EPR active spin label to the target biomacromolecules, especially a peptide/protein, at a residue that reacts specifically with the labeling compound. [21-23] Typical information from EPR is the site-specific backbone dynamics of the labeled site, which is dependent on and reports the local environment (crowding, polarity) of macromolecular systems. [14,24-31]

In this work, we choose two polymers, S10 made from PEG (molecular weight 1,000 g/mol) and sebacic acid and $PEG_{600}PTHF_{650}$, synthesized from PEG (molecular weight 600 g/mol) and PTHF (molecular weight 650 g/mol) from currently existing AIPs library (**Fig. 4.1**) and use SDSL-EPR to understand how the incorporated peptide molecules behave in micellar interior under different micellar conformations and if they can be released from the IMAs using micellar inversion mechanism in a controlled way. To trigger conformational changes, an organic solvent (acetone) was added into the peptide-loaded IMAs aqueous solutions. It has been shown that no AIPs micellization occurs in acetone. SDSL-EPR was used to probe the local environment of a model hydrophobic peptide at various acetone concentrations. Increasing in acetone percentage clearly impacts IMAs extent of conformational changes (extent of inversion) as reported by the labeled peptide and quantified by semi-quantitative spectral simulation. Those changes are different for the S10 and $PEG_{600}PTHF_{650}$ differing in the macromolecular composition and HLB (**Table 4.1**). It confirms that micellar inversion relates to HLB of the polymers and can certainly be meaningful in controlling the IMAs-mediated peptide release.

4.3. Experimental

4.3.1. Materials

N-hydroxysuccinimide (NHs, 99%) and 1-Ethyl-3-(3-dimethylaminopropyl) carbodiimide were purchased from the Oakwood Chemicals while the 4-Amino-TEMPO (NH_2-TEMPO) was purchased from Sigma Aldrich. All other reagents were purchased from Fisher Scientific and directly use without any purification.

4.3.2. Polymer syntheses

S10 and $PEG_{600}PTHF_{650}$ were synthesized as described in our previous work. [10,32] Chemical composition of S10 and $PEG_{600}PTHF_{650}$ was confirmed using FTIR- and ^1H NMR spectroscopy (data not shown). Weight and number average molecular weights and the corresponding polydispersity index of the AIP were measured using gel permeation chromatography (GPC).

4.3.3. Peptide spin-labeling

The HA peptide (6 mg, 3.73 µmol), EDC (11.3 mg,73 µmol), N-hydroxysuccinimide (1.70 mg, 14.8 µmol) and NH_2-TEMPO (1.5 mg, 8 µmol) were mixed in 338 µL anhydrous DMF and further diluted to 5 mL using anhydrous THF. The mixture was shaken at ambient temperature for 3 days and the extra THF was removed via vacuum distillation. The residue part was precipitated in the 10 mL ether three time to remove the unreacted reagents, then dispersed in 200 µL DMF and stored in 4 °C for future use. To calibrate the concentration of spin labeled HA, a series of standard NH_2-TEMPO solution in DMF were prepared and corresponding EPR spectra were collected as our standards in the calibration.

4.3.4. Mass spectrometry

For mass spectrometry (MS) analysis, 20 pmol of spin-labeled peptide was injected onto Waters HDX coupled with Synapt G2-Si Q-ToF and equipped with an ESI ion source operating in positive resolution ion model. The following characteristic factors, including capillary voltage, 3.8 kV; source offset, 35; desolvation temperature, 250°C; desolvation gas follow, 300 L/Hr and cone voltage, 3.0 kV150 L, were applied for acquiring the spectra.

4.3.5 Formation of peptide-loaded micellar assemblies

HA-loaded IMAs were prepared using the thin film technique. [34] According to this technique, appropriate amounts of polymers and peptide were dissolved in 1 mL of DMF. The solvent was removed by rotary evaporation at 60°C for 1 h to obtain a solid AIP/HA matrix. Residual solvent remaining in the AIP/HA matrix was evaporated overnight under vacuum. The resultant thin film was hydrated with appropriate amount of Millipore water. The solutions were left for at least 16 h to equilibrate at room temperature. The appropriate amount of acetone was added to the solutions prior to the measurements.

4.3.6. EPR data acquisition

Approximately 20 µL of sample was loaded into a borosilicate capillary tube (0.70 mm i.d./1.25 mm o.d.; VitroGlass, Inc.), which was mounted in a Varian E-109 spectrometer fitted with a cavity resonator. All continuous wave (CW) EPR spectra were obtained with an observe power of 12.5 mW. All spectra were obtained with a modulation frequency of 100 kHz and modulation amplitudes of 0.5-1.0 G.

Table 4.1. Characteristics of the AIPs

AIP	M_w, g/mol	x[a]	y[b]	HLB[c]	cmc, mg/L
S10	9,600	22.3	8	15.4	490
$PEG_{600}PTHF_{650}$	9,700	13.2	8.8	13.8	3.5

[a] *x* represents the average number of ethylene oxide units in hydrophilic fragments in the main AIP backbone (**Fig. 4.1**);
[b] *y* represents the number of methylene groups in hydrophobic fragments in the main S10 backbone or the average number of tetramethylene oxide units in hydrophobic fragments in the main $PEG_{600}PTHF_{650}$ backbone (**Fig. 4.1**);
[c] HLB is the hydrophilic-lipophilic balance of the polymers calculated according to Ref. [33]

4.4. Results and discussions

4.4.1. Probing peptide location in IMAs

Antigenic glycoprotein, HA (Hemagglutinin) is a swine-origin Influenza A (H1N1) surface protein. It facilitates viral attachment to the cell that is being infected by swine flu. The HA can also draw immune responses that prevent infection and is a good candidate drug for influenza virus entry inhibition. In our previous work, the HA was chosen as a model cargo to demonstrate IMAs-peptide interactions IMAs ability to incorporate peptide molecules. In this work, we will choose the same model peptide.

We choose the NHS/EDC (EDC, 1-ethyl-3-(3-dimethylaminopropyl) carbodiimide; NHS, N-hydroxysuccinimide) catalyzed, amide formation between –COOH of the peptide and -NH_2 of a TEMPO radical (4-Amino-TEMPO; NH_2-TEMPO; see **Scheme 4.1**) to label the peptide due to the mild reaction condition. There are 3 -COOH groups in the HA peptide. The excess 4-Amino-TEMPO in our labeling reactions was used to ensure that at least one –COOH is labeled. The number of labeled –COOH groups is confirmed with mass spectrometry, which indicates that 2-3 –COOH groups are labeled (**Fig. 4.2**). Unreacted TEMPO and catalysts were removed via dialysis. The labeled HA peptide has a poor solubility in water but is soluble in DMF, THF, or Acetone.

The EPR spectra of the HA peptide in these three solvents all show three sharp lines (**Fig. 4.3A**). The line shape of each spectrum is broader than that of 4-Amino-TEMPO (**Fig. 4.3B**; the broadening is most significant in the high field peak wherein the half-height peak width is 3.7 G for the labeled peptide and 2.9 G for TEMPO alone), which indicates that TEMPO is attached to the peptide. This is because the HA peptide increases the molecular weight of 4-Amino-TEMPO and reduces its rotational tumbling rates, which leads to an increase in linewidth. Simulations of all spectra are shown as dotted curves in Figures. Key parameters resultant from the simulation are consistent with the motion of TEMPO or a TEMPO-labeled peptide in organic solvents.

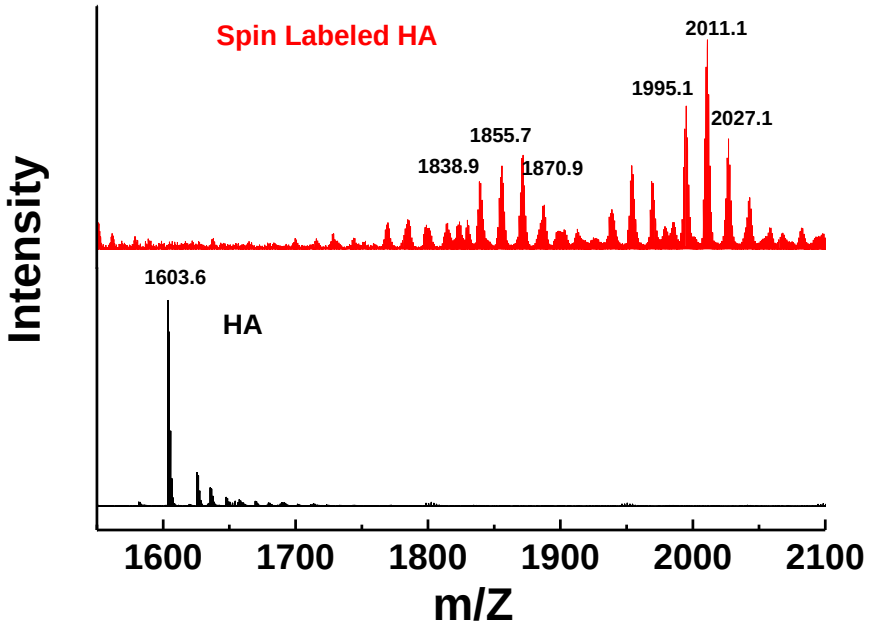

Figure 4.2. Mass spectra of HA peptide (black) and spin labeled HA peptide (red).

The fact that the labeled HA peptide shows three sharp lines regardless of the solvent indicates that the labels within one peptide molecule are separated by at least 10 Å; otherwise dipole-dipole interactions between nearby labels would cause additional line broadening to the CW EPR spectrum. [25] The concentration of the labeled peptide was estimated based on the spin

concentration reported by the double integrated EPR spectral intensity via a calibration method. The stock solution of the spin labeled HA peptide in this work was 8.16 mM.

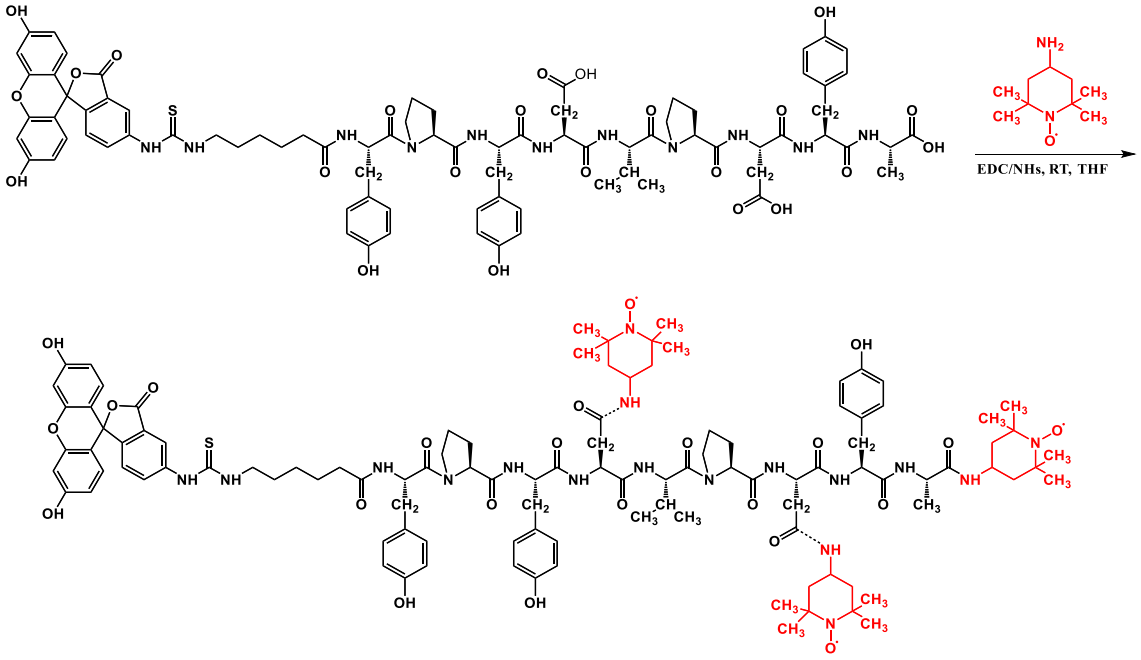

Scheme 4.1. Spin labeling of the HA peptide.

Once trapped in IMAs, the peptide location is related to the label's microenvironment, polarity and the crowding extent, which depends on the "depth" of the labeled peptide with respect to the IMA surface; the closer the peptide to the surface, the less crowding. Ideally multiple sites of the peptide should be labeled and probed for obtaining a thorough picture of peptide location. However, since one end of our model peptide is already labeled with a hydrophobic group, most likely the peptide would anchor its N-terminus to the core and stretch its C-terminus toward the shell/surface of the IMAs (**Fig. 4.4**). Therefore, only the –COOH groups near the C-terminus are labeled in this work and studied via EPR.

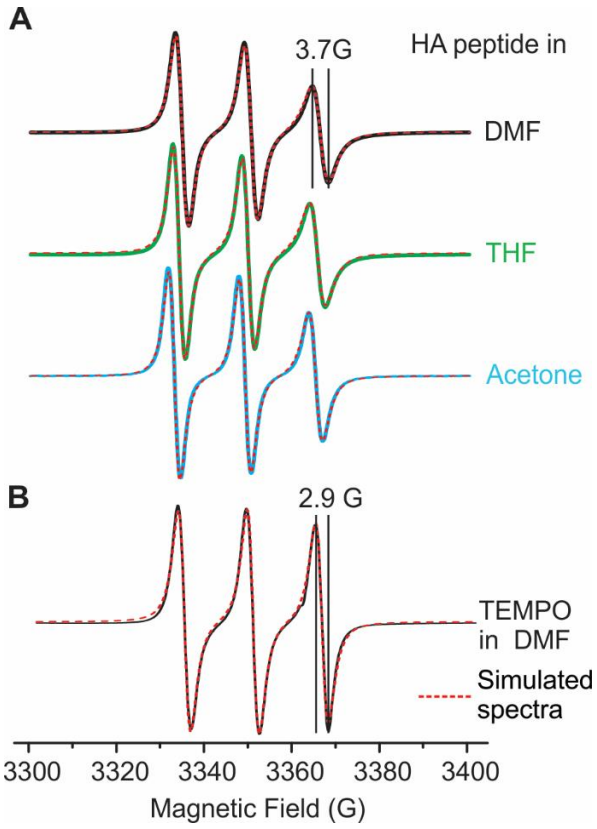

Figure 4.3. (A) CW EPR spectra of spin labeled HA peptide in various organic solvents. (B) CW EPR spectrum of TEMPO in DMF. Dotted red curves are simulated spectra. The half-height peak width of the high-field peak of the labeled peptide and TEMPO are measured.

In principle, the EPR spectrum of a labeled peptide is dependent on three factors, peptide rotational tumbling, backbone dynamics, and the intrinsic motion of the spin label side chain. [14,35,36] For a short peptide like HA in solvents, the rotational tumbling dominates the net effect of the three motions and results in a sharp spectrum due to motional average (**Fig. 4.3A**). Upon spatially trapped in IMAs, the peptide loses the fast rotational tumbling because of the large molecular weight of the IMAs; herein the IMAs still have some rotational motion but the rate is too slow to contribute to the EPR spectrum. The spectrum now becomes dependent on peptide backbone dynamics and spin label intrinsic motions. In micelles, it is possible that the peptide encounters various degrees of crowding which limits both motions depending on the peptide

location in the micelle, either in or near the intensively parked hydrophobic core or near the less-intense hydrophilic edge. Such difference in crowding results in a broad and a narrow spectral spectrum, respectively (also known as the immobile and mobile components, respectively). In case that a peptide exists in both locations, a linear combination of the two spectra will be resolved.

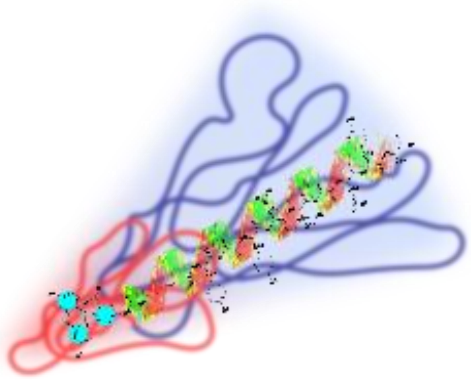

Figure 4.4. Apparent placement of the HA peptide inside the AIP micelle (for better resolution, only a fragment of micelle is schematically depicted) in aqueous environment. We expect that the peptide (green) anchors its N-terminus (cyan) in the hydrophobic core (red) while places the rest to the hydrophilic shell (blue) of the micelle.

This is essentially what we observed from EPR (**Fig. 4.5A, B**). With 1.0 mM peptide entrapped, both S10- and $PEG_{600}PTHF_{650}$ –based IMAs show two spectral components, a broad and a narrow one. A more careful look at these spectra indicates that the degree of broadening (low-field shift; see red triangle) of the S10 spectrum is more significant than that of the $PEG_{600}PTHF_{650}$. This indicates that the restriction in labeled site's motion in S10 is higher than that in $PEG_{600}PTHF_{650}$. A possible rationalization of such difference will be provided in later discussions.

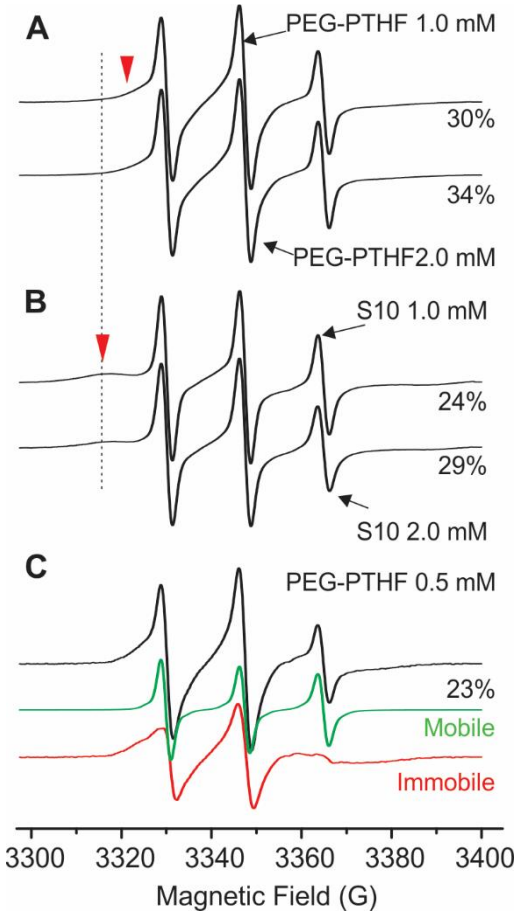

Figure 4.5. EPR spectra of the spin labeled HA peptide in $PEG_{600}PTHF_{650}$ (A) and S10 (B) IMAs with different peptide concentrations. The percentage values listed next to each spectrum indicate the relative population of the mobile component from our spectral analysis. Representative semi-quantitative spectral analysis (C) resolves two spectral components, a mobile (green) and an immobile (red) one.

Increasing concentration of the peptide in these two micelles causes subtle changes in the relative peak intensity of the two components for $PEG_{600}PTHF_{650}$, wherein at high peptide concentrations we observe a slight increase in the peak intensity of the narrow component, indicating more peptide molecules tend to locate toward the edge. Note that, although 2-3 labels can be attached to the peptide, they do not interfere each other's spectrum due to the large separation. The obtained spectrum is the summation of all labeled sites but since they are all near

the C-terminus, all labels report the local microenvironments of the C-terminus of the peptide. To quantify the population of these components, we performed a semi-quantitative spectral analysis.

4.4.2. Semi-quantitative EPR spectral analysis

EPR spectral analysis algorithms have been established by Freed and coworkers based on first-principles for both single-component and multiple-component spectra. [35,37] Typical outcomes of the spectral analysis include the rate of spin label motion, spatial restriction of the motion (order parameters), as well as local polarity and g-tensors. [35] By far the best results are reported from relatively homogeneous systems with 1 or 2 well-defined components; heterogeneous systems are challenged to reach convergent fittings. We attempted a 2-component spectral fitting to data shown in **Figure 4.3** but failed to reach acceptable fittings. This indicates high heterogeneity of our system, which is not a complete surprise because the labeled sites of peptide could be located in heterogeneous microenvironment. We, therefore, performed a semi-quantitative spectral analysis, wherein only the sharp component was simulated based on first-principles using a package developed by Hubbell and coworkers based on the same algorithms introduced above. The relative population of the broad component for each spectrum was then obtained by subtracting the sharp component from the total spectrum.

As a result, we found that HA trapped in S10 micelles has 24% sharp component at 1.0 mM peptide concentration, meaning ~ 24% peptides were located closer to the edge while ~76% closer to the core, while 29 % if [HA] is increased to 2.0 mM. The same trend is observed for $PEG_{600}PTHF_{650}$ wherein the sharp component was increased from 23% to 34 % with [HA] increased from 0.5 to 2.0 mM (**Fig. 4.5 A,C**).

4.4.3. Monitoring peptide behavior upon conformational change of IMAs

As introduced before, acetone as a "poor" solvent of IMAs can be used to loosen the micellar packing and induce IMAs conformational changes. Here we use acetone to investigate the influence of micelle packing on peptide location/microenvironment, which may "mimic" the process of peptide release upon polarity changes. We choose the same model IMAs, S10 and $PEG_{600}PTHF_{650}$, and keep the peptide concentration at 1.0 mM in both micelles. Acetone concentration of 5 to 50 % was introduced for each IMA and the obtained EPR spectra are shown in **Figures 4.6** and **4.7**. The semi-quantitative spectral analysis for both series of spectra was also performed. The relative population of the mobile component (when the HA peptide is closer to the edges of micelles) is listed for each spectrum in both figures. As is evident from **Figure 4.6**, upon addition of acetone to the $PEG_{600}PTHF_{650}$, the mobile component population is slowly increased from 29% to 31 % from 0 to 10% acetone, and gradually increased to 80 % from 10 to 50% acetone. In contrast, for the peptide in S10, 10% acetone causes a rapid increase in the mobile component population (from 24 % to 44 %). Then, the rate of mobile component increase becomes close to that in the $PEG_{600}PTHF_{650}$–based IMAs; the final mobile component also ends at ~80% with 50 % acetone. The plot of the mobile component population for each IMA increase is shown in **Figure 4.8**, wherein the error bars were obtained from three independent trials of our semi-quantitative spectral analysis.

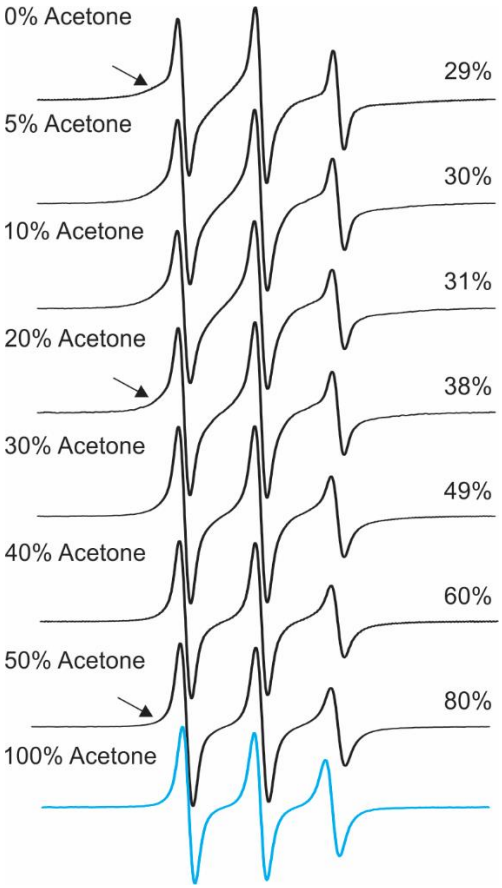

Figure 4.6. EPR spectra of the labeled HA peptide in $PEG_{600}PTHF_{650}$ -based IMA under different acetone percentage (left). The relative population of the mobile (sharp) component is listed on the right.

Overall, the trend shown in **Figure 4.8** is reasonable given the morphologies of IMAs based on two different AIPs, wherein assemblies from S10 are known to have less densely packed interior than $PEG_{600}PTHF_{650}$–based IMAs due to the overall higher hydrophobicity and longer hydrophobic PTHF segments of the $PEG_{600}PTHF_{650}$ if compared to S10. [4, 5] This results in better ability of acetone to solvate fragments of macromolecules in S10-based IMAs and reduce their intermolecular interactions which lead to emptier spatial areas ("gaps") within micellar assemblies that can be sensed by the HA peptide. Such "gap" introduces more space (or less crowding) to the peptide which yields an increase in the sharper component in an EPR spectrum (**Fig. 4.9A**). The

HA peptide could also "move" toward the edge of the loosened IMAs (**Fig. 4.9A**), which also results in an increase in the sharper component population. It is difficult to distinguish the two phenomena at this stage. However, the EPR spectra (**Fig. 4.6**) do provide an indication of how densely packed is the interior of the micellar assemblies, or their capability to be inverted (*micellar inversion*).

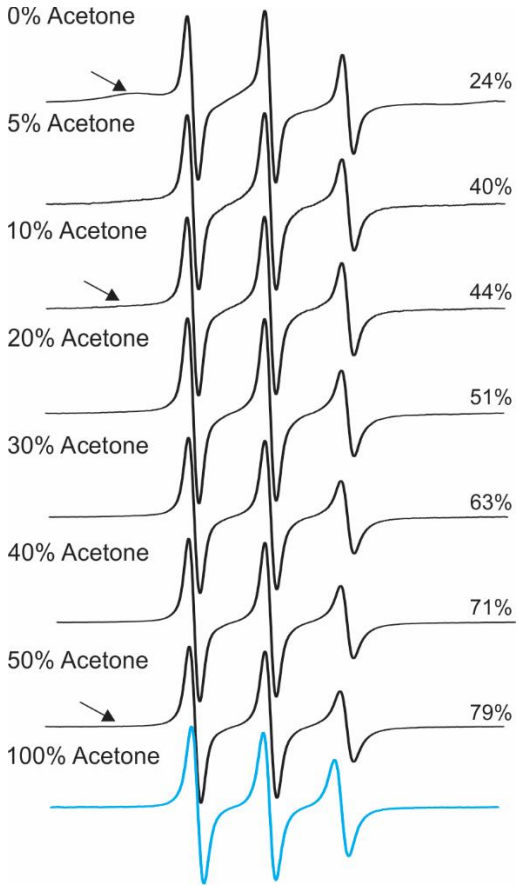

Figure 4.7. EPR spectra of the labeled HA peptide in S10 IMA under different acetone percentage (left). The relative population of the mobile (sharp) component is listed on the right.

In contrast, for $PEG_{600}PTHF_{650}$, since the interior is more densely packed, 10% acetone seems to cause no major changes to the morphology (a 2% increase in the sharp component population). Higher amount of acetone begins to influence the line shapes but overall the sharp component population is lower than that in the S10-based IMAs, until 50% acetone. At this point,

both micelles show an 80% sharp component indicating at this high acetone concentration, the micelles have similar packing density. This is reasonable because at 50% acetone both IMAs are likely loosely packed and the HLB does not play a key role in IMA conformation. It is also possible that some HA peptide was released from the interior and is located into the solvent (comparing the high-field region of the EPR spectra of 50% and 100% acetone of **Figures 4.6** and **4.7**).

4.4.4. Differences in low-field shift of EPR spectra

The $PEG_{600}PTHF_{650}$ IMAs possess more densely packed micellar interior, which does not allow much space for the HA peptide C-terminus (the labeled end) to approach to the crowding core. Therefore, the peptide molecules contributing to the immobile component are more likely experiencing less crowding (**Fig. 4.9B**) or kept some distances away from the core. This results in a lower extent of low-field shift (red arrows in **Figure 4.4A** *VS* **4.4B**). The S10 assemblies have lower density of the micellar interior, wherein the labeled end of the HA peptide may be allowed for approaching the core. This gives a higher extent of crowding and correspondingly a lower low-field shift (see **Figures 4.8C** and **4.4A** red arrow).

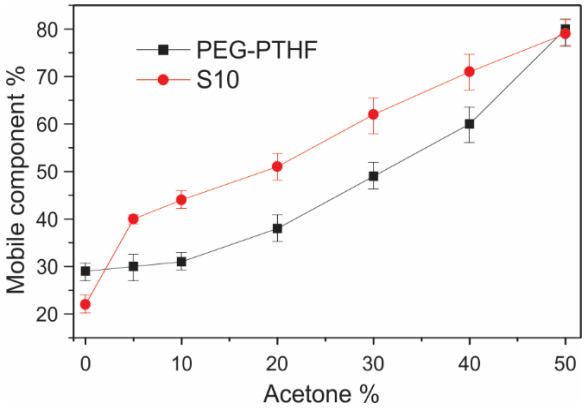

Figure 4.8. A plot of the relative population of the mobile component of the HA peptide in different IMAs (black= $PEG_{600}PTHF_{650}$; red=S10) under different acetone percentages. Error bars see main text.

4.4.5. Using EPR and peptide labeling as a tool to probe cargo position and IMA inversion

Our results suggest that combing peptide spin labeling and EPR spectroscopy can help depict the position of a macromolecular cargo in IMAs. Furthermore, since the measurements can be conducted under arbitrary conditions (solvent, polarity, heterogeneity), this approach can be used to monitor the cargo release process and probe the release mechanisms. An important property of IMAs is its capability to be inverted under various conditions. Using peptide position/microenvironment change as an indicator of the packing density (crowding extent) of the micelles can be informative for quantifying the *micellar inversion* of IMAs in general.

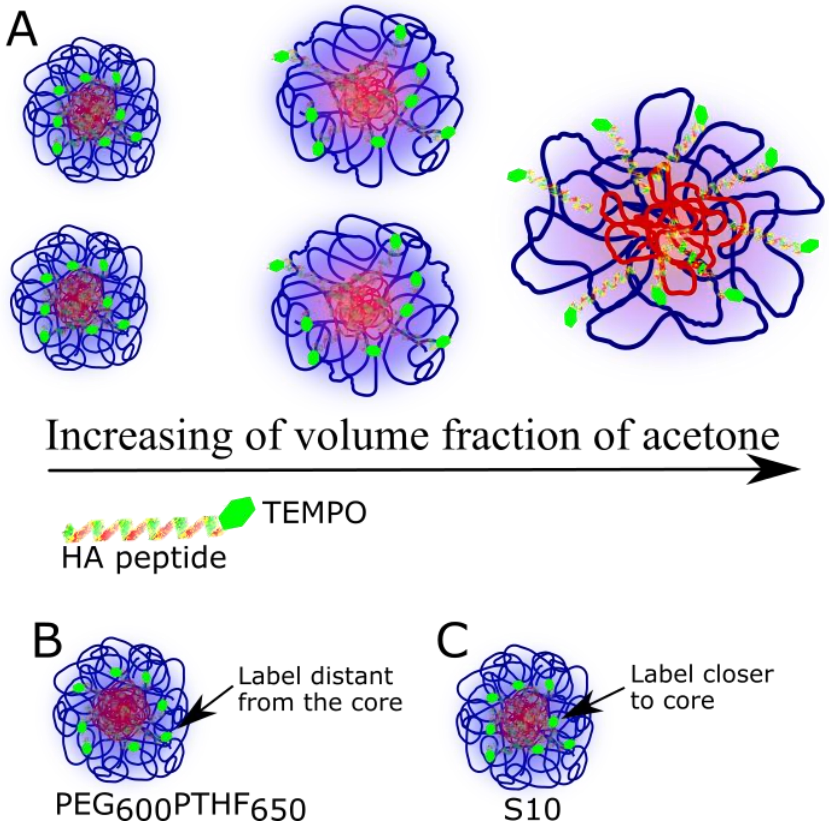

Figure 4.9. (A) Schematic illustration of acetone reducing the packing density of IMAs interior. (B) and (C) Schematic illustrations of the possible peptide position in the two IMAs based on S10 and $PEG_{600}PTHF_{650}$ with different HLB. Details see main text. Color density scales with micellar interior packing density for both the hydrophobic (red) and hydrophilic (blue) portions.

4.5. Conclusions

In conclusion, an antigenic glycoprotein, HA, was spin labeled at the C-terminus with a stable nitroxide radical to probe the peptide position and dynamics in IMAs, made from two amphiphilic invertible polymers, $PEG_{600}PTHF_{650}$ and S10 differing in macromolecular composition and HLB. The success of peptide spin labeling is confirmed with MS and EPR spectroscopy. The labeled peptide was incorporated into the IMAs from both polymers as indicated by the EPR spectral changes, which show contributions from peptide primarily in two areas/regions, near the more compact, crowding IMA interior (core) and the less compact exterior (shell). The relative contribution of each component was semi-quantitatively analyzed. Furthermore, increasing acetone concentration was used to trigger the conformation changes of IMAs. Such change was monitored with the labeled peptide and EPR as well, wherein for both IMAs the mobile spectral component consistent with peptide located within the IMA's exterior was increased as acetone concentration was increased. This finding is consistent with the expectation that acetone triggers IMAs demicellization and creates more space within the micellar assemblies for the peptide to move more dynamically or toward the IMA exterior. Interestingly, the rate of increase in the percentage of the mobile component was different for the two IMAs, which is consistent with the general understanding of the two IMAs morphology wherein S10 has less densely packed interior and, therefore, can be easily loosened with low acetone percentage. Conformational changes clearly relate to HLB of the polymers and can certainly be meaningful in controlling the IMAs-mediated peptide release.

4.6. References

(1) Kohut, A.; Voronov, A. Hierarchical Micellar Structures from Amphiphilic Invertible Polyesters: 1H NMR Spectroscopic Study *Langmuir* **2009**, *25*, 4356-4360.

(2) Kohut, A.; Dai, X.; Pinnick, D.; Schulz, D. L.; Voronov, A. "Host-Guest" Interaction between Cyclohexasilane and Amphiphilic Invertible Macromolecules *Soft Matter* **2011**, *7*, 3717-3720.

(3) Kohut, A.; Kudina, O.; Dai, X.; Schulz, D. L.; Voronov, A. Host-Guest Interactions between a Nonmicellized Amphiphilic Invertible Polymer and Insoluble Cyclohexasilane in Acetonitrile *Langmuir* **2011**, *27*, 10356-10359.

(4) Kudina, O.; Kohut, A.; Tarnavchyk, I.; Hevus, I.; Voronov, A. Solvent-Responsive Self-Assembly of Amphiphilic Invertible Polymers Determined with SANS *Langmuir* **2014**, *30*, 3310-3318.

(6) Hevus, I.; Kohut, A.; Voronov, A. Amphiphilic Invertible Polyurethanes: Synthesis and Properties *Macromolecules* **2010**, *43*, 7488-7494.

(7) Hevus, I.; Modgil, A.; Daniels, J.; Kohut, A.; Sun, C.; Stafslien, S.; Voronov, A. Invertible Micellar Polymer Assemblies for Delivery of Poorly Water-Soluble Drugs *Biomacromolecules* **2012**, *13*, 2537-2545.

(8) Maran, A.; Yaszemski, J. M.; Kohut, A.; Voronov, A. Curcumin and Osteosarcoma: Can Invertible Polymeric Micelles Help? *Materials* **2016**, *9*.

(9) Voronov, A.; Vasylyev, S.; Kohut, A.; Peukert, W. Surface Activity of New Invertible Amphiphilic Polyesters Based on Poly(Ethylene Glycol) and Aliphatic Dicarboxylic Acids *J. Colloid Interface Sci.* **2008**, *323*, 379-385.

(10) Hevus, I.; Kohut, A.; Voronov, A. Interfacial Micellar Phase Transfer using Amphiphilic Invertible Polymers *Polym. Chem.* **2011**, *2*, 2767-2770.

(11) Hevus, I.; Kohut, A.; Voronov, A. Micellar Assemblies from Amphiphilic Polyurethanes for Size-Controlled Synthesis of Silver Nanoparticles Dispersible Both in Polar and Nonpolar Media *J. Nanopart. Res.* **2012**, *14*, 820.

(12) Hevus, I.; Voronov, A.; Yaszemski, J. M.; Maran, A.; Kohut, A.; Voronov, S. In *Nanostructures Cancer Therapy*; Ficai, A., Grumezescu, A. M., Eds.; Elsevier: **2017**, p 351-382.

(13) Kudina, O.; Shogren, K. L.; Gustafson, C. T.; Yaszemski, M. J.; Maran, A.; Voronov, A. Invertible Micellar Polymer Nanoassemblies Target Bone Tumor Cells But Not Normal Osteoblast Cells *Future Sci. OA* **2015**, *1*.

(14) Hubbell, W. L.; López, C. J.; Altenbach, C.; Yang, Z. Technological Advances in Site-Directed Spin Labeling of Proteins *Curr. Opin. Struct. Biol.* **2013**, *23*, 725-733.

(15) Cafiso, D. S. Identifying and Quantitating Conformational Exchange in Membrane Proteins Using Site-Directed Spin Labeling *Acc. Chem. Res.* **2014**, *47*, 3102-3109.

(16) Fanucci, G. E.; Cafiso, D. S. Recent Advances and Applications of Site-Directed Spin Labeling *Curr. Opin. Struct. Biol.* **2006**, *16*, 644-653.

(17) Ji, M.; Ruthstein, S.; Saxena, S. Paramagnetic Metal Ions in Pulsed ESR Distance Distribution Measurements *Acc. Chem. Res.* **2014**, *47*, 688-695.

(18) McHaourab, H. S.; Steed, P. R.; Kazmier, K. Toward the Fourth Dimension of Membrane Protein Structure: Insight into Dynamics from Spin-Labeling EPR Spectroscopy *Structure* **2011**, *19*, 1549-1561.

(19) Qin, P. Z.; Haworth, I. S.; Cai, Q.; Kusnetzow, A. K.; Grant, G. P. G.; Price, E. A.; Sowa, G. Z.; Popova, A.; Herreros, B.; He, H. Measuring Nanometer Distances in Nucleic Acids using A Sequence-Independent Nitroxide Probe *Nat. Protoc.* **2007**, *2*, 2354-2365.

(20) Edwards, D.; Huber, T.; Hussain, S.; Stone, K.; Kinnebrew, M.; Kaminker, I.; Matalon, E.; Sherwin, M.; Goldfarb, D.; Han, S. Determining the Oligomeric Structure of Proteorhodopsin by Gd3+-Based Pulsed Dipolar Spectroscopy of Multiple Distances *Structure* **2014**, *22*, 1677-1686.

(21) Fleissner, M. R.; Brustad, E. M.; Kálai, T.; Altenbach, C.; Cascio, D.; Peters, F. B.; Hideg, K.; Peuker, S.; Schultz, P. G.; Hubbell, W. L. Site-Directed Spin Labeling of A Genetically Encoded Unnatural Amino Acid *Proc. Natl. Acad. Sci.* **2009**, *106*, 21637-21642.

(22) Todd, A. P.; Cong, J.; Levinthal, F.; Levinthal, C.; Hubbell, W. L. Site-Directed Mutagenesis of Colicin E1 Provides Specific Attachment Sites for Spin Labels Whose Spectra Are Sensitive to Local Conformation *Prot. Struct. Funct. Bioinform.* **1989**, *6*, 294-305.

(23) Pan, Y.; Neupane, S.; Farmakes, J.; Oh, M.; Bentz, K.; Choi, Y.; Yang, Z. Insights on the Structure, Molecular Weight and Activity of an Antibacterial Protein-Polymer Hybrid *ChemPhysChem* **2018**, *19*, 651-658.

(24) Hubbell, W. L.; Cafiso, D. S.; Altenbach, C. Identifying Conformational Changes with Site-Directed Spin Labeling *Nat. Struct. Biol.* **2000**, *7*, 735 - 739.

(25) Pan, Y.; Neupane, S.; Farmakes, J.; Liu, B.; Sun, W.; Yang, Z. Spin-Labeling of Polymeric Micelles and Application in Probing Micelle Swelling using EPR Spectroscopy *J. Polym. Sci. B Polym. Phys.* **2017**, *55*, 1770-1782.

(26) Ruthstein, S.; Frydman, V.; Goldfarb, D. Study of the Initial Formation Stages of the Mesoporous Material SBA-15 Using Spin-Labeled Block Co-polymer Templates *J. Phys. Chem. B* **2004**, *108*, 9016-9022.

(27) Ruthstein, S.; Schmidt, J.; Kesselman, E.; Popovitz-Biro, R.; Omer, L.; Frydman, V.; Talmon, Y.; Goldfarb, D. Molecular Level Processes and Nanostructure Evolution During the Formation of the Cubic Mesoporous Material KIT-6 *Chem. Mater.* **2008**, 20, 2779-2792.

(28) Kielmann, U.; Jeschke, G.; García-Rubio, I. Structural Characterization of Polymer-Clay Nanocomposites Prepared by Co-Precipitation Using EPR Techniques *Materials* **2014**, 7, 1384-1408.

(29) Jeschke, G. In *Advanced ESR Methods in Polymer Research*; Schlick, S., Ed.; John Wiley & Sons, Inc.: Hoboken, New Jersey, **2006**, p 133-164.

(30) Pilař, J. In *Advanced ESR Methods in Polymer Research*; Schlick, S., Ed.; John Wiley & Sons, Inc.: Hoboken, New Jersey, **2006**, p 133-164.

(31) Shvartzman-Cohen, R.; Monje, I.; Florent, M.; Frydman, V.; Goldfarb, D.; Yerushalmi-Rozen, R. Self-Assembly of Amphiphilic Block Copolymers in Dispersions of Multiwalled Carbon Nanotubes As Reported by Spin Probe Electron Paramagnetic Resonance Spectroscopy *Macromolecules* **2010**, *43*, 606-614.

(32) Voronov, A.; Kohut, A.; Vasylyev, S.; Peukert, W. Mechanism of Silver Ion Reduction in Concentrated Solutions of Amphiphilic Invertible Polyesters in Nonpolar Solvent at Room Temperature *Langmuir* **2008**, *24*, 12587-12594.

(33) Davies, J. T.; Rideal, E. K. *Interficial Phenomena*; Academic Press: New York, 1961.

(34) Zhang, X.; Jackson, J. K.; Burt, H. M. Development of Amphiphilic Diblock Copolymers as Micellar Carriers of Taxol *Inter. J. Pharm.* **1996**, *132*, 195-206.

(35) Budil, D. E.; Lee, S.; Saxena, S.; Freed, J. H. Nonlinear-Least-Squares Analysis of Slow-Motion EPR Spectra in One and Two Dimensions Using a Modified Levenberg-Marquardt Algorithm *J. Magn. Reson. A* **1996**, *120*, 155-189.

(36) López, C. J.; Fleissner, M. R.; Guo, Z.; Kusnetzow, A. K.; Hubbell, W. L. Osmolyte Perturbation Reveals Conformational Equilibria in Spin-Labeled Proteins *Prot. Sci.* **2009**, *18*, 1637-1652.

(37) López, C. J.; Fleissner, M. R.; Brooks, E. K.; Hubbell, W. L. Stationary-Phase EPR for Exploring Protein Structure, Conformation, and Dynamics in Spin-Labeled Proteins *Biochemistry* **2014**, *53*, 7067-7075.

CHAPTER 5. MACROMOLECULAR INVERSION-DRIVEN POLYMER INSERTION INTO MODEL LIPID BILAYER MEMBRANES*

5.1. Abstract

Macromolecules of amphiphilic invertible polymers (AIPs) are capable of self-assembly into micellar assemblies of various morphologies in solvents of different polarities. The micellar assemblies in aqueous media are capable of encapsulating poorly aqueous soluble cargo and can undergo inverse conformational change and cargo release in contact with non-polar media, including potentially, cell membranes. Thus, invertible micellar assemblies have significant potential in drug delivery and related domains. However, to date there have been few investigations into their interactions with lipid membranes.

Herein, we investigate the interactions of three recently developed AIPs of varying hydrophilic-lipophilic balance (HLB) with a highly fluidic microcavity supported 1,2-dioleoyl-sn-glycero-3-phosphocholine lipid bilayer. We combined electrochemical impedance spectroscopy with fluorescence correlation spectroscopy to understand how the AIP micellar assemblies impacted bilayer permeability and fluidity respectively, across polymer concentrations above and below their critical micelle concentrations. At concentration as above their cmcs, all of the AIPs

* The material in this chapter was co-authored by Oksana Zholobko, Sivaramakrishnan Ramadurai, Ananiy Kohut, Nirod Kumar Sarangi, Vladimir A. Baulin, Tia E. Keyes, and Andriy Voronov. Oksana Zholobko had the primary responsibilities of synthesizing and characterizing polymers, preparing the micellar assemblies, and incorporating the dye into them. Oksana Zholobko and Ananiy Kohut were charged with characterizing the micellar solutions by UV-Vis Spectroscopy. Sivaramakrishnan Ramadurai helped Oksana Zholobko perform and analyze results of FLCS and EIS experiments. Oksana Zholobko was involved in drafting and revising all versions of this chapter. Vladimir A. Baulin, Tia E. Keyes and Andriy Voronov helped explain and describe the interactions of micellar assemblies with model lipid membrane. Published article can be found at https://doi.org/10.1016/j.jcis.2019.01.093.

explored increased permeability and decreased the fluidity of the lipid membrane. The extent of impact depended on the hydrophobicity of the AIP. $PEG_{600}PTHF_{650}$, the most hydrophobic of the polymers, synthesized from PEG (molecular weight 600 g/mol) and PTHF (molecular weight 650 g/mol) exerted the greatest influence on the bilayer's physical properties and fluorescence imaging and correlation data indicate that PEG_{600}-$PTHF_{650}$ micelles loaded with BODIPY probes adsorb and invert at the lipid membrane with release of cargo into the bilayer.

5.2. Introduction

Amphiphilic polymers that incorporate short hydrophilic and hydrophobic chains in the backbone can form intra-chain or single-molecule micelles in selective solvents. There are three classes of chain architecture that can form intra-chain micelles: (i) polysoaps that contain short amphiphiles in the chain; (ii) grafted copolymers; and (iii) amphiphilic invertible polymers (AIPs). These classes of amphiphilic polymers exhibit similar micellization behavior [1] at low polymer concentrations in selective solvents: they form intra-chain micelles of single polymers with critical micellar concentration (cmc) close to zero, at higher concentrations they exhibit a second cmc corresponding to inter-chain micellization, first in form of spherical micelles and then cylindrical micelles at even higher concentrations.

Here, recently synthesized AIPs consisting of alternating hydrophilic and hydrophobic fragments (**Fig. 5.1A**) and their interaction with phospholipid bilayers that also contain amphiphilic lipids were studied. The AIP alternating structure of short hydrophilic and hydrophobic blocks makes them highly responsive to changes in the solvent quality (**Fig 5.1**): in polar solvents they form direct micelles with hydrophobic exterior and hydrophilic corona, while in non-polar solvents they form inverted micelles with hydrophilic groups in the exterior and hydrophobic groups in the corona (**Fig. 5.1B**) [2]. Abrupt changes of the conformational state

makes them suitable candidates for applications as switchable and responsive functional devices, where small variations in the environment can trigger a function [3].

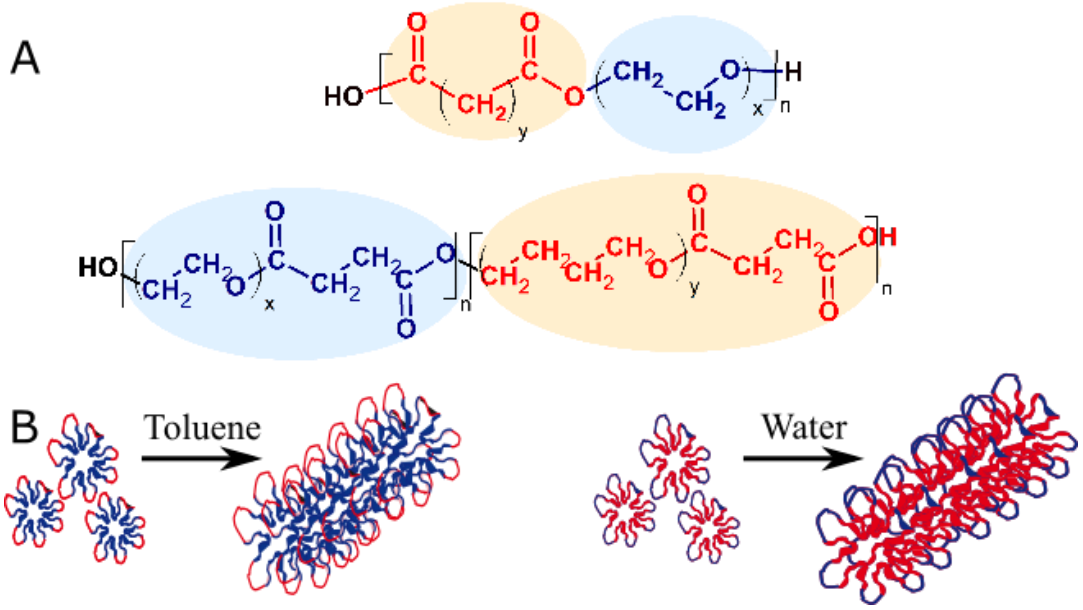

Figure 5.1. (A) Chemical structures of two AIP classes (B) AIP inter-chain spherical and cylindrical micelles formed by increasing polymer concentration in water and toluene, respectively.

The size and morphology of the resulting micelles in both polar and nonpolar environments, can be controlled via the number and length of hydrophilic and hydrophobic blocks of the AIPs for a given function. A combined ^{1}H NMR spectroscopy/SANS study demonstrated [2,4–8] that the hydrophilic and hydrophobic fragments of the chain tend to replace each other in the exterior and corona of the micelles in response to changes to the environmental polarity from polar to nonpolar making the AIPs invertible. The invertibility of the AIPs is an especially promising feature that allows rapid and controlled self-assembly in applications such as drug delivery, that require simultaneous utility in polar and nonpolar media.[9,10] Loaded with a hydrophobic drug, AIP micelles can successfully deliver cargo molecules from an aqueous medium to a polar/nonpolar interface and release the drug upon inverting the macromolecular

conformation by entering/contacting the less polar biomembrane medium. The ability of AIP micelles to solubilize otherwise insoluble substances, both in polar and nonpolar solvents, was demonstrated using a number of compounds, including poorly water-soluble dyes [11–13] and drugs.[14] Hydrophobic drug molecules can be loaded into the hydrophobic exterior of a direct micelle in an aqueous solution and released upon change of the selective solvent. In a recent study [15], it was shown that the presence of the anti-cancer drug curcumin, loaded in the AIP micelle essentially reduced cell survival in three human osteosarcoma cell lines. Confocal microscopy studies confirmed that curcumin was readily taken up into osteosarcoma cells when delivered by the AIP micelles, but not into the normal cells.[9,10,14,15] Remarkably, the AIPs with no cargo, when tested at the same concentrations, had no effect on the survival of normal cells.

Given their potential value in the field of drug delivery, understanding how the AIPs interact with lipid membranes, and the factors facilitating AIPs-mediated interaction with lipid bilayers, is important. Through such understanding the basic principles underlying the effective design of AIP-based polymeric carriers as membrane-active compounds can be established.

In this work, from an existing AIPs library [9,12,16-18], we chose three polymers; i.e. S10, made from PEG (molecular weight 1,000 g/mol) and sebacic acid, D10, made from PEG (molecular weight 1,000 g/mol) and dodecanedioic acid, and $PEG_{600}PTHF_{650}$, synthesized from PEG (molecular weight 600 g/mol) and PTHF (molecular weight 650 g/mol) for examination of the AIP micellar assemblies interactions with lipid membrane.

The interaction of the AIP micelles with a microcavity supported phospholipid membrane (MSLB) was examined. The MSLB provides highly fluidic, but also stable lipid bilayers that are addressable by both optical and electrochemical methods. AIP adsorption at the MSLB, permeation through the MSLB and capacity of the micelles to release an encapsulated fluorescent

probe into the hydrophobic core of a DOPC lipid bilayer were evaluated using fluorescence lifetime correlation spectroscopy (FLCS) and Electrochemical Impedance spectroscopy (EIS).

5.3. Experimental

5.3.1. Materials

1,2-Dioleyl-sn-glycerophosphocholine (DOPC) in powder form was purchased from Avanti polar lipids (Instruchemie, The Netherlands). Phosphate buffer saline (PBS) tablets were purchased from Sigma-Aldrich (Wicklow, Ireland), DOPE-atto655 (ex. 650/em. 670nm) was purchased from Atto-tech GmbH (Siegen, Germany). Poly(ethylene glycol) (PEG, molecular weight 600 and 1000 g/mol), polytetrahydrofuran (PTHF, Terathane, molecular weight 650 g/mol), sebacic acid, and succinic anhydride were received from Sigma-Aldrich (St. Louis, MO, USA). Dodecanedioic acid was obtained from TCI (Portland, OR, USA). All other chemicals were of HPLC grade and were used as purchased. The buffers were prepared from MilliQ water (>18MΩ).

The stock solutions of DOPC and DOPE-Atto655 (ATTO) were prepared in chloroform. The lipid, along with the fluorescent lipid probe were mixed in a ratio of 5000:1 mol/mol in a glass tube. The chloroform was removed under a gentle stream of Nitrogen gas and then placed under vacuum for 2 hours to 12 hours to remove residual solvents. This results in a dry lipid film which was then used for vesicle preparation. The lipid films were prepared in the same way, but without the fluorescent marker, for EIS measurements.

5.3.2. Vesicle preparation

The dried lipid films were rehydrated in 1 ml of 0.01 M phosphate buffer saline (PBS) and vortexed for a period of 30-60 seconds. Next, the lipid suspensions were extruded 11 times through

a 100 nm polycarbonate filter using a mini-extruder (Avanti Polar Lipids) to form large unilamellar vesicles (LUV) and diluted to final concentration of 0.25 mg/ml.

5.3.3. Synthesis of AIPs

AIPs were prepared using previously reported methods.[12,16] Briefly, D10 and S10 (chemical structures shown in **Fig 5.2**) were synthesized *via* a polycondensation reaction of equimolar amounts of poly(ethylene glycol) with a molecular weight of 1000 g/mol and either dodecanedioic (for D10) or sebacic (for S10) acid. The polycondensation was carried out in a boiling toluene solution in the presence of sulphuric acid as a catalyst for about 20 h.[16] PEG_{600}-$PTHF_{650}$ was synthesized using a two-stage procedure. In the first step, polytetrahydrofuran with a molecular weight of 650 g/mol and succinic anhydride at a molar ratio of 1:2 were melted together and the melt was maintained at 95°C for 3 h to give an acid-terminated prepolymer. In the second stage, a toluene solution of the acid-terminated prepolymer and poly(ethylene glycol) with a molecular weight of 600 g/mol (molar ratio as 1 : 1) was refluxed with a Dean-Stark trap in the presence of sulphuric acid as a catalyst for about 20 h.[12]

5.3.4. Preparation of stock solutions of AIPs

The stock solutions of AIPs were prepared by dissolving 0.05 g of a corresponding polymer in 5 mL of 0.01 M phosphate buffer saline and vortexing for 3-5 min. The solutions were left for 24 h to equilibrate at room temperature with gentle agitation before measuring. The final AIP concentration in these stock solutions was 10 mg/mL.

5.3.5 Preparation of AIP micelles loaded with BODIPY

AIP micelles loaded with a previously reported hydrophobic naphthalene BODIPY (4,4-difluoro-4-bora-3a,4a-diaza-s-indacene)(derivative, 8a, were prepared by thin film method.[9,17] Following this method, 0.1 g of a corresponding AIP was dissolved in 10 mL of acetone and 0.5

mL of acetone solution of BODIPY with a concentration of 1.0 mg/mL was added. The solvent was removed by rotary evaporation. The resultant solid BODIPY/AIP thin film was hydrated with 10 mL of 0.01 M phosphate buffer saline and vortexing for 3-5 min. The solution was left for 24 h to equilibrate at room temperature with gentle agitation. The unincorporated BODIPY aggregates were removed by passing through 0.45 μm filters.

5.3.6. Determination of the BODIPY Concentration in Aqueous Phase

The concentration of BODIPY in aqueous solution was estimated using UV−vis spectroscopy. UV−vis spectra were recorded on a Cary 5000 UV−vis-NIR spectrophotometer (Varian, Inc.). The absorbance values were measured in the range of 350−800 nm. The height of a BODIPY adsorption peak at 531 nm was attributed to a particular dye concentration using the calibration method. If necessary, BODIPY-loaded solution samples were diluted with the corresponding 10 mg/mL aqueous AIP solution to maintain measurable absorbance levels. To build a calibration curve, 10 mg/mL micellar solutions for PEG_{600}-$PTHF_{650}$ containing $1 \cdot 10^{-4}$, $2 \cdot 10^{-4}$, $4 \cdot 10^{-4}$, $7 \cdot 10^{-4}$, $1 \cdot 10^{-3}$, $2 \cdot 10^{-3}$, and $4 \cdot 10^{-3}$ % of solubilized BODIPY were prepared by thin film method. To this end, 0.05 g of PEG_{600}-$PTHF_{650}$ was dissolved in 5 mL of acetone and, respectively, 5, 10, 20, 35, 50, 100, and 200 μL of acetone solution of BODIPY with a concentration of 1.0 mg/mL was added. The acetone was removed in vacuum, the resultant thin films were hydrated with 5 mL of 0.01 M PBS, UV-vis spectra of the solutions were taken, absorbance at 531 nm was determined for each solution and plotted versus the BODIPY concentration.

5.3.7. Microcavity array supported lipid bilayers

Lipid bilayers were suspended across aqueous filled microcavity arrays according to protocols modified slightly from previous reports.[19,20] For fluorescence studies the microcavity arrays were made from air plasma treated polydimethylsiloxane (PDMS) [Sylgard 184 base and curing kit, Dow Corning]. Briefly, PDMS was cast onto a dried film of polystyrene spheres of 4.61 μm diameters, formed on freshly cleaved mica, and cured. The PDMS was peeled off the mica and the spheres removed to form open spherical cavities embedded in PDMS. The PDMS substrate was air plasma cleaned for 5 minutes, followed by 1hr of sonication in PBS buffer to ensure the cavities were filled with aqueous solution.

Following filling of the array micropores with aqueous buffer, a Langmuir monolayer of DOPC was spread across the micropore array. This was achieved using a Model KN2006, KSV-NIMA, Langmuir-Blodgett Alternate Frame. DOPC was prepared in chloroform at a concentration of 1 mg/ml and 50 μL of this solution was suspended on the water sub-phase. Fifteen minutes was allocated for evaporation of the solvent, prior to lipid monolayer compression. The lipid monolayer was compressed at 25 cm^2/min, until surface pressure reached 40 mN/m and this the compression process was repeated twice. Then the rate of compression was maintained at 50 cm^2/min and a constant surface pressure of 32 mN/m was maintained during the transfer of DOPC monolayer from the water-air interface to the aqueous filled microcavity array. During LB transfer, the rate of the dipper motion was 10 mm min^{-1} to ensure adequate transfer. The monolayer coated template was incorporated into the flow chamber by sticking the edges of the PDMS to a microscope cover slip using adhesive (Araldite, UK). DOPC lipid vesicles containing lipid probe were injected into the flow chamber where the spontaneously disrupt to form a free-spanning lipid bilayer. After 10 minutes, the flow chamber was flushed with 1ml of 0.01 M PBS buffer to remove excess vesicles

and to maintain the aqueous media above the bilayer. Lipid bilayers formed in this way were found from FLCS to be stable for a minimum of 2 days. The microcavity array prepared for EIS measurements had an analogous structure to the PDMS array but were prepared by electrodeposition of gold through polystyrene sphere templates at gold coated silicon wafers, as reported previously.[20] Briefly, silicon wafers coated with 100 nm gold on 50nm titanium were purchased from AMS biotechnology, UK. The wafers were cut to 2 X 1 cm and polystyrene spheres of 2.88 μm were drop cast on the wafers and left to dry overnight. The sphere modified wafers were dipped into commercial gold electrodeposition solution until the metal had grown to the equator of the PS spheres. After rinsing with milliQ water to remove excess salts or electrolyte, the microcavity array substrates were then selectively modified by immersing the substrate in an ethanolic solution of 1 mM hexa-mercaptoethanol for at least 18 hrs in at room temperature. This step was carried out leaving the polystyrene spheres in place, as this prevented the modification of the inner cavity surface, meaning that only the top surface was exposed to the thiol and thus modified. Following top surface self assembled monolayer (SAM) modification, the substrates were sonicated in THF for 15 minutes to remove the polystyrene spheres. The quality and uniformity of the microcavity array was confirmed by scanning electron microscopy as reported previously.[20] We had previously confirmed that the ethanol deposition solution does not remove the templating spheres.[21] The microcavity array was then sonicated for 20 minutes with the PBS buffer before the DOPC bilayer by LB/vesicle fusion deposition as described above. The aqueous filled lipid bilayer coated gold cavity array was placed inside glass cell containing PBS buffer along with the reference and auxiliary electrodes and electrochemical impedance spectroscopy was measured as described below.

5.3.8. Fluorescence lifetime Correlation Spectroscopy (FLCS)

Fluorescence lifetime correlation spectroscopy (FLCS) experiments were performed using a Microtime 200 system (PicoQuant GmBH, Germany) consisting of confocal optics, dual single avalanche photo diode (SPAD) detection unit, time correlated single photon counting (TCSPC), and inverted microscope model Olympus X1-71 with an Olympus UPlanSApo 60x/1.2 water immersion objective. The lipid labelled fluorophores ATTO-655 were excited using pulsed picosecond laser at 640 nm LDH-P-C-640B Picoquant. The BODIPY loaded AIP micellar solutions were excited using 532nm laser PicoTA from Toptica (Picoquant). A single mode optical fiber guides the two lasers to the main unit and provides a homogeneous Gaussian profile for the both excitations. The lasers were pulsed at 20 MHz, corresponding to an interval of 50 ns. The emitted fluorescence was collected through the microscope objective and dichroic mirror z532/635rpc blocked the backscattered light and HQ550lp AHF/Chroma for 532 nm and HQ670lp AHF/Chroma for 640 nm filters were used to clean up the signal. A 50 μm pinhole was used to confine the volume of detection in the axial direction. Fluorescence was detected using SPAD from MPD (Picoquant). The time-correlated single photon counting system (PicoHarp 300 from Picoquant), enabled simultaneous assessment of the lifetime in a nanosecond range along with the time of diffusion in the millisecond range.[22] Using TCSPC allowed us to filter the any contribution from after-pulsing, suppress scattered light and parasitic signals and background,[23,24] and in parallel to calculate the fluorescence lifetime of the lipid probes *in-situ*.

To calibrate the FCS confocal volume, Rhodamine 6G (532nm) and Atto655 (640nm) dyes with known diffusion coefficient were used.[25] The volume was determined at the start of each set of experiments and at least 15 data points were collected from each sample and each data point was measured for 30 sec. The time-dependent fluctuations of the fluorescence intensity d$I(t)$ were

recorded and analyzed by an autocorrelation function $G(t)= I + <dI(t´)\, dI(t´+t)>/<dI(t´)>^2$. As has been shown theoretically for an ensemble of *m* different types of freely diffusing species, $G(t)$ has the following 2-dimensional analytical form:[26]

$$G_{2D}(t) = \left(1 + \frac{f_T}{1 - f_T} e^{-t/\tau_T}\right) \cdot \frac{1}{\langle N \rangle} \cdot \frac{1}{1 + \left(\frac{\tau}{\tau_D}\right)^{\alpha}} \qquad \textbf{(5.1)}$$

Here $<N>$ is the average number of diffusing fluorescence species in the observation volume, f_T and τ_T are the fraction and the decay time of the triplet state, τ_D is the diffusion time of molecule diffusing through confocal volume, α is anomalous exponent, respectively. The anomalous exponent (α) indicates the extent of deviation of diffusion coefficient (D) from Brownian motion and it can vary between 0 to 2. A value of 1 indicates the free diffusion.[27,28] The experimentally obtained $G(t)$ is fitted with equation (1), to yield the diffusion time, τ_D which is related to the diffusion coefficient D through $D = r_0^2/4\tau_D$, where r_0 is the lateral radius of the confocal volume. The fits of the autocorrelation curves were carried out using the Picoquant software package using a least square Marquard-Levenberg algorithm. All measurements were carried out at 20°C.

5.3.9. Electrochemical Impedance spectroscopy (EIS)

Electrochemical impedance spectroscopy was performed on a CH660A potentiostat (CH Instruments, Germany). A standard 3-electrode cell was employed which comprised of an Ag/AgCl reference electrode, a platinum auxiliary electrode and the gold microcavity array which constituted the working electrode. The EIS was measured over a frequency range of 1 MHz to 0.01Hz with an AC modulation amplitude of 5 mV at a potential bias of 0 V (vs Ag/AgCl). All measurements were carried out in a glass cell containing 20 ml of PBS buffer, pH 7.4. The EIS of

the aqueous filled microcavity array coated with the DOPC lipid bilayer was measured initially prior to addition of probes to ensure signal stability and then titrate solutions in the glass cell containing PBS buffer and the electrochemical impedance response of the lipid bilayer following probe introduction was measured for each concentration. Each measurement takes approximately 10 minutes and the measurements were carried out at room temperature (22 °C).

Equivalent circuit model for MSLB

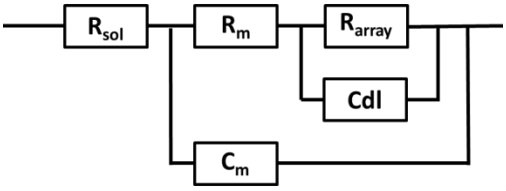

Scheme 5.1. Equivalent circuit model used to fit AC impedance data.

In order to extract the resistance and capacitance values for the MSLBs, the EIS data were fitted to the equivalent circuit model (ECM) shown in **Scheme 5.1** which was described previously for the lipid bilayer modified microcavity array electrode.[29] The circuit consists of the solution resistance (R_{sol}) in series with a resistor and a capacitor, which are in parallel and correspond to the electric and dielectric properties respectively of membrane deposited on the electrode surface (R_m, C_m). The ECM also contains an additional component to account for the resistance of the cavity arrays (R_{array}), and the double layer capacitance (C_{dl}). The data for the bare cavities and cavities upon treatment with ME were fitted with a $R_{sol.}$(Rm||Cm), as at this stage, in the absence of the bilayer, the resistance and capacitance are expected to be uniform along the surface of the electrodes. A Constant Phase Element (CPE) was used in the equivalent circuit instead of pure capacitors to account for surface defects on both the electrode surface and the lipid bilayer. The impedance of a CPE is given by $Z_{CPE} = Q^{-1}(j\omega)^{-\alpha}$ where Q is the magnitude of the capacitance of

the CPE, ω is the angular frequency, and α is a real number between 1 and 0 (the closer α gets to 1, the more ideal the capacitive behavior of the CPE).

As increasing concentrations of AIP were titrated into the contacting electrolyte solution, it is expected that R_{sol} values may change depending on the nature of the macromolecules, e.g. where it hydrophilic-lipophilic balance changes but everything else remains static. R_{array} is not expected to vary within a sample as there are no changes occurring in this component of the electrical system. C_m and R_m are connected in parallel. The membrane acts as semi-impermeable and insulating medium in biological cells as both the intracellular and extracellular environments contain various concentrations of ionic salt solutions permitted by the membrane. Similarly, in the MSLB, there is an external and internal environment comprising PBS buffer separated by a semi-permeable phospholipid bilayer. Essentially, this insulating bilayer is separating two ionic phases and is thus acting as a capacitor.

5.4. Results and discussion

5.4.1. Synthesis of AIPs

The synthesis of AIPs was performed via a polycondensation method that results in alternating invertible amphiphilic polyester structures with various ratios of hydrophilic and hydrophobic blocks corresponding to different HLB. In this study, three representative AIPs were used (**Fig. 5.2**), to understand better the effect of AIPs composition on interactions with biological membrane as well as the role of AIP invertibility in these interactions.

The interactions of the AIPs with the model lipid membrane were examined at polymer concentrations below and above the inter-chain cmc.

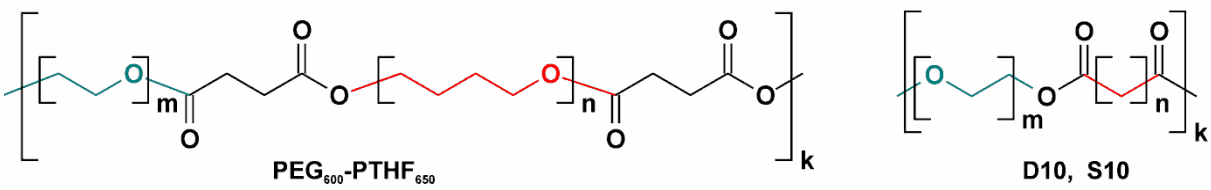

AIP	m	n	HLB	M_w	PDI	CMC, μg/mL
PEG_{600}-$PTHF_{650}$	13.2	8.8	13.8	9 700	1.52	3.5
D10	22.3	10	14.4	7 600	1.53	33
S10	22.3	8	15.4	11 700	1.59	490

Figure 5.2. Chemical structure and characteristics of AIPs. D10 is made from dodecanedioic acid and polyethylene glycol with an average M_n 1000 g/mol (PEG-1000). S10 is based on PEG-1000 and sebacic acid. The PEG_{600}-$PTHF_{650}$ is synthesized from PEG-600 and polytetrahydrofuran with an average M_n 650 g/mol (PTHF-650).

5.4.2. AIP interaction with membrane—FLCS

Interaction of AIPs with lipid bilayer was studied using fluorescence lifetime correlation spectroscopy, to understand how the diffusion of a lipid probe; DOPE labelled with ATTO, was altered by the presence of each polymer above and below cmc. **Figure 5.3** (green curve) shows representative FLCS data for ATTO lipid probe diffusing in a DOPC membrane suspended across a buffer filled with PDMS microcavity array (green curve) and the same substrate following incubation with PEG_{600}-$PTHF_{650}$ at a concentration (1mg/mL) that exceeds its cmc (blue curve). The ACF curves were fit to the 2-dimensional diffusion model given in **Equation 5.1** and the fits are shown as solid lines in the **Fig. 5.3**. The average lipid diffusion coefficient was calculated from this data as 10.60 ± 0.70 $\mu m^2 s^{-1}$ for the DOPC membrane supported across the pore aperture in the absence of AIP and this value is consistent with values previously reported in literature on MSLB lipid diffusion.[30] It is also consistent with the lipid lateral diffusion values reported for giant unilamellar vesicles of DOPC,[31] reflecting the high degree of fluidity of the lipids in the MSLB.

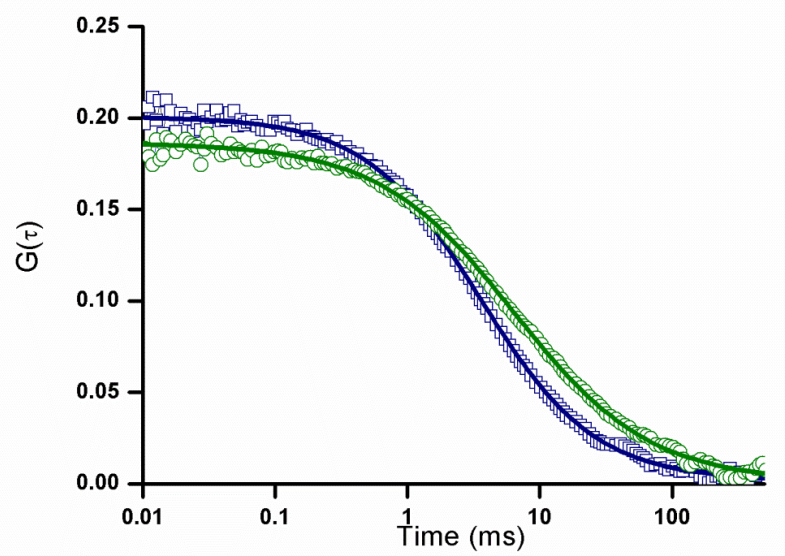

Figure 5.3. Representative ACF curves for ATTO labelled DOPC lipid membrane and 1 mg/ml PEG_{600}-$PTHF_{650}$ on micro-cavity supported lipid bilayer. The DOPC lipid bilayer was suspended across the buffer filled microcavity array using Langmuir-Blodgett technique and vesicle disruption method. The excitation wavelength for ATTO-DOPE was 645nm. The typical FLCS curve obtained after normalizing the fluctuation signals and the true autocorrelation function was obtained by using fluorescence lifetime signature. The blue squares correspond to experimental data from lipid marker ATTO labelled DOPE for the DOPC bilayer alone and green circles correspond to ATTO labelled DOPE for the DOPC bilayer in the presence of 1 mg/ml PEG_{600}-$PTHF_{650}$. The solid lines show the 2D-diffusion model fit from which diffusion time and subsequently diffusion coefficients were calculated.

For each AIP, their concentration at the DOPC bilayer was systematically increased from below to above their cmc values and the lipid diffusion time and diffusion coefficient of the ATTO-DOPE were evaluated at each concentration.[9] **Table 5.1** shows the calculated diffusion coefficients for the lipid probe. Below their cmc's, none of the polymers had a measurable impact on the fluidity of the DOPC bilayer. However, above their cmc's the AIPs impacted the ATTO-DOPE diffusion to an extent that depends on the polymer HLB. For PEG_{600}-$PTHF_{650}$, the AIP with the lowest HLB, at concentrations exceeding 100 µg/ml the lipid lateral diffusion decreased significantly from 10.72 ± 0.90 $\mu m^2 s^{-1}$ in the absence of polymer to 6.8 ± 0.7 $\mu m^2 s^{-1}$. Conversely for D10, no changes to *D* were observed over the full range of concentrations below and above

cmc even up to 10mg/mL which is 30 times the cmc concentration suggesting little or no D10-membrane interaction within the limit of FLCS sensitivity. In the case of S10, *D* of ATTO -DOPE decreases to 10.06 ± 0.55 $\mu m^2 s^{-1}$ at 10 mg/ml and then notably to 8.5 ± 0.55 $\mu m^2 s^{-1}$ for 30 mg/ml (around 6 times cmc) indicating the AIP micelles interact with the lipid membrane at concentrations well above its cmc. The molecular brightness and fluorescence lifetime of ATTO-DOPE in the DOPC membrane was estimated as 6000 ± 1200 cpsm and 3.38 ± 0.05 ns and found to be unchanged in the presence of AIP. Similarly, the anomalous parameter α remained approximately 1 across the polymer concentrations explored, indicating that the lipid diffuses normally with no deviation from Brownian motion in the presence of AIPs.

Table 5.1. Calculated lipid diffusion coefficients (ATTO) for different concentrations of PEG_{600}-$PTHF_{650}$, D10 and S10 on DOPC membrane spread across buffer filled MSLB. α was approximately 1 for all measurements. The lipid diffusion values for AIPs above their cmc are highlighted in grey.

Concentration (mg/ml)	***D* ($\mu m^2 s^{-1}$)**		
	PEG_{600}-$PTHF_{650}$	**D10**	**S10**
0	10.72 ± 0.90	10.72 ± 0.90	10.72 ± 0.90
0.001	10.90 ± 1.00		
0.010	11.00 ± 1.10	10.60 ± 0.60	
0.100	6.70 ± 1.60	10.45 ± 0.60	11.00 ± 0.80
1.000	6.80 ± 0.70	10.20 ± 0.60	10.62 ± 1.00
10		10.62± 0.99	10.06 ± 0.60
30			8.50 ± 0.55

The reduced lateral mobility of lipid observed in the presence of the PEG_{600}-$PTHF_{650}$ and to a lesser extent S10, above their cmc indicates an increase in membrane viscosity is induced by adsorption of the AIP micelles on the membrane. This may be due to insertion AIP

macromolecules into the bilayer and suggests inversion of the micelle on exposure to the hydrophobic bilayer environment.

The data suggests that for both S10 and PEG_{600}-$PTHF_{650}$ upon interaction with the DOPC lipid bilayer, the inversion of macromolecular conformation occurs, but to different extents for PEG_{600}-$PTHF_{650}$ and S10. As a result of the particular flexibility of both the PEG and PTHF blocks, the AIP chains of PEG_{600}-$PTHF_{650}$ possess higher invertibility with the membrane, thus, impacting the diffusivity of the lipid probe.

Conversely no change to the diffusion of lipid was seen in the presence of D10 over a full range of polymer concentrations well in excess of its cmc. For D10 this can be attributed to this AIP's much less expressed inversion due to the presence of longer $–(CH_2)_{10}–$ moieties of dodecanedioic acid in the macromolecular chains that are more firmly packed in the micellar interior.[6]

5.4.3. AIP interaction with DOPC membrane-EIS studies

Whereas FLCS provides insight into the impact of AIP on bilayer fluidity, to understand the impact of the AIP micelles on the permeability of the lipid bilayers, electrochemical impedance spectroscopy (EIS) was used. In EIS, a small amplitude alternating voltage, scanned over a range of frequencies is applied to the working electrode, in this case the MSLB, and the amplitude and phase shift in the current response is monitored. These parameters reflect the electrochemical impedance of the system and fitting this response to an appropriate equivalent circuit allows direct and sensitive evaluation of changes to membrane resistivity. In the present experiments, the DOPC bilayer was suspended over PBS filled gold cavity arrays that serve as the working electrode. An Ag/AgCl electrode and platinum wire served as reference and auxiliary electrode respectively and the PBS buffer served as electrolyte. Each impedance spectrum was collected over a frequency

range of 0.01 to 10000 Hz at a potential of 0 V with a modulation amplitude of 5 mV. Before introducing the AIP, the DOPC bilayer membrane resistance on gold cavity array was measured as 7.6 ± 1.0 MΩcm^2 and capacitance was 8.5 ± 1.7 µF/cm^2, which is consistent with previously reported values for MSLBs.[29]

AIP was titrated into the electrochemical cell, as per the FLCS experiments, over a range of concentrations that encompassed the cmc and the impedance spectrum was recorded at each polymer concentration. **Figure 5.4** (panel **a,b,c**) shows representative Nyquist plots for DOPC MSLBs in contact with different concentrations of PEG_{600}-$PTHF_{650}$, D10 or S10. The impedance of the MSLB system decreases sharply in the presence of PEG_{600}-$PTHF_{650}$ (cmc: 3.3 µg/ml) up to 10 µg/ml and then remains constant over further additions (to 100 and 1000 µg/ml) of this AIP. For D10 (cmc: 33 µg/ml) the impedance changes are negligible up to 1 mg/ml, above which, the impedance decreases but modestly compared to PEG_{600}-$PTHF_6$. Similarly, no change in the impedance was observed for S10 (cmc: 490 µg/ml) in contact with bilayer at low concentrations, however, at concentrations exceeding 1 mg/ml a significant decreases in the impedance was observed which are of similar order of magnitude to the changes observed for PEG_{600}-$PTHF_{650}$ (**Fig. 5.4d**).

The bilayer resistance and capacitance were calculated from the electrochemical impedance spectra by fitting the data to the ECM model described in **Scheme 5.1**. The resulting changes to the resistivity of the film compared to the untreated DOPC lipid bilayer are plotted versus AIP concentrations in **Figure 5.4d** and the data is shown in **Table 5.2**.

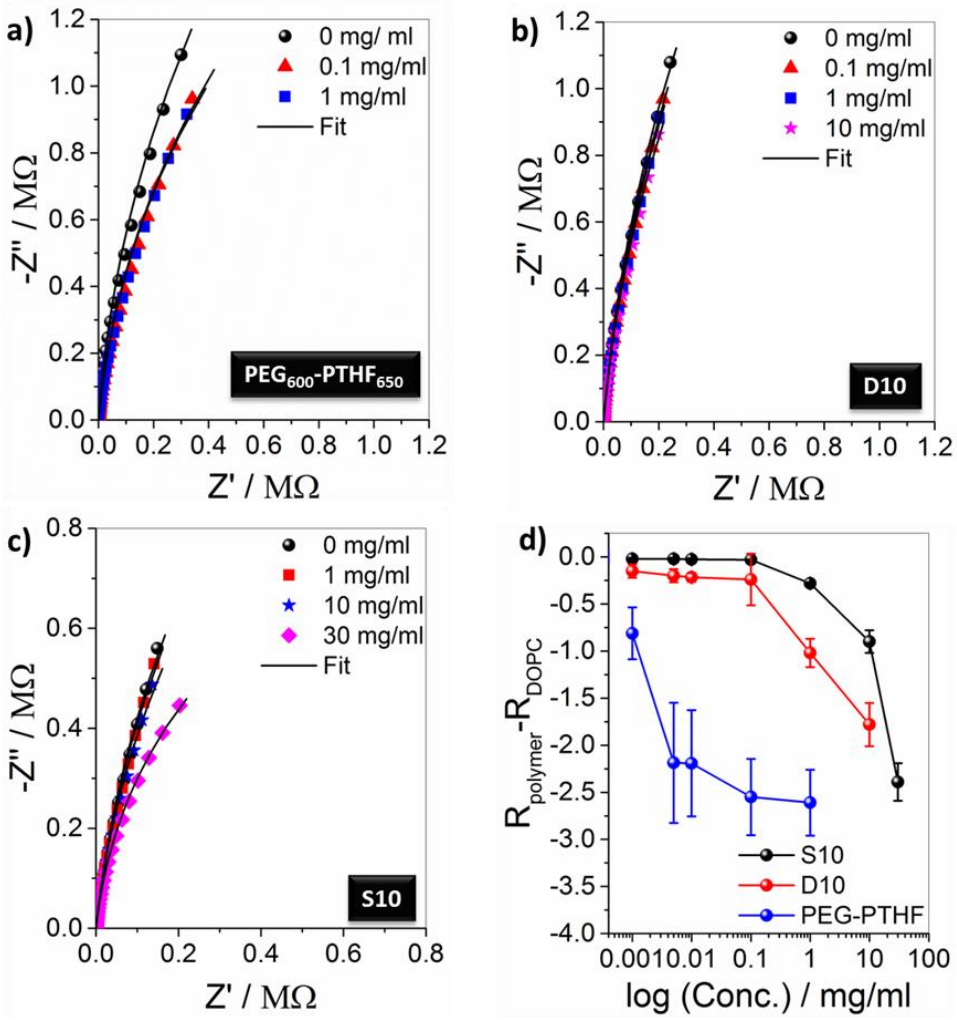

Figure 5.4. Representative Nyquist plots for DOPC lipid bilayers and different AIPs formed on a 1 cm diameter gold microcavity array electrode. Panels a,b,c correspond to EIS response for PEG_{600}-$PTHF_{650}$, D10 and S10 for different concentrations and solid line represents ECM model fit. The frequency range was 0.01 Hz to $1x10^5$ Hz. The glass cell was filled with PBS buffer and cavities are fully inserted into the buffer. The gold microcavities act as working electrode along with reference electrode (Ag/AgCl) and counter electrode (platinum flag). (d) The impact of the AIPs interaction with DOPC lipid bilayer is reflected as changes in bilayer resistivity (ΔR). The bilayer resistance was calculated from ECM fitting model and change in the resistivity for different concentration of AIPs with respect to untreated DOPC lipid bilayer were plotted against its concentration. Values shown are experimental means and standard error on mean.

Decreasing resistivity of the bilayer indicates that the permeability of the bilayer to ion/water is increasing. Thus, the very significant decrease in the bilayer resistivity of the film in contact with PEG_{600}-$PTHF_{650}$ above its cmc, indicates the bilayer is significantly permeabilized,

i.e. rendered leaky or porous by contact with this polymer. Taken together with the impact the PEG_{600}-$PTHF_{650}$ has on membrane fluidity it is evident that this AIP, above its cmc, has a very significant impact on the lateral packing of the lipid bilayer structure. The resistance decreases are accompanied by large increases in capacitance of the film indicating decreased membrane thickness.

In the case of the D10, the bilayer resistivity is also observed to decrease in contact with this AIP above its cmc and this change is accompanied by an increased in film capacitance. However, the changes are more modest observed for PEG_{600}-$PTHF_{650}$, noting that D10 did not measurably affect lateral fluidity of the membrane in FLCS measurements.

Similarly, below its cmc, S10 does not significantly impact on the bilayer resistivity or capacitance. However, above 1mg/ml, the bilayer resistance decreases but more gradually than for the other AIPs until 30 mg/ml concentration where the resistance changes match that observed for PEG_{600}-$PTHF_{650}$. Notably, unlike the other polymers, the S10 capacitance increases only marginally on contact with this AIP micelle. The EIS response correlates well with the FLCS data where no significant change to diffusivity in the bilayer was observed until 30 mg/ml for S10.

For each AIP, changes to the bilayer resistivity were most significant above their respective cmc's, with negligible interaction below cmc for both S10 and D10 and very weak interaction for PEG_{600}-$PTHF_{650}$. We hypothesize the differences in extent of membrane interaction arise from different surface activity of the AIPs. Based on resistance and capacitance data the extent of interaction follows the following trend: PEG_{600}-$PTHF_{650}$ > D10 > S10. The higher surface activity of an AIP, the more permeable membrane due to the higher affinity of macromolecules for membrane and, thus, AIP – membrane interactions.

The EIS data reflect changes to the film resistivity and capacitance at concentrations closely aligned with the reported cmcs for the polymers. Whereas changes to the diffusion coefficient of the labelled DOPE were observed invariably at concentrations well in excess of the cmc. This is attributed to the sensitivity of the EIS measurement and the fact that it interrogates directly the impact of the AIP on the membrane structure. Whereas FLCS is a more indirect measurement. As it studies the diffusion of a probe through the lipid membrane, it is likely that the impact of the AIP micelles does not affect the diffusion of the labelled lipid until they are above a concentration where probability of the probe meeting aggregate membrane associated micelle at the bilayer surface is sufficiently high within the time window of ACF collection.

Table 5.2. Change in resistivity of DOPC bilayer for different concentrations of AIPs compared to DOPC membrane alone. The resistance and capacitance values above cmc were highlighted in grey color.

[Conc.] (mg/ml)	**ΔR (MΩcm^2)**			**ΔC (μF/cm^2)**		
	PEG_{600}-$PTHF_{650}$	D10	S10	PEG_{600}-$PTHF_{650}$	D10	S10
0.001	-0.81± 0.27	-0.15± 0.07	-0.02 ± 0.01	0.25 ± 0.14	0.10 ± 0.05	0.03± 0.005
0.010	-2.19± 0.56	-0.2 ± 0.04	-0.02 ± 0.01	0.88 ± 0.45	0.22 ± 0.06	0.05± 0.008
0.100	-2.55± 0.80	-0.25± 0.27	-0.025 ± 0.005	1.57 ± 0.24	0.73 ± 0.25	0.054± 0.01
1.000	-2.38± 0.75	-1.02± 0.15	-0.28 ± 0.01	2.20 ± 0.3	1.2 ± 0.20	0.07± 0.01
10	-	-1.78± 0.15	-0.9± 0.12	-	1.57± 0.21	0.14± 0.03
30	-	-	-2.39± 0.23	-	-	0.16± 0.03

5.4.4. Incorporation of BODIPY in AIP micelles

To evaluate transfer of an encapsulated probe from the micellar AIPs to the bilayer, micellar BODIPY was prepared using a thin film method. In contrast to more typical direct aqueous solubilization, high encapsulation efficiencies are often reached in the thin film method, as both an amphiphilic AIP and the probe are initially dissolved in a common organic solvent. In

this method, following a mixing step, the solvent is removed, usually with heat and vacuum, to form a thin film on the flask walls. The resulting solid film of the probe and polymer can later be hydrated to form a micellar solution when desired. This is advantageous from shelf-life perspective. Aqueous micellar systems can eventually deteriorate, meaning that long-term storage in such a format is not always desirable. Also, the thin film hydration technique tends to produce micellar structures with probe loading, which may exceed that obtained under equilibrium conditions. In our study, acetone was used to create a solution of an AIP and BODIPY. It was selected as a good FLCS probe and also because, due to aggregation induced quenching, it is poorly emissive in aqueous solution but exhibits a high quantum yield in organic media or when associated with the membrane.[17]

Upon evaporation of the acetone in vacuum, the solid BODIPY/AIP matrix in a form of a thin film was hydrated with PBS to afford a clear, single-phase stock solution. The final AIP concentration in the stock solutions was 10 mg/mL.

The concentration of micellar BODIPY in the aqueous stock solutions was estimated using UV−vis spectroscopy. This method assumes that absorbance of the BODIPY dye is proportional to its concentration in solution. A linear calibration plot of the absorbance as a function of the BODIPY concentration was obtained first in the following manner: sets of 10 mg/mL micellar solutions for PEG_{600}-$PTHF_{650}$ containing known amounts of solubilized BODIPY were prepared and their UV−vis spectra were recorded (**Fig. 5.5A**). From the spectra, the height of a BODIPY adsorption peak at 531 nm was found out and plotted versus dye concentration (**Fig. 5.5B**).

At an AIP concentration of 10 mg/mL, micelles are formed in water, and the hydrophobic BODIPY is solubilized in the micellar interior. **Figure 5.6** shows UV-vis-spectra of BODIPY in the 10 mg/mL aqueous solutions of the AIPs. When BODIPY is solubilized by S10 in an aqueous

solution, significantly lower absorption intensity in comparison to AIPs D10 and PEG_{600}-$PTHF_{650}$ was observed (**Fig. 5.6**).

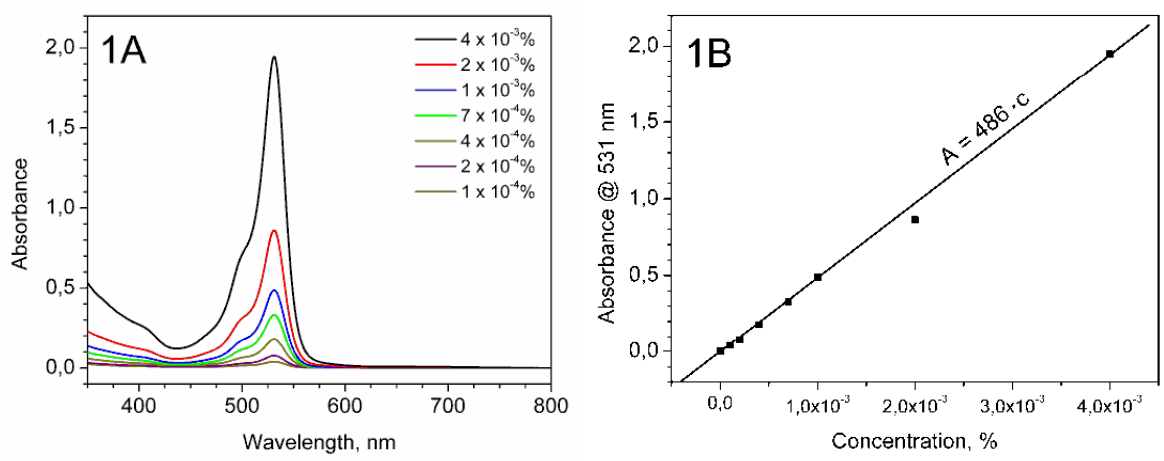

Figure 5.5. UV-vis-spectra of BODIPY at different concentrations in the 10 mg/mL aqueous solutions of PEG_{600}-$PTHF_{650}$ (A). The intensity a BODIPY adsorption peak at 531 nm in the 10 mg/mL aqueous solutions of PEG_{600}-$PTHF_{650}$ *vs.* BODIPY concentration (B).

Although the S10 chains did sequester the dye, a smaller number of hydrophobic molecules were accommodated. The latter effect can be explained by higher hydrophobicity of D10 and PEG_{600}-$PTHF_{650}$ in comparison to S10. The differences in HLB values also explain the marked difference in absorption intensity observed in BODIPY sequestration by D10 compared to PEG_{600}-$PTHF_{650}$. These data are consistent with our previous results on the Nile red and curcumin solubilization.[9,12]

As determined by the calibration method, the PEG_{600}-$PTHF_{650}$ micelles were loaded with 0.005%, D10 loaded with 0.0026%, and S10 loaded with 0.001% of BODIPY (the values represent the dye concentration in the entire solution). It should be noticed that all BODIPY molecules introduced into the PEG_{600}-$PTHF_{650}$ thin film were sequestered by the PEG_{600}-$PTHF_{650}$ micelles upon hydration.

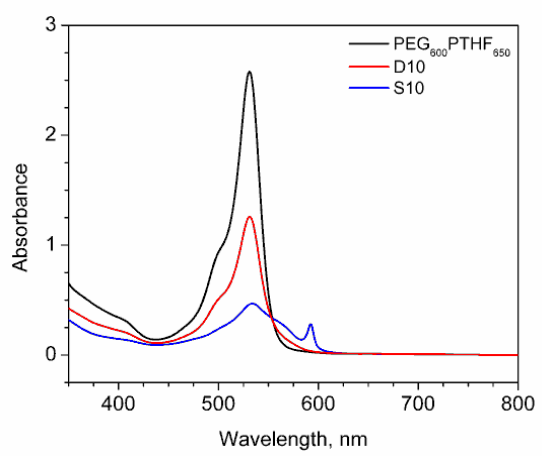

Figure 5.6. UV-vis-spectra of BODIPY in 10 mg/mL aqueous solutions of AIPs.

5.4.5. Interaction of BODIPY loaded micelles with DOPC lipid membrane

To evaluate the diffusion coefficients of the dye loaded micelles, 20 µL of BODIPY loaded micelle solution was placed on a coverslip and fluorescence fluctuations were measured for 150 seconds to generate autocorrelation functions. In the case of BODIPY loaded PEG_{600}-$PTHF_{650}$ micelles, homogenous fluctuations of fluorescence molecules were observed and on fitting the resulting ACF curves to a 3-dimensional diffusion model, *D* was obtained as 29 ± 11 $\mu m^2 s^{-1}$ (**Fig. 5.7**). Conversely, the fluorescence traces of BODIPY loaded D10 and S10 micelles showed evidence of dye aggregates with intermittent appearance of intense spikes in fluorescence intensity over the experimental window (**Fig. 5.8**). The data is comparable to that observed for free BODIPY in aqueous solution when there is presence of dye aggregates (Data not shown). Thus D was not obtained for individual micelles of D10 and S10.

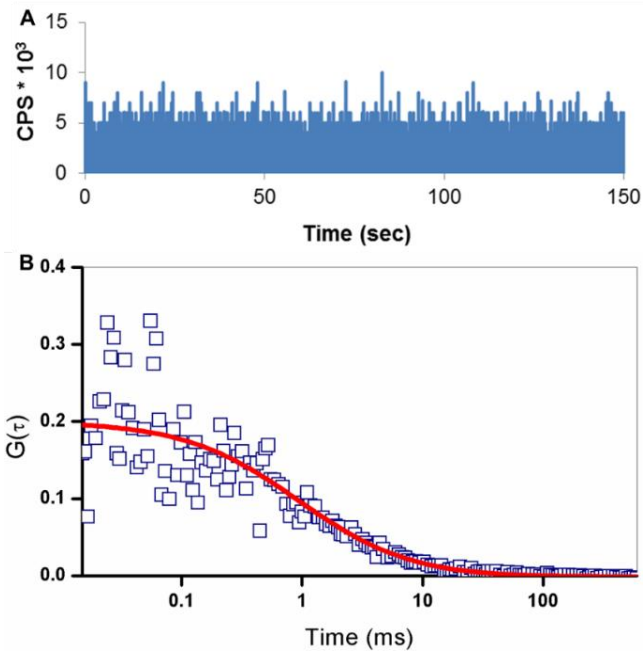

Figure 5.7. Fluorescence fluctuations of BODIPY loaded in PEG_{600}-$PTHF_{650}$ and corresponding ACF curve in solution. (A) fluorescence fluctuation of 10 ug/ml concentration of BODIPY encapsulated PEG_{600}-$PTHF_{650}$ and measured for 150 seconds. (B) Respective autocorrelation function curve in the solution.

Next, the BODIPY loaded AIP micellar solutions were introduced into the MSLB chamber and allowed to interact with the membrane for 15 minutes. The microcavities were then imaged using confocal fluorescence microscopy. **Figure 5.9** shows representative fluorescence images of DOPC membrane MSLBs in contact with AIP micelles. The bilayers are labelled with ATTO and the fluorescence of the ATTO probe in the DOPC membrane was homogenously distributed above aqueous filled cavities as expected for a suspended lipid bilayer. Some bright ring structures are observed in **Fig. 5.9** and these are attributed to cavities that failed to fill with aqueous solution and thus where free standing bilayer did not form. The ATTO and BODIPY probes in the membrane were excited by 640 nm and 532 nm pulsed lasers at the same time and imaged simultaneously using separate fluorescence channels.

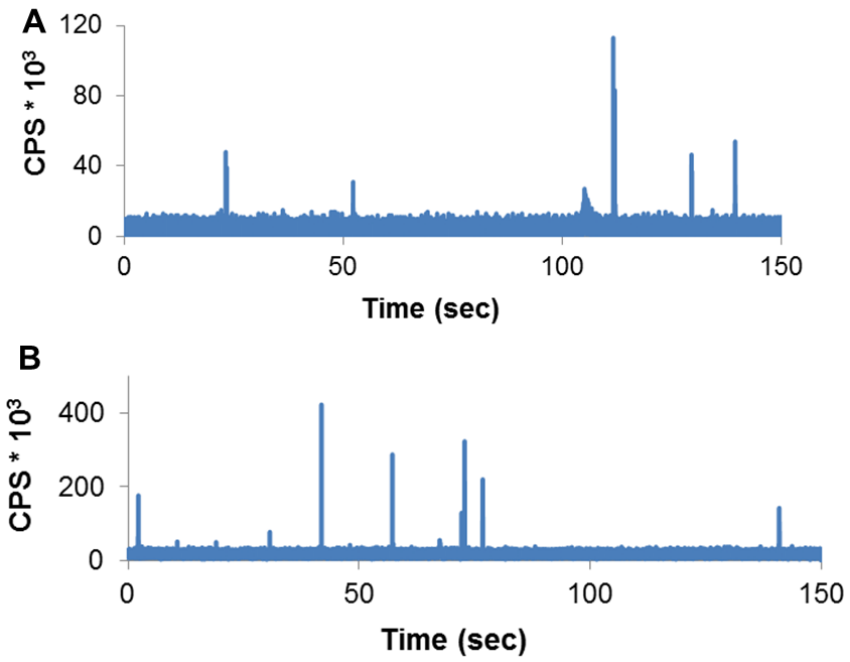

Figure 5.8. Representative fluorescence fluctuations of BODIPY encapsulated in D10 and S10 polymer micelles measured for 150 seconds. (A)100 µg/ml of D10 and (B) 1 mg/ml S10 polymer solution were made and concentrations were above their CMC values.

Uptake of BODIPY into the bilayer or aggregation of BODIPY containing micelles was clearly distinguishable, where it occurred, from the strong homogeneous fluorescence from this probe over the pores and this is evident in **Figure 5.9A** in the BODOPY fluorescence channel for the MSLBs post treatment with dye loaded PEG_{600}-$PTHF_{650}$ micelles. Aggregation of BODIPY dye or dye containing micelles on the membrane could be also readily distinguished.

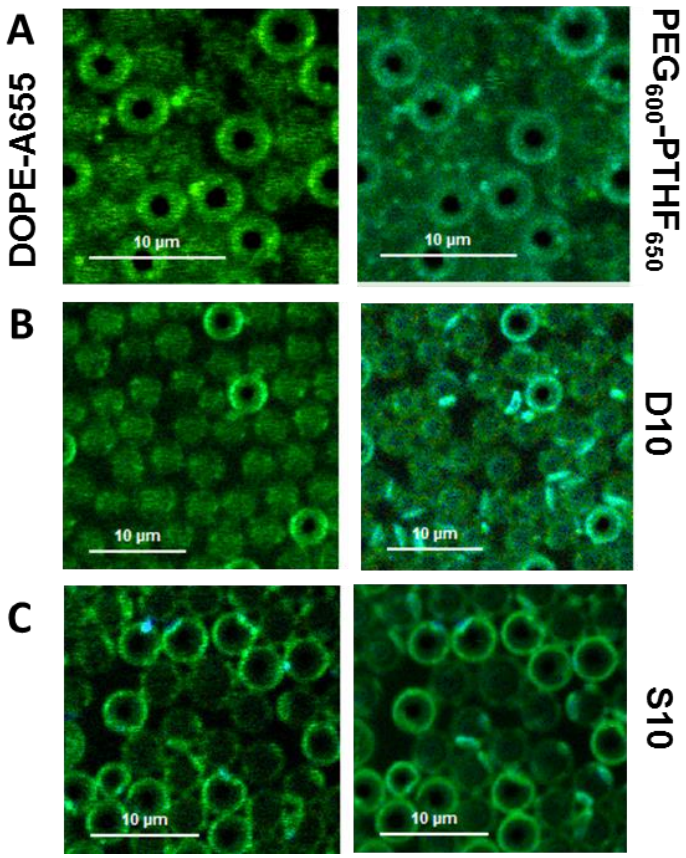

Figure 5.9. Confocal images of AIP micelles: (A) PEG_{600}-$PTHF_{650}$; (B) D10; (C) S10; interacting with DOPC membrane suspended across aqueous filled microcavity supported lipid bilayer. The ATTO and BODIPY probes in the membrane were excited by 640 nm and 532 nm pulsed laser at the same time and imaged simultaneously. The images on the left show the ATTO channel and the superimposed BODIPY and ATTO channels. The cavities were made from polystyrene spheres of diameter 4.61 µm. The polymer micelle solution was prepared at the concentration of 10 µg/ml for PEG_{600}-$PTHF_{650}$, 100 µg/ml for D10, 1000 µg/ml for S10, which was above the cmc and injected into the home-made microfluidic chamber and imaged the interaction of micelles with the membrane in real time. Fluorescent images show the presence of ATTO in DOPC membrane and BODIPY encapsulated polymer micelles above the cavities. The bright ring -like structures in the images correspond to unfilled cavities where bilayer failed to span.

Such aggregation was minimal in the case of PEG_{600}-$PTHF_{650}$ but is clearly evident in images of D10 micelles where there is relatively weak contribution from free BODIPY but extensive evidence of micelle aggregation at the bilayer interface (**Fig. 5.9B**). For S10 there is some evidence of aggregation and there is no evidence of BODIPY uptake by the bilayer (**Fig.**

5.9C). The weaker emission from the aggregates is likely because the S10 micelles of the inherently more weakly emissive because of lower probe loading.

Next, the lateral mobility of BODIPY was evaluated at the arrays following incubation of the dye loaded AIP micelles with the bilayer using FLCS. The cavities were imaged using confocal microscopy, then with the laser excitation oriented at the center of a bilayer suspended cavity the fluorescence fluctuations of ATTO and BODIPY encapsulated AIP micelles were recorded for 30 seconds. This experiment was repeated across the substrates and diffusion data were averaged across 25 and 30 micropores per substrate.

As expected, fluctuations of the lipid probe (DOPE-ATTO) were homogenous across all MSLBs in contact with the AIP micelles. Fluctuations from BODIPY loaded in PEG_{600}-$PTHF_{650}$ micelles in contact with the membrane surface (**Fig. 5.10A**) clearly show homogenous fluorescence for BODIPY, indicating that the probes were released near the hydrophobic core of the membrane. The diffusion value for the BODIPY released by PEG_{600}-$PTHF_{650}$ (**Fig. 5.10B**) and the ATTO label are tabulated in **Table 5.3**.

Diffusion coefficient *D* of BODIPY was evaluated as 7.7 ± 1.2 $\mu m^2 s^{-1}$ this value indicates the probes were released into the membrane core. The slow diffusion of BODIPY relative to ATTO in the DOPC membrane may indicate some aggregation of probe at the membrane is occurring. Although, the unlabeled micelle studies above showed that the diffusion coefficient of the ATTO probe is also reduced on contact with the PEG_{600}-$PTHF_{650}$ micelle, so the relatively slow BODIPY diffusion may be attributable to changes in viscosity of the membrane in contact with the micelles from PEG_{600}-$PTHF_{650}$ as the surface active AIP causes localized dissolution of the bilayer. The fluorescence lifetime of BODIPY in micelle in solution and in the membrane was determined as 1.51 ns.

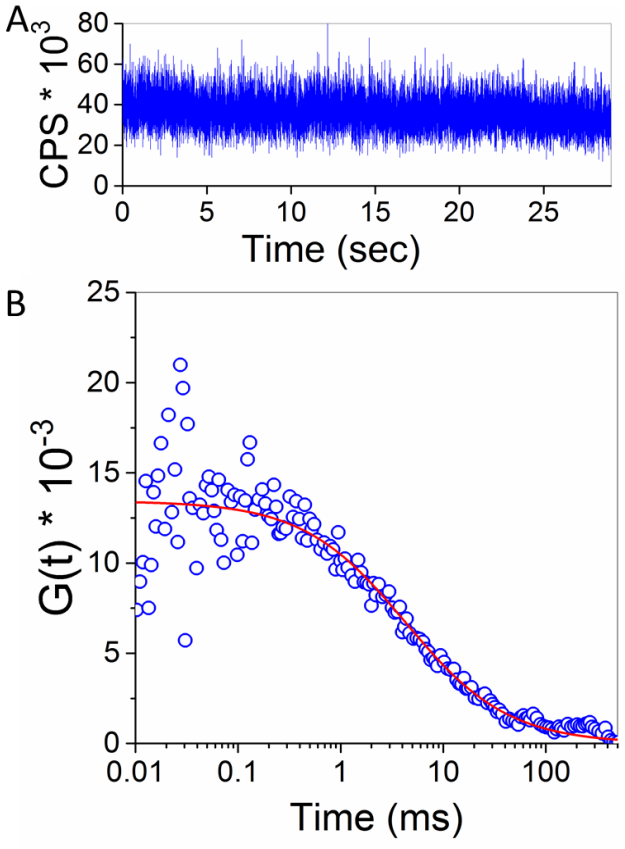

Figure 5.10. Representative Counts Per Second (CPS) and autocorrelation function (ACF) curve of BODIPY loaded PEG_{600}-$PTHF_{650}$, which interacts with DOPC supported lipid bilayer. (A) Fluorescence fluctuation of 10 µg/ml of dye loaded AIP micelle was allowed to interact with the membrane, (B) corresponding ACF curve of BODIPY incorporated in the membrane. The circles correspond to ACF curve while solid line is 2D-diffusion model fit.

Table 5.3. Calculated diffusion coefficient (D) of ATTO and BODIPY with PEG_{600}-$PTHF_{650}$ embedded in the membrane.

Conc (µg/ml)	BODIPY PEG_{600}-$PTHF_{650}$		DOPE-ATTO655	
	α	D_B **(µm²s⁻¹)**	α	D_L **(µm²s⁻¹)**
0			0.98 ± 0.05	10.60 ± 0.70
0.005	0.90 ± 0.10	7.7 ± 1.2	0.95 ± 0.04	10.10 ± 0.80
0.01	0.97 ± 0.10	7.4 ± 1.8	0.94 ± 0.06	9.22 ± 0.85

D_L: diffusion coefficient of ATTO, D_B: diffusion coefficient of BODIPY probe

For D10 and S10 AIP micelles in contact with the membrane, exponential decreases in fluorescence counts within 5 seconds of the FLCS collection was observed and counts were reduced by almost 25% after 30 seconds (**Fig. 5.11 and 5.12**) indicating that the BODIPY is bleaching. This indicates that the loaded D10 and S10 micelles are adsorbed at the bilayer but immobile or very slowly diffusing. (**Fig. 5.11B and 5.12B**). This is consistent with the imaging which indicates the micelles are aggregating at the membrane interface with relatively little release of BODIPY from the D10 and S10 micelles to the bilayer. These observations are in agreement with less expressed inversion observed in this study for S10 and, especially, D10 chains if compared to PEG_{600}-$PTHF_{650}$

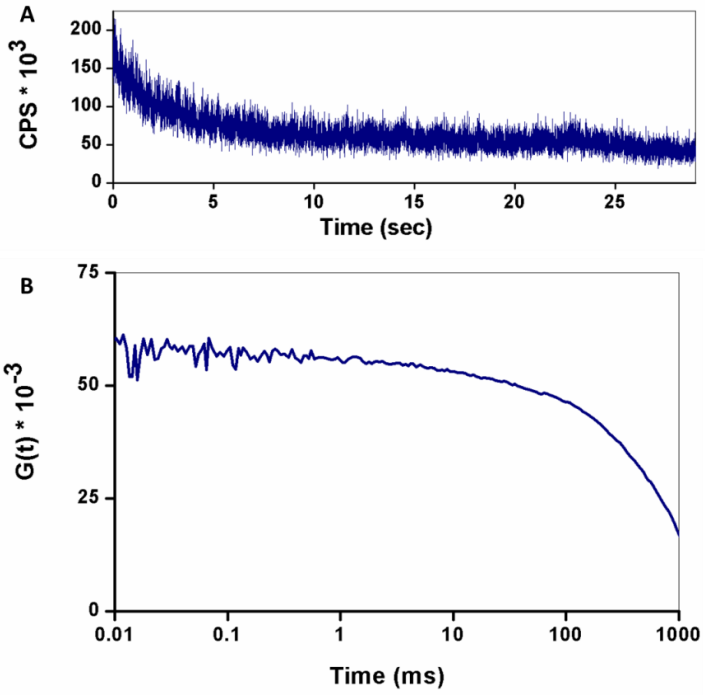

Figure 5.11. Representative, typical CPS and ACF curve of BODIPY loaded in D10 polymer micelles on DOPC membrane that was formed on the buffer filled microcavity supported lipid bilayer. (A) CPS of 100 ug/ml of dye loaded polymer micelle on membrane, (B) corresponding ACF curve of BODIPY incorporated in the membrane.

The PEG_{600}-$PTHF_{650}$ micelles loaded with BODIPY demonstrated the absorption and release of the probe into the DOPC membrane followed by the BODIPY lateral diffusion with D between 7 and 8 $\mu m^2 s^{-1}$. These data are consistent with the FLCS and EIS studies which showed that, among the studied AIPs, the PEG_{600}-$PTHF_{650}$ has the strongest impact on the DOPC membrane diffusivity and permeability, as well as most expressed conformational change. Hence, the capability of AIP micelles to deliver and release solubilized lipophilic cargo molecules into the DOPC membrane was demonstrated in this study.

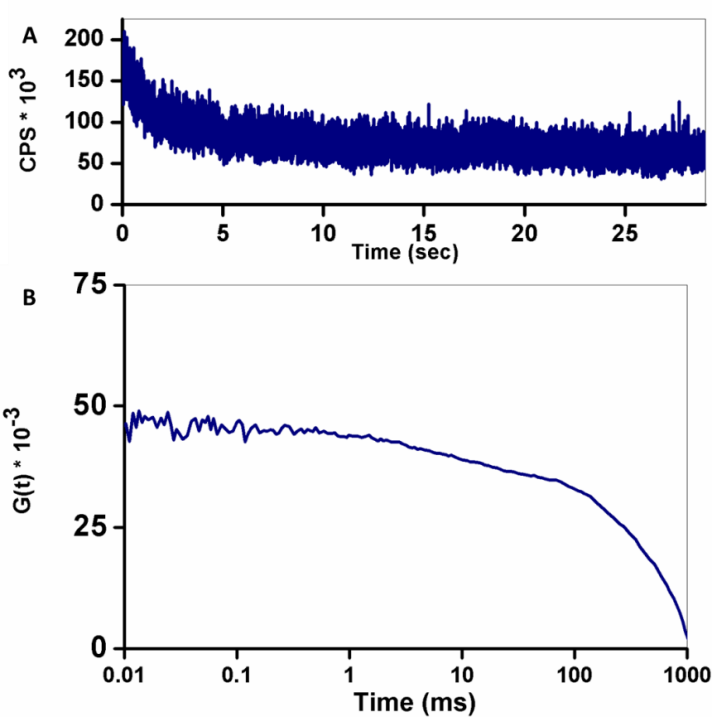

Figure 5.12. CPS and ACF curve of BODIPY encapsulated in S10 polymer micelles on DOPC lipid membrane spread across the buffer filled mSLB. (A) Fluorescence fluctuation of 1000 ug/ml of probe loaded polymer micelle on the membrane, (B) corresponding ACF curve of BODIPY incorporated in the membrane.

Upon contact with the membrane, conformational inversion of the AIP macromolecules is triggered in response to changing environmental polarity from the polar aqueous medium to the less polar membrane medium. The absorption and release of BODIPY into the DOPC membrane

are different for the investigated polymers and depend on the AIP properties (HLB, surface activity, and invertibility). Conversely, for D10 and S10 dye loaded micelles, BODIPY diffusion is low and indicates that it is remaining within the micelle without release to the bilayer, suggesting that the micelle is adsorbing but not inverting (or inverting slowly) in contact with the bilayer at the time-scale explored here.

The AIP micelles based on the most hydrophobic macromolecules; PEG_{600}-$PTHF_{650}$ (HLB = 13.8) showed strongest interaction with the membrane and delivered the hydrophobic fluorescent probe (BODIPY) to the core of the membrane. In case of AIP micelles of the more hydrophilic D10 (HLB = 14.4), whereas no changes were observed to lipid lateral mobility, modest changes in membrane resistivity were induced above the cmc. Similarly, for AIP micelles from the most hydrophilic S10 (HLB = 15.4), lateral mobility and membrane resistivity were decreased only for high concentration of this polymer. The BODIPY loaded D10 and S10 micelles, showed extensive aggregation at the lipid bilayer and from confocal imaging and FLCS data little or no BODIPY was released from these micelles to the bilayer, although the micelles appear to adsorb at the bilayer interface without delivering their payload to the membrane. The latter can be explained by the fact that being adsorbed on a membrane both S10 and D10 undergo much less expressed conformational changes (inversion) which are not sufficient for the efficient cargo delivery.

Overall, the obtained data indicate that two factors –affinity of invertible AIP macromolecules to lipid membrane and ability of macromolecules to undergo conformational changes (inversion) – are important for the AIPs (micellar assemblies from AIPs) to be promising in drug delivery applications. In this regard while AIP-membrane interactions (AIP affinity to membrane) are mainly responsible for the micelle–mediated cargo transport *to the membrane*, the

following macromolecular inversion *at the membrane* triggers release of cargo molecules from the micellar interior *into the membrane*.

As the obtained data show, AIP affinity to the lipid membrane can be related directly to the HLB of macromolecules, with the most hydrophobic PEG_{600}-$PTHF_{650}$ providing highest effective binding constant and very fast adsorption of micellar assemblies on membrane surface. For the efficient inversion (and, thus, cargo release) though, flexibility of macromolecular fragments is important to undergo conformational changes. From comparison of S10 and D10 data, one can see that the more surface active and more affine to the membrane D10, in fact, is more immobile at the membrane (less invertible), due to the longer less flexible hydrophobic fragments of dodecanedioic acid, packed in the micellar core. The latter complicates release of payload from the micellar interior.

5.5. Conclusions

In this study, micellar assemblies from three AIPs with different hydrophilic-lipophilic balance (ratio of hydrophilic and hydrophobic fragments in macromolecular chain) were put in contact with microcavity supported DOPC lipid membrane and the impact of the AIP micellar assemblies on membrane diffusivity and permeability were measured using Fluorescence lifetime correlation spectroscopy and Electrochemical Impedance Spectroscopy.

The AIP micelles, based on the most hydrophobic macromolecule; PEG_{600}-$PTHF_{650}$, showed strongest interaction with the membrane, above its cmc, across the three polymers explored and released a hydrophobic fluorescent probe (BODIPY) encapsulated in the micelle to the core of the lipid membrane.

From FLCS, the lateral mobility of the DOPC bilayer was significantly reduced in the presence of micellar assemblies of the most hydrophobic polymer PEG_{600}-$PTHF_{650}$ and to a lesser

degree by S10 suggesting increases to membrane viscosity attributed to adsorption of micelles at the bilayer interface. In the case of D10 however, there was no measurable change to the mobility of the lipid bilayer even at concentrations many times above D10 cmc. EIS studies reflected a strong decrease in DOPC membrane resistivity on contact with PEG_{600}-$PTHF_{650}$ micellar assemblies consistent with increased permeability of the bilayer, whereas more modest decreases to membrane resistance were induced by D10 with no change to electrochemical impedance observed for S10 except at its highest concentration. Overall, the data indicates that PEG_{600}-$PTHF_{650}$ micellar assemblies interact intimately with the bilayer decreasing membrane diffusivity whilst increasing permeability, but effects were much weaker for the more hydrophilic AIP micelles. Consistent with this data, micellar assemblies formed from PEG_{600}-$PTHF_{650}$ and loaded with BODIPY probes were demonstrated from fluorescence microscopy to adsorb at, and release BODIPY into, the DOPC membrane. The released BODIPY then diffuses laterally after release with D of between 7 and 8 $\mu m^2 s^{-1}$ consistent with bilayer lateral diffusion coefficient when measured in contact with the micelle. Our data indicate that PEG_{600}-$PTHF_{650}$ micelles undergo inversion and release of cargo into the bilayer. Whereas for D10 and S10, there was no evidence for dye-cargo release from the assemblies, rather the AIP micelles appeared to adsorb at the membrane interface where they were immobile (where inversion does not occur or occurs slowly).

This is the first report on the interaction of AIPs with a model lipid membrane and it provides useful new insights that should facilitate the design of AIPs for cell membrane cargo transport and delivery.

5.6. References

(1) O.V. Borisov, A. Halperin, Micelles of Polysoaps: The Role of Bridging Interactions, *Macromolecules.* **1996**. *29*, 2612–2617. doi:10.1021/ma951565w

(2) A. Kohut, A. Voronov, Hierarchical Micellar Structures from Amphiphilic Invertible Polyesters: 1H NMR Spectroscopic Study, *Langmuir.* **2009.** *25,* 4356–4360. doi:10.1021/la900700u.

(3) M. Antonietti, Nanostructured materials: Self-organization of functional polymers, *Nat. Mater.* **2003.** *2,* 9–10. doi:10.1038/nmat791.

(4) A. Kohut, X. Dai, D. Pinnick, D.L. Schulz, A. Voronov, "Host–guest" interaction between cyclohexasilane and amphiphilic invertible macromolecules, *Soft Matter.* **2011.** *7,* 3717–3720. doi:10.1039/C0SM01337D.

(5) A. Kohut, O. Kudina, X. Dai, D.L. Schulz, A. Voronov, Host–Guest Interactions between a Nonmicellized Amphiphilic Invertible Polymer and Insoluble Cyclohexasilane in Acetonitrile, *Langmuir*. **2011.** *27,* 10356–10359. doi:10.1021/la201883f.

(6) O. Kudina, A. Kohut, I. Tarnavchyk, I. Hevus, A. Voronov, Solvent-Responsive Self-Assembly of Amphiphilic Invertible Polymers Determined with SANS, *Langmuir*. **2014.** *30,* 3310–3318. doi:10.1021/la404939w.

(8) I. Hevus, A. Kohut, A. Voronov, Amphiphilic Invertible Polyurethanes: Synthesis and Properties, *Macromolecules.* **2010.** *43,* 7488–7494. doi:10.1021/ma101175k.

(9) I. Hevus, A. Modgil, J. Daniels, A. Kohut, C. Sun, S. Stafslien, A. Voronov, Invertible Micellar Polymer Assemblies for Delivery of Poorly Water-Soluble Drugs, *Biomacromolecules.* **2012**. *13,* 2537–2545. doi:10.1021/bm3007924.

(10) A. Maran, M.J. Yaszemski, A. Kohut, A. Voronov, Curcumin and Osteosarcoma: Can Invertible Polymeric Micelles Help?, *Materials.* **2016**. *9,* 520. doi:10.3390/ma9070520.

(11) A. Voronov, S. Vasylyev, A. Kohut, W. Peukert, Surface activity of new invertible amphiphilic polyesters based on poly(ethylene glycol) and aliphatic dicarboxylic acids, *J. Colloid Interface Sci.* **2008.** *323,* 379–385. doi:10.1016/j.jcis.2008.04.053.

(12) I. Hevus, A. Kohut, A. Voronov, Interfacial micellar phase transfer using amphiphilic invertible polymers, *Polym. Chem.* **2011**. *2*, 2767–2770. doi:10.1039/C1PY00399B.

(13) I. Hevus, A. Kohut, A. Voronov, Micellar assemblies from amphiphilic polyurethanes for size-controlled synthesis of silver nanoparticles dispersible both in polar and nonpolar media, *J. Nanoparticle Res.* **2012**. *14,* 820. doi:10.1007/s11051-012-0820-x.

(14) I. Hevus, A. Voronov, M.J. Yaszemski, A. Maran, A. Kohut, S. Voronov, Chapter 14 - Anticancer efficiency of curcumin-loaded invertible polymer micellar nanoassemblies, in: A. Ficai, A.M. Grumezescu (Eds.), Nanostructures Cancer Ther., Elsevier, **2017**: pp. 351–382. doi:10.1016/B978-0-323-46144-3.00014-3.

(15) O. Kudina, K.L. Shogren, C.T. Gustafson, M.J. Yaszemski, A. Maran, A. Voronov, Invertible micellar polymer nanoassemblies target bone tumor cells but not normal osteoblast cells, *Future Sci. OA.* **2015**. *1*. doi:10.4155/fso.15.14.

(16) L. Sieburg, A. Kohut, V. Kislenko, A. Voronov, Amphiphilic invertible polymers for adsolubilization on hydrophilic and hydrophobized silica nanoparticles, *J. Colloid Interface Sci.* **2010.** *351,* 116–121. doi:10.1016/j.jcis.2010.07.061.

(17) A. Martin, R.D. Moriarty, C. Long, R.J. Forster, T.E. Keyes, Inside Cover: Naphthyridyl-Substituted 4,4-Difluoro-4-bora-3a,4a-diaza-s-indacene (BODIPY) Luminophores: Photophysics and Application as Molecular Imaging Probes in Live Cells (*Asian J. Org. Chem.* **2013.** *9*), *Asian J. Org. Chem.* **2013.** *2,* 694–694. doi:10.1002/ajoc.201390025.

(18) B. Jose, C.T. Mallon, R.J. Forster, C. Blackledge, T.E. Keyes, Lipid bilayer assembly at a gold nanocavity array, *Chem. Commun.* **2011.** *47,* 12530–12532. doi:10.1039/C1CC15709D.

(19) H. Basit, V. Gaul, S. Maher, R.J. Forster, T.E. Keyes, Aqueous-filled polymer microcavity arrays: versatile & stable lipid bilayer platforms offering high lateral mobility to incorporated membrane proteins, *Analyst.* **2015.** *140,* 3012–3018. doi:10.1039/C4AN02317J.

(20) B. Jose, R. Steffen, U. Neugebauer, E. Sheridan, R. Marthi, R.J. Forster, T.E. Keyes, Emission enhancement within gold spherical nanocavity arrays, *Phys. Chem. Chem. Phys.* **2009.** *11,* 10923–10933. doi:10.1039/B908385E.

(21) C.T. Mallon, C. Zuliani, T.E. Keyes, R.J. Forster, Single nanocavity electrodes: fabrication, electrochemical and photonic properties, *Chem. Commun.* **2010.** *46,* 7109–7111. doi:10.1039/C0CC00418A.

(22) M. Böhmer, M. Wahl, H.-J. Rahn, R. Erdmann, J. Enderlein, Time-resolved fluorescence correlation spectroscopy, *Chem. Phys. Lett.* **2002.** *353,* 439–445. doi:10.1016/S0009-2614(02)00044-1.

(23) A. Benda, V. Fagul'ová, A. Deyneka, J. Enderlein, M. Hof, Fluorescence Lifetime Correlation Spectroscopy Combined with Lifetime Tuning: New Perspectives in Supported Phospholipid Bilayer Research, *Langmuir.* **2006.** *22,* 9580–9585. doi:10.1021/la061573d.

(24) H. Basit, S.G. Lopez, T.E. Keyes, Fluorescence correlation and lifetime correlation spectroscopy applied to the study of supported lipid bilayer models of the cell membrane, *Methods.* **2014.** *68,* 286–299. doi:10.1016/j.ymeth.2014.02.005.

(25) T. Dertinger, V. Pacheco, I. von der Hocht, R. Hartmann, I. Gregor, J. Enderlein, Two-Focus Fluorescence Correlation Spectroscopy: A New Tool for Accurate and Absolute Diffusion Measurements, *ChemPhysChem.* **2007.** *8,* 433–443. doi:10.1002/cphc.200600638.

(26) E. Haustein, P. Schwille, Fluorescence Correlation Spectroscopy: Novel Variations of an Established Technique, A*nnu. Rev. Biophys. Biomol. Struct.* **2007.** *36,* 151–169. doi:10.1146/annurev.biophys.36.040306.132612.

(27) G. Guigas, M. Weiss, Sampling the Cell with Anomalous Diffusion—The Discovery of Slowness, *Biophys. J.* **2008.** *94,* 90–94. doi:10.1529/biophysj.107.117044.

(28) P. Kapusta, R. Macháň, A. Benda, M. Hof, Fluorescence Lifetime Correlation Spectroscopy (FLCS): Concepts, Applications and Outlook, *Int. J. Mol. Sci.* **2012.** *13,* 12890–12910. doi:10.3390/ijms131012890.

(29) S. Maher, H. Basit, R.J. Forster, T.E. Keyes, Micron dimensioned cavity array supported lipid bilayers for the electrochemical investigation of ionophore activity, *Bioelectrochemistry.* **2016.** *112,* 16–23. doi:10.1016/j.bioelechem.2016.07.002.

(30) S. Ramadurai, M. Werner, N.K.H. Slater, A. Martin, V.A. Baulin, T.E. Keyes, Dynamic studies of the interaction of a pH responsive, amphiphilic polymer with a DOPC lipid membrane, *Soft Matter.* **2017.** *13,* 3690–3700. doi:10.1039/C6SM02645A.

(31) L. Li, M. Dwivedi, N. Erwin, S. Möbitz, P. Nussbaumer, R. Winter, Interaction of KRas4B protein with C6-ceramide containing lipid model membranes, *Biochim. Biophys. Acta BBA - Biomembr.* **2018.** *1860,* 1008–1014. doi:10.1016/j.bbamem.2018.01.016.

CHAPTER 6. AN AMPHIPHILIC INVERTIBLE POLYMER INCORPORATED M2E-HA2-HA1 PEPTIDE VACCINE PROTECTS AGAINST INFLUENZA A (H1N1) PDM09 VIRAL CHALLENGE IN PIGS[*]

Short title: Improved delivery of epitope-based peptide vaccines for pigs

6.1. Abstract

Influenza A viruses (IAVs) are a group of genetically diverse and economically important zoonotic pathogens. Despite decades of research, effective and broadly protective vaccines are yet to be developed. Recent breakthroughs in epitope-based immunization for influenza viruses identify conserved regions of the HA2 and M2e proteins as capable of inducing broad protection against multiple influenza strains. The M2e and HA2 peptides have been evaluated in mice but not as a combination in pigs, which play an important role in the transmission and evolution of IAV. However, peptides are inherently weak immunogens; and effective delivery of peptide antigens is challenging. To enhance the delivery and immunogenicity of peptide-based vaccines, the conserved M2e and HA2 and a strain-specific HA1 epitope of Influenza A (H1N1) pdm09 were expressed as a chain in a bacterial expression system and entrapped in a novel biodegradable

[*] The material in this chapter was co-authored by Oksana Zholobko, Gagandeep Singh, Angela Pillatzki, Brett Webb, Eric Nelson, Sheela Ramamoorthy, and Andriy Voronov. Oksana Zholobko had the primary responsibilities of synthesizing and characterizing polymers and preparing polymer-peptide micellar assemblies. Oksana Zholobko was also charged with characterizing the polymer-peptide micellar assemblies by ^{1}H NMR Spectroscopy. Gagandeep Singh helped Oksana Zholobko perform and analyze results of in-vitro peptide delivery experiments. Angela Pillatzki and Eric Nelson helped Oksana Zholobko and Gagandeep Singh perform the in-vivo experiments using pigs. Oksana Zholobko was involved in drafting and revising all versions of this chapter. Sheela Ramamoorthy and Andriy Voronov helped explain and describe the results obtained by Oksana Zholobko and Gagandeep Singh. Published article can be found at https://doi.org/10.1016/j.vaccine.2019.06.030.

amphiphilic invertible polymer, made from polyethylene glycol (PEG, molecular weight 600 g/mol) and polytetrahydrofuran (PTHF, molecular weight 650 g/mol), $PEG_{600}PTHF_{650}$. Piglets vaccinated with polymeric peptide vaccine mounted significantly stronger antibody responses against the peptide construct when compared to piglets immunized with the multi-epitope peptide alone. When vaccinated pigs were challenged with Influenza A (H1N1) pdm09, viral shedding in nasal secretions and lung lesion scores were significantly reduced when compared to the unvaccinated controls and pigs vaccinated with the peptide alone at six days post-challenge. Thus, the combination of the $PEG_{600}PTHF_{650}$ polymer and trimeric peptide construct enhanced delivery of the peptide antigen, acted as an adjuvant in stimulating strong antibody responses, and induced protective immunity in vaccinated pigs.

6.2. Introduction

Influenza A viruses (IAV) of the *Orthomyxoviridae* family are important zoonotic pathogens. Genetic and antigenic variation associated with IAV renders the succesful development of broadly-protective human and swine vaccines against IAV, a long-standing challenge. Pigs serve as "mixing vessels" for human and avian influenza viruses and support the emergence of new influenza virus strains [1, 2]. Thus, vaccines that provide effective and broad protection against several strains of influenza virus in pigs would be very valuable in controlling the emergence of new strains.

Recently, vaccines containing certain conserved antigenic epitopes of influenza viruses were shown to elicit broad protection against a number of genetically diverse strains in mouse models [3-12]. The extracellular N-terminal domain of the M2 protein (M2e) is a 23 amino acid peptide which is highly conserved in all influenza A viruses [13]. M2e- based peptide vaccines were shown to provide heterogenetic immunity against IAV in mice, but were not as effective in

swine models [10, 14, 15]. Similarly, the fusion peptide located in the HA2 protein is highly conserved among the different influenza virus strains [13, 16, 17] and provided broad protection in mice, but has not been tested in swine [18, 19]. Nor has a combination of the HA2 and M2e peptides been tested in pigs [3-12]. In this study, we test the hypothesis that a polypeptide encoding a combination of the M2e and HA2 conserved epitopes with one type specific epitope would be effective in preventing IAV infection in pigs [13].

Highly specific, small peptides are weak immunogens and vulnerable to degradation [20], necessitating the development of improved systems for peptide vaccine delivery. Polymers are well-established as substances that can enhance vaccine delivery, reduce dosage, and act as adjuvants, to broaden vaccine-induced immune protection. In addition, self-assembled polymeric architectures can increase the duration of immunity due to slow and sustained release of the antigen over time [21-23]. Amphiphilic polymers which enable customizing of peptide antigen delivery by varying the macromolecular structure and also act as adjuvants provide significant value to the development of peptide vaccines [24]. We have previously synthesized a library of amphiphilic invertible polymers (AIPs) which self-assemble into polymeric micelles as AIP concentration increases, both in polar and nonpolar solvents, and can rapidly switch their conformation in response to changes in the environmental polarity, thus facilitating the micellar inversion [25, 26]. The AIP conformational inversion is a promising tool for rapid and controlled self-assembly in applications that require simultaneous utility in polar and nonpolar media, e.g., in drug delivery systems. In our previous studies, the incorporation of two different peptides into micellar assemblies of AIP, made from polyethylene glycol (PEG, molecular weight 600 g/mol) and polytetrahydrofuran (PTHF, molecular weight 650 g/mol), $PEG_{600}PTHF_{650,}$ were characterized

and described in detail, as well as micellar inversion of this AIP loaded with peptides was demonstrated.

In this study, the three selected influenza A virus epitopes described above (conserved M2e, HA2, and type-specific HA1) were expressed as a chain in a bacterial expression system and incorporated into the $PEG_{600}PTHF_{650}$ micellar assemblies. The efficacy of the AIP micellar assemblies as a peptide antigen delivery system was evaluated in vitro and in pigs. The data presented below demonstrates that the $PEG_{600}PTHF_{650}$ micellar assemblies are effective in delivering the peptide cargo to cells, and act as an adjuvant in stimulating strong antibody responses against the delivered antigen in vaccinated pigs.

6.3. Experimental

All experiments described below were carried out in compliance with the Institutional Biosafety Committee (IBC) and Institutional Animal Care and Use Committee (IACUC) regulations of North Dakota State University (NDSU) and South Dakota State University (SDSU).

6.3.1. Cells and viruses

To prepare the virus stock culture for both the challenge of vaccinated pigs and hemagglutination inhibition (HI) assay, Influenza A (H1N1) pdm09 virus was cultured using Madin-Darby Canine Kidney (MDCK) cells as previously described [29]. After 48h of incubation, virus particles were harvested by three freeze-thaw cycles, followed by clarification at 10,000xg for 10 mins at 4°C to remove cellular debris. The titer was assessed using the tissue culture infectious dose 50% [$TCID_{50}$] assay and the Reed–Muench formula [30].

6.3.2. Preparation of the peptide antigen

The vaccine antigen was prepared using three well-characterized antigenic IAV peptides, fused by cloning, and bacterially expressed as a single peptide with the sequence

MGSSHHHHHHSSGLVPRGSHMASMTGGQQMGRGSSLLTEVETPTRSEWECRCSDSSGS GSGSRGLFGAIAGFIEGGWGGGGSGGGGSATGLRNIPSIQSRLEHHHHHH. The coding sequence for the previously characterized conserved peptides HA2 and M2e [31, 32] and a strain-specific HA1 epitope [33], were commercially synthesized (Integrated DNA Technologies, USA) as a chain with glycine-serine linkers and BamHI and NcoI restriction sites on the ends. The synthesized DNA was inserted into the pET28a (+) (MilliporeSigma, USA) bacterial protein expression vector. The expressed recombinant peptide was purified by using Ni-NTA affinity chromatography under native conditions and characterized by a western blot using an anti-M2e peptide-specific monoclonal antibody (**Fig. 6.1**). The purified M2e-HA1-HA2 peptide was dissolved in dimethyl sulfoxide (DMSO) and stored in aliquots at -80^{o}C until further use.

Figure 6.1. Western blot image of the purified peptide. Ni-NTA purified M2e-HA1-HA2 peptide construct was subject to western blot using a M2e peptide-specific monoclonal antibody. Left lane showing the 11KDa M2e-HA1-HA2 peptide and the right lane showing the molecular weight ladder.

6.3.3. Amphiphilic invertible polymer (AIP) synthesis

The AIP, $PEG_{600}PTHF_{650}$, was synthesized as previously reported from PEG (molecular weight 600 g/mol) ,and PTHF (molecular weight 650 g/mol) using polycondensation reaction [26,

34]. Chemical composition of $PEG_{600}PTHF_{650}$ was confirmed by FTIR- and ^{1}H NMR spectroscopy, weight and number average molecular weights and the corresponding polydispersity index of the AIP was measured using gel permeation chromatography (GPC) (data not shown).

6.3.4. Cellular cytotoxicity of $PEG_{600}PTHF_{650}$ micellar assemblies

To ensure the $PEG_{600}PTHF_{650}$ is not toxic to cells, cytotoxicity of polymer micellar assemblies was assessed in vitro using the MTT (3-(4,5-dimethylthiazol-2-yl) Tr-2,5-diphenyltetrazolium- bromide) assay [35]. Micellar assemblies were prepared using different concentrations of $PEG_{600}PTHF_{650}$ (0.05, 0.2, 0.5, 0.75 and 1.0 w/v%) by the thin film technique using DMSO as solvent [27]. One hundred µl/well of each prepared solution was added into 96 well cell culture plates (VWR, USA) containing monolayers of Vero cells and incubated for 8h at 37ºC in a CO_2 incubator. After incubation, the solution from the wells was removed and the wells were washed three times with Hank's balanced salt solution (HBSS). The MTT was dissolved to 0.5mg/ml in sterile PBS, and 100µl was added to each well. Plates were incubated in a CO_2 incubator for 4h to reduce MTT into formazan. The supernatant from each well was carefully removed by aspiration without disturbing the cells. To solubilize the intracellular formazan, 100µl of DMSO was added to each well, mixed well by vigorous pipetting, and incubated for 5 mins. Plates were read at 570 nm in microplate reader.

6.3.5. Interaction between $PEG_{600}PTHF_{650}$ micellar assemblies and M2e-HA1-HA2 peptide

To investigate the interaction between $PEG_{600}PTHF_{650}$ micellar assemblies and M2e-HA1-HA2 peptide, ^{1}H NMR spectra were recorded on an AVANCE III HDTM 400 high-performance digital NMR spectrometer at 400MHz and 22.5°C. Proton spectra were collected for 0.5 w/v% PEG_{600}-$PTHF_{650}$ or polymer-peptide micellar assemblies containing 0.005 w/v% peptide added to 0.5 w/v% $PEG_{600}PTHF_{650}$ formed in deuterated water by thin film technique. The spectra were

obtained for polymer samples with or without the peptide and referenced to a 3-(Trimethylsilyl) propionic-2,2,3,3-d4 acid sodium salt (TMSP) signal as an internal standard.

6.3.6. Relative antigen loading capacity

The peptide loading capacity of the $PEG_{600}PTHF_{650}$ micellar assemblies was assessed by a whole cell enzyme-linked immunosorbent assay (ELISA), capable of detecting intracellular peptide. Polymer-peptide micellar assemblies were prepared using different concentrations of $PEG_{600}PTHF_{650}$ (0.05, 0.2, 0.5, 0.75, and 1.0 w/v%) and a constant M2e-HA1-HA2 peptide concentration of 0.5 µg/µl. One hundred µl/well of prepared assemblies were added into 96 well cell culture plates (VWR, USA) containing a monolayer of Vero cells, and incubated for 8h at 37ºC in a CO_2 incubator. The peptide alone or wells with no treatment were used as controls. After 8h incubation, the solution from wells was removed, and wells were washed three times with phosphate buffered saline with tween (PBST). To each well, 100µl of anti-M2e monoclonal primary antibody diluted 1:100 in blocking buffer (PBST +2% Bovine serum albumin, BSA) was added and incubated for 1h at 37ºC with 5% CO_2 followed by washing. 100µl of HRPO conjugated anti-mouse IgG secondary antibody (KPL, USA) was added and incubated for 1h at 37ºC with 5% CO_2. After washing, the reaction was developed with 3,3′,5,5′-tetramethylbenzidine substrate (TMB) (KPL, USA) and stopped after 15 minutes with 1M Hydrochloric acid. The optical density values were read at 450 nm using a microplate reader (BioTek Instruments, Winooski, VT).

6.3.7. In-vitro peptide delivery by Immuno-Fluorescence Assay (IFA)

The effectiveness of the $PEG_{600}PTHF_{650}$ micelles in delivering the M2e-HA2-HA1 peptide into the cells was observed by an immunofluorescence (IFA) assay. Polymer-peptide assemblies were prepared using 1w/v% of $PEG_{600}PTHF_{650}$ and 0.5 µg/µl M2e-HA2-HA1. 100 µl/well of prepared solution were added into an 8-well Nunc® Lab-Tek™ chamber slide system containing

a Vero cell monlayer and incubated for 1, 2, 4, and 8h at 37ºC with 5% CO_2. Wells with no treatment or peptide alone were used as controls. After incubation, the solution was aspirated from the wells and wells were washed three times with HBSS. To detect intracellular antigen, cells were fixed using chilled acetone: methanol (1:1). Following overnight fixation, the chamber slides were washed three times using PBST and 100 µl of 1:100 anti-M2e monoclonal antibody diluted in blocking buffer was added to each well,incubated at 37ºC for 1h and washed with PBST. 100 µl of 1:500 anti-mouse IgG fluorescein-conjugated secondary antibody (KPL, USA) was added to each well and incubated at 37ºC for 1h. Washed slides were mounted with 50% glycerol, followed by fluorescent microscopic examination (**Fig 6.4**).

6.3.8. Vaccine formulation

Twenty-four, 3-week old, SIV negative piglets of both sexes were assigned to four groups as follows: Group I – Unvaccinated control (N=7), Group II –$PEG_{600}PTHF_{650}$/M2e-HA1-HA2 peptide micelles (SIV-VAC) (N=7), Group III – M2e-HA1-HA2 peptide only (N=5) or Group IV-$PEG_{600}PTHF_{650}$ polymer assemblies only (N=5). For each vaccine dose, 0.8 ml of M2e-HA1-HA2 peptide (1 mg/ml) dissolved in DMSO was added to a 30ml Pyrex glass vial containing 40mg of $PEG_{600}PTHF_{650}$ and mixed well by vortexing. A thin film was prepared and subsequently hydrated with 4ml of DMEM to form $PEG_{600}PTHF_{650}$/ M2e-HA1-HA2 micellar assemblies. For each animal in the M2e-HA1-HA2 peptide control group, a thin film was obtained from 0.8 ml of M2e-HA1-HA2 peptide (1mg/ml) dissolved in DMSO and hydrated with 4ml of DMEM to prepare the M2e-HA1-HA2 peptide solution. Similarly, for each animal in the $PEG_{600}PTHF_{650}$ control group, a thin film was obtained from 40mg of $PEG_{600}PTHF_{650}$ dissolved in DMSO hydrated with 4ml of DMEM to prepare 1 w/v% of the $PEG_{600}PTHF_{650}$ solution. Therefore, the effective vaccine dose

for each piglet was 0.8mg (0.2 µg/µl) of M2e-HA1-HA2 peptide antigen and 1 w/v% of $PEG_{600}PTHF_{650}$ polymer per dose.

6.3.9. Swine immunization and challenge

At the day of vaccination (DPV 0), piglets in each group were treated with 4ml of innocula (2ml intransal and 2ml subcutaneous) as described above. At the second and third week post-vaccination (DPV 14 and DPV 20, respectively) piglets were boosted with the same doses and routes. At DPV 35 (0 day post-challenge or DPC 0), two pigs from group I and group II were sacrificed prior to challenge with the virulent virus, to assess vaccine safety. All remaining pigs were challenged intranasally with $10^{5.5}$ $TCID_{50}$/ml of the virulent Influenza A (H1N1) pdm09. All piglets were euthanized at 41 DPV (DPC 6) for necropsy. Pathology procedures were carried out as described below. Serum was collected from all piglets on DPV 0, 14, 20, 35 and 41 to detect antibodies to the peptide by ELISA. Nasal swabs were collected from all piglets at DPV 35, 38 and 41 (or DPC 0, 3 and 6) and tested by qPCR for shedding of the challenge virus.

6.3.10. Clinical observation and pathological examination

Piglets were observed every day post-challenge for clinical signs of SIV including fever, nasal discharge, coughing, anorexia, and lethargy. Weight and temperatures were measured every day post-challenge.

Pathological evaluation and scoring was carried out in a blinded fashion by a board-certified veterinary pathologist. Heart, liver, spleen, kidney and lymph node tissues were collected from two pigs each euthanized prior to challenge from the vaccine group and unvaccinated control group to assess vaccine safety [36]. Lung sections were prepared from the right and left cranial, medial and caudal lobes and accessory lobes. Hematoxylin and eosin-stained tissue sections were observed for microscopic changes indicating viral infection. In addition, the lung sections were

stained with the anti-M2e monoclonal antibody to determine localization of the M2e-HA1-HA2 peptide by immunohistochemistry (IHC).

For the remaining animals sacrificed on the 6th day after challenge, protection against the development of gross lesions due to virulent viral challenge was assessed as the percentage of the tissue affected in each of the six lung regions listed above. The total percentage of lungs affected for the 5 pigs/group is shown in **Table 6.1**. Similarly, microscopic lesions were assessed using hematoxylin and eosin stained sections, as previously described, with some modifications [37, 38]. Briefly, bronchial/bronchiolar epithelial changes, and/or bronchitis and bronchiolitis were assessed as a percentage value for each of the six lung sections examined using the following scoring matrix: 25% airways affected =1, 26-50% airways affected =2, 51-75% airways affected =3, 76-100% airways affected = 4. Interstitial pneumonia (IP) was scored as 0 = none, 1 = mild, focal to multifocal IP, 2 = moderate, locally extensive to multifocal IP, 3 = moderate, multifocal to coalescing IP, 4 = severe, coalescing to diffuse. Peribronchiolar lymphocytic cuffing was scored as 0 = none, 1 = minimal, loosely formed, 2 = mild, loosely formed, 3 = moderate, well formed, 4 = severe, thick, well-formed cuffs. Total values were calculated as a sum for the five pigs per group (**Table 6.1**).

Lung sections were stained with an SIV specific monoclonal antibody for IHC and scored as weak =1, moderate = 2, strong = 3. The sum of the number of sections positive for antigen and the scores for each group is listed in Table 1. Consolidated total lesion scores were calculated as the sum of the gross, microscopic and IHC scores per group. The Mann-Whitney U test was applied to determine whether there were significant differences between groups at $p \leq 0.05$.

6.3.11. Antibody responses to the M2e-HA1-HA2 peptide

Sera collected from the experimental pigs were assessed for antibody responses against the M2e-HA1-HA2 peptide using an indirect ELISA. Briefly, 96-microwell ELISA plates (Corning, USA) were coated with 100µl/well of 1:200 recombinant M2e-HA1-HA2 peptide (0.3 mg/ml in water) diluted in carbonate coating buffer (pH 9.6), and incubated overnight at room temperature, followed by five washes with PBST. Plates were blocked with 200µl/well of blocking buffer (2% BSA in 1X PBST) for 2h at 37 °C. After blocking, plates were washed five times using 1X PBST. To each well, 50µl of 1:50 serum diluted in PBST was added in duplicate and incubated for 2h at 37 °C. After washing five times with PBST, 50 µl/well of a 1:2500 diluted anti-swine IgG peroxidase-conjugated secondary antibody (KPL, USA) was added, and the plates were incubated at 37 °C for 1h. After washing five times, 50 µl/well of TMB substrate (KPL, USA) was added to plates and incubated in the dark for 15 minutes at room temperature to catalyze the reaction. Finally, 50 µl/well of 1 M HCl was added to stop the reaction. The OD readings were obtained at 450 nm using a microplate reader (BioTek Instruments, Winooski, VT).

6.3.12. Hemagglutination inhibition (HAI) assay

The HAI assay was performed using 0.5% chicken RBCs and four hemagglutinating units of Influenza A (H1N1) pdm09 as per World Health Organization [29].

6.3.13. Detection of Challenge Virus Shedding by qPCR

Virus shedding in nasal secretions was assessed by a diagnostic one-step qRT-PCR using a commercial kit; the Path-ID RT-PCR Kit (Thermo Fisher, USA). The assay was performed in duplicate by NDSU VDL, as per the manufacturer's instructions, following standardized operating procedures.

6.3.14. Statistical analysis

The antibody titers, HAI titer and the viral load in nasal secretions were compared by Student's T-test using Microsoft Excel 2016. The histology scores were compared by Mann-Whitney U-test using SPSS software (IBM, USA). Data analysis were considered significant at $p<0.05$**.**

6.4. Results

6.4.1. The peptide antigen interacts with the exterior of the micellar assemblies

The structure of PEG_{600}-$PTHF_{650}$ macromolecules contains 6 proton sites **a**, **b**, **c**, **d**, **e** and **f**, with **d** and **f** localizing to the hydrophobic PTHF fragments (**Fig. 6.2, panel 1**). Proton spectra collected from solutions of 0.5 w/v% PEG_{600}-$PTHF_{650}$ alone or 5 w/v% polymer and 0.005% peptide assemblies in deuterated water showed that addition of peptide to the PEG_{600}-$PTHF_{650}$ micellar solution led to a shift of the signals for the hydrophilic PEG protons **a** and **c** (**Fig 6.2A** and **6.2C**). The broadening of the signals (half-height width increases from 2.8 Hz to 6.5 Hz for protons **c**) implied that the mobility of the PEG fragments became limited at those locations, presumably due to their interaction with M2e-HA1-HA2 molecules. The exterior of the polymer-peptide assemblies appears to be more tightly packed as evidenced by signal broadening, due to the association of the polar fragments of the peptide at these zones, which is in good agreement with previous studies for $PEG_{600}PTHF_{650}$ and two model peptides.

A slight shift of the signals of protons **a** and **c** toward lower ppm values indicates that the polarity in the micellar exterior becomes lower after polymer interaction with M2e-HA1-HA2, when compared with those of the micelles with no incorporated peptide molecules. The finding can be explained by the replacement of highly polar water molecules with the less polar hydrophilic fragments of M2e-HA1-HA2 upon peptide incorporation.

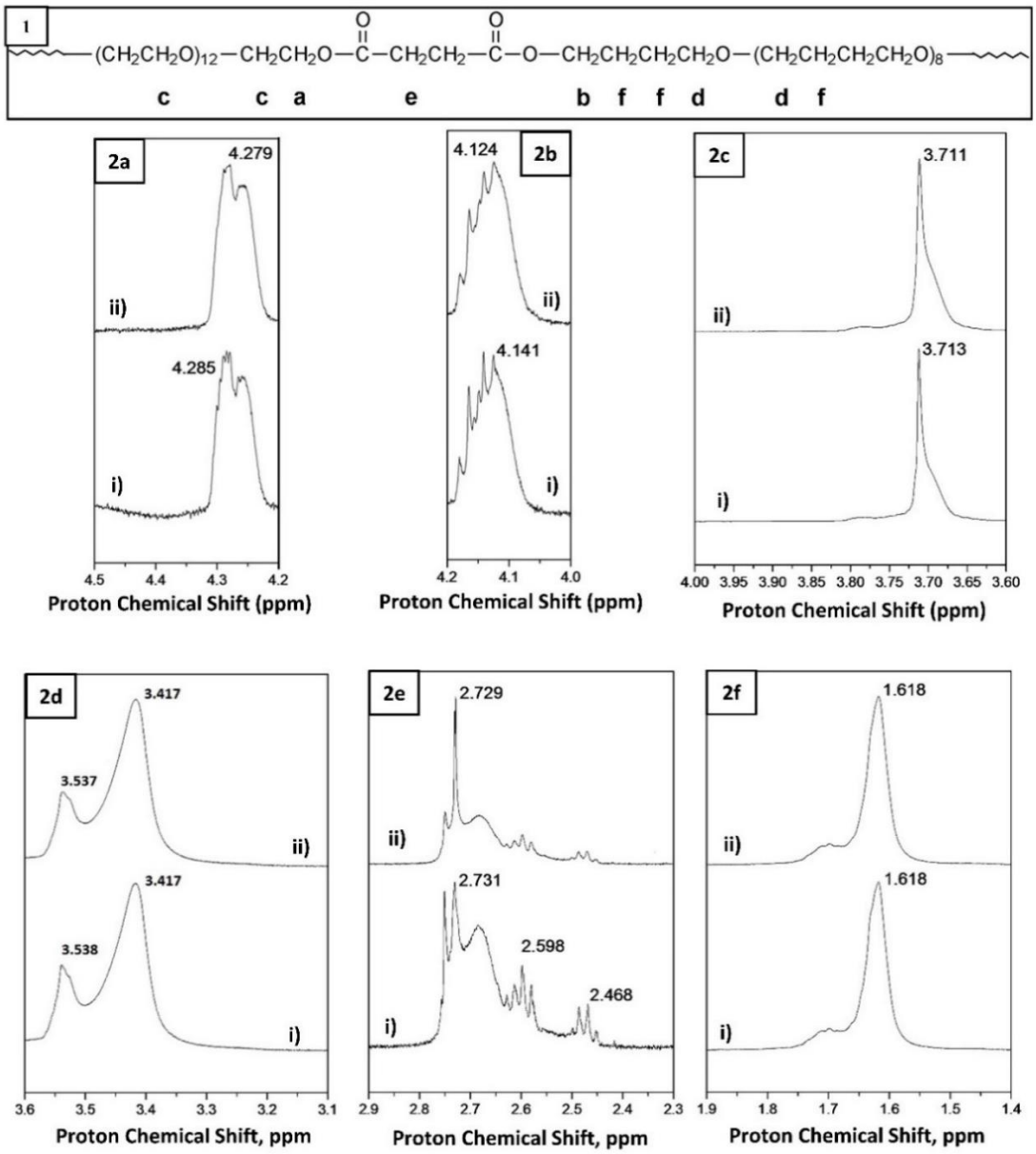

Figure 6.2. ^{1}H NMR spectra of the $PEG_{600}PTHF_{650}$ solution (0.5 w/v%) in D_2O. Panel 1- The chemical structure of $PEG_{600}PTHF_{650}$ with protons labeled a-f. Panel 2a through 2f correspond to the peaks representing the protons a - f depicted in panel 1 respectively. X-axis – proton chemical shift measured as ppm (parts per million). i) Spectrum of the 0.5 w/v% $PEG_{600}PTHF_{650}$ solution alone (ii) Spectrum after the addition of M2e-HA1-HA2 peptide to the 0.5 w/v% $PEG_{600}PTHF_{650}$ solution .

After adding the M2e-HA1-HA2 peptide, the signals for protons **b** and **e** shifted upfield, implying changes in the microenvironmental polarity of the area where the protons **b** and **e** are

localized. ^{1}H shift of the protons **b** and **e** corresponding to methylene group in the α position of the carbonyl groups in the PTHF moieties and succinic acid moieties respectively, indicates that these protons are transferred into a less polar micellar core (**Fig. 6.2b** and **6.2e**). Addition of the peptide to the 0.5 w/v% solution of $PEG_{600}PTHF_{650}$ did not lead to chemical shifts of the signals of protons **d** and **f** attributed to the hydrophobic PTHF fragments (**Fig. 6.2d** and **6.2f**). Hence, it can be concluded that the M2e-HA1-HA2 molecules are preferentially localized into the exterior of the $PEG_{600}PTHF_{650}$ micellar assemblies.

6.4.2. Micellar assemblies formed by 1 w/v% $PEG_{600}PTHF_{650}$ are efficient in peptide delivery

The purified M2e-HA1-HA2 peptide was detected at the expected molecular weight of 11kDa by a M2e-specific monoclonal antibody provided by Dr. Eileen Thacker, Iowa State University (**Fig. 6.1**). No significant cytotoxicity was detected at any of the tested concentrations of 0.05, 0.2, 0.5, 0.75, and 1.0 w/v% $PEG_{600}PTHF_{650}$ by the MTT assay compared to untreated cells (data not shown). Further assesment of the antigen loading capacity at the same concentrations of polymer showed that the 1 w/v% concentration of $PEG_{600}PTHF_{650}$ had a significantly higher antigen loading capacity than the next lower dilution of 0.75 w/v% $PEG_{600}PTHF_{650}$ and all other dilutions tested (**Fig. 6.3**). As there was also no significant cytotoxicity at the 1 w/v% $PEG_{600}PTHF_{650}$, this concentration was used for further testing and vaccine formulation (**Fig. 6.3**).

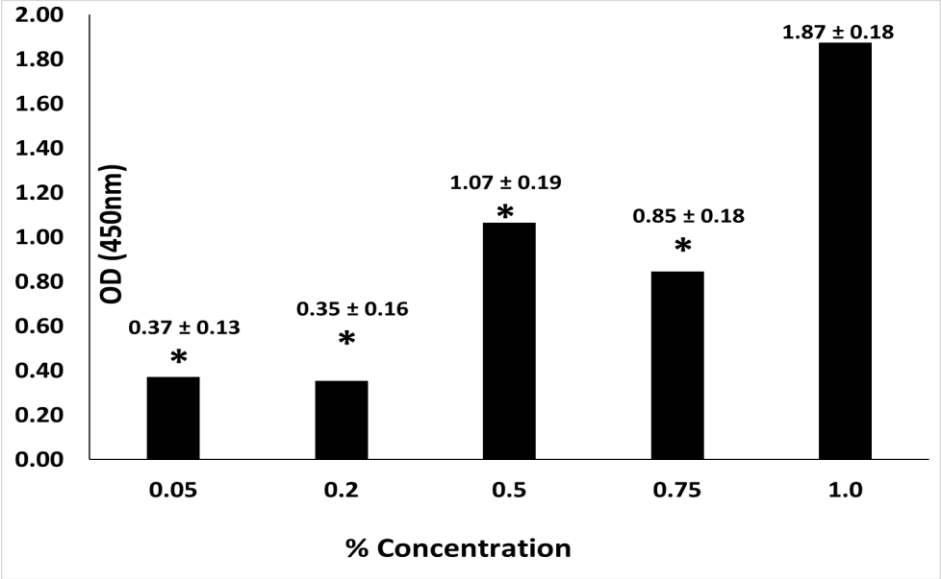

Figure 6.3. Antigen loading capacity of $PEG_{600}PTHF_{650}$ micellar assemblies. Intracellular delivery of peptide antigen as measured by an antigen detection ELISA using an M2e peptide-specific monoclonal antibody. Y-Axis: optical density (OD) at 450 nm, Y axis – w/v% concentration of $PEG_{600}PTHF_{650}$. Vero cells monolayers incubated with micellar assemblies prepared with 0.05, 0.2, 0.5, 0.75, and 1.0 w/v% of $PEG_{600}PTHF_{650}$ and a constant concentration of 0.5 µg/µl of the M2e-HA1-HA2 peptide for 8h. Intracelluar delivery of antigen was detected by ELISA using a M2e peptide-specific monoclonal detecting antibody after 24hrs. * - significantly different from micellar assemblies prepared from 1.0 w/v% polymer ($P<0.05$).

When the effectiveness of intracellular delivery of the incorporated peptide was assessed by an immunofluorescence assay (IFA), the control recombinant M2e-HA1-HA2 peptide could not penetrate cells by itself as it is highly hydrophobic in nature and, thus, poorly water-soluble. It could only be internalized with the help of delivery vehicle. With an increase in incubation time from1h to 8h, the $PEG_{600}PTHF_{650}$ micellar assemblies at the selected 1 w/v% concentration level delivered proportionately more M2e-HA1-HA2 peptide into the cells as determined by an increasing fluorescent signal by IFA (**Fig. 6.4**).

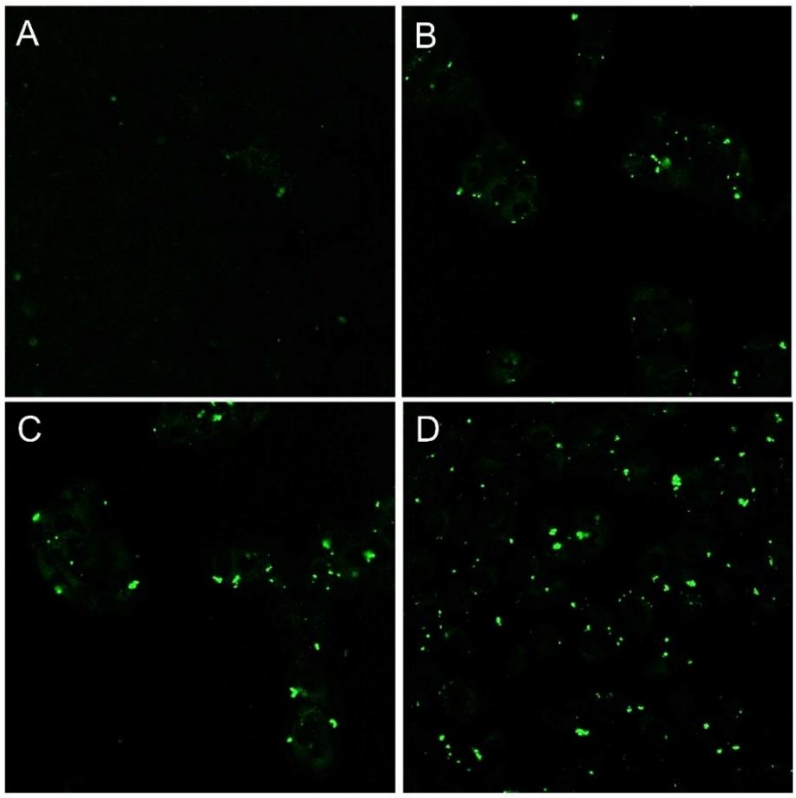

Figure 6.4. Intracellular delivery of M2e-HA1-HA2: Vero cell monolayers were incubated with micellar assemblies prepared with 1.0 w/v% of $PEG_{600}PTHF_{650}$ and 0.5 µg/µl of M2e-HA1-HA2 peptide for 1 h (A), 2 h (B), 4 h (C), and 8 h (D) and assessed by IFA using a M2e peptide-specific monoclonal antibody. Increasing green fluorescence is indicative increasing accumulation of intracellular peptide over time.

6.4.3. Vaccination induces strong antibody responses against the peptide antigen

Piglets vaccinated with $PEG_{600}PTHF_{650}$/M2e-HA1-HA2 micelles and M2e-HA1-HA2 peptide alone mounted strong antibody responses against the M2e-HA1-HA2 peptide. The antibody titers increased with the boosters on DPV 20 and 35. The mean optical density values remained significantly different ($P<0.05$) from pigs vaccinated with PBS and $PEG_{600}PTHF_{650}$ micelles alone for the duration of the study. Piglets vaccinated with $PEG_{600}PTHF_{650}$/M2e-HA1-HA2 micellar assemblies mounted significantly stronger antibody responses when compared to

M2e-HA1-HA2 peptide alone on DPV 20 and DPV 35 indicating that $PEG_{600}PTHF_{650}$ acts as an adjuvant by enhancing antibody responses (**Fig. 6.5**).

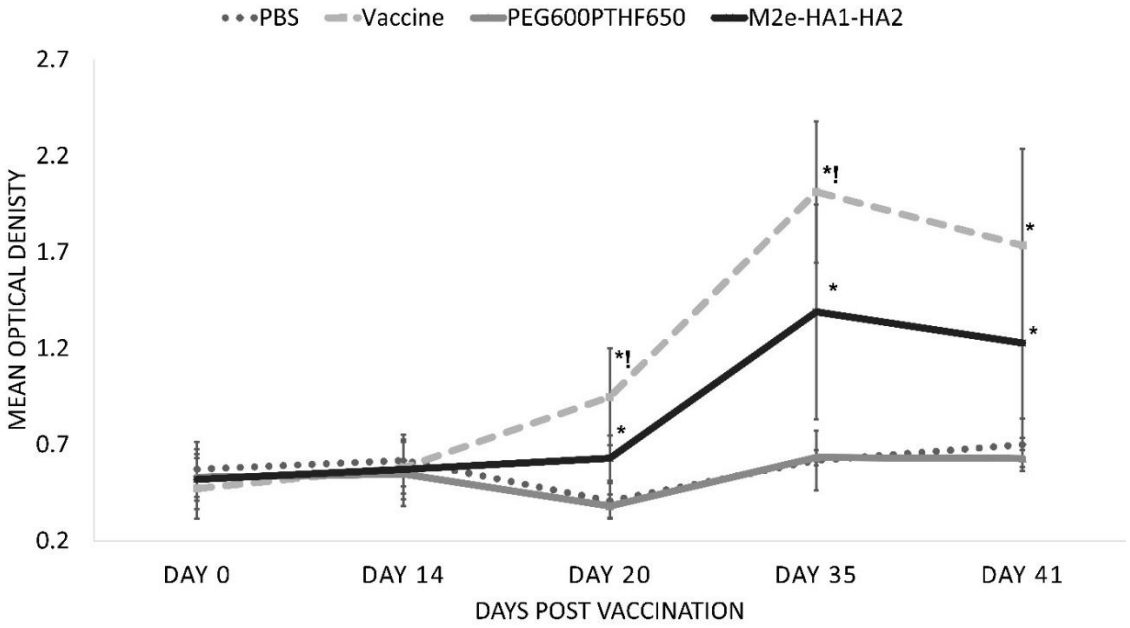

Figure 6.5. Antibody response in vaccinated pigs. Antibody response against M2e-HA1-HA2 peptide measured as ELISA OD values. Y-axis - mean OD reading (450nm) for each group, x-axis - days post vaccination (DPV). An asterisk (*) symbol represents the groups were statistically different ($p<0.05$) from the PBS group at the respective days post vaccination (DPV). An exclamation (!) symbol represents $PEG_{600}PTHF_{650}$/M2e-HA1-HA2 micellar assemblies accinated group is significantly different ($P<0.05$) from M2e-HA1-HA2 peptide group at the respective timepoint.

The hemaglutination inhibtion (HAI) titers for all piglets for the duration of the study were <40, with no significant differences between groups [data not shown], suggesting that the antibodies generated against the M2e-HA1-HA2 peptide were not neutralizing in nature.

6.4.4. Vaccination reduces lung pathology

No clinical signs of IAV infection such as pyrexia, respiratory distress or body weight loss was observed in any of the piglets throughout the study. One of the five vaccinated pigs did not

develop any gross or microscopic lesions (**Table 6.1**). The unvaccinated pigs had a total microscopic lesion score of 111.00 while the vaccinated pigs had a score of 69.00 (**Table 6.1**).

Table 6.1. Lesion scores at necropsy

Group	Gross Lesion Score/ No of positive animals	Microscopic Lesions Score/ No of positive animals	Immunohisto-Chemistry Score/ No of positive animals	Total Lesion Score
PBS	24.000 ± 4.658 (5/5)	111.000 ± 11.692 (5/5)	56.000 ± 5.070 (5/5)	191.000 ± 19.967
$PEG_{600}PTHF_{650}$	15.000 ± 1.732 (5/5)	90.000 ± 2.550 (5/5)	26.000 ± 1.095 [a] (5/5)	131.000 ± 1.924
M2e-HA1-HA2 Peptide	19.000 ± 3.701 (5/5)	97.000 ± 13.390 (5/5)	24.000 ± 3.421 [a] (5/5)	140.000 ± 20.162
Vaccine ($PEG_{600}PTHF_{650}$/ M2e-HA1-HA2)	18.000 ± 2.966 (4/5)	69.000 ± 6.229 (4/5)	17.000 ± 3.130 [a] (4/5)	97.000 ± 11.760 [a]

Gross lesion scores – Total percentage of lungs affected (N= 5 pigs/group)
Microscopic lesion scores – Sum of the percentage of each lung section affected (N= 5 pigs/group, 6 lung sections per pig), scored as follows:
Bronchial/bronchiolar epithelial changes, and/or bronchitis and bronchiolitis - Scoring -25% airways affected =1, 26-50% airways affected =2 =, 51-75% airways affected =3, 76-100% airways affected = 4
Interstitial pneumonia (IP) - Scoring - 0 = none, 1 = mild, focal to multifocal IP, 2 = moderate, locally extensive to multifocal IP, 3 = moderate, multifocal to coalescing IP, 4 = severe, coalescing to diffuse
Peribronchiolar lymphocytic cuffing - 0 = none, 1 = minimal, loosely formed, 2 = mild, loosely formed, 3 = moderate, well formed, 4 = severe, thick, well-formed cuffs
Immunohistochemistry (IHC) scores – Sum of the number of sections positive for antigen as detected by a SIV specific monoclonal antibody and IHC score (N= 5 pigs/group, 6 lung sections per pig), Scoring - weak =1, moderate = 2, strong = 3.
Total lesion scores – Sum of the gross, microscopic and IHC scores: a- significantly different from the PBS group, b- significantly different from the $PEG_{600}PTHF_{650}$ group, c- significantly different from the M2e-HA1-HA2 peptide group. Mann-Whitney U test at $p \leq 0.05$.

While the gross and microscopic lesion scores for the vaccinated and control pigs immunized with the peptide alone were lesser than those of the unvaccinated pigs, these differences were not statistically significant. However, the amount of viral antigen detected by

IHC was significantly different between the unvaccinated and vaccinated pigs. The consolidated total lesion score for the unvaccinated group (191.00) was significantly different from that of the vaccinated pigs (97.00). While the total scores for the peptide (141.00) and polymer (130.00) groups were considerably lower than those of the unvaccinated pigs but higher than the vaccinated pigs (97.00), statistical significance was not detected by the Mann Whitney U test (**Table 6.1**).

6.4.5. Vaccination induces delayed but significant reduction of viral shedding

Protection against nasal shedding of the challenge virus by vaccination as measured with a matrix gene-specific qPCR unexpectedly showed that viral loads in pigs vaccinated with the peptide alone or the polymer-peptide vaccine were significantly higher than the PBS control group, at 3 days post challenge (DPC 3). However, values for the pigs administered the polymer alone were similar to those of the PBS control group, indicating that early enhancement of viral replication was due to the peptide vaccine contruct and not the AIP-based delivery system. Three days later, on the 6^{th} day post challenge, the trend reversed to where nasal shedding of the challenge virus was significantly lower in the pigs administered the vaccine and peptide alone compared to unvaccinated pigs, while the viral loads continued to increase in pigs administered PBS or the polymer alone. The difference in viral loads between DPC 3 and DPC 6 in the pigs administered either the peptide alone or the polymer-peptide vaccine were statistically different, indicating that infleunza-specific protection induced by vaccination was delayed but robust, resulting in a significant reduction in challenge viral shedding during the 3 days period (**Fig. 6.6**).

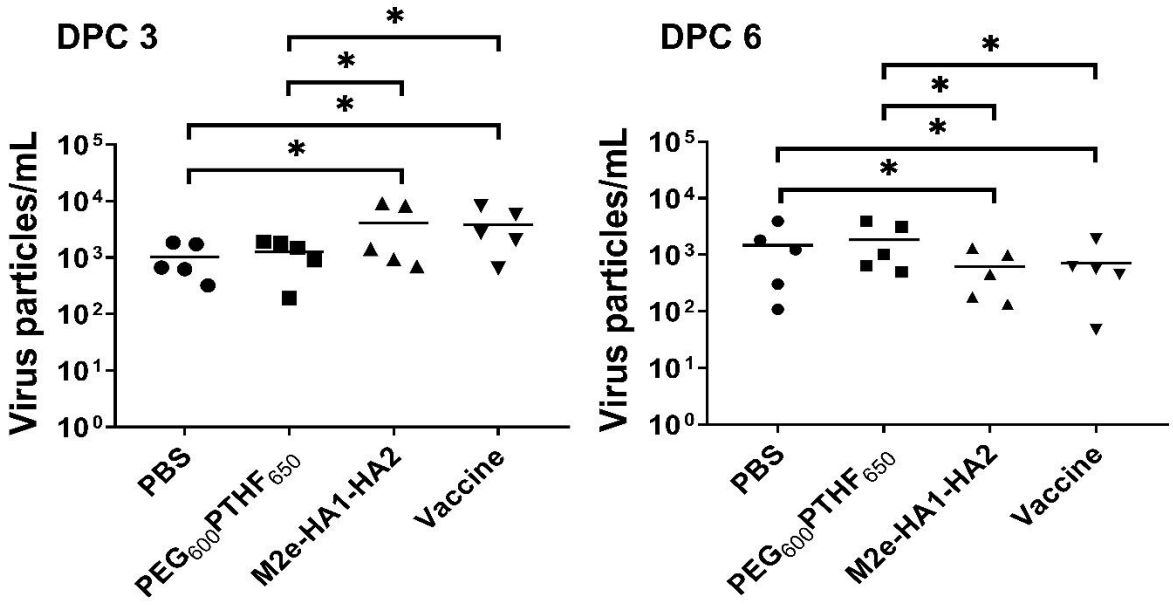

Figure 6.6. Detection of viral load in nasal secretions. The challenge pH1N1 viral particles in nasal secretions swabs for each treatment group on day 3 and 6 post-challenge (DPC) were determined by qRT-PCR. X-Axis – Groups, Y-axis – Mean viral particles/ml in individual pig. An asterisk (*) symbol represents the groups were statistically different ($p<0.05$) from each other. Horizontal bars represents the mean viral particles/ml in the group.

6.4.6. The $PEG_{600}PTHF_{650}$ peptide vaccine was safe

No untoward clinical signs were observed in vaccinated animals prior to challenge. Similarly, no gross or microscopic lesions were observed in the vaccinated piglets euthanized prior to challenge, indicating the $PEG_{600}PTHF_{650}$/M2e-HA1-HA2 vaccine did not cause any side effects. Localization of the M2e-HA1-HA2 peptide by immunohistochemistry using the M2e peptide-specific monoclonal antibody showed antigen-specific staining in the alveolar septa, alveolar spaces and perivascular areas of the lung tissue of one vaccinated pig and lymph node sections of the 2nd vaccinated pig. Representative images are depicted in **Figure 6.7**. This observation suggests that $PEG_{600}PTHF_{650}$/M2e-HA1-HA2 complexes were taken up by antigen presenting

cells and transported to the germinal center in lymph nodes. Antigen specific staining was absent in the PBS control pigs sacrificed prior to challenge.

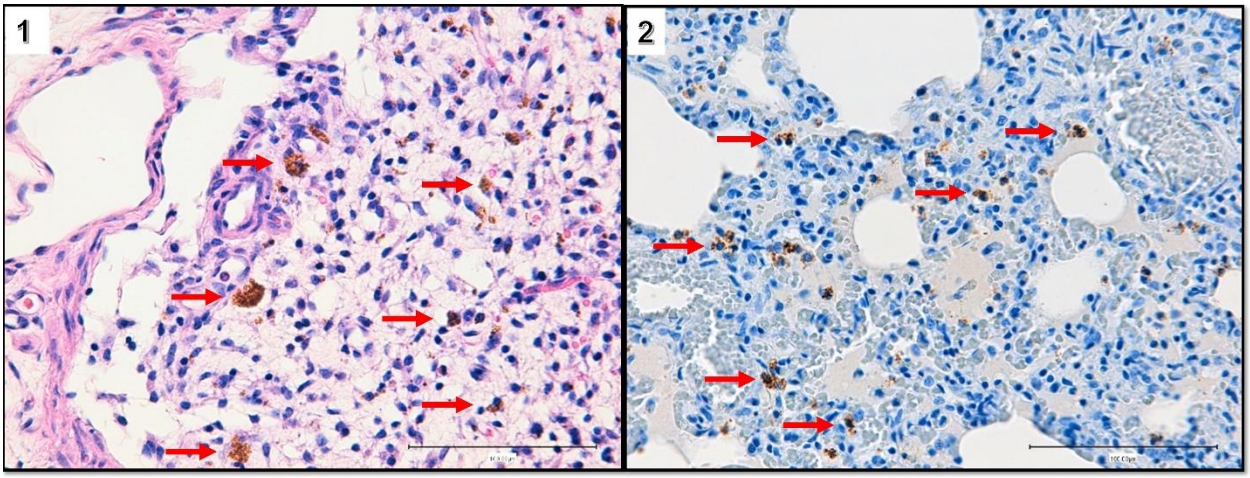

Figure 6.7. Localization of vaccine antigen in pigs vaccinated with $PEG_{600}PTHF_{650}$/M2e-HA1-HA2. 1- Lymph node, 2-Lung. Arrows indicate brown staining of the peptide antigen detected by a M2e-specific monoclonal antibody. No antigen was detected in unvaccinated pigs (data not shown).

6.5. Discussion

The discovery that the highly conserved M2e and HA2 epitopes can confer broad protection against influenza viruses was a major break through in the development of universal vaccines against influenza viruses [8]. These epitopes have been tested extensively and succesfully in mice; individually or in conjugation with other immunogenic proteins and peptides [3, 5, 7, 8, 13, 39, 40]. However, in pig models they fail to reduce challenge virus shedding and ameliorate disease outcomes [3, 5-8, 13-16, 39, 40]. A combination of the M2e and HA2 epitopes, together with a H1N1strain-specific HA1 epitope has not been tested before in pigs to determine if there are syngergistic protective effects. Similarly, this study addresses the need for effective delivery systems for peptide antigens which are inherently poor immunogens [16, 41] but have great promise in inducing epitope-specific, broad coverage. Our results support our hypothesis that the

micellar assemblies from amphiphilic invertible polymers (AIPs), represented in this study by $PEG_{600}PTHF_{650}$, effectively deliver the peptide vaccine cargo and act as an adjuvant in stimulating a strong humoral immune response against the delivered peptide.

While several conserved influenza epitopes have been identified, the M2e and HA2 epitopes are the most widely tested [4, 5, 8-10, 33]. The HA2 epitope is an 11 amino acid conserved sequence in the N-terminal of the HA2 subunit of HA protein. In mice models, vaccination with the HA2 peptide provided complete protection against IAV; whereas, this has not been studied yet in pig models [42, 43]. The M2e epitope is a 23 amino acid long, highly conserved peptide chain from the M2 protein. M2e-based vaccine was also completely protective against multiple-strains in mice models [4, 5, 9, 10], whereas, in ferrets [44] and chicken [45, 46] M2e vaccination was only able to reduce the virus shedding and pathological symptoms. However, in pigs M2e-based vaccines resulted in enhanced challenge viral infection [14, 15]. The strain-specific HA1 epitope used in this study was untested in swine but reduced viral shedding and pathology in a mouse model [33]. While the experimental conditions in our study do not exactly match those referenced above, the early enhancement of viral replication seen in the multi-epitope peptide-immunized animals was similar to observations in other studies cited above. Previous studies in mice suggest that the enhancement of infection in mice immunized with a chimeric peptide encoding the M2e and HA2 epitopes occurs via Fc region based antibody dependent enhancement of infection of macrophages [11, 47].

However, unlike other studies, vaccination had a significantly protective effect between day 3 and day 6 post-challenge as evidenced by the reduction in viral shedding in vaccinated animals. Had the observation period been continued beyond 6 days, it is likely that data would show that vaccinated animals had succesfully cleared the infection. The protective effect is most

likely due to cell mediated immunity or non-neutralizing mechanisms of antibody mediated protection. While the detailed characterization of these mechanisms is not within the scope of this study, our hypothesis that a combination of the AIP packaged epitopes will improve protection against influenza infection is well supported by the similar trends in the pathology and viral load data showing lower values for vaccinated animals. However, the improved protection seen this study can also be attributed to differences in the vaccine construct, dose, route of vaccination and infection, challenge virus strain and culture conditions used [48-52]. Further improvements in design, possibly by the addition of other B or T cells epitopes, could further improve the early immune responses and viral clearance.

Several approaches such as linking epitopes with immunogenic peptides or proteins, using multiple copies of epitopes, creating virus-like particles or using amphiphilic polymers [3-6, 8, 18, 24] have been previously used to improve the weak immunogenicity of peptide antigens [16, 41]. Amphiphilic polymers have several advantages; they can form micelles and micellar assemblies that can load antigen in a controllable manner, can be used for controlled antigen release and are generally immunologically safe [53]. Efficient entrapment and delivery of the hydrophobic drug , curcumin, into cancerous (breast carcinoma, and osteosarcoma) cells as a potential treatment for breast and bone cancer was previously demonstrated for the invertible micellar assemblies from AIP macromolecules used as the vaccine delivery vehicles in this study [54]. AIP interact with M2e-HA1-HA2 resulting in the formation of miccelar assemblies. However, unlike previous studies, the peptide molecules are preferentially localized within the PEG exterior of the $PEG_{600}PTHF_{650}$ micellar assemblies, which can be attributed to the higher molecular weight of the M2e-HA1-HA2 peptide (11 kDa, while 1.6-1.9 kDa for model peptides), differences in peptide sequence and conformation of the molecules. Hence, we hypothesized that it could also serve as a

successful vaccine delivery system for peptide antigens, and also act as an adjuvant. While there is no previously published data on the possible biological mechanisms of action of the AIP, it is evident that incorporation of M2e-HA1-HA2 peptide in aqueous solution into micellar assemblies resulted in protection and effective delivery of the antigen vaccination. While the peptide alone was not uptaken by Vero cells due to its hydrophobic nature the micellar assemblies clearly enhanced the bioavailability and delivery of the M2e-HA1-HA2 peptide into cells in vitro (**Fig. 6.4**) and in vivo (**Fig. 6.7**) Since the M2e-HA1-HA2 peptide was found in the lymph nodes, the AIP micellar assemblies most likely faciltiated peptide uptake by antigen presenting cells. The adjuvant effects in enhancing antibody mediated immunity are clearly substantiated by the significantly higher peptide-specific antibody titers in piglets vaccinated with $PEG_{600}PTHF_{650}$/M2e-HA1-HA2 micellar assemblies compared to control piglets vaccinated with M2e-HA1-HA2 peptide alone. Further, as no toxicity was noted in vitro or in vivo, the described AIP-based vaccine formulation has significant promise as a peptide antigen delivery system, especially to stimulate strong antibody responses for effective protection. The AIP's efficacy in delivering hydrophilic peptides or other complex peptides with diverse physical properties remains to be tested.

M2e antibodies can prevent the release of viral RNA genome by preventing ion channel activity of the M2 protein [55]. HA2 antibodies are reported to bind with the fusion peptide of HA2 protein hence preventing the fusion of the viral envelope with the endosomal membrane [56]. Hence, anti-M2e and HA2 antibodies are non-neutralizing and likely do not prevent virus attachment and initial infection [11, 13, 15, 16] but likely act via other mechanisms which are not fully understood. Studies in mice suggest that anti-M2e and anti-HA2 antibodies could reduce the viral replication by eliminating infected cells by antibody dependent cell-mediated phagocytosis

[40]. While characterization of cell mediated or innate immune mechanisms was not undertaken in this study due to constraints with resources, similar mechanisms were likely involved in this study, as animals vaccinated with $PEG_{600}PTHF_{650}$/M2e-HA1-HA2 micellar assemblies had fewer lung lesions compared to the control groups in the absence of neutralizing antibody responses. The HA1 epitope-specific antibodies could be expected to bind to the cleavage site of precursor HA0 protein thus prevent the formation of HA1-HA2 mature protein [33] and can be expected to have a neutralizing effect. While we did not measure the levels of HA1-specific antibodies in this study, it is likely that the magnitude of the antibody reponse to this epitope at pre-challenge sample collection time point was below the detection threshold of the HI assay used. Other limitations of this study are that the level of IgA antibodies were not determined and protection was assessed only against the Influenza A (H1N1) pdm09 strain.

6.6. Conclusions

The use of multiple epitopes and the adjuvant effects of the micellar assemblies from AIP macromolecules were effective in enhancing epitope-based immunization approaches against influenza viruses. A more detailed characterization of the mechanisms by which the $PEG_{600}PTHF_{650}$ assemblies modulate immunity will help to fully exploit its use as a delivery system and adjuvant.

6.7. References

(1) Imai M, Kawaoka Y. The role of receptor binding specificity in interspecies transmission of influenza viruses. *Current opinion in virology.* **2012***;2*:160-7.

(2) Ma W, Lager K, Vincent A, Janke B, Gramer M, Richt J. The role of swine in the generation of novel influenza viruses. *Zoonoses and public health.* **2009***;56*:326-37.

(3) De Filette M, Min Jou W, Birkett A, Lyons K, Schultz B, Tonkyro A, et al. Universal influenza A vaccine: optimization of M2-based constructs. *Virology.* **2005***;337*:149-61.

(4) De Filette M, Fiers W, Martens W, Birkett A, Ramne A, Lowenadler B, et al. Improved design and intranasal delivery of an M2e-based human influenza A vaccine. *Vaccine.* **2006***;24*:6597-601.

(5) De Filette M, Ramne A, Birkett A, Lycke N, Lowenadler B, Min Jou W, et al. The universal influenza vaccine M2e-HBc administered intranasally in combination with the adjuvant CTA1-DD provides complete protection. *Vaccine.* **2006***;24*:544-51.

(6) Huleatt JW, Nakaar V, Desai P, Huang Y, Hewitt D, Jacobs A, et al. Potent immunogenicity and efficacy of a universal influenza vaccine candidate comprising a recombinant fusion protein linking influenza M2e to the TLR5 ligand flagellin. *Vaccine.* **2008***;26*:201-14.

(7) Fiers W, De Filette M, El Bakkouri K, Schepens B, Roose K, Schotsaert M, et al. M2e-based universal influenza A vaccine. *Vaccine.* **2009***;27*:6280-3.

(8) Du L, Zhou Y, Jiang S. Research and development of universal influenza vaccines. *Microbes Infect.* **2010***;12*:280-6.

(9) Zhao G, Lin Y, Du L, Guan J, Sun S, Sui H, et al. An M2e-based multiple antigenic peptide vaccine protects mice from lethal challenge with divergent H5N1 influenza viruses. *Virology journal.* **2010***;7*:9.

(10) Wen F, Ma J-H, Yu H, Yang F-R, Huang M, Zhou Y-J, et al. A novel M2e-multiple antigenic peptide providing heterologous protection in mice. *Journal of veterinary science.* **2016***;17*:71-8.

(11) Ameghi A, Pilehvar-Soltanahmadi Y, Baradaran B, Barzegar A, Taghizadeh M, Zarghami N, et al. Protective immunity against homologous and heterologous influenza virus lethal challenge by immunization with new recombinant chimeric HA2-M2e fusion protein in BALB/C mice. *Viral immunology.* **2016***;29*:228-34.

(12) Wu K-W, Chien C-Y, Li S-W, King C-C, Chang C-H. Highly conserved influenza A virus epitope sequences as candidates of H3N2 flu vaccine targets. *Genomics.* **2012***;100*:102-9.

(13) Staneková Z, Varečková E. Conserved epitopes of influenza A virus inducing protective immunity and their prospects for universal vaccine development. *Virology journal.* **2010***;7*:351.

(14) Opriessnig T, Gauger PC, Gerber PF, Castro AM, Shen H, Murphy L, et al. Comparison of the efficacy of a commercial inactivated influenza A/H1N1/pdm09 virus (pH1N1) vaccine and two experimental M2e-based vaccines against pH1N1 challenge in the growing pig model. *PloS one.* **2018***;13*:e0191739.

(15) Heinen PP, Rijsewijk FA, de Boer-Luijtze EA, Bianchi AT. Vaccination of pigs with a DNA construct expressing an influenza virus M2–nucleoprotein fusion protein exacerbates disease after challenge with influenza A virus. J*ournal of General Virology.* **2002***;83*:1851-9.

(16) Chun S, Li C, Van Domselaar G, Wang J, Farnsworth A, Cui X, et al. Universal antibodies and their applications to the quantitative determination of virtually all subtypes of the influenza A viral hemagglutinins. *Vaccine.* **2008***;26*:6068-76.

(17) Daniels R, Downie J, Hay A, Knossow M, Skehel J, Wang M, et al. Fusion mutants of the influenza virus hemagglutinin glycoprotein. *Cell.* **1985***;40*:431-9.

(18) Stanekova Z, Kiraly J, Stropkovska A, Mikušková T, Mucha V, Kostolanský F, et al. Heterosubtypic protective immunity against influenza A virus induced by fusion peptide of the hemagglutinin in comparison to ectodomain of M2 protein. *Acta virologica.* **2011***;55*:61-7.

(19) Wang TT, Tan GS, Hai R, Pica N, Ngai L, Ekiert DC, et al. Vaccination with a synthetic peptide from the influenza virus hemagglutinin provides protection against distinct viral subtypes. *Proceedings of the National Academy of Sciences.* **2010***;107*:18979-84.

(20) Fosgerau K, Hoffmann T. Peptide therapeutics: current status and future directions. *Drug discovery today.* **2015***;20*:122-8.

(21) Moghimi SM, Hunter AC. Poloxamers and poloxamines in nanoparticle engineering and experimental medicine. *Trends in biotechnology.* **2000***;18*:412-20.

(22) Newman MJ, Todd CW, Balusubramanian M. Design and development of adjuvant-active nonionic block copolymers. *Journal of pharmaceutical sciences.* **1998***;87*:1357-62.

(23) Greenland JR, Letvin NL. Chemical adjuvants for plasmid DNA vaccines. *Vaccine.* **2007***;25*:3731-41.

(24) Adams JR, Haughney SL, Mallapragada SK. Effective polymer adjuvants for sustained delivery of protein subunit vaccines. *Acta biomaterialia.* **2015***;14*:104-14.

(25) Voronov A, Kohut A, Peukert W, Voronov S, Gevus O, Tokarev V. Invertible architectures from amphiphilic polyesters. *Langmuir.* **2006***;22*:1946-8.

(26) Voronov A, Kohut A, Vasylyev S, Peukert W. Mechanism of silver ion reduction in concentrated solutions of amphiphilic invertible polyesters in nonpolar solvent at room temperature. *Langmuir.* **2008***;24*:12587-94.

(29) Organization WH. Manual for the laboratory diagnosis and virological surveillance of influenza. **2011**.

(30) Reed LJ, Muench H. A simple method of estimating fifty per cent endpoints 1 2. *American journal of epidemiology.* **1938***;27*:493-7.

(31) Neirynck S, Deroo T, Saelens X, Vanlandschoot P, Jou WM, Fiers W. A universal influenza A vaccine based on the extracellular domain of the M2 protein. *Nature medicine.* **1999***;5*:1157.

(32) Hashem AM, Van Domselaar G, Li C, Wang J, She Y-M, Cyr TD, et al. Universal antibodies against the highly conserved influenza fusion peptide cross-neutralize several subtypes of influenza A virus. *Biochemical and biophysical research communications.* **2010***;403*:247-51.

(33) Horváth A, Tóth GK, Gogolák P, Nagy Z, Kurucz I, Pecht I, et al. A hemagglutinin-based multipeptide construct elicits enhanced protective immune response in mice against influenza A virus infection. *Immunology letters.* **1998***;60*:127-36.

(34) Hevus I, Kohut A, Voronov A. Interfacial micellar phase transfer using amphiphilic invertible polymers. *Polymer Chemistry.* **2011***;2*:2767-70.

(35) Mosmann T. Rapid colorimetric assay for cellular growth and survival: application to proliferation and cytotoxicity assays. *Journal of immunological methods.* **1983***;65*:55-63.

(36) Opriessnig T, Patterson AR, Madson DM, Pal N, Ramamoorthy S, Meng XJ, et al. Comparison of the effectiveness of passive (dam) versus active (piglet) immunization against porcine circovirus type 2 (PCV2) and impact of passively derived PCV2 vaccine-induced immunity on vaccination. *Veterinary microbiology.* **2010***;142*:177-83.

(37) Halbur P, Paul P, Frey M, Landgraf J, Eernisse K, Meng X-J, et al. Comparison of the pathogenicity of two US porcine reproductive and respiratory syndrome virus isolates with that of the Lelystad virus. *Veterinary pathology.* **1995***;32*:648-60.

(38) Gauger PC, Vincent AL, Loving CL, Henningson JN, Lager KM, Janke BH, et al. Kinetics of lung lesion development and pro-inflammatory cytokine response in pigs with vaccine-associated enhanced respiratory disease induced by challenge with pandemic (2009) A/H1N1 influenza virus. *Veterinary pathology.* **2012***;49*:900-12.

(39) Adar Y, Singer Y, Levi R, Tzehoval E, Perk S, Banet-Noach C, et al. A universal epitope-based influenza vaccine and its efficacy against H5N1. *Vaccine.* **2009***;27*:2099-107.

(40) El Bakkouri K, Descamps F, De Filette M, Smet A, Festjens E, Birkett A, et al. Universal vaccine based on ectodomain of matrix protein 2 of influenza A: Fc receptors and alveolar macrophages mediate protection. *The Journal of Immunology.* **2011***;186*:1022-31.

(41) Feng J, Zhang M, Mozdzanowska K, Zharikova D, Hoff H, Wunner W, et al. Influenza A virus infection engenders a poor antibody response against the ectodomain of matrix protein 2. *Virology journal.* **2006***;3*:102.

(42) Bommakanti G, Citron MP, Hepler RW, Callahan C, Heidecker GJ, Najar TA, et al. Design of an HA2-based Escherichia coli expressed influenza immunogen that protects mice from pathogenic challenge. *Proceedings of the National Academy of Sciences.* **2010***;107*:13701-6.

(43) Steel J, Lowen AC, Wang TT, Yondola M, Gao Q, Haye K, et al. Influenza virus vaccine based on the conserved hemagglutinin stalk domain. *MBio.* **2010***;1*:e00018-10.

(44) Fan J, Liang X, Horton MS, Perry HC, Citron MP, Heidecker GJ, et al. Preclinical study of influenza virus A M2 peptide conjugate vaccines in mice, ferrets, and rhesus monkeys. *Vaccine.* **2004***;22*:2993-3003.

(45) Zhang X, Liu M, Liu C, Du J, Shi W, Sun E, et al. Vaccination with different M2e epitope densities confers partial protection against H5N1 influenza A virus challenge in chickens. *Intervirology.* **2011***;54*:290-9.

(46) Reese KA, Lupfer C, Johnson RC, Mitev GM, Mullen VM, Geller BL, et al. A novel lactococcal vaccine expressing a peptide from the M2 antigen of H5N2 highly pathogenic avian influenza A virus prolongs survival of vaccinated chickens. *Veterinary medicine international.* **2013**;2013.

(47) Dutry I, Yen H, Lee H, Peiris M, Jaume M. Antibody-Dependent Enhancement (ADE) of infection and its possible role in the pathogenesis of influenza. *BMC Proc* **2011**. P62.

(48) Mozdzanowska K, Zharikova D, Cudic M, Otvos L, Gerhard W. Roles of adjuvant and route of vaccination in antibody response and protection engendered by a synthetic matrix protein 2-based influenza A virus vaccine in the mouse. *Virology journal.* **2007***;4*:118.

(49) Price GE, Lo C-Y, Misplon JA, Epstein SL. Reduction of influenza virus transmission from mice immunized against conserved viral antigens is influenced by route of immunization and choice of vaccine antigen. *Vaccine.* **2018**.

(50) Schepens B, De Vlieger D, Saelens X. Vaccine options for influenza: thinking small. *Current opinion in immunology.* **2018***;53*:22-9.

(51) Kim Y-J, Lee Y-T, Kim M-C, Lee Y-N, Kim K-H, Ko E-J, et al. Cross-Protective Efficacy of Influenza Virus M2e Containing Virus-Like Particles Is Superior to

Hemagglutinin Vaccines and Variable Depending on the Genetic Backgrounds of Mice. *Frontiers in immunology.* **2017***;8*:1730.

(52) Wolf AI, Mozdzanowska K, Williams KL, Singer D, Richter M, Hoffmann R, et al. Vaccination with M2e-based multiple antigenic peptides: characterization of the B cell response and protection efficacy in inbred and outbred mice. *PloS one.* **2011***;6*:e28445.

(53) Shakya AK, Nandakumar KS. Applications of polymeric adjuvants in studying autoimmune responses and vaccination against infectious diseases. *Journal of the Royal Society Interface.* **2013***;10*:20120536.

(54) Hevus I, Modgil A, Daniels J, Kohut A, Sun C, Stafslien S, et al. Invertible micellar polymer assemblies for delivery of poorly water-soluble drugs. *Biomacromolecules.* **2012***;13*:2537-45.

(55) Schnell JR, Chou JJ. Structure and mechanism of the M2 proton channel of influenza A virus. *Nature.* **2008***;451*:591.

(56) Imai M, Sugimoto K, Okazaki K, Kida H. Fusion of influenza virus with the endosomal membrane is inhibited by monoclonal antibodies to defined epitopes on the hemagglutinin. *Virus research.* **1998***;53*:129-39.

CHAPTER 7. ENZYME-POLYMER CONJUGATES FOR BIOMASS HYDROLYSIS*

7.1. Abstract

Polymeric cellulosomes are enzyme-polymer conjugates (EPCs) synthesized by covalent conjugation of commercial cellulase mixtures with polymer scaffolds made from poly(ethylene glycol) methyl ether methacrylate (PEGMA) and glycidyl methacrylate (GMA). EPCs catalytic activity, adsorption, hydrolysis yield, and glucose inhibition were examined using soluble and insoluble substrates. Optimal conjugation conditions based on enzyme catalytic activity were determined to be at a 10:1 ratio of polymer and enzyme. Increasing molecular weight of the polymer scaffold limited enzyme loading levels on the polymeric cellulosomes. Compared to the free enzymes, EPCs exhibited improved catalytic activity with soluble substrate and similar activity in insoluble substrate. Moreover, EPCs reduced the inhibitory effect of glucose during hydrolysis which could facilitate higher hydrolysis rates at higher substrate loadings.

7.2. Introduction

Enzymatic hydrolysis is an important step in the production of lignocellulosic biofuels and biochemicals. Hydrolytic enzyme activity is challenged due to lignocellulosic biomass properties including cellulose crystallinity, structural complexity of cell wall polysaccharides, water

* The material in this chapter was co-authored by Oksana Zholobko, Ademola Hammed, Andrey Zakharchenko, Sergiy Minko, Scott W. Pryor, and Andriy Voronov. Oksana Zholobko had the primary responsibilities of synthesizing and characterizing polymers and preparing enzyme-polymer conjugates. Oksana Zholobko and Andrey obtained the optimal conjugation conditions for the EPCs. Oksana Zholobko was also responsible for characterizing the EPCs conjugation efficiency, catalytic activity, adsorption, and hydrolysis yield. Ademola Hammed helped Oksana Zholobko perform and analyze results of enzymatic hydrolysis of biomass and glucose inhibition experiments. Oksana Zholobko was involved in drafting and revising all versions of this chapter. Sergiy Minko, Scott W. Pryor, and Andriy Voronov helped explain the results obtained by Oksana Zholobko, Ademola Hammed, and Andrey Zakharchenko .

insolubility, and presence of lignin-polyphenol [1,2]. Although lignocellulosic resources are abundant and promising for second generation biofuel production, industrial bioprocessing is still economically challenging. Enzymes account for about 50% of biomass hydrolysis costs and about 20% of total cost of cellulosic bioethanol processing [3]. Therefore, feasibility of lignocellulosic bioprocessing will improve reducing costs in the enzymatic hydrolysis stage. Hydrolysis costs can be potentially reduced through immobilized enzyme recovery and reuse.

While most enzymatic hydrolysis research uses free enzyme systems, some of the most efficient living systems have developed enzyme immobilization mechanisms to centralize diverse and complementary groups of enzymes into extracellular structures called cellulosomes. Natural cellulosomes are assemblies of enzymes with various catalytic functions linked to a large scaffoldin protein. Cellulosomes from different organisms exhibit a wide variety of architectural forms, however, they all co-localize a variety of cellulases, hemicellulases and pectinases to synergistically breakdown plant biomass. Industrial use of cellulosomes could improve biomass hydrolysis rates and yields, but microbes secrete small quantities of cellulosomes that are not produced in amounts feasible for industrial operation [4,5].

Polymeric cellulosomes are a mimicry of cellulosome that replaces the scaffoldin protein with synthetic nanoscale polymer. Several studies showed that using non-biological nanostructures in place of the scaffoldin eliminates the need to prepare specific cellulosome-derived scaffold proteins. It may also allow more highly clustered and diverse structures in comparison to free cellulosomes [4–10]. Recent studies on polymeric cellulosomes have reported several advantages including retention or improvement of enzyme activity, increase in substrate binding affinity, and improvement of enzyme stability with changes in temperature and pH [11–14]. However, polymeric cellulosomes have some technological challenges including enzyme leaching, and

reduction in substrate penetration. In addition, research on polymeric cellulosome hydrolysis often uses pure cellulases with low enzyme loadings and soluble substrate that are not fully representative of lignocellulosic hydrolysis [10,14,15].

In this study, we synthesized polymeric cellulosomes by covalently conjugating a cellulase mixture with different copolymers. We then measured the conjugation efficiency on each polymer system and the hydrolytic activity using several model substrates. We evaluated the specific ranges of hydrolysis conditions, such as enzyme concentration, type of substrate, and biomass pretreatment type in which developed polymeric cellulosomes showed enhanced catalytic activity over free enzymes. The effect of polymer support on enzyme inhibition by glucose was also investigated.

7.3. Experimental section

7.3.1. Materials

Materials purchased from MilliporeSigma (St. Louis, MO) include: Cellulase mixture from *Trichoderma reesei* Celluclast® 1.5L, glycidyl methacrylate (GMA), poly(ethylene glycol) methyl ether methacrylates ($PEGMA_{300}$ –average molecular weight 300 g/mol; $PEGMA_{950}$ – number average molecular weight 950 g/mol), MEHQ and BHT inhibitor remover beads, methyl ethyl ketone (MEK), 2,2′-Azobis(2-methylpropionitrile) (AIBN), carboxy methyl cellulose (CMC), and Avicel cellulose. Diethyl ether was purchased from BTC (VWR International; Batavia, IL). bicinchoninic acid assay (BCA) Protein Assay Kit II was purchased from BioVision (VWR International, Batavia, IL). All other chemicals were obtained from VWR International (Batavia, IL). Citrate buffer was prepared from sodium citrate dihydrate, citric acid, Millipore water, and stabilized with 0.04% NaN_3. Phosphate buffer was prepared from monobasic sodium phosphate dibasic sodium phosphate, and Millipore water.

7.3.2. Polymer synthesis

Poly(GMA-*co*-PEGMA) was synthesized by solution free-radical polymerization using a previously reported method [12]. MEHQ inhibitor remover beads were added to glycidyl methacrylate (GMA) prior to synthesis, and MEHQ and BHT inhibitor remover beads were added to poly(ethylene glycol) methyl ether methacrylate ($PEGMA_{300}$ and $PEGMA_{950}$, average molecular weight 300 and 950 g/mol, respectively) dissolved in MEK prior to synthesis. Both monomers were stirred for 45 min. Monomers were filtered through 0.2-μm syringe filters into the reaction flask together with AIBN dissolved in MEK. The GMA:PEGMA molar ratio was varied from 10:90 to 80:20, the overall monomer concentration was 0.5 M, and the AIBN concentration was 0.01 M. The nitrogen was bubbled through the solution for 45 min. The polymerization mixture was immersed in a 50 ˚C preheated water bath for 1.5 h for GMA-*co*-$PEGMA_{950}$ and for 20 h for GMA-*co*-$PEGMA_{300}$. The polymerization reaction was terminated by opening the flask and removing the reactor from the water bath. The resulting polymer was purified by precipitation with diethyl ether and centrifugation, and dissolved in MEK after pouring off supernatant. This process was repeated three times to remove unreacted monomer and initiator.

7.3.3. Characterization of polymers.

NMR spectroscopy. Polymer samples for ^{1}H NMR spectroscopy were prepared by dissolving an appropriate amount of polymer in deuterated water under gentle agitation. ^{1}H NMR spectra were recorded on an AVANCE III HDTM 400 high-performance digital NMR spectrometer at 400 MHz and 22.5°C. The spectra were referenced to a TMS signal as an internal standard.

Viscosity measurements. Ubbelohde type viscometer was used to measure a wide spread flow time at 25 ºC. Flow time of MEK, as a solvent, and copolymer solutions were measured. The

increment in the solution viscosity, η, with respect to that of the pure solvent, η_0, the relative viscosity, is the ratio $\eta_r = \eta/\eta_0$. Obtained η_r were in range between 1.1÷1.5.

Intrinsic viscosity [η] can be obtained by linear extrapolation of the inherent viscosity, according to the Kraemer equation:

$$\ln \eta_r/c=[\eta]-k_K[\eta]^2c, \quad (7.1.)$$

where k_K is the Kraemer constant. In the Kraemer plot, $(\ln \eta_r)/c$ *vs* c, [η] is the intercept, and the slope should be $-k_K[\eta]^2$.

7.3.4. Synthesis of enzyme-polymer conjugates (EPC)

Concentrated (10% w/w) cellulase enzyme mixture (3 ml) was added to 50 ml of phosphate buffer (pH 7.4, 10 mM) and stirred for 10 minutes. Polymer aqueous solution (25% w/w) (12 ml) was added dropwise to the mixture under vigorous stirring. The reaction was carried out for 4.5 h at room temperature with continued stirring. Citrate buffer (pH 4.6, 100 mM) was added to a final volume of 100 ml and stirred for an additional 15 minutes. The pH was adjusted to 4.6 using citric acid. The obtained mixture was used as a stock solution in later experiments. The concentration of the conjugates used in further experiments was calculated based on the amount of enzymes (μg/ml).

7.3.5. Hydrolytic efficiency of EPC on soluble substrate

CMC was dissolved in citrate buffer (pH 4.6) to a concentration of 1% (w/w) and reacted with free enzymes or EPC (1-8 μg/ml) for 60 minutes at 45 °C. Vials were incubated at 88 °C for 10 minutes to stop the enzymatic reaction. The total reducing sugar concentration was measured using the BCA assay as described below.

7.3.6. Hydrolytic efficiency of EPC on insoluble substrates

The hydrolytic efficiency of the EPC using insoluble substrate was measured using Whatman #1 paper disks, and also with acid- and alkaline-pretreated switchgrass. Conditions for acid pretreatment were 3% (w/v) solids in 1% H_2SO_4 at 140 ^oC for 20 minutes. Alkaline pretreatment was done using a 1:6 solid-to-liquid ratio in 15 % aqueous ammonia, at 60 °C for 24 h. Free enzymes and EPCs were diluted in citrate buffer before adding the substrate. For filter paper, a 50-mg strip (1 cm x 6 cm) of Whatman filter paper was incubated at 45 ^oC and 300 rpm agitation in a heated water bath. Hydrolysis duration was varied based on experimental design. After incubation, all samples were centrifuged to separate the semi-hydrolyzed paper slurry from soluble sugars. The supernatant sugar content was analyzed using the BCA assay. For alkaline- and acid-pretreated switchgrass, a mass of 1% glucan equivalent was incubated at 50 ^oC and 130 rpm. Xylanase (Novozymes, Cellic(R) HTec CDN010105) (30 XU) was added to alkaline-pretreated switchgrass in order to ensure xylan hydrolysis. Samples were collected at 4, 12 and 24 h and analyzed for glucose content.

7.3.7. Enzyme inhibition

The effect of enzyme product inhibition on EPCs was tested by adding glucose to the hydrolysis media. The reaction was set up as described in section 2.5 for pretreated switchgrass with initial glucose concentrations of 45 and 90 mg/ml. Samples were collected at 24 and 72 h and measured for glucose and xylose concentrations.

7.3.8. Reducing sugars determination

Reducing sugar concentrations were determined using the BCA assay. BCA solution was prepared before each experiment. Reagent A was mixed with reagent B in a ratio of 50:1. The reaction mixture (for soluble substrate) or supernatant (for insoluble substrate) (0.03 ml) was

mixed with freshly prepared BCA solution at 37 °C for 50 minutes to allow color formation from the reaction between released reducing sugars and BCA molecules. Samples were analyzed using UV-Vis spectroscopy at 560 nm. BCA forms a color complex with reducing sugars and the concentration of sugars was evaluated using a calibration plot obtained with a glucose standard.

7.3.9. Conjugation efficiency

Conjugation efficiency was determined using dialysis followed by Bradford assay to quantify enzyme concentration. EPC stock solution (0.1 ml) was diluted in 5.9 ml of citrate buffer (pH 4.6) to a final enzyme concentration 50 µg/ml. The conjugates were placed into membrane tubes with a 100-kDa MWCO and dialyzed for 24 h to allow free enzymes to pass through while retaining EPCs. Enzyme concentrations before and after dialysis were determined by Bradford protein assay. For this, 0.1 ml of conjugate solution was mixed with 1 ml of Bradford reagent and incubated at room temperature for 5 minutes. UV-Vis absorbance was measured against blank solution at 595 nm. The enzyme concentration was calculated using a calibration plot obtained for the Bovine serum albumin (BSA) standard. The fraction of conjugated enzymes was calculated as a ratio between the concentration of enzymes after dialysis to the concentration before dialysis.

7.3.10. Adsorption study

The stock solution of EPC or free enzymes was mixed with citrate buffer at pH 4.6 to make 2 mL of 50 µg/ml enzyme solution. Avicel cellulose (100 mg) was added to the mixture and incubated at 45 °C while mixing. Vials were removed from the bath at a different incubation times (0-240 minutes) and left for 30 minutes for sedimentation of cellulose. The fractional adsorption of free or conjugated enzymes on cellulose was determined by comparing the concentration of enzymes remaining in the solution to the initial enzyme concentration. The concentrations were determined using Bradford assay as described above.

7.3.11. Fermentable sugar quantification

Fermentable sugar (cellobiose, glucose, and xylose) yield from enzymatic hydrolysis was determined using a Waters (Milford, MA) HPLC system with Bio-Rad (Hercules, CA) Aminex HPX-87P column and refractive index detector (85 °C). Nanopure (18 mΩ) water was used as mobile phase at a flow rate 0.6 mL/min with a column of temperature 50 °C. Prior to HPLC, 1 mL of liquid dispersion phase was filtered using a 0.2-μm nylon filter (Pall Corporation; West Chester, PA).

7.4. Results and Discussion

7.4.1. Synthesis of polymers

In order to investigate effects of polymer structure and properties on hydrolytic activity of conjugated enzymes, copolymers of GMA and PEGMA with different molecular weights were synthesized. The copolymer composition was calculated according to ^{1}H NMR spectrum (**Fig. 7.1**). For poly (GMA-*co*-PEGMA), synthesized from PEGMA with the molecular weight 950 g/mol and GMA:PEGMA molar ratio 0.2:0.8 (GP_{950} 0.2:0.8), the molar ratio calculated by proton counting was 30.1:69.9 corresponding to a mass ratio of 6.0:94.0.

High dilution of the copolymer solution (1:2000) was used for experiments with enzymes immobilized by GP_{950} 0.2:0.8 because of the high molecular weight of that polymer and the large size of the resulted macromolecules. With increasing polymer concentration, the solution becomes more viscous which may lead to decreasing enzyme mobility and activity. Changing the polymer molecular weight as well as its chemical composition can, probably, improve EPCs activity. Therefore, a range of random copolymers and terpolymers, composed from PEGMA with the molecular weight 300 g/mol (GP_{300} and $GP_{300}P_{950,}$ respectively), were synthesized (**Table 7.1**). Due to inability to measure the molecular weight of GP_{950} 0.2:0.8 using gel permeation

chromatography (GPC), intrinsic viscosity measurements were used. According to the Mark–Houwink–Sakurada equation, intrinsic viscosity (η) relates to the molecular weight (M): $\eta = KM^{\alpha}$, where K is a constant and α is a scalar which relates to the "stiffness" of the polymer chains. It was shown that with the increasing amount of $PEGMA_{300}$ in the polymer composition, the intrinsic viscosity and molecular weight decreases. The intrinsic viscosity of poly(GMA-*co*-PEGMA), synthesized from PEGMA with the molecular weight 300 g/mol (GP_{300} 0.3:0.7) was measured as 0.168, while it was 0.945 for GP_{950} 0.2:0.8.

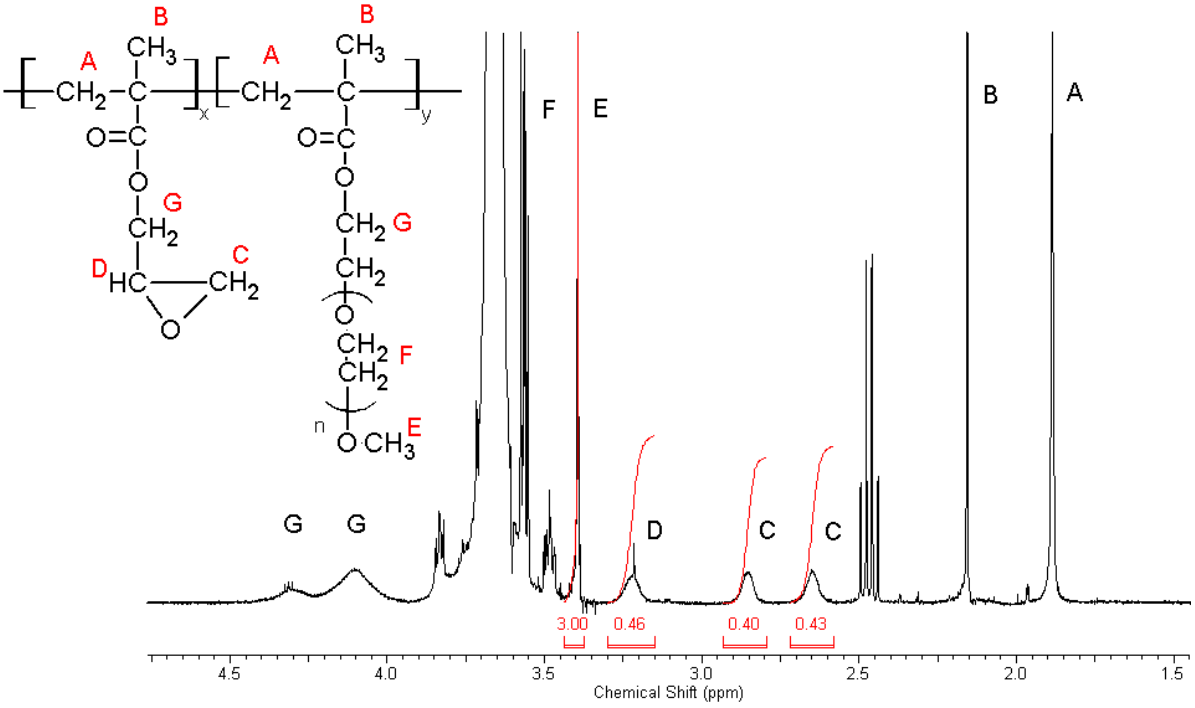

Figure 7.1. ^{1}H NMR spectrum of poly(GMA-*co*-PEGMA).

Table 7.1. Characteristics of polymers

Sample	*Copolymer composition GMA:PEGMA*	*Intrinsic viscosity*	*Average coil diameter, nm*
GP_{950} 0.2:0.8	0.31:0.69	0.945	25±4
$GP_{300}P_{950}$ 0.2:0.1:0.7	0.286:0.714	0.725	50±2
$GP_{300}P_{950}$ 0.2:0.3:0.5	0.282:0.718	0.734	33±2.5
$GP_{300}P_{950}$ 0.2:0.5:0.3	0.277:0.723	0.507	25±2
GP_{300} 0.1:0.9	0.135:0.865	0.234	21±0.5
GP_{300} 0.2:0.8	0.252:0.748	0.207	20±1
GP_{300} 0.3:0.7	0.37:0.63	0.168	
GP_{300} 0.5:0.5	0.563:0.437	0.126	

7.4.2. Formation of enzyme-polymer conjugates (EPC)

A commercial cellulase enzyme cocktail isolated from the *Trichoderma reesei* was used to model industrial conditions of biomass hydrolysis. The mixture of cellulases that is used in this study consists primarily of endoglucanases and cellobiohydrolases with smaller amounts β-glucosidase and other supplementary enzymes. Enzyme concentrations were determined using both Bradford assay and BCA using BSA standard and showed that original supplied protein concentration of the enzyme mixture was approximately 10% w/w. The conjugation of enzymes with the water-soluble polymer ligand (PL) poly(GMA-*co*-PEGMA) is shown in **Scheme 7.1**. Combination of the reactive epoxy functional groups and oligomeric PEGMA side groups in the polymer structure was used in order to improve the enzymatic catalytic activity for the biomass hydrolysis. PL's epoxy functionalities react with multiple amino groups of the enzyme lysine creating a covalently bonded enzyme-polymer conjugate. PEGMA fragments ensure solubility of the copolymer in aqueous solutions and steric stabilization of EPC.

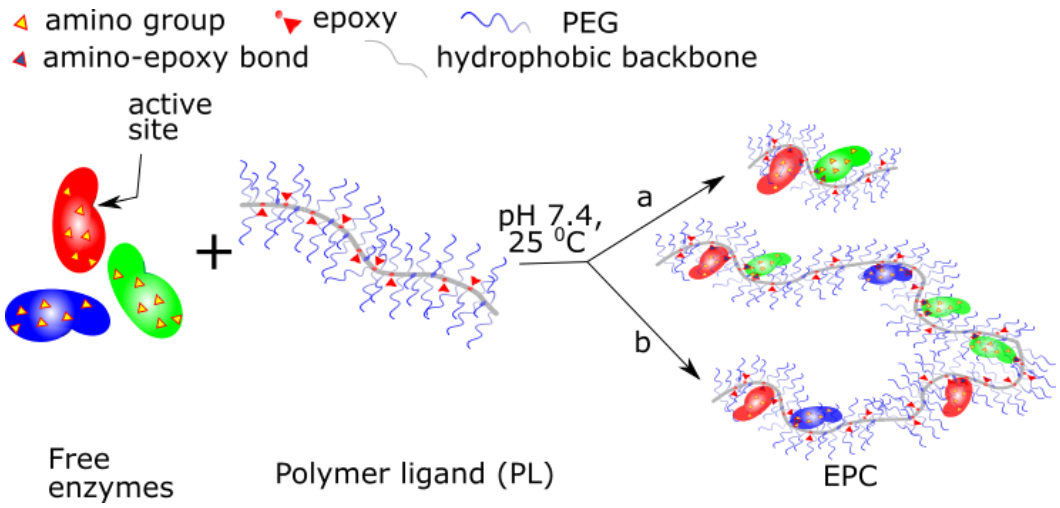

Scheme 7.1. Schematic representation of the enzyme-polymer conjugate (EPC) formation (a – EPC from GP300, b – EPC from GP950).

7.4.3. Optimization of polymer-enzyme conjugation on soluble substrate

To improve EPC performance, optimal conjugation conditions were experimentally found. In general, the conjugation reaction is sensitive to pH and polymer:enzyme ratio. At a pH range of 7-8.5 during conjugation, the reactivity of enzyme aliphatic amine groups is higher than other groups leading to increased activity and faster conjugation [17]. However, the highest enzymatic activity during hydrolysis was reported to be at a pH values 4-5 [18]. Therefore, in this work the conjugation was performed at a pH of 7.4 and adjusted to 4.6 for subsequent experiments. Optimal polymer concentration for conjugation with enzymes was found in a series of experiments by fixing the reaction time at 60 minutes, temperature at 45 °C, and enzyme concentration at 2 µg/ml. Total polymer concentration was varied from 0 µg to 50 µg (w/w) added per µg of enzyme. It was shown that increasing enzyme concentration on the PL leads to a gradual increase in sugar release until the sugar concentration approaches a maximum level at a 10 µg of the PL per 1 µg of the enzymes **(Fig. 7.2)**. Thus, the optimal ratio of 1:10 for enzyme:polymer was obtained for the

commercial enzyme cocktail. This ratio was used for all additional experiments to characterize enzyme activity.

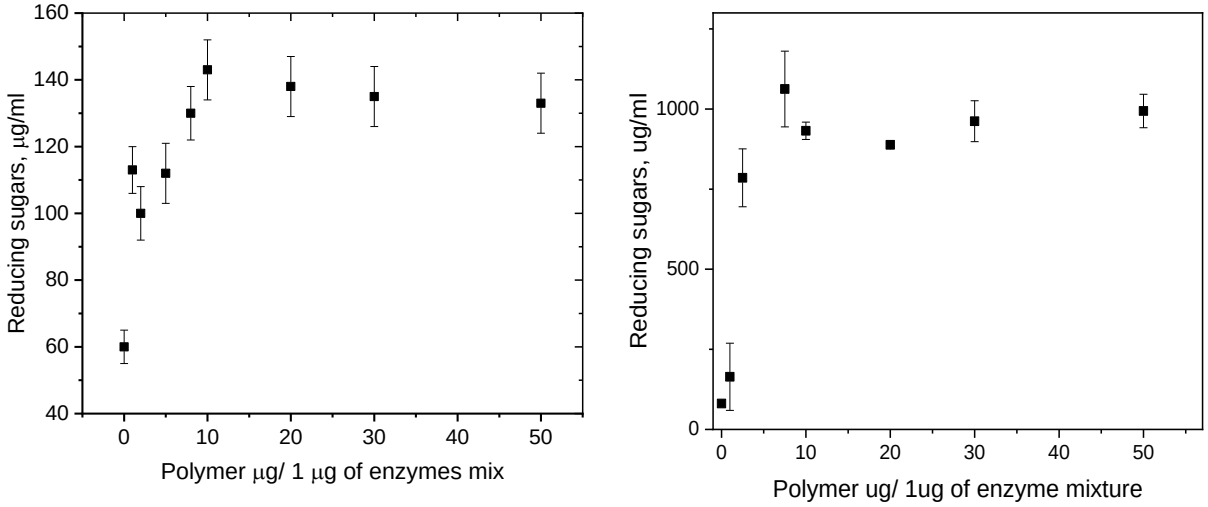

Figure 7.2. Reducing sugar yield for different polymer/enzyme ratios: left – GP_{950} EPC, right – GP_{300} EPC.

In order to quantify the amount of cellulases conjugated to the PL, a dialysis procedure was used. For this purpose, samples of conjugates were dialyzed for 24 h using the dialysis membranes with MWCO of 100 kDa. The free cellulase concentration was determined for each sample before and after the dialysis to calculate the conjugation efficiency. The results are shown in **Table 7.2**. The conjugates made from GP_{300} showed higher conjugation efficiency than the conjugate made from GP_{950}. The higher molecular weight of GP_{950} and longer $PEGMA_{950}$ side chains may result in more steric hindrance and, therefore, a lower conjugation rate.

Table 7.2. Conjugation efficiency of EPCs

Sample	***Amount of epoxy groups per molecule***	***Amount of conjugated enzyme, %***
GP_{300}0.3:0.7	91	70.8 ± 1.4
GP_{300}0.2:0.8	61	64.2 ± 1.5
GP_{950}0.2:0.8	1290	53.7 ±1.5

To estimate the influence of the polymer amount on conjugation efficiency, EPCs with different polymer:enzyme ratios were tested. The amount of conjugated enzyme for samples with different polymer:enzyme ratio increases with the polymer quantity and reaches the saturation at above 5 µg of the polymer per 1 µg of the enzymes (**Table 7.3**). Such behavior can be attributed to the average number of epoxy groups available for the conjugation reaction. The decreasing of the amount of PL in the system results in fewer epoxy groups and, therefore, lower conjugation efficiency. Thus, the optimal enzyme:polymer ratio of 1:10 for the conjugation also showed high conjugation efficiency.

Table 7.3. Conjugation efficiency for GP_{300} EPC for different polymer:enzyme ratios

GP_{300} 0.3:0.7:Enzyme ratio	***1:1***	***2.5:1***	***5:1***	***7.5:1***	***10:1***	***20:1***	***30:1***	***50:1***
Amount of conjugated enzyme, %	59.1	66.5	86.4	82.4	82.9	88.6	86.2	89.1

To compare the activity of the EPCs and free enzymes, the concentration of soluble sugars released from CMC was evaluated over several hours (**Fig. 7.3**). Vials were loaded with the commercial enzyme cocktail (2 µg/ml) and EPC with the same cellulase concentration. Both samples were simultaneously mixed with the substrate prior to reaction, incubated, and sampled periodically as shown in **Figure 7.3**. The resulting sugar concentration was plotted as a function of time. The optimized EPC demonstrated a higher hydrolysis rate and yield than the free enzymes (**Fig. 7.2**). These results indicate that the enzyme-polymer conjugates demonstrate a higher catalytic activity on soluble substrate.

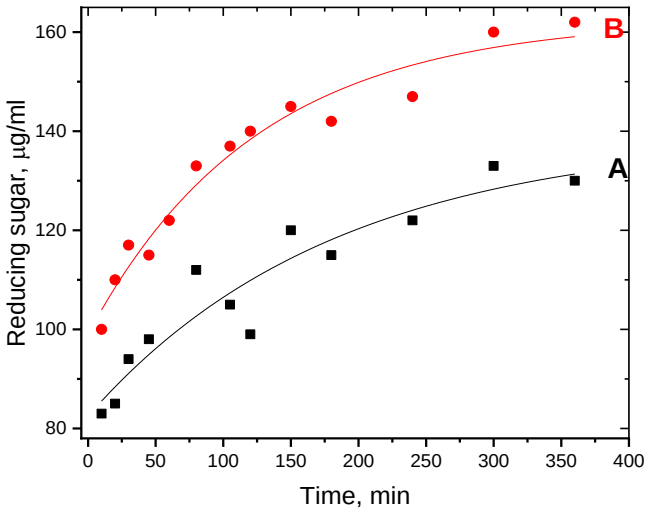

Figure 7.3. Sugar release *vs.* time: A- control enzymatic cocktail; B- GP_{950} EPC.

The influence of free enzymes in the system was also evaluated. Conjugate mixtures were dialyzed for 24 h and used for enzymatic hydrolysis. During dialysis, the unconjugated enzymes were separated from the conjugated enzymes. The concentration of the conjugated enzymes in EPCs were determined and adjusted to the original 3.75 µg/ml using citrate buffer (pH 4.6). The same concentration of enzymes (3.75 µg/ml) was maintained for all samples (dialyzed and non-dialyzed), and the activity of the conjugates before and after dialysis was measured using the BCA assay. As seen in **Figure 7.4**, the activity of free enzymes is less than that of dialyzed conjugates demonstrating that the conjugation affect enzyme activity. At the same time, the dialyzed conjugates show lower hydrolysis yield than the non-dialyzed conjugates (mixture of free and conjugated enzymes). This observation indicates that using a mixture of free and conjugated enzymes is beneficial for the EPCs preparation costs.

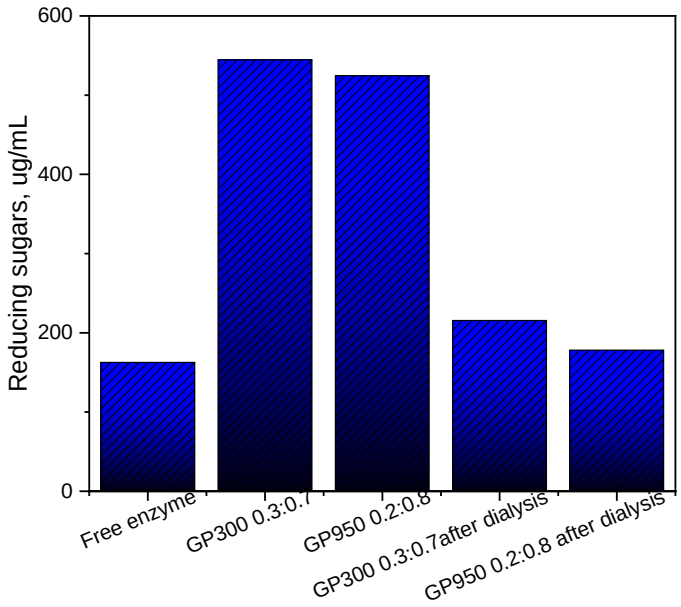

Figure 7.4. Reducing sugar yield for free enzyme, GP_{300} 0.3:0.7 EPC, and GP_{950} 0.2:0.8 EPC before the dialysis (3.75 µg/ml enzyme concentration) and after the dialysis.

Previous reports showed that enzymes can act in a synergistic or cooperative manner [5]. Synergism among different cellulases depends on the composition and concentration of enzymes, the substrate nature, the enzyme to substrate ratio, cellulase affinity for substrate, and stereospecificity of components [12]. Our results showed that both free and conjugated enzymes act synergistically to improve the overall activity. Dialysis might result in changing the enzyme composition (amount of endoglucanases, exoglucanases etc.) and such changes could be responsible for the activity reduction in dialyzed conjugates.

7.4.4. Hydrolytic efficiency of EPCs on insoluble substrate – filter paper

Industrial bioconversion processes use complex, insoluble substrates. In order to evaluate the EPCs activity on insoluble substrates, filter paper was first used as a model substrate. The conjugate hydrolytic efficiency was measured with higher enzyme concentrations and a longer incubation time. The hydrolytic efficiency of EPCs and free enzymes with insoluble substrate (**Fig.**

7.5) was evaluated by measuring the amount of reducing sugars released from filter paper at different enzyme concentrations after 16 h of hydrolysis. EPCs showed higher hydrolytic efficiency than the free enzymes within the concentration range. However, the efficiency difference decreases with increasing enzyme concentrations.

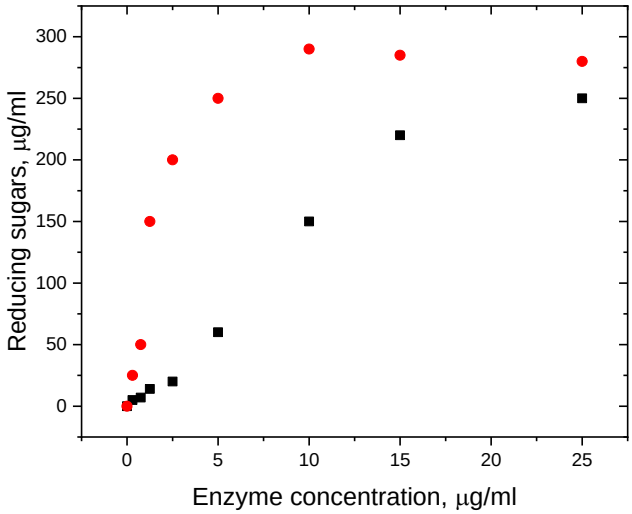

Figure 7.5. Sugar release evaluated for Whatman #1 filter paper substrate: free enzymes – squares, GP_{950} EPC –circles

The highest difference in activity between EPC and free enzymes was obtained at 3.75 µg/ml. Therefore, time courses of filter paper hydrolysis with EPCs and free enzymes were investigated at this concentration (**Fig. 7.6)**. Two sets of vials were loaded with commercial cellulase cocktail and EPCs. Although the initial hydrolysis rate was similar for the conjugates and free enzymes, a significant increase in the concentration of reducing sugars was observed with the EPCs after 20 hours.

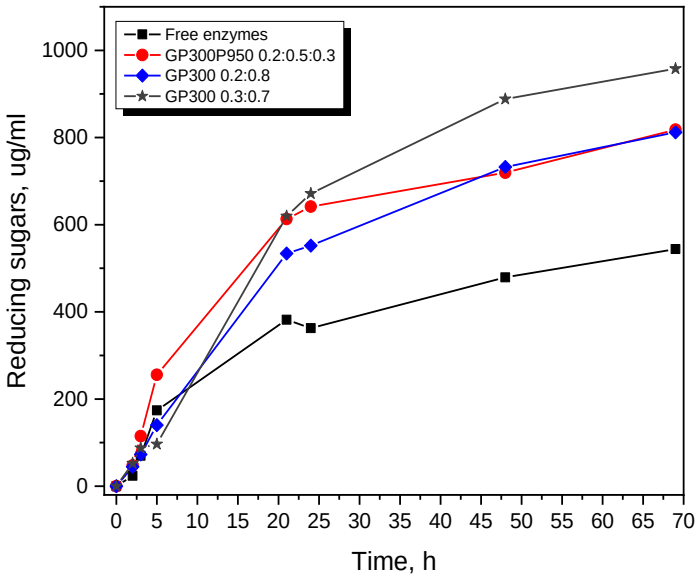

Figure 7.6. Sugar release using free enzyme and enzyme- polymer conjugates *vs* time. Enzyme concentration – 3.75 µg/mL.

Higher concentrations of EPCs were also investigated to determine if similar trends would be observed. **Table 7.4** shows hydrolysis results with the conjugates and free enzymes at higher enzyme loadings. Similar to previous result, increasing cellulase loading diminishes the difference in activity between EPCs and free enzymes, but attachment is still not detrimental. Reduction of the increased EPC activity at higher enzyme concentrations could be attributable to the crowding effect. Enzyme crowding allows synergistic interaction and improves substrate hydrolysis. With increasing concentration, free enzymes can also benefit from the crowding effect, reducing the advantage of EPCs.

However, the cellulase concentration that was used is far lower than the usual enzyme concentration that will yield more than 90% of sugar in biomass. To evaluate EPCs' hydrolytic yield at even higher cellulase concentrations, high performance liquid chromatography (HPLC) was used to measure the resulting higher sugar concentrations. The final cellulase concentrations

were 3.75, 10, 50, 100, 500, and 2000 µg/ml. The highest cellulase concentration for GP_{950}0.2:0.8-enzyme conjugate was 500 µg/ml. Results are shown in **Table 7.5**.

Table 7.4. Hydrolysis results using free and conjugated enzymes at different concentrations.

Concentration of enzyme, µg/mL	***Reducing sugars, µg/ml***		
	Free enzyme	**GP_{300} 0.3:0.7 EPC**	**GP_{950} 0.2:0.8 EPC**
3.75	573.5	710.0	911.0
10	1406.0	1558.5	1790.0
50	3079.5	3149.5	2954.0

Increasing enzyme concentration enables 70% cellulose conversion in 24 h. As shown in the previous experiment, the difference in activity between conjugates and free enzymes was negligible. Unlike the results using the BCA assay which is used to measure carbohydrate reducing ends, HPLC quantifies glucose and cellobiose but not larger oligomers. At lower enzyme concentrations, more glucose oligomers can be present, resulting in higher concentrations of reducing ends with the conjugates than with free enzymes. Glucose and cellobiose concentrations were similar for free enzymes and EPCs.

The reduction of the activity advantage for conjugated enzymes at higher enzyme concentrations suggests that the enzymes are crowded on the cellulose substrate. This phenomenon was recently studied using high-speed atomic force microscopy [13]. Cellulose surface roughness can cause cellulases to form molecular traffic jams. At the same time, the formation of these surface clusters can be controlled by the enzyme concentration bound on the cellulose surface. Therefore, addition of higher amount of enzymes will cause enzyme crowding and diminish the difference in effectiveness between EPCs and free enzymes.

Table 7.5. Hydrolysis yield of free and conjugated enzymes at different concentrations via HPLC

Concentration of enzyme, μg/mL	***Free enzyme***		***GP_{300} 0.3:0.7 EPC***		***GP_{950} 0.2:0.8 EPC***	
	Glucose, g/L	Cellobiose, g/L	Glucose, g/L	Cellobiose, g/L	Glucose, g/L	Cellobiose, g/L
3.75	0.3	0.6	0.3	0.7	0.3	0.9
10	0.3	1.0	0.4	1.1	0.4	1.0
50	0.9	2.4	1.0	2.0	1.0	2.1
100	1.4	2.8	2.0	2.9	2.0	3.0
500	4.8	2.6	5.0	2.7	4.8	2.6
2000	7.0	1.1	7.0	0.9		

In principle, enzymatic action is based on a lock-and-key mechanism. Therefore, the adsorption of enzyme on substrate during hydrolysis can be negatively affected when attached to polymers or any other immobilization matrix. Cellulases usually perform in a processive manner moving along the polysaccharide chain. A large complex containing tens to hundreds of immobilized enzymes is unlikely to be able to process across the substrate surface [10,16,17].

Avicel (60−80% crystallinity) was used as a substrate to compare the adsorption of free and conjugated enzymes on cellulose. Adsorption isotherms were evaluated at 45 °C using enzymes at 50 μg/ml. Isotherms for EPCs and free enzymes are shown in **Figure 7.7**. Enzyme binding reaches saturation in 15 minutes, and enzyme conjugation reduced adsorption relative to the free enzymes. According to the previous studies, the presence of polyethylene glycol (PEG) fragments in the molecule changes enzyme adsorption parameters [21] by facilitating enzyme desorption from catalytic sites. The PL used for EPC formation contain PEG fragments in their structure. The presence of PEG fragments may cause the reduction of EPC adsorption on cellulose. At the same time, conjugates made from GP_{300} also showed lower adsorption than the GP_{950} EPC.

This could be possibly due to the lower molecular weight of polymer scaffold for GP_{300} resulting in higher mobility of conjugate.

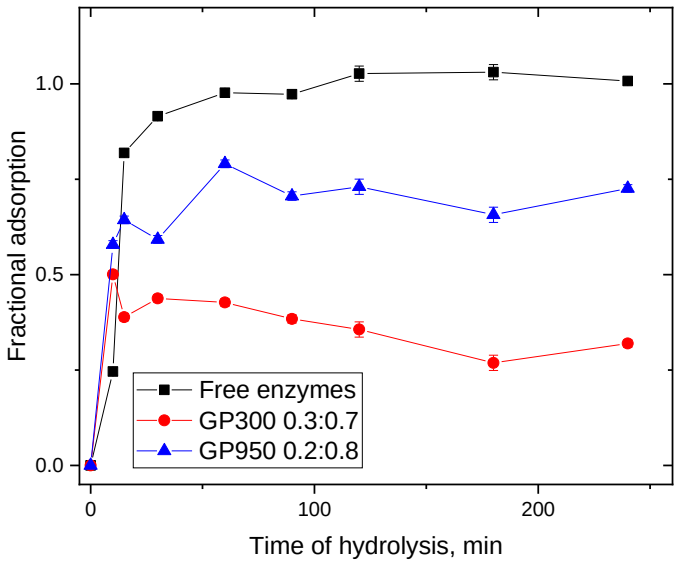

Figure 7.7. Adsorptions isotherms of the free and conjugated enzymes on Avicel. Enzyme concentration – 50 μg/mL.

7.4.5. Hydrolysis yield with EPCs using pretreated biomass

Unlike filter paper or other model substrates that consist of pure cellulose, lignocellulosic biomass contains cellulose, hemicellulose, and lignin. Pretreatment is essential to begin cell wall deconstruction and reduce recalcitrance. Acid and alkaline pretreatment are common techniques used to increase enzyme accessibility by altering biomass structure and composition [18–21]. Effective enzymatic hydrolysis requires sufficient cellulase loading to produce an appreciable yield (>85 %) [22]. Therefore, different enzyme concentrations were used in order to evaluate the influence of enzyme concentration on the hydrolysis of pretreated biomass.

The use of polymer supports for enzyme immobilization can either increase or decrease hydrolysis yield. Some polymers that reduce enzyme movement or restrict substrate accessibility will hinder enzyme activity while those that adsorbed to lignin will prevent lignin nonproductive

interaction with enzyme thus enhance hydrolysis yield [25,27]. Therefore, the hydrolysis yield with EPCs and free enzymes was investigated to determine the effect of the polymer support. The results **(Fig. 7.8)** show that EPCs produce similar yields with free enzymes at all enzyme concentrations. Hydrolysis yields continued to increase with higher enzyme concentration and acid-pretreated biomass. However, yields from alkaline-pretreated biomass increased more gradually and produced little improvement beyond 500 µg/mL (6.1 g/L for free enzymes, 6.4 g/L for EPCs). Hydrolysis yields from acid-pretreated switchgrass reached 100% of theoretical (11.11 g/L) with the GP_{300} EPC.

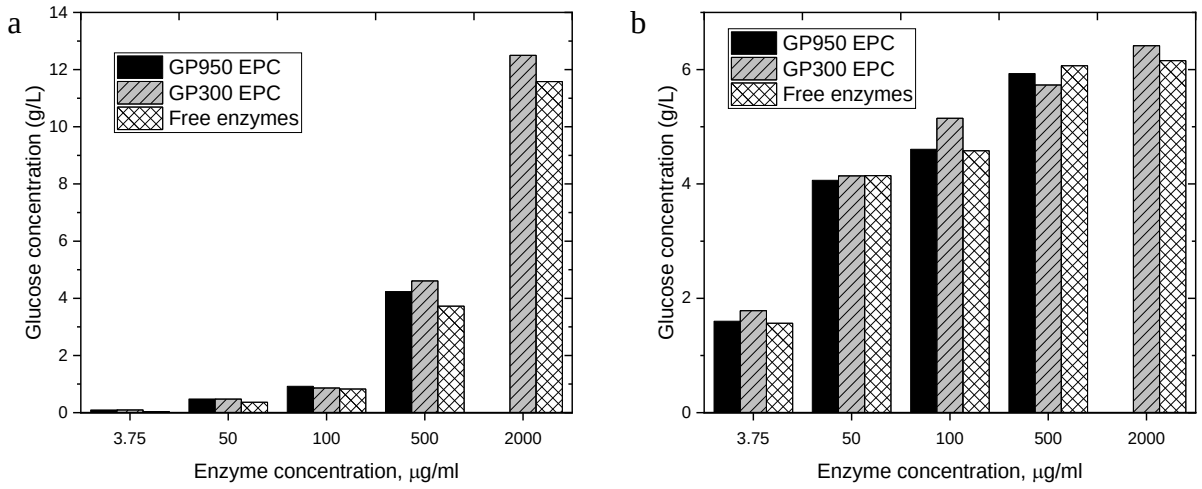

Figure 7.8. Glucose yield in hydrolysis of biomass pretreated using different methods: a – DA pretreated switchgrass at 24h, b – SAA pretreated switchgrass at 24h.

EPC hydrolysis yields were consistently higher than those of free enzymes at all times. PEG has been reported to interact with lignin through hydrophobic and hydrogen bond interactions, and reduce nonproductive enzyme adsorption to lignin [27,28]. Acid-pretreated biomass contains higher lignin content than alkaline pretreated biomass. Therefore, the presence of PEG fragments in EPCs is expected to be more pronounced with acid-pretreated biomass in agreement with our result.

Interestingly, yields with alkaline-pretreated substrate were higher than those with acid-pretreated substrate at concentrations below 2000 µg/mL. The lack of increase in hydrolysis yield above ~6 g/L with alkaline-pretreated samples, even at higher enzyme concentrations, could be associated with hemicellulose composition. Unlike acid-pretreated samples, alkaline-pretreated samples are high in hemicellulose [26]. Structurally, hemicellulose matrix embeds cellulose microfibrils, and prevents cellulase accessibility [31]. Therefore, the reduction in cellulase accessibility to cellulose could have prevented further increase in hydrolysis yield of alkaline-pretreated samples.

7.4.6. Glucose inhibition of EPCs

As cellulose hydrolysis progresses, glucose concentrations increase resulting in enzyme product inhibition. Currently, lower substrate loadings (~ 1% glucan substrate equivalent) are used to reduce glucose inhibition. Therefore, the effect of different concentrations of glucose (45 and 90 mg/ml) on EPC hydrolysis yield was investigated using alkaline-pretreated switchgrass that could provide information on effect of hemicellulose on enzyme inhibition.

Results (**Fig. 7.9a and 7.9b**) show that glucose inhibits free enzymes and EPCs differently. Generally, free enzymes were inhibited more than EPCs. Xylose yields were effected less than glucose yields. Although glucose inhibition was evident with EPCs at 24 h, by 72 h hydrolysis levels were not different than treatments with free enzymes or EPCs without glucose addition. EPCs were able to overcome the initial inhibitory effect of glucose even when supplemented with 90 mg/ml.

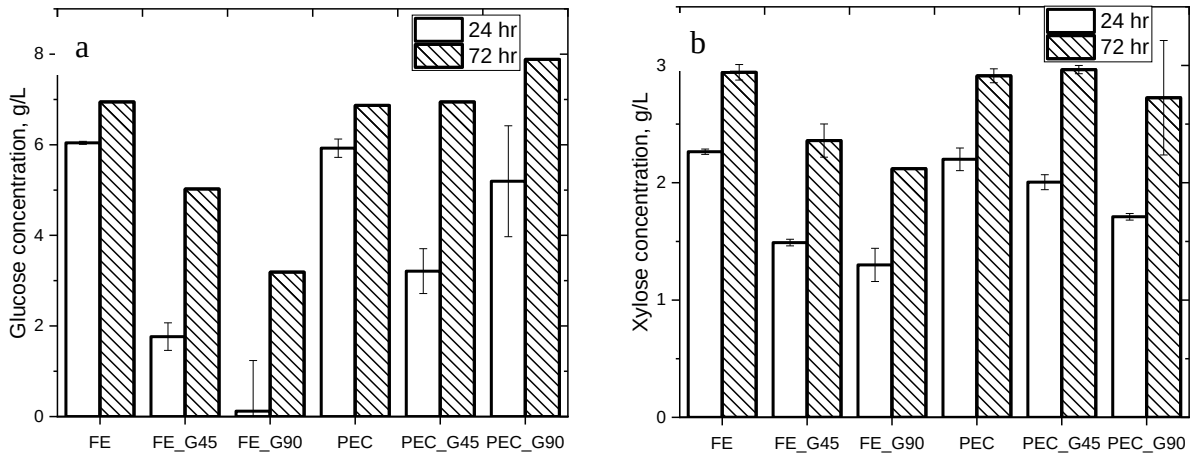

Figure 7.9. Hydrolysis yield of enzyme (FE) and GP9500.2:0.8 EPC at 500 μg/mL in presence of different concentrations of glucose (45 and 90 mg/ml, G45 and G90, respectively), a: glucose yield and b: xylose yield.

EPC resistance to glucose inhibition is promising for application with higher hydrolysis substrate loadings. Although the mechanism of EPC inhibition resistance is unclear, it is possible that glucose interaction with the EPC polymers causes changes in EPC conformation. A coil conformation of the EPC may create a micro-environment shielding the attached enzyme from the higher concentrations of glucose in the bulk medium.

7.5. Conclusions

The formation of artificial polymeric cellulosomes from cellulases and poly (GMA-*co*-PEGMA) provides the ability to increase the catalytic efficiency of cellulose hydrolysis. The copolymers with different molecular weight and composition were synthesized and the influence of polymer structure on enzymatic activity of EPCs was evaluated. The difference in activity between free and conjugated enzymes is more pronounced at lower enzyme concentrations. However, conjugation and formation of covalent bonds between enzyme and the polymers does not lead to a decrease in catalytic efficiency. The pretreated biomass experiments showed that the hydrolysis yield depends on the biomass pretreatment. Enzyme attachment in the conjugates

reduced or eliminated the effect of glucose inhibition during the hydrolysis the at tested loading levels. Future work will include attachment of magnetic nanoparticle to EPCs to facilitate enzyme recovery and reuse.

7.6. References

(1) Eriksson, T.; Karlsson, J.; Tjerneld, F. A Model Explaining Declining Rate in Hydrolysis of Lignocellulose Substrates with Cellobiohydrolase I (Cel7A) and Endoglucanase I (Cel7B) of Trichoderma Reesei. *Appl. Biochem. Biotechnol.* **2002**, *101* (1), 41–60. https://doi.org/10.1385/ABAB:101:1:41.

(2) Holtzapple, M.; Cognata, M.; Shu, Y.; Hendrickson, C. Inhibition OfTrichoderma Reesei Cellulase by Sugars and Solvents. *Biotechnol. Bioeng.* **1990**, *36* (3), 275–287. https://doi.org/10.1002/bit.260360310.

(3) Yang, B.; Dai, Z.; Ding, S.-Y.; Wyman, C. E. Enzymatic Hydrolysis of Cellulosic Biomass. *Biofuels* **2011**, *2* (4), 421–449. https://doi.org/10.4155/bfs.11.116.

(4) Fierobe, H.-P.; Mingardon, F.; Mechaly, A.; Bélaïch, A.; Rincon, M. T.; Pagès, S.; Lamed, R.; Tardif, C.; Bélaïch, J.-P.; Bayer, E. A. Action of Designer Cellulosomes on Homogeneous *Versus* Complex Substrates: Controlled Incorporation Of Three Distinct Enzymes Into A Defined Trifunctional Scaffoldin. *J. Biol. Chem.* **2005**, *280* (16), 16325–16334. https://doi.org/10.1074/jbc.M414449200.

(5) Mingardon, F.; Chanal, A.; Lopez-Contreras, A. M.; Dray, C.; Bayer, E. A.; Fierobe, H.-P. Incorporation of Fungal Cellulases in Bacterial Minicellulosomes Yields Viable, Synergistically Acting Cellulolytic Complexes. *Appl. Environ. Microbiol.* **2007**, *73* (12), 3822–3832. https://doi.org/10.1128/AEM.00398-07.

(6) Murashima, K.; Kosugi, A.; Doi, R. H. Synergistic Effects on Crystalline Cellulose Degradation between Cellulosomal Cellulases from Clostridium Cellulovorans. *J. Bacteriol.* **2002**, *184* (18), 5088–5095. https://doi.org/10.1128/JB.184.18.5088-5095.2002.

(7) Doi, R. H.; Kosugi, A.; Murashima, K.; Tamaru, Y.; Han, S. O. Cellulosomes from Mesophilic Bacteria. *J. Bacteriol.* **2003**, *185* (20), 5907–5914. https://doi.org/10.1128/JB.185.20.5907-5914.2003.

(8) Chang, R. H.-Y.; Jang, J.; Wu, K. C.-W. Cellulase Immobilized Mesoporous Silica Nanocatalysts for Efficient Cellulose-to-Glucose Conversion. *Green Chem.* **2011**, *13* (10), 2844. https://doi.org/10.1039/c1gc15563f.

(9) Krauss, J.; Zverlov, V. V.; Schwarz, W. H. *In Vitro* Reconstitution of the Complete Clostridium Thermocellum Cellulosome and Synergistic Activity on Crystalline Cellulose. *Appl. Environ. Microbiol.* **2012**, *78* (12), 4301–4307. https://doi.org/10.1128/AEM.07959-11.

(10) Cho, E. J.; Jung, S.; Kim, H. J.; Lee, Y. G.; Nam, K. C.; Lee, H.-J.; Bae, H.-J. Co-Immobilization of Three Cellulases on Au-Doped Magnetic Silicananoparticles for the Degradation of Cellulose. *Chem Commun* **2012**, *48* (6), 886–888. https://doi.org/10.1039/C2CC16661E.

(11) Kamat, R. K.; Ma, W.; Yang, Y.; Zhang, Y.; Wang, C.; Kumar, C. V.; Lin, Y. Adsorption and Hydrolytic Activity of the Polycatalytic Cellulase Nanocomplex on Cellulose. *ACS Appl. Mater. Interfaces* **2013**, *5* (17), 8486–8494. https://doi.org/10.1021/am401916k.

(12) Yadavalli, N. S.; Borodinov, N.; Choudhury, C. K.; Quiñones-Ruiz, T.; Laradji, A. M.; Tu, S.; Lednev, I. K.; Kuksenok, O.; Luzinov, I.; Minko, S. Thermal Stabilization of

Enzymes with Molecular Brushes. *ACS Catal.* **2017**, *7* (12), 8675–8684. https://doi.org/10.1021/acscatal.7b03138.

(13) Nidetzky, B.; Claeyssens, M. Specific Quantification Oftrichoderma Reesei Cellulases in Reconstituted Mixtures and Its Application to Cellulase-Cellulose Binding Studies. *Biotechnol. Bioeng.* **1994**, *44* (8), 961–966. https://doi.org/10.1002/bit.260440812.

(14) Igarashi, K.; Uchihashi, T.; Koivula, A.; Wada, M.; Kimura, S.; Okamoto, T.; Penttila, M.; Ando, T.; Samejima, M. Traffic Jams Reduce Hydrolytic Efficiency of Cellulase on Cellulose Surface. *Science* **2011**, *333* (6047), 1279–1282. https://doi.org/10.1126/science.1208386.

(15) Kamat, R. K.; Zhang, Y.; Anuganti, M.; Ma, W.; Noshadi, I.; Fu, H.; Ekatan, S.; Parnas, R.; Wang, C.; Kumar, C. V.; et al. Enzymatic Activities of Polycatalytic Complexes with Nonprocessive Cellulases Immobilized on the Surface of Magnetic Nanoparticles. *Langmuir* **2016**, *32* (44), 11573–11579. https://doi.org/10.1021/acs.langmuir.6b02573.

(16) Wang, Y.; Chen, D.; Wang, G.; Zhao, C.; Ma, Y.; Yang, W. Immobilization of Cellulase on Styrene/Maleic Anhydride Copolymer Nanoparticles with Improved Stability against PH Changes. *Chem. Eng. J.* **2018**, *336*, 152–159. https://doi.org/10.1016/j.cej.2017.11.030.

(17) Balasubramanya, V. Antibody Conjugation. *Mater. Methods* **2018**, *8*. https://doi.org/10.13070/mm.en.8.2670.

(18) Vazquez-Duhalt, R.; Tinoco, R.; D'Antonio, P.; Topoleski, L. D. T.; Payne, G. F. Enzyme Conjugation to the Polysaccharide Chitosan: Smart Biocatalysts and Biocatalytic Hydrogels. *Bioconjug. Chem.* **2001**, *12* (2), 301–306. https://doi.org/10.1021/bc000095u.

(19) Ting, C. L.; Makarov, D. E.; Wang, Z.-G. A Kinetic Model for the Enzymatic Action of Cellulase. *J. Phys. Chem. B* **2009**, *113* (14), 4970–4977. https://doi.org/10.1021/jp810625k.

(20) Igarashi, K.; Koivula, A.; Wada, M.; Kimura, S.; Penttilä, M.; Samejima, M. High Speed Atomic Force Microscopy Visualizes Processive Movement of *Trichoderma Reesei* Cellobiohydrolase I on Crystalline Cellulose. *J. Biol. Chem.* **2009**, *284* (52), 36186–36190. https://doi.org/10.1074/jbc.M109.034611.

(21) Park, J. W.; Takahata, Y.; Kajiuchi, T.; Akehata, T. Effects of Nonionic Surfactant on Enzymatic Hydrolysis of Used Newspaper. *Biotechnol. Bioeng.* **1992**, *39* (1), 117–120. https://doi.org/10.1002/bit.260390117.

(22) Dadi, A. P.; Varanasi, S.; Schall, C. A. Enhancement of Cellulose Saccharification Kinetics Using an Ionic Liquid Pretreatment Step. *Biotechnol. Bioeng.* **2006**, *95* (5), 904–910. https://doi.org/10.1002/bit.21047.

(23) Chundawat, S. P. S.; Beckham, G. T.; Himmel, M. E.; Dale, B. E. Deconstruction of Lignocellulosic Biomass to Fuels and Chemicals. *Annu. Rev. Chem. Biomol. Eng.* **2011**, *2* (1), 121–145. https://doi.org/10.1146/annurev-chembioeng-061010-114205.

(24) Norvell, K.; Nghiem, N. Soaking in Aqueous Ammonia (SAA) Pretreatment of Whole Corn Kernels for Cellulosic Ethanol Production from the Fiber Fractions. *Fermentation* **2018**, *4* (4), 87. https://doi.org/10.3390/fermentation4040087.

(25) Ávila-Lara, A. I.; Camberos-Flores, J. N.; Mendoza-Pérez, J. A.; Messina-Fernández, S. R.; Saldaña-Duran, C. E.; Jimenez-Ruiz, E. I.; Sánchez-Herrera, L. M.; Pérez-Pimienta, J. A. Optimization of Alkaline and Dilute Acid Pretreatment of Agave Bagasse by

Response Surface Methodology. *Front. Bioeng. Biotechnol.* **2015**, *3*. https://doi.org/10.3389/fbioe.2015.00146.

(26) Pryor, S. W.; Karki, B.; Nahar, N. Effect of Hemicellulase Addition during Enzymatic Hydrolysis of Switchgrass Pretreated by Soaking in Aqueous Ammonia. *Bioresour. Technol.* **2012**, *123*, 620–626. https://doi.org/10.1016/j.biortech.2012.07.040.

(27) Ouyang, J.; Dong, Z.; Song, X.; Lee, X.; Chen, M.; Yong, Q. Improved Enzymatic Hydrolysis of Microcrystalline Cellulose (Avicel PH101) by Polyethylene Glycol Addition. *Bioresour. Technol.* **2010**, *101* (17), 6685–6691. https://doi.org/10.1016/j.biortech.2010.03.085.

(28) Hsieh, C. C.; Cannella, D.; Jørgensen, H.; Felby, C.; Thygesen, L. G. Cellobiohydrolase and Endoglucanase Respond Differently to Surfactants during the Hydrolysis of Cellulose. *Biotechnol. Biofuels* **2015**, *8* (1). https://doi.org/10.1186/s13068-015-0242-y.

(29) Mackenzie, K. J.; Francis, M. B. Recyclable Thermoresponsive Polymer–Cellulase Bioconjugates for Biomass Depolymerization. *J. Am. Chem. Soc.* **2013**, *135* (1), 293–300. https://doi.org/10.1021/ja309277v.

(30) Sipos, B.; Szilágyi, M.; Sebestyén, Z.; Perazzini, R.; Dienes, D.; Jakab, E.; Crestini, C.; Réczey, K. Mechanism of the Positive Effect of Poly(Ethylene Glycol) Addition in Enzymatic Hydrolysis of Steam Pretreated Lignocelluloses. *C. R. Biol.* **2011**, *334* (11), 812–823. https://doi.org/10.1016/j.crvi.2011.06.005.

(31) Silveira, R. L.; Stoyanov, S. R.; Gusarov, S.; Skaf, M. S.; Kovalenko, A. Plant Biomass Recalcitrance: Effect of Hemicellulose Composition on Nanoscale Forces That Control Cell Wall Strength. *J. Am. Chem. Soc.* **2013**, *135* (51), 19048–19051. https://doi.org/10.1021/ja405634k.

(32) Kataoka, K.; Miyazaki, H.; Okano, T.; Sakurai, Y. Sensitive Glucose-Induced Change of the Lower Critical Solution Temperature of Poly[N,N-(Dimethylacrylamide)-Co-3-(Acrylamido)-Phenylboronic Acid] in Physiological Saline. *Macromolecules* **1994**, *27* (4), 1061–1062. https://doi.org/10.1021/ma00082a028.

(33) VandenBerg, M. A.; Webber, M. J. Biologically Inspired and Chemically Derived Methods for Glucose-Responsive Insulin Therapy. *Adv. Healthc. Mater.* **2019**, 1801466. https://doi.org/10.1002/adhm.201801466.

(34) Guo, Q.; Zhang, T.; An, J.; Wu, Z.; Zhao, Y.; Dai, X.; Zhang, X.; Li, C. Block versus Random Amphiphilic Glycopolymer Nanopaticles as Glucose-Responsive Vehicles. *Biomacromolecules* **2015**, *16* (10), 3345–3356. https://doi.org/10.1021/acs.biomac.5b01020.

(35) Ito, Y.; Casolaro, M.; Kono, K.; Imanishi, Y. An Insulin-Releasing System That Is Responsive to Glucose. *J. Controlled Release* **1989**, *10* (2), 195–203. https://doi.org/10.1016/0168-3659(89)90063-1.

CHAPTER 8. CONCLUSIONS AND FUTURE WORK

8.1. Conclusions

The goal of this work is to investigate interactions between range of new polymers and various cargo molecules and determine whether those interactions affect the physicochemical properties of the resulted colloids. For this purpose, two types of colloid systems were explored: i) peptide-loaded invertible micellar assemblies (IMAs), formed using hydrophobic interactions between amphiphilic invertible polymers (AIP) and peptides (HA, V5, or peptide-based vaccine), and ii) polymeric cellulosomes made from polymer ligand (PL), copolymer of glycidyl methacrylate (GMA) and poly(ethylene glycol) methyl ether methacrylate (PEGMA) and mixture of cellulases, using covalent bonding. The purpose of the research was to evaluate if colloids properties are affected by changes in responsive polymer characteristics as well as if the developed macromolecular structure and composition need further synthetic modification/optimization.

Library of AIPs were synthesized from poly(ethylene glycol) (PEG) (as the hydrophilic constituent) and either aliphatic dicarboxylic acids or polytetrahydrofurane (PTHF) (as the hydrophobic constituent). AIPs can self-assemble into micellar architectures with the increasing of AIP concentration and rapidly switch macromolecular conformation in response to changes in solvent polarity.

A detailed ^{1}H NMR spectroscopic study along with DLS measurements were used to confirm “host–guest” interactions between IMAs from AIPs and two different peptides (HA and V5) (Chapter 3). Mixed micellar assemblies with incorporated peptide molecules were formed in an aqueous solution at different AIP concentrations and the polymer/peptide ratio. The inner part of the assemblies consists predominantly of the hydrophobic moieties of both the polymer and the peptide, whereas the hydrophilic fragments of the polymer and peptide comprise the exterior of

the mixed micellar nanostructures. The peptide loci in the assemblies appear to depend on the peptide chemical structure (particularly, specific interactions between amino acids and AIP fragments).

Further, spin labeling along with the EPR spectroscopy were used to probe the peptide position and dynamics in IMAs (Chapter 4). The success of peptide spin labeling is confirmed with MS and EPR spectroscopy. The labeled peptide was incorporated into the IMAs from both polymers as indicated by the EPR spectral changes, which show contributions from peptide primarily in two areas/regions, near the more compact, crowding IMA interior (core) and the less compact exterior (shell). Furthermore, increasing acetone concentration was used to trigger the conformation changes of IMAs. For both IMAs the mobile spectral component consistent with peptide located within the IMA's exterior was increased as acetone concentration was increased. This finding is consistent with the expectation that acetone triggers IMAs demicellization and creates more space within the micellar assemblies for the peptide to move more dynamically or toward the IMA exterior.

As the next step, AIPs micellar assemblies were put in contact with microcavity supported DOPC lipid membrane and the impact of the AIP micellar assemblies on membrane diffusivity and permeability were measured using Fluorescence lifetime correlation spectroscopy and Electrochemical Impedance Spectroscopy (Chapter 5). The AIP micelles, based on the most hydrophobic macromolecule; PEG_{600}-$PTHF_{650}$ (among the three AIPs explored), showed strongest interaction with the membrane, above its cmc. Overall, the data indicate that PEG_{600}-$PTHF_{650}$ micellar assemblies interact intimately with the bilayer decreasing membrane diffusivity whilst increasing permeability, but effects were much weaker for the more hydrophilic AIP micelles. Consistent with this data, micellar assemblies formed from PEG_{600}-$PTHF_{650}$ and loaded with dye

were demonstrated from fluorescence microscopy to adsorb at, and release the dye into, the DOPC membrane. The data indicate that PEG_{600}-$PTHF_{650}$ micelles undergo inversion and release of cargo into the bilayer. Whereas for two other more hydrophilic polymers, D10 and S10, there was no evidence for dye-cargo release from the assemblies, rather the AIP micelles appeared to adsorb at the membrane interface where they were immobile (where inversion does not occur or occurs slowly).

In order to evaluate the efficacy of the AIP micellar assemblies as a peptide antigen delivery system, the peptide-based vaccine was incorporated into the $PEG_{600}PTHF_{650}$ micellar assemblies and evaluated in vitro and in pigs (Chapter 6). While the peptide alone was not uptaken by Vero cells due to its hydrophobic nature the micellar assemblies clearly enhanced the bioavailability and delivery of the peptide into cells in vitro and in vivo. The adjuvant effects in enhancing antibody mediated immunity are clearly substantiated by the significantly higher peptide-specific antibody titers in piglets vaccinated with AIP-peptide micellar assemblies compared to control piglets vaccinated with peptide alone.

Other type of colloids was formed by covalent bonding of copolymers synthesized from GMA and PEGMA and cellulases (Chapter 7). We assign the term “polymeric cellulosomes” over definition of these enzyme-polymer conjugates (EPCs). The formation of polymeric cellulosomes provided the ability to increase the catalytic efficiency of cellulose hydrolysis. The copolymers with different molecular weight and composition were synthesized and the influence of polymer structure on enzymatic activity of EPCs was evaluated. It was noticed, that the difference in activity between free and conjugated enzymes is more pronounced at lower enzyme concentrations. The pretreated biomass experiments showed that the hydrolysis yield depends on

the biomass pretreatment. Enzyme attachment in the conjugates reduced or eliminated the effect of glucose inhibition during the hydrolysis the at tested loading levels.

In summary, adjusting the structure of the polymers and the interactions between the polymer and the cargo (peptides or enzymes) can be considered as a promising tool in regulating the properties of peptide/enzyme-polymer colloids. The results of this study can be used to optimize the polymeric colloid structures with an appropriate properties for the specific application in the field of drug delivery and bioconversion.

8.2. Future work

8.2.1. Evaluation of the morphology of micellar assemblies from AIPs and peptides

The experiments from Chapter 3 and 4 demonstrate the formation of mixed micellar assemblies from AIPs and peptides as well as location of peptide within the micellar interior. While previous research conducted in our group investigated the morphology of micellar assemblies from AIPs using small angle neutron scattering (SANS), the shape and size of the AIP-peptide micellar assemblies still need to be investigated. Therefore, SANS would be used to evaluate the shape, size, internal structure, and composition of the assemblies. At the same time, all the experiments would be carried out at two temperatures: 25 and 37 °C which are needed for the drug delivery systems.

8.2.2. Detailed location investigation of peptide within IMAs

The experiments from Chapter 4 evaluate the peptide position and dynamics in IMAs. However, the peptide was spin labeled only to C-terminus end and the position of the peptide was determined only for that part of the molecule. Therefore, the more detailed investigation of the peptide location will be performed. For this, the label molecule will be attached to the N-terminus, C-terminus end, and in the middle of the peptide chain in order to determine the more precise

position of the peptide molecule within the micellar assemblies and evaluated by EPR spectroscopy.

AIPs have been showed to form the micelles and micellar assemblies in both polar and nonpolar media. While the position of the peptide within the micellar interior in polar aqueous media was evaluated, the location of the peptide in nonpolar solvent such as toluene still should be examined. At the same time, the behavior of the peptide within the micelle upon the changes of environment polarity will be evaluated by triggering the changes by the addition of acetone to the system. For this, the EPR study would be performed.

8.2.3. In vivo evaluation of the IMAs loaded with the real drug

The experiments from Chapter 5 evaluated the IMAs interactions with the model membrane and release of the dye onto it. However, replacing the dye with real drug and investigation of the AIP-based drug delivery system in vivo is still necessary. Therefore, anticancer drug paclitaxel or another poorly water-soluble drug, would be loaded into IMAs and tested in vivo in order to evaluate the use of AIPs-based systems in drug delivery systems.

8.2.4. Improvement of reusability of polymeric cellulosomes

Industrial biomass hydrolysis is still economically challenging. Enzymes account almost 50% of biomass hydrolysis and 20 % of total cost of cellulosic bioethanol production. Therefore, the possibility to reduce the cost in enzymatic stage is important. It can be potentially reduced by improving the enzymes recovery and reuse. In Chapter 7, the polymeric cellulosomes were formed from cellulases and copolymers. In order to improve the reusability of the cellulosomes, the EPCs will be attached to the magnetic nanoparticles. The goal of this work will be to create and characterized the magnetic EPCs particles in order to improve the catalytic activity and reusability of the enzymes.